Application of Electroseismic Techniques to Geohydrological Investigations in Karoo Rocks

by

Francois Daniel Fourie

Submitted in fulfilment of the requirements for the degree of

Doctor of Philosophy

in the Faculty of Natural and Agricultural Sciences, Department of Geohydrology, at the University of the Free State, Bloemfontein, South Africa

November 2003

Promoter: Prof. J.F. Botha (Ph.D.)

Acknowledgements

Many people contributed in some way to the success of this study. I would like to express my sincere gratitude to each of the following people:

Firstly, I would like to thank Professor Jopie Botha, my promotor for this study, for his kind assistance and the long discussions we had on issues regarding my research, as well as other interesting topics. His experience and expertise saw this project through.

I am also very grateful to Professor Alain Cloot for his friendly support. His office was always open when I needed help and his advice was always much appreciated.

The National Research Foundation and the Water Research Commission provided funding for the research conducted in this study. Their financial assistance was greatly appreciated.

All the personnel at IGS are thanked for their eagerness to assist and their interesting conversations. I would especially like to thank Professor Frank Hodgson, director of IGS, Professor Gerrit van Tonder, Mr Eelco Lucas, Doctor Brent Usher and Ms Jane van der Heever for all their help during the years that I have spent as a student at IGS.

My girlfriend Anita Venter supported me throughout this study, especially during the frustrating periods when my research progressed too slowly to my liking. I will always be thankful to her.

Last, but not least, I would like to thank my parents, Frans and Anita Fourie, for all their love and help (financial and other) throughout my life and during my studies. I have truly been blessed to have had them as a part of my life.

TABLE OF CONTENTS

LIST OF FIGURES

LIST OF TABLES

LIST OF SYMBOLS

LATIN SYMBOLS

a	Consolidation factor of sedimentary rocks (Section 3.2.2)	[1]
	Constant in Archie's law depending on rock parameters (Section 5.1)	[1]
$\mathbf{b}_i^{\mp}$	Electroseismic eigenvector for down-going (-) or up-going (+) wave of type i (Section 3.3.2)	
b	Consolidation factor of sedimentary rocks (Section 3.2.2)	[1]
$b/2$	Tuning thickness (Section 3.2.1)	[s]
b_+	Ionic mobility of cations (Appendix B)	[m s^{-1} N^{-1}]
b_-	Ionic mobility of anions (Appendix B)	[m s^{-1} N^{-1}]
d	Debye length (Section 2.1 and Appendix B)	[m]
	Distance used in illustrating Fresnel zone concepts (Section 3.1)	[m]
	Depth of interface below ground surface	[m]
d_1, d_2	Distances used in illustrating Fresnel zone concepts (Section 3.1)	[m]
$\tilde{d}$	Length parameter, less than or equal to the Debye length (Appendix B)	[m]
$\mathbf{e}_i$	Unit vector pointing in the direction of increasing i	[1]
e	Electronic charge	[C]
e_{kl}	Strain tensor	[1]
$\mathbf{f}$	Body forces (Section 2.2.2)	[N m^{-3}]
	Column vector giving the depth-dependencies of the physical quantities that are continuous across a welded interface (Appendix C1)	
$\mathbf{f}_i$	Column vector giving the depth-dependencies of the physical quantities in medium i that are continuous across a welded interface (Appendix C3)	
f_0	Dominant frequency	[Hz]
g	Gravitational acceleration	[m s^{-2}]
$\mathbf{h}$	Column vector containing values of the non-zero physical quantities that are continuous across a welded interface (Appendix C1)	
h	Thickness of upper layer in contact with the air (Section 3.1.4)	[m]
$\mathbf{i}$	Cartesian unit vector	[1]
$\mathbf{j}$	Cartesian unit vector	[1]
$\mathbf{k}$	Cartesian unit vector	[1]
	Propagation vector (Section 2.3)	[m^{-1}]
k_B	Boltzmann constant	[J K^{-1}]
k_{ij}	Reflection coefficients for currents flowing from medium i to medium j (Section 3.1)	[1]

k_{em}	Propagation constant of electromagnetic wave	$[m^{-1}]$
k_s	Propagation constant of seismic wave	$[m^{-1}]$
k_i	Propagation constant of seismic wave in medium *i* (Section 3.3)	$[m^{-1}]$
k	Dynamic hydraulic permeability	$[m^2]$
k_0	Low frequency hydraulic permeability	$[m^2]$
$l_{1,}\ l_2$	Distances used in illustrating Fresnel zone concepts (Section 3.1)	[m]
m	Measure of pore connectivity (Section 5.2)	[1]
	Dimensionless number consisting of geometric terms of the porous medium (Appendix B)	[1]
$\mathbf{n}$	Unit vector normal to a surface	[1]
n	Measure of pore connectivity (Section 5.2)	[1]
n^0	Ionic concentration far from grain surface in fluid-saturated porous media	$[m^{-3}]$
n_+	Ionic concentration of cations in pore fluid	$[m^{-3}]$
n_-	Ionic concentrations of anions in pore fluid	$[m^{-3}]$
$\mathbf{p}$	Electric dipole moment per unit area	$[C\ m^{-1}]$
$\mathbf{p}_{ij}$	Electric dipole moment per unit area on the interface between media *i* and *j*	$[C\ m^{-1}]$
p	Horizontal phase slowness	$[s\ m^{-1}]$
q_i	Vertical phase slowness in medium *i* (Section 3.3)	$[s\ m^{-1}]$
$\mathbf{r}$	Position vector	[m]
$\mathbf{r_{sd}}$	Displacement vector from the seismic source to an electric dipole	[m]
$\mathbf{r_{dm}}$	Displacement vector from an electric dipole to the measurement position	[m]
r_i	Distance from measurement position to the interface between media *i* and *i*+1 (Section 3.3.1)	[m]
s_i	Phase slowness of wave type *i*	$[s\ m^{-1}]$
t	Time	[s]
$\mathbf{u}$	Solid displacement vector	[m]
$\mathbf{u}_{pf}$	Solid displacement vector associated with the fast pressure wave	[m]
$\mathbf{u}_{ps}$	Solid displacement vector associated with the slow pressure wave	[m]
u_{ij}	Solid displacement at the interface between media *i* and *j* (Section 3.3)	[m]
v	Wave velocity	$[m\ s^{-1}]$
v_i	Seismic wave velocity in medium *i* (Section 3.1)	$[m\ s^{-1}]$
v_s	Shear wave velocity (Section 4.2)	$[m\ s^{-1}]$
$\mathbf{w}$	Relative fluid/solid displacement multiplied by porosity	[m]

$\mathbf{w}_i$	Weighting vector in medium i (Section 3.3.2, Appendix C3)	[1]
$\mathbf{x}$	Position vector	[m]
z	Ionic valence	[1]
z_0	Reference depth for phase considerations (Appendix C3)	[m]
z_i	Thickness of layer i (Section 3.3.1)	[m]
	Depth to bottom of layer i (Appendix C3)	[m]
$\mathbf{A}$	Constant matrix used in the description of the matrix method (Appendix C1)	
	Auxiliary matrix used to investigate the thin layer response (Appendix C3)	
$\mathbf{B}$	Magnetic induction field	[T]
	Auxiliary matrix used to investigate the thin layer response (Appendix C3)	
$\mathbf{C}$	Auxiliary matrix used to investigate the thin layer response (Appendix C3)	
C	Elastic constant	[Pa]
	Salinity (Section 3.2)	[mol L^{-1}]
C_{em}	Excess conductance associated with electromigration of double layer ions (Appendix B)	[S]
C_{os}	Electro-osmotic conductance (Appendix B)	[S]
C_{ijkl}	Elasticity tensor	[Pa]
$\mathbf{D}$	Displacement current density	[A m^{-2}]
	Matrix formed from the electroseismic eigenvectors (Appendix C1, Chapter 5)	
	Auxiliary matrix used to investigate the thin layer response (Appendix C3)	
$\mathbf{E}$	Electric field	[V m^{-1}]
$\mathbf{E}_i$	Matrix containing the eigenvectors of medium i as columns (Appendix C)	
E	Young's modulus for a continuum (Section 2.2)	[Pa]
	Electric field amplitude	[V m^{-1}]
E^*	Young's modulus for a continuum	[Pa]
E_{fr}	Young's modulus for a dry porous frame	[Pa]
$\mathbf{F}$, $\mathbf{G}$	Matrices containing the solutions to the eigenvalue problem (Appendix C)	
G	Shear modulus of porous frame	[Pa]
G_s	Shear modulus of solid material	[Pa]
H	Elastic constant	[Pa]
$\mathbf{H}$	Magnetic field	[A m^{-1}]
$\mathbf{I}$	Identity tensor	[1]
I	Electrical current	[A]
$\mathbf{J}$	Electric current density	[A m^{-2}]
$\mathbf{J_c}$	Conduction current density	[A m^{-2}]
$\mathbf{J_s}$	Streaming current density	[A m^{-2}]

K_h	Horizontal hydraulic conductivity	[m s^{-1}]
K	Bulk modulus	[Pa]
K_s	Bulk modulus of solid material	[Pa]
K_f	Bulk modulus of fluid	[Pa]
K_{fr}	Bulk modulus of porous frame	[Pa]
K_{pore}	Bulk modulus of fluid-saturated pores	[Pa]
L	Electrokinetic coupling coefficient	[A s^2 kg^{-1}]
L_0	Low frequency electrokinetic coupling coefficient	[A s^2 kg^{-1}]
L_{pf}	Electroseismic transfer function for the fast pressure wave	[V m^{-2} s^{-2}]
L_{ps}	Electroseismic transfer function for the slow pressure wave	[V m^{-2} s^{-1}]
$\mathbf{M}$	Matrix formed from the electroseismic eigenvectors and phase factors	
M	Elastic constant	[Pa]
M_s	Specific surface of porous material (Section 5.2)	[m^{-1}]
N	Ionic concentration	[m^{-3}]
P	Fluid pressure above hydrostatic pressure	[Pa]
P_0	Auxiliary term (Appendix B)	
$\mathbf{P}$	Electric dipole moment	[C m]
R_{ij}	Reflection coefficient for wave modes converted from type i to type j	[1]
$\mathbf{T}$	Traction	[Pa]
T	Temperature	[K]
	Magnetoseismic transfer function for the shear wave (Section 4.1)	[A m^{-2} s^{-1}]
T_{ij}	Transmission coefficient for wave modes converted from type i to type j	[1]
T_R	Temporal resolution	[s]
U	Amplitude of solid grain displacement	[m]
W	Amplitude of relative fluid/solid displacement	[m]

GREEK SYMBOLS

α	Attenuation coefficient for wave propagation	[m^{-1}]
α_1, α_2	Auxiliary parameters (Section 3.3)	[1]
α_∞	Tortuosity	[1]
α_K^{HS}	Constant used in the modulus/porosity relations of Hashin-Shtrikman	[1]
α_G^{HS}	Constant used in the modulus/porosity relations of Hashin-Shtrikman	[1]
$\beta_{s,em}$	Auxiliary term for shear waves and electromagnetic waves	[1]

$\beta_{pf,ps}$	Auxiliary term for fast and slow pressure waves	[1]
$\beta_{sv,tm}$	Auxiliary term for shear waves with vertical polarisation and electromagnetic waves with transverse magnetic fields	[1]
γ	Auxiliary parameter	[s^2 m^{-2}]
δ_{ij}	Kronecker delta	[1]
δ	Electromagnetic skin depth	[m]
δ_v	Viscous skin depth	[m]
ϵ	Dielectric permittivity of bulk material	[C^2 N^{-1} m^{-2}]
ϵ_s	Dielectric permittivity of solid material	[C^2 N^{-1} m^{-2}]
ϵ_f	Dielectric permittivity of fluid	[C^2 N^{-1} m^{-2}]
$\tilde{\epsilon}$	Electrical permittivity	[C^2 N^{-1} m^{-2}]
ζ	Electric potential at the slipping plane of the electric double layer	[V]
	Auxiliary term (Section 3.3)	[1]
η	Fluid viscosity	[Pa s]
θ	Cylindrical coordinate (Section 3.1.4)	[rad]
θ_{ij}	Critical angle for wave modes converted from type *i* to type *j*	[rad]
λ	Lamé constant for a homogeneous, isotropic continuum (Section 2.2)	[Pa]
	Wavelength of light wave (Section 3.1)	[m]
	Wavelength of seismic wave (Section 3.2)	[m]
	Eigenvalue (Appendix B)	[m^{-1}]
λ_0	Dominant seismic wavelength (Section 3.3)	[m]
λ^*	Lamé constant for a fluid-saturated porous medium	[Pa]
λ^*	Lamé constant for dry porous frame	[Pa]
λ_s	Wavelength of seismic wave	[m]
λ_{em}	Wavelength of electromagnetic wave	[m]
μ	Lamé constant for a homogeneous, isotropic continuum (Section 2.2, Appendix C1)	[Pa]
	Magnetic permeability	[Wb A^{-1} m^{-1}]
μ^*	Lamé constant for a fluid-saturated porous medium	[Pa]
ν	Poisson's ratio for a continuum	[1]

ν^*	Poisson's ratio for a fluid-saturates porous medium	[1]
ν_{fr}	Poisson's ratio for a dry porous frame	[1]
ξ	Auxiliary term (Section 3.3)	[1]
ρ	Mass density of bulk material	[kg m^{-3}]
	Cylindrical coordinate (Section 3.1.4)	[m]
ρ_s	Mass density of solid material	[kg m^{-3}]
ρ_f	Mass density of fluid	[kg m^{-3}]
$\tilde{\rho}$	Effective density	[kg m^{-3}]
ρ_t	Density parameter (defined in Section 2.2.1.1)	[kg m^{-3}]
σ	Bulk electrical conductivity	[S m^{-1}]
σ_0	Low frequency electrical conductivity of bulk material (Appendix B)	[S m^{-1}]
σ_i	Bulk electrical conductivity of medium *i*	[S m^{-1}]
τ, τ_{ij}	Stress tensor	[Pa]
ϕ	Porosity	[1]
$\Delta\phi$	Phase difference between wave components (Section 3.1.3)	[rad]
φ	Electric potential	[V]
φ_0	Electric potential at the fluid/solid interface of fluid-saturated porous media	[V]
φ_δ	Electric potential at the transition from the Stern- to the Gouy layer	[V]
ω	Angular frequency	[rad s^{-1}]
ω_t	Transition angular frequency	[rad s^{-1}]
Γ	Auxiliary term (Section 4.4)	[Pa^2]
Δ	Elastic parameter	[Pa^2]
Λ	Weighted volume-to-surface ratio of porous material (Appendix B)	[m]
Λ_i	Matric containing the vertical phase factors in medium i (Appendix C)	[1]
Σ	Surface area of interface contributing to electroseismic energy conversion	[m^2]

Notation

Throughout this thesis a right-handed Cartesian co-ordinate system is employed, unless otherwise stated. The following notation conventions are used:

- Scalar quantities (0^{th} order tensor quantities) are indicated by symbols in italic print:

$$u, A, \phi$$

- Vector quantities (1^{st} order tensor quantities) are indicated by lower case symbols in bold print, or in the index notation by lower case italic symbols with the index as a subscript:

$$\mathbf{u}, \mathbf{p}, \mathbf{r} \qquad u_i, p_i, r_i$$

- Matrices and tensors of order two and higher are indicated by upper case symbols or Greek symbols in bold print, or in the index notation by upper case italic symbols or italic Greek symbols with the indexes as subscripts:

$$\mathbf{A}, \mathbf{K}, \boldsymbol{\tau} \qquad A_{ij}, K_{ij}, \tau_{ij}$$

- Cartesian unit vectors are written in one of the following formats, depending on convenience:

$$\mathbf{e}_x, \mathbf{e}_y, \mathbf{e}_z \qquad \mathbf{i}, \mathbf{j}, \mathbf{k} \qquad \hat{\mathbf{x}}, \hat{\mathbf{y}}, \hat{\mathbf{z}}$$

- Non-Cartesian unit vectors are written in one of the following formats, depending on convenience:

$$\mathbf{e}_1, \mathbf{e}_2, \mathbf{e}_3 \qquad \hat{\mathbf{x}}_1, \hat{\mathbf{x}}_2, \hat{\mathbf{x}}_3$$

- Einstein's summation convention for repeated indexes is used throughout this work:

$$e_{ii} = e_{11} + e_{22} + e_{33}$$

$$\frac{\partial \tau_{ji}}{\partial x_j} = \frac{\partial \tau_{1i}}{\partial x_1} + \frac{\partial \tau_{2i}}{\partial x_2} + \frac{\partial \tau_{3i}}{\partial x_3}$$

- When repeated indexes do not imply summation, square brackets around the indexes are employed:

$$e_{[ii]}$$

- Partial differentiation with respect to the i^{th} co-ordinate is also written in compact form by employing a comma between the indexes. The summation convention still applies:

$$\frac{\partial \tau_{ji}}{\partial x_j} = \tau_{ji,j}$$

- First and second time-derivatives are indicated by one or two dots placed above the symbol:

$$\frac{\partial \mathbf{u}}{\partial t} = \dot{\mathbf{u}} \qquad \frac{\partial^2 \mathbf{u}}{\partial t^2} = \ddot{\mathbf{u}}$$

- When convenient, brackets are used to describe a vector quantity in terms of its components:

$$\mathbf{u} = u_1\mathbf{e}_1 + u_2\mathbf{e}_2 + u_3\mathbf{e}_3 = (u_1, u_2, u_3)$$

- The symbol i is used to indicate the imaginary part of a complex quantity. Where convenient, brackets are used to express a complex quantity in terms of its real and imaginary parts:

$$z = x + iy = (x, y)$$

Terminology

In this thesis terminology from the seismic and electromagnetic branches of geophysics will be employed.

- The term **acoustic wave** in geophysics generally refers to a longitudinal (dilatational-, pressure-, *P*-) wave that may travel through fluids and solid media.
- The **offset** is the horizontal distance from the seismic source to the observation position or the position of interest.
- **Quasi-static** refers to phenomena that undergo temporal changes at low frequencies. Quasi-static flow, for example, occurs at frequencies that are adequately low so that viscous flow dominates over inertial flow.
- The term **seismic velocity** is used in geophysics to describe the scalar quantity that would more correctly be called *seismic speed*, that is, the speed at which a seismic disturbance propagates in a medium.
- A **half-space** is a model of the earth bounded by only one plane surface. The model is so large in the other dimensions that only one boundary affects the results.
- A **whole-space** is an unbounded model of the earth. The model is so large in dimension that no boundary effects need to be considered.
- A seismic **shot** is the application of impulsive source of seismic energy.
- **Stacking** is the averaging of a number of transient signals.
- A **trace** is a time-record of the data recorded at specific position for a specific shot.
- The application of **gain** to a time-record compensates for signal amplitude loss over time due to spherical spreading of seismic waves and other loss mechanisms.

CHAPTER 1 INTRODUCTION

1.1 General

The 1996 constitution of South Africa considers the availability of drinking water a basic human right. Considerable emphasis is therefore currently placed on the identification of sustainable water supplies. Groundwater is the sole source of potable water for many urban and rural communities in South Africa and efficient methods of exploration, development and management of groundwater resources are required.

The vast majority of South African aquifers are of the secondary type, that is, their water-bearing properties were developed through secondary processes such as faulting or fracturing. It is estimated that approximately 90% of South African groundwater occurs in secondary aquifers. More than 50% of South Africa is underlain by rocks of the Karoo Supergroup. These rocks are typically dense and not extensively fractured so that their permeabilities are low when compared with primary porous formations.

The existing geophysical techniques, particularly magnetic, electromagnetic and resistivity methods, have been used for many years to locate groundwater in South Africa, but with varying degrees of success. The magnetic method is used almost exclusively to locate and delineate intrusive magmatic bodies and the contact zones between the intrusive bodies and the host rock are then considered to be targets in groundwater exploration. The electromagnetic and resistivity methods are used to map the subsurface conductivity distribution of the area under investigation. From the conductivity information inferences regarding the subsurface geology are made and geological structures are mapped.

Although highly weathered zones containing groundwater will in some instances produce large enough conductivity contrasts to allow direct detection by means of the electromagnetic or resistivity method, groundwater exploration by geophysical means is in general an indirect process whereby subsurface geological structures that may act as, or be associated with aquifers are identified.

In the past groundwater exploration in Karoo rocks mostly targeted intrusive dolerite bodies. When such bodies do not occur in the area being explored, the magnetic method is of little use for groundwater exploration. The electromagnetic and resistivity methods on the other hand are also frequently unsuccessful in locating Karoo aquifers due to a lack of conductivity contrast between the fractured zones and the surrounding host rock.

One method that promises to circumvent many of the difficulties associated with conventional geophysical techniques in siting water in Karoo aquifers, is the electroseismic (ES) technique. This method, which is based on the conversion of seismic energy to electromagnetic energy in deformable fluid-filled porous rocks, does not only depend on the rock properties but also the fluid. Indeed there are indications that the method may hold particular advantages for Karoo formations, where bedding-parallel fractures often form the main conduits of water to boreholes Botha *et al.* (1998).

The rock properties that play a particular important role in ES techniques include the bulk and shear moduli of deformation. The same parameters also determine the extent to which rocks will deform under the influence of stresses, with a corresponding reduction in the apertures of fractures present in the rock (Makurat, 2001) and the ability of the fracture to transmit water (Botha and Cloot, 2002). Indeed, Botha *et al.* (1998) show that a 20% decrease in the aperture of the fracture will cause a drop of almost 50% in the yield of a fracture and that the over-pumping of a borehole could cause the fracture to collapse. ES techniques may therefore not only be useful in siting boreholes, but also provide information on the elastic properties of the rock matrix that is vital for the management of boreholes in fractured rock formations.

1.2 Geology and geohydrology of Karoo rocks

Botha *et al.* (1998) give a comprehensive treatment of the geology and geometry of Karoo aquifers. The Karoo rocks underlie approximately 50% of South Africa, as can be seen in Figure 1.2.1 where a map of Southern Africa is shown with the occurrence of Karoo rocks roughly outlined.

The rocks of the Karoo Sequence were formed when sediments filled an intracratonic basin on Gondwanaland, 300 to 160 million years ago. The sediments were deposited under varying depositional environments, resulting in clearly distinguishable groups of sediments. The Karoo sedimentation was ended by the outpour of the Drakensberg lavas, which buried the sediments to depths of between 2 500 and 3 500 m. The increased pressure and temperature caused the sediments to lithify to the sandstone, siltstone and mudstone layers one finds in the Karoo rocks. Lithification also resulted in a large decrease of porosity. The porosities of the sedimentary rocks were decreased even further by the deposition of secondary minerals containing carbonates and silica. A further result of lithification was the decrease in elasticity of the Karoo rocks.

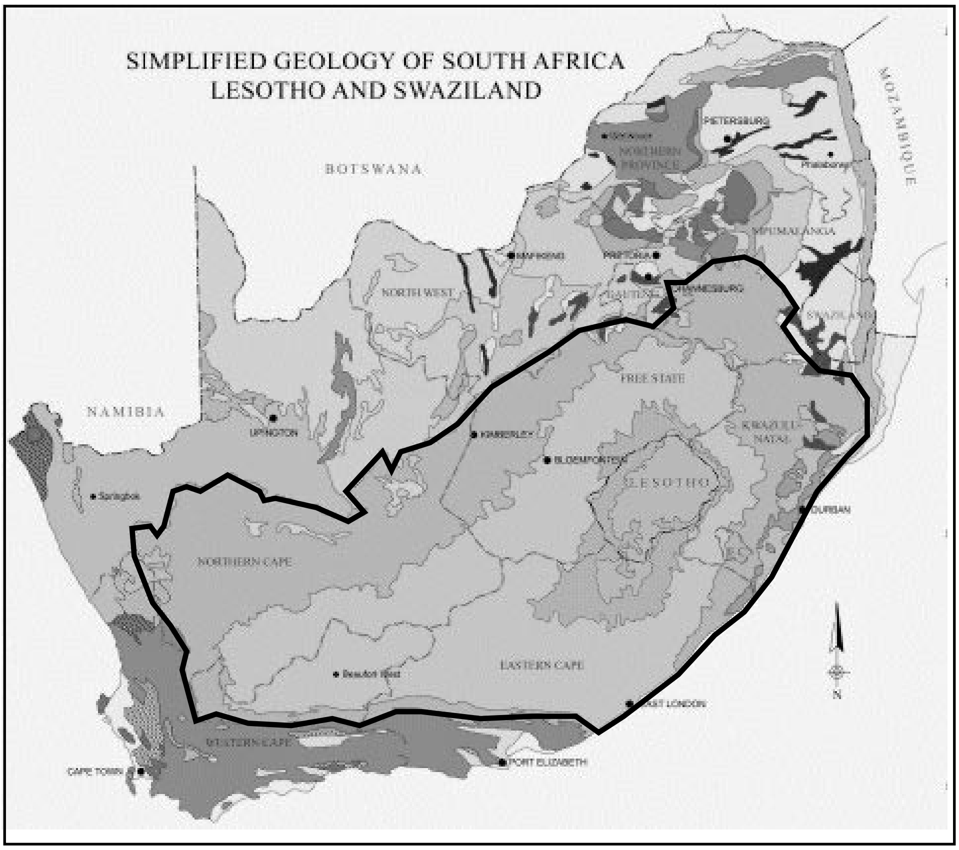

Figure 1.2.1. The occurrence of rocks of the Karoo Supergroup in South Africa.

Rapid weathering and erosion caused large volumes of Karoo rocks to be eroded away in a relatively short time. The resulting mass deficit led to isostatic upliftment of the Karoo rocks, which caused fracturing of the lithified sediments. As a result of fracturing, the average porosity and permeability of the strata increased. The relatively more inelastic sandstones in the Karoo formations are more likely to be fractured than the more elastic siltstone and mudstone layers. Contact planes between the various strata of the Karoo rocks are also favourable positions for the development of fractures.

Most of the fracturing of the Karoo rocks developed due to widespread volcanism during the Jurassic Age. Apart from the outflow of the Drakensberg lavas, intrusion of dolerite laccoliths, sills and dykes greatly contributed to the fracturing of the sedimentary rock formations.

Experience has shown that a borehole in a Karoo aquifer will only have a significant yield if it intersects a fracture. In addition, the water-yielding fractures in Karoo rocks are usually horizontal and have aperture widths in the millimetre range up to a few centimetres. The fractures usually occur at depths of less than 50 m. Although the areal extent of the fractures may be considerable, fracturing is not uniformly present.

The physical dimensions of the fractures do not allow large quantities of water to be stored in the fractures themselves. The main water supply to a borehole intersecting a fracture must therefore be the sedimentary rock matrix that surrounds the fracture. Fractures in Karoo rocks act as conduits that transport water from the sedimentary rock matrix to the borehole. Two types of flow are therefore found in Karoo aquifers, namely: matrix flow and fracture flow. For a borehole intersecting a fracture, flow in the matrix is predominantly vertical and linear, and not radial and horizontal (Botha *et al.*, 1998). The flow velocities in the fractures are usually very high, while low flow velocities can be expected in the matrix. For a borehole not intersecting a fracture, matrix flow is radial and horizontal. Figure 1.2.2 summarises the above observations.

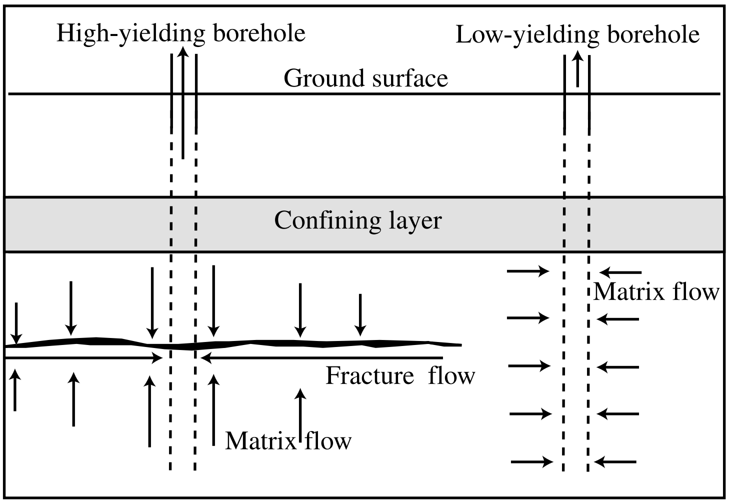

Figure 1.2.2. Matrix and fracture flow in Karoo aquifers.

1.3 Electroseismic field measurements and theory from a historical perspective

1.3.1 Field measurements of electroseismic phenomena

In 1932 Blau and Statham (1936) filed for patent rights on an apparatus for seismic-electric prospecting. The patent rights were eventually awarded in 1936. This is the earliest published work on the combined use of seismic and electric methods for prospecting. The method consisted of applying a constant voltage to a pair of electrodes and measuring the change in electric current flow due to changes in the ground resistivity caused by the passing of a seismic wave. The apparatus proposed by Blau and Statham (1936) is essentially a different form of a geophone, measuring changes in the applied electric current rather than the displacement of the solid earth material at surface.

The method of Blau and Statham (1936) was also employed by Thompson (1936) in a series of field measurements. In a follow-up paper, Thompson (1939) showed that the changes in current are indeed due to changes in the ground resistivity and not due to changes in the contact resistance between the electrodes and the ground caused by vibration. The author could, however, not provide a definite answer as to the mechanism of resistance change, but suggested that it was due to some loose contact phenomenon between the particles of the earth.

Ivanov (1939) measured electric fields generated by seismic waves without the application of voltages to the ground. Apart from the electric field that travels with the seismic pulse (the co-seismic electric field) he also recorded an electric pulse that reached the antennæ several milliseconds before the arrival of the seismic pulse and called this the electroseismic effect of the 2nd kind. This electroseismic effect of the 2nd kind was also observed by Martner and Sparks (1959) when conducted a study using explosive seismic sources and electric antennæ. From an examination of the electromagnetic arrival times they showed that seismic-to-electromagnetic energy conversion can take place at depth, resulting in measurable electric fields at surface. From the field data they recorded during their study, they noted that the energy of the electroseismic effect of the 2nd kind seemed to be generated at the bottom of a weathered zone at their survey site. Although there was uncertainty as to whether the electric signal associated with the electroseismic effect of the 2nd kind was derived from a change in resistivity near the boundary or from a boundary-dependent mechanism, the observation was the first step towards the realisation that electroseismic energy conversion can occur at interfaces between dissimilar media.

Long and Rivers (1975) performed further investigations into the modulation of electrical currents in the earth caused by the propagation of seismic waves. They again used the method of Blau and Statham (1936) but employed a standard Wenner electrode array to introduce steady currents into the earth and measured the changes in voltage. The co-seismic response they measured was shown to correlate best with the low frequency surface wave called the Rayleigh wave.

Maxwell *et al.* (1992) recorded electromagnetic responses from seismically excited targets. They measured responses from a shallow overburden overlying a crystalline basement, quartz veins and sulphide ores. Apart from electroseismic energy arrivals with frequency content similar to the seismic waves, they also recorded high-frequency impulsive responses that seemed to have their origin in highly non-linear processes. They showed that these responses emanated from the sulphide ore bodies and thus demonstrated the possibility of employing ES techniques in mineral exploration. Further field trials in the use of electroseismic methods for the detection of massive sulphides were conducted by Kepic *et al.* (1995). They confirmed that high frequency electroseismic energy conversion takes place when a pressure wave arrives at the ore-body boundary. Russell *et al.* (1997) also investigated the use of electroseismic techniques for the exploration of sulphide ore bodies. They recorded high frequency signals from the target bodies and were successful in making reasonable geological interpretations from the recorded field data.

Thompson and Gist (1993) conducted field measurements showing that electromagnetic disturbances can be caused by seismic waves propagating in fluid-saturated sediments. They recorded both seismic and electric data over a test site and were able to show that surface measurable electric fields can be recorded when seismic waves traverse an interface between two different fluid-saturated rocks. The electroseismic effect of the 2nd kind observed by Ivanov (1939) and Martner and Sparks (1959) was thus shown to be an interface response. Their data also showed that while some of the observed electric events may be correlated to seismic reflectors, other events were probably due to electric rather than mechanical contrasts.

Further evidence for the existence of an interface response was obtained by Butler *et al.* (1996). They recorded an electroseismic response from a shallow boundary between road fill and glacial till. In their field data they distinguished between signals belonging to the interface response and co-seismic energy. They also proposed a simple electrostatic model to account for their observations. Mikhailov *et al.* (1997) also conducted electroseismic field measurements at a test site where the geology consists of topsoil overlying glacial till, which in turn overlies the bedrock consisting of fractured granite. They interpreted the recorded signal in terms of electroseismic conversion at the soil/glacial till interface, the water table and the glacial till/bedrock interface. In addition they recorded co-seismic electric fields generated by the head wave traversing the soil/glacial till interface.

Millar and Clarke (1997) developed the first commercial electroseismic system for hydrogeological site investigations. Their technique employs a two-channel system that analyses the recorded signal in an attempt to obtain information on the porosity and permeability of the fluid-saturated porous rocks near the measurement position. The technique is called Electrokinetic Sounding (EKS).

Beamish and Peart (1998) performed electroseismic field measurements using both two- and multi-channel equipment. They concluded that two channel systems, as employed in the Electrokinetic Sounding technique, provide insufficient data to describe the spatial and temporal nature of the generated electric fields. They measured both seismic and electromagnetic responses at a test location in Zimbabwe where their results clearly showed the distinction between co-seismic energy arriving at the measurement positions and the interface responses. Beamish (1999) systematically conducted further field measurements using both two- and multi-channel equipment. He showed that the received voltages are largely independent of electrode type. He also investigated the effects of antenna length and concluded that the received voltages are largely independent of dipole length when the position of the electrode nearest to the seismic source remains at a fixed offset. Small offset locations were shown to provide the largest horizontal electric field amplitudes and the highest degree of sensitivity. The multi-channel field measurements again showed different manifestations of co-seismic energy and the interface response.

Mikhailov *et al.* (2000) used borehole electroseismic measurements to detect and characterize fractured zones along the length of the borehole. They measured the co-seismic electric field induced by a Stoneley wave and were able to derive a porosity log from the electroseismic measurements that agreed with laboratory measurements. Hunt and Worthington (2000) performed similar investigations in which they used electroseismic borehole logging procedures to obtain an amplitude correlation between the electroseismic response and previously obtained hydrogeological data, such as hydraulic conductivity.

Garambois and Dietrich (2001) performed detailed field measurements of electroseismic responses at a test site for hydrogeological studies in France. By applying a band-pass filter to the record data they were able to separate the responses due to co-seismic fields from the interface responses. Their results show the relative weakness of the interface response as compared with the co-seismic fields. In order to measure the weaker interface response Haines *et al.* (2001) conducted field experiments in which they used an artificial vertical trench filled with saturated sand, with the seismic source on one side of the trench and the electrodes on the other. This experimental geometry allowed the interface response to be recorded prior to the arrival of the co-seismic energy. The authors also showed that measured response has similarities with the electric field that can be expected from an electric dipole situated on the interface vertically below the seismic source.

1.3.2 Development of electroseismic theory

The first development in the theory of electroseismic phenomena can be attributed to Frenkel (1944). The author postulated equations that describe the relative fluid-solid flow induced by a seismic wave. He considered the electric fields induced by fluid flow by employing the Helmholtz-Smoluchowski equation. This equation only allows for co-seismic electric fields and does not take into consideration the generation of electromagnetic waves at interfaces (the interface response). Since the Helmholtz-Smoluchowski equation considers only the electric fields caused by pressure gradients, it fails to take account of the electroseismic energy conversion associated with shear waves.

Electroseismic phenomena are closely associated with the relative fluid-solid flow caused by seismic waves. The theory of the propagation of seismic waves in fluid-saturated porous media, developed in a series of papers by Maurice A. Biot (Biot, 1956a, 1956b, 1962a, 1962b) is therefore of prime importance, and could be seen as the next step in the development of electroseismic theory. According to Biot's theory a seismic disturbance will propagate through fluid-saturated porous media in the form of one rotational (shear) and two dilatational (pressure) waves. The two pressure waves are commonly referred to as waves of the first and second kind. Pressure waves of the first kind correspond to the solid and fluid parts moving in phase, whereas waves of the second kind correspond to the solid and fluid parts moving out of phase. Biot also shows that the pressure waves of the second kind propagate at lower velocities than waves of the first kind. These waves are therefore frequently referred to in literature as the Biot slow and fast waves, respectively. Biot's theory indicates that the slow waves are dissipative in nature and die out rapidly with distance from the source. These waves are however again generated when fast waves intersect interfaces between dissimilar fluid-saturated porous media (Geertsma and Smit, 1961).

Nourbehecht (1963) fails to make use of Biot's theory when he studies irreversible thermodynamic coupling effects in the porous earth and he investigates electrokinetic coupling by assuming stationary solid material and only allows for fluid flow. Again, no attention is given to the electroseismic energy conversion associated with shear waves. His results do, however show that the angle of incidence of pressure waves impinging on a boundary between two fluid-saturated porous media needs to be non-zero for the generation of a surface detectable electric signal.

Neev and Yeatts (1989) propose equations that attempt to model the coupling between mechanical waves and electric fields. Because their work is not based on the full set of Maxwell's equations, they too incorrectly conclude that shear waves do not generate electromagnetic waves. The first theoretical development in electroseismic theory that incorporates the full set of Maxwell's equation is attributed to Pride (1994). The author uses volume-averaging arguments to derive a set of macroscopic governing equations that describe electroseismic phenomena. These equations consist of Biot's equations coupled to Maxwell's equations by means of two transport equations satisfying Onsager's principle of reciprocity of coupled flows.

Haartsen (1995) and Pride and Haartsen (1996) use the governing equations of electroseismic phenomena to study plane waves in homogeneous porous media. Their results show that for plane longitudinal waves the streaming current induced by pressure gradients is balanced by an equivalent and opposite conduction current driven by the co-seismic electric field. There is therefore no net electrical current within the seismic wave.

As a result, no electromagnetic wave radiation takes place. Similarly, plane shear waves in homogeneous media may cause relative fluid-solid flow due to displacement of the solid grains, thus setting up a co-seismic magnetic field and a small induced co-seismic electric field that travel along with the shear wave. Since there is no current imbalance within the shear wave, no electromagnetic waves are generated. When the seismic wave is, however, incident on an interface between media of different electroseismic properties, a dynamic current imbalance is caused by the variation in the streaming current density across the interface. This current imbalance generates an electromagnetic wave that propagates independently from the seismic wave, thus giving rise to the interface response (the electroseismic effect of the 2^{nd} kind), as observed in the field data of Ivanov (1939), Martner and Sparks (1959), Thompson and Gist (1993), Butler *et al.* (1996), Mikhailov *et al.* (1997), Garambois and Dietrich (2001) and Haines *et al.* (2001).

Haartsen and Pride (1997) use the governing equations of electroseismic phenomena and the Global Matrix Solution method to investigate electroseismic waves from point sources in layered media. Their results indicate that the interface response show similarities with the wavefield that would be obtained if the interface were replaced by an equivalent oscillating electric dipole positioned on the interface directly below the seismic source. This observation confirms that the interface response is due to the generation of independently propagating electromagnetic waves at the boundary between dissimilar fluid-saturated porous media. Haartsen *et al.* (1998) further use Biot theory to calculate the amount of induced relative flow by Green's function solution. In this way they study the dynamic streaming currents from seismic point sources in homogeneous poro-elastic media as a function of salinity, porosity and permeability.

By using a method related to the Global Matrix Method Ranada Shaw *et al.* (2000) arrive at expressions for the electroseismic reflection and transmission coefficients belonging to an interface between two porous media. They investigate the influence of porosity/permeability and salinity contrasts on the magnitude of the interface response.

Garambois and Dietrich (2001) derive electroseismic (and magnetoseismic) transfer functions for the co-seismic electric and magnetic fields. The electroseismic transfer functions give linear relations between the amplitudes of the solid grain displacement associated with the fast and slow pressure waves and the amplitudes of the resulting co-seismic electric fields. Similarly, the magnetoseismic transfer gives a linear relation between the amplitude of the solid grain displacement due to the passing of a shear wave and the amplitude of the induced magnetic field. The correctness of the transfer functions is confirmed by comparison with recorded field data.

1.4 General description of electroseismic techniques

ES techniques make use of the fact that seismic and electromagnetic (EM) energies are generally coupled in wetted porous rocks. With these techniques the earth is seismically excited and an electromagnetic response is measured.

Although various mechanisms exist whereby seismic and EM energies can couple in wetted rocks, Haartsen (1995) suggests that mechanically induced relative flow of charges is likely to cause the largest effects. The surfaces of the mineral grains in rocks usually display net electric charge. As a result the electric charges within the fluid separate into an electric double layer (EDL). The inner layer consists of ions adsorped onto the solid surface, while the outer layer is formed by ions under the combined influence of ordering electrical and disordering thermal forces (Shaw, 1969). A mechanical disturbance that propagates through such a fluid-saturated medium will cause a displacement of the solid phase relative to the fluid phase and a resulting shearing of the ions in the EDL. In this way an electric current is produced in the medium. This phenomenon is generally known as the electrokinetic effect and the resulting macroscopic electric current is called the streaming current. In ES phenomena the streaming current is related to the pressure gradient (and grain acceleration) caused by the travelling seismic wave through the electrokinetic coupling coefficient (Pride, 1994). This coefficient is dependent on the properties of both the solid and the fluid and is influenced by parameters such as the porosity and permeability of the solid and the salinity of the fluid.

The propagation of a disturbance in a porous medium saturated with a viscous fluid may be described mathematically by Biot's theory (Biot, 1956a, 1956b, 1962a, 1962b) which indicates that the disturbance will propagate in the form of one shear wave and two pressure waves (the fast and slow Biot waves). Both pressure waves and the shear wave may cause relative fluid/solid motion and therefore result in the generation of streaming currents in fluid-saturated porous media.

Pride and Haartsen (1996) show that two different types of electroseismic coupling may occur in fluid-saturated porous rock. When pressure waves propagate in homogeneous fluid-saturated porous media, an electric field is generated that is trapped within the pressure wave. Similarly, when shear waves propagate in homogeneous porous media a magnetic field and a small, induced electric field are carried along with the shear wave. No radiated EM waves are therefore produced by seismic waves in homogeneous fluid-saturated porous media. The electric and magnetic fields that travel along with the seismic waves may therefore be classified as *co-seismic* fields and contain information only on the properties of the porous medium in the immediate vicinity of the seismic disturbance. However, when seismic waves are incident on an interface between dissimilar media, a variation in the streaming current density across the interface may be produced, thus setting up a charge separation that varies with the time signature of the incident seismic wave. The time-varying charge separation acts as oscillating electric dipole sources spread over the interface and generates an EM wave that propagates independently from the seismic wave. This radiated EM wave may be recorded at the ground surface. The electroseismic energy conversion at an interface is referred to as the *interface response*. Due to the high velocity of propagation of the generated EM wave, the interface response leads to time-independent arrivals (on a seismic time-scale) at an array of surface antennæ.

A seismic disturbance may give rise to a number of different elastic and acoustic waves propagating in the subsurface. In an infinite homogeneous isotropic medium, only pressure and shear waves exist. However, in bounded media waves that travel along the interfaces may be generated. Examples of such waves are Rayleigh and Love waves that travel along the surface of the earth, and critically refracted waves that travel along the interfaces between media of different elastic properties and/or densities. In fluid-saturated porous media, critically refracted shear waves with vertical polarisation may give rise to relative motion between fluid and solid (due to solid grain acceleration) across an interface of different electrokinetic coupling properties, thus resulting in an interface response. Critically refracted pressure waves and critically refracted shear waves with horizontal polarisation, on the other hand, do not lead to fluid flow across the interface and do therefore not result in an interface response. In these waves the co-seismic electric field is confined to the surface wave travelling along the interface and the electric field recorded at a surface array of antennæ exhibits time-dependent arrivals as the seismic wave propagates past the antennæ. The arrival times of the co-seismic energy therefore correspond to the arrival times of the seismic energy.

A graphical representation of the different ways in which seismic and electromagnetic energies may be coupled in fluid-saturated porous media is given in Figure 1.4.1.

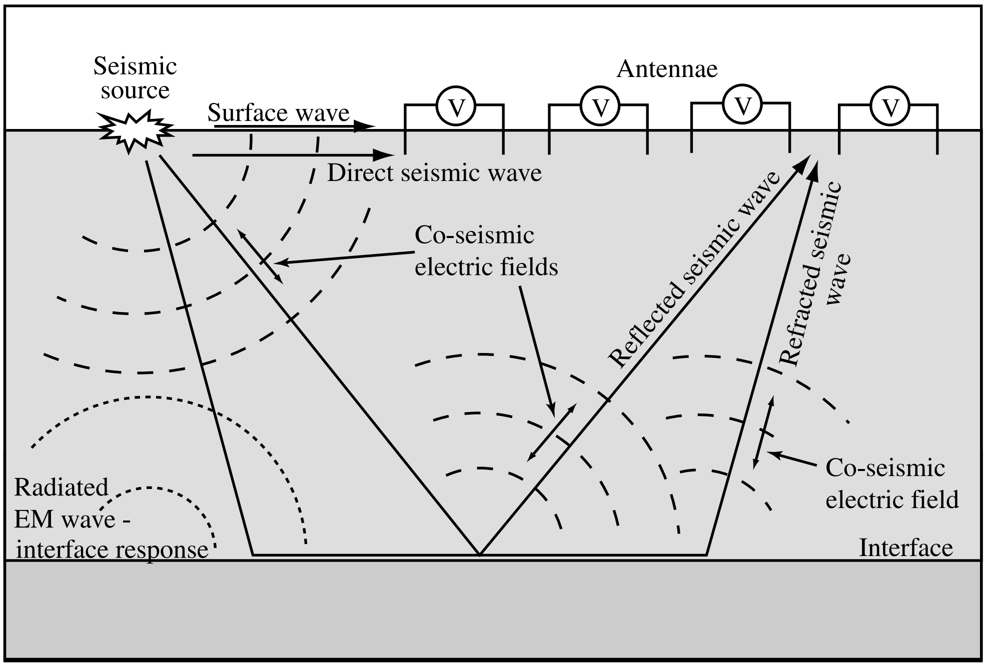

Figure 1.4.1. Electroseismic coupling mechanisms in fluid-saturated porous media.

Apart from surface ES techniques, that is, ES techniques where the antennæ occur on the ground surface, measurement of the electromagnetic response induced by seismic excitation of the earth may also be done vertically down a borehole. In this case the techniques are called borehole ES techniques.

1.5 Aims of the thesis

This thesis is primarily concerned with the use of surface ES methods for groundwater exploration in fractured Karoo rocks. Since the occurrences of fractures in Karoo rocks are localized both vertically and laterally, the problem of groundwater exploration becomes a study of the lateral and vertical resolution and detection criteria for thin fluid-saturated layers imbedded in fluid-saturated half-spaces.

Secondly, this thesis investigates the possibility of obtaining information on the elastic properties of Karoo rocks by the analyses of borehole electroseismic data. Such information could be used in assessing the deformability of fractures in these rocks and could assist in the establishment of long-term groundwater management strategies to avoid over-exploitation of Karoo aquifers.

Lastly, this thesis examines the influence of aquifer parameters, such as porosity and permeability, on ES reflection in Karoo rocks in an attempt to determine whether Karoo aquifers may be characterized on the basis of their hydraulic properties from the analyses of ES data.

1.6 Thesis outline

This thesis is structured as follows:

In Chapter 2 the theoretical background on which the later chapters of the thesis are based is given. Since the electric double layer (EDL) at the solid-fluid interface of fluid-saturated porous rocks plays an important role in ES phenomena, the chapter starts off by giving a general description of the electric double layer. Next the fundamental concepts of elasticity theory and Hooke's law for deformation of isotropic solids are discussed. Biot's equations for the propagation of dilatational and rotational waves in fluid-saturated porous media are discussed and shown to be an extension of Hooke's law to isotropic fluid-saturated porous media. The governing equations for ES waves, as derived by Pride (1994), are discussed. These equations consist of Biot's equations coupled to Maxwell's equation by two transport equations. Plane-wave solutions in a homogeneous, isotropic whole-space are illustrated for longitudinal and transversal waves.

Since the ability of surface ES techniques to detect localised fractures depends on the resolving capabilities of ES data, Chapter 3 investigates the vertical and lateral resolution criteria of surface ES data and investigates the ES thin bed response. The lateral resolution criteria are established by extending the Fresnel zone concept, as used in seismic investigations, to electroseismic data. Fresnel zones for both monochromatic and broadband sources are discussed. The vertical resolution criteria for ES data are also obtained by adapting the vertical resolution criteria used in seismics to be applicable to ES data. Both broadband and monochromatic sources are again considered. The thin bed response is investigated by means of a simplified model that separately considers excitation by the fast and slow Biot waves, as well as by using a matrix method that simultaneously takes account of all converted wave modes.

Chapter 4 examines the possibility of obtaining information on the elastic parameters of aquifers by simultaneously measuring the solid displacement caused by a seismic wave and the accompanying electric or magnetic fields. This is done by considering the dependency of the electroseismic and magnetoseismic transfer functions, giving the relation between the amplitudes of the seismic and electric or magnetic fields, on the various physical and chemical parameters that influence ES energy conversion. The influence of porosity changes due to aquifer deformation on ES energy conversion is also investigated by allowing variations in all the porosity-dependent parameters.

Chapter 5 investigates the influence of porosity and permeability contrasts on ES reflection in Karoo rocks by examining the ES reflection coefficient at a sandstone/mudstone interface. A matrix method is employed to obtain the ES reflection coefficients for different rock and fluid parameters. Sensitivity investigations are also performed to determine which rock or fluid parameters have the greatest influence on ES reflection.

In Chapter 6 the results of a field survey on the Campus Test Site are presented. During this survey the ES response was measured above a known bedding-plane fracture, as well as at a position where no fracture is thought to occur. Comparison of the responses is done to investigate whether any energy arrivals at surface may be associated with the fracture, thus indicating that surface ES methods may be successful in detecting such fractures. The results presented in this chapter may be seen as a first verification of the results obtained in Chapter 3.

Chapter 7 summarises the findings of this thesis and makes recommendations for future work in electroseismics.

CHAPTER 2 THEORETICAL BACKGROUND

In this chapter the theoretical background on which later chapters are based is discussed. First a description of the electric double layer at the solid-fluid interface of fluid-saturated porous rocks is given. Next the fundamental concepts of elasticity theory and Hooke's law for deformation of isotropic solids are discussed. Biot's equations (Biot, 1956a, 1956b, 1962a, 1962b) for the propagation of dilatational and rotational waves in fluid-saturated porous media are discussed and shown to be an extension of Hooke's law to isotropic fluid-saturated porous media. The governing equations for electroseismic waves, as derived by Pride (1994), are discussed. These equations consist of Biot's equations coupled to Maxwell's equation by two transport equations. Plane-wave solutions in a homogeneous, isotropic whole-space are obtained for longitudinal and transversal waves.

2.1 The electric double layer

Electrokinetic phenomena have their origin in the electric double layer (EDL) associated with the interface between minerals and pore fluid. The model of the EDL described in this section is of the Stern-Gouy type, as described by Tuman (1963), Shaw (1969), Ishido (1981) and Pride and Morgan (1991).

The surfaces of the mineral grains in rocks usually display net electric charges due to the presence of unsatisfied chemical bonds (Fitterman, 1978) whereas groundwater is electrolytic in nature. In water-saturated porous rocks an electric potential is therefore usually produced at the contact between the water and solid. As a result the electric charges within the fluid separate into an electric double layer. The EDL consists, as the name implies, of two layers. The inner or Stern layer consists of ions adsorbed onto the solid surface through electrostatic and Van der Waal's forces, while the outer diffuse or Gouy layer in the water is formed by ions under the influence of ordering electrical and disordering thermal forces, Figure 2.1.1.

The Stern layer is usually only one ion in thickness and the electric potential falls rapidly from the contact potential (ϕ_0) to ϕ_δ across this layer as the adsorped ions partially screen off the effects of the charged solid surface. For low electrolyte concentrations (less than 0.1 moles per liter) the concentration of the ions in the Gouy layer may be described by Boltmann distributions. For a symmetric electrolyte with ionic valence of z, the distributions are of the form

$$n_+(x) = n^0 \exp\left(\frac{-ze\,\varphi(x)}{k_B T}\right) \tag{2.1}$$

$$n_-(x) = n^0 \exp\left(\frac{ze\,\varphi(x)}{k_B T}\right) \tag{2.2}$$

where n_+ and n_- are the ionic concentrations of the cations and anions at a distance x from the solid grain surface, n^0 is the ionic concentration far from the grain surface, e is the electronic charge, k_B is the Boltzmann constant, T is the temperature in Kelvin and $\varphi(x)$ is the electric potential at a distance x from the solid grain surface. The electric potential in the Gouy layer falls exponentially with distance (x) from the charged surface and is given by

$$\varphi(x) = \varphi_0 \exp(-x/d) \tag{2.3}$$

where d is the Debye length which is often used to describe the "thickness" of the EDL.

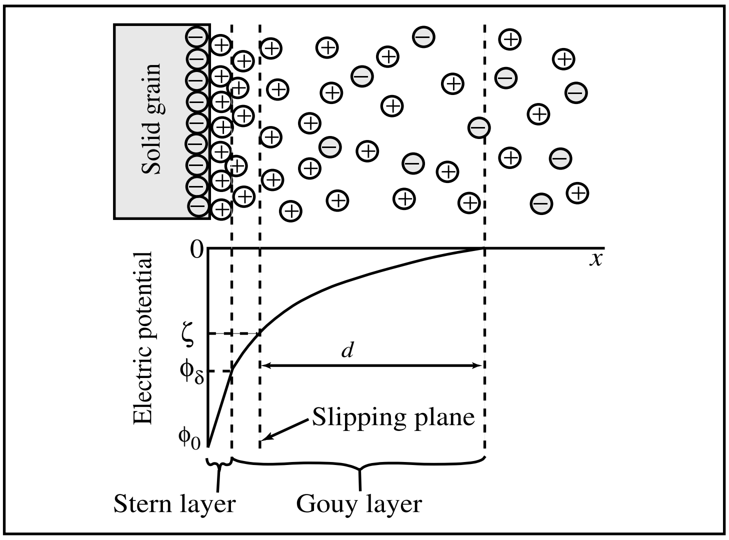

Figure 2.1.1. The electric double layer.

Any relative motion between the solid and the water will cause a relative motion between the outer diffuse ions and inner strongly bound ions. The plane at which the ions of the inner and outer layers are sheared from each other, is called the slipping or shearing plane, and the electric potential in the plane the zeta (ζ)-potential. This plane does in general not coincide with the outer plane of the Stern layer. The zeta potential plays an important role in electrokinetic phenomena, since it is contained in the electrokinetic coupling coefficient, which determines the existence and magnitude of the induced electric and magnetic fields, as is discussed in Section 2.4.

2.2 Fundamental elasticity theory for a homogeneous, isotropic continuum

To describe the mechanics of motion in a continuum either the Lagrangian or Eulerian descriptions may be employed. In seismology the distinction between the two approaches rarely needs to be made since the wavelengths of concern are much greater than the particle displacements (Aki and Richards, 1980). The linear theory of elasticity is conceptually simpler to develop with the Lagrangian description, and this is the framework adopted in this thesis.

Throughout this chapter a right-handed Cartesian coordinate system is employed. Suppose a particle initially at position $\mathbf{x}$ is moved to a position $\mathbf{x} + \mathbf{u}$ as the result of applied stresses, then the relation $\mathbf{u} = \mathbf{u}(\mathbf{x})$ may be used to describe the displacement field. The distortion of the part of the medium that was located in the vicinity of $\mathbf{x}$ may be studied by considering the displaced position of a particle that initially occurred at a position $\mathbf{x} + \mathbf{dx}$, as in Figure 2.2.1. This position is given by $\mathbf{x} + \mathbf{dx} + \mathbf{u}(\mathbf{x}+\mathbf{dx})$. If distortion of the medium occurs the vector joining $\mathbf{u}(\mathbf{x})$ and $\mathbf{u}(\mathbf{x}+\mathbf{dx})$ will differ from $\mathbf{dx}$ by an amount $\mathbf{du}$ given by

$$\mathbf{du} = \mathbf{u}(\mathbf{x} + \mathbf{dx}) - \mathbf{u}(\mathbf{x}) \tag{2.4}$$

$\mathbf{u}(\mathbf{x}+\mathbf{dx})$ may be expanded by means of a Taylor series and at leading order we may write $\mathbf{u}(\mathbf{x}+\mathbf{dx}) \approx \mathbf{u}(\mathbf{x}) + \mathbf{dx}\bullet\nabla\mathbf{u}$ (see Appendix A6).

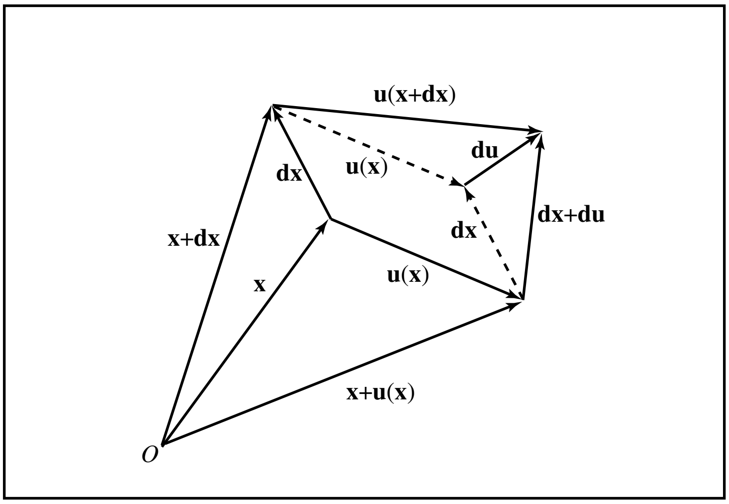

Figure 2.2.1. Distortion of a solid medium under stress.

$\nabla\mathbf{u}$ is a second order tensor given in index notation by $u_{j,i}$ (see Appendix A2). We therefore have

$$\mathbf{du} = \mathbf{dx} \bullet \nabla\mathbf{u} = (\nabla\mathbf{u})^T \bullet \mathbf{dx} \tag{2.5}$$

or in index notation

$$du_i = u_{i,j}\ dx_j \tag{2.6}$$

The tensor $u_{i,j}$ may be written as the sum of a symmetric and antisymmetric tensor as

$$\begin{aligned} u_{i,j} &= \left[\frac{1}{2}\left(u_{i,j} + u_{j,i}\right) + \frac{1}{2}\left(u_{i,j} - u_{j,i}\right)\right] \\ &= \qquad e_{ij} \qquad + \qquad w_{ij} \end{aligned} \tag{2.7}$$

In literature e_{ij} is called the strain tensor representing deformation of the medium, whereas w_{ij} represents pure rigid-body rotation of the medium and is called the rotation tensor.

2.2.1 Hooke's law for homogeneous, isotropic solids

Hooke's law for the deformation of isotropic media states that the components of the stress tensor are linearly dependent on the components of the strain tensor, as long as the elastic limit is not exceeded. In index notation this law is given by

$$\tau_{ij} = C_{ijkl}\, e_{kl} \tag{2.8}$$

where τ_{ij} is the stress tensor giving the forces per unit area acting on the medium and C_{ijkl} is a fourth order isotropic tensor called the stiffness or elasticity tensor. C_{ijkl} may be written as a linear combination of linearly independent 4th order isotropic tensors. Only three such tensors are possible (D'Arnaud Gerkens, 1989) and C_{ijkl} may consequently be written as

$$C_{ijkl} = \lambda\delta_{ij}\delta_{kl} + \mu(\delta_{ik}\delta_{jl} + \delta_{il}\delta_{jk}) + \nu(\delta_{ik}\delta_{jl} - \delta_{il}\delta_{jk}) \tag{2.9}$$

where δ_{ij} is the Kronecker delta, itself a 2nd order tensor, given by

$$\delta_{ij} = \begin{cases} 1 & if \quad i = j \\ 0 & if \quad i \neq j \end{cases} \tag{2.10}$$

Substituting Equation (2.9) into Equation (2.8) and noting the properties $\delta_{ij}\, e_{ij} = e_{ii}$, $\delta_{jl}\, e_{kl} = e_{kj}$ and $\delta_{jk}\, e_{kl} = e_{jl}$ gives

$$\tau_{ij} = \lambda\delta_{ij}e_{kk} + \mu(e_{ij} + e_{ji}) + \nu(e_{ij} - e_{ji}) \tag{2.11}$$

where e_{kk} is the change in volume per unit volume of the medium and is called the *dilatation* (or *compression* if $e_{kk} < 0$). Since $e_{ij} = e_{ji}$ the final form of Hooke's law in index notation is

$$\tau_{ij} = \lambda\delta_{ij}e_{kk} + 2\mu e_{ij} \tag{2.12}$$

The coefficients λ and μ are the so-called Lamé constants. The constant λ is a measure of the resistance to dilatation while μ is a measure of the resistance to shearing strain and is often called the *shear modulus* of the medium. In vector notation Hooke's law is given by

$$\tau = \lambda(\nabla \bullet \mathbf{u})\mathrm{I} + \mu\left[\nabla\mathbf{u} + (\nabla\mathbf{u})^T\right] \tag{2.13}$$

where **I** is the identity tensor.

2.2.2 The equation of motion for isotropic continua

Consider a small volume V of the continuum with surface S, as shown in Figure 2.2.2. Let **n** be the unit vector normal to the surface and **T**(**n**) be the force per unit area exerted on the surface by the material on the side to which **n** points. To obtain the equation of motion for an isotropic continuum, one equates the rate of change of momentum of particles within the volume V with the forces acting on the particles. If **f** is the vector representing the body forces acting on the medium per unit volume, then we have

$$\frac{\partial}{\partial t}\iiint_V \rho \frac{\partial \mathbf{u}}{\partial t}\, dV = \iiint_V \mathbf{f}\, dV + \iint_S \mathbf{T}(\mathbf{n})\, dS \tag{2.14}$$

where ρ is the mass density of the medium. This relation is based on the Lagrangian description whereby V and S move along with the particles. The left-hand side of Equation (2.14) may therefore be written as $\iiint_V \rho\ddot{\mathbf{u}}\, dV$, since the particle mass $\rho\, dV$ is constant in time.

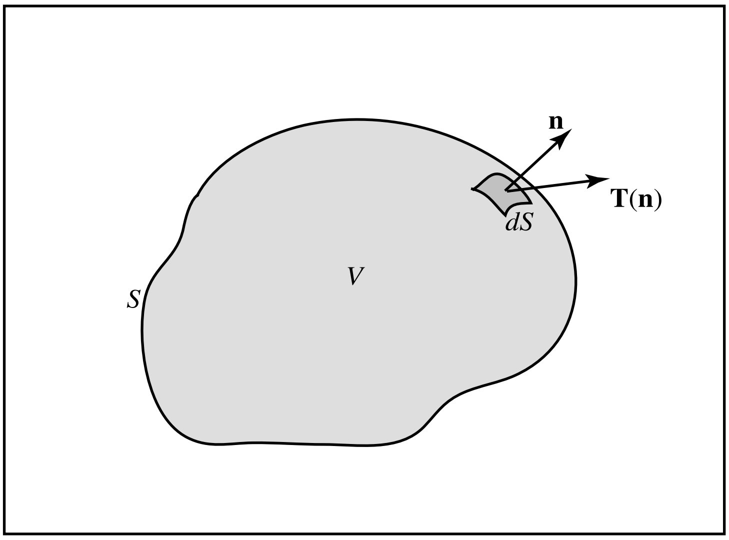

Figure 2.2.2. The definition of traction T acting at a point on the internal surface *S* with normal n.

In index notation **T**(**n**) is given by

$$T_i = \tau_{ji} n_j \tag{2.15}$$

Using Gauss's divergence theorem we have

$$\iint_S T_i \, dS = \iint_S \tau_{ji} n_j \, dS = \iiint_V \tau_{ji,j} \, dV \tag{2.16}$$

so that Equation (2.14) becomes

$$\iiint_V \left(\rho \ddot{u}_i - f_i - \tau_{ji,j} \right) dV = 0 \tag{2.17}$$

The above expression is true for all volumes *V*, so that the local equation of motion is given by

$$\rho \ddot{u}_i = f_i + \tau_{ji,j} \tag{2.18}$$

In the absence of body forces the equation of motion may be written in vector notation as

$$\nabla \bullet \boldsymbol{\tau} = \rho \ddot{\mathbf{u}} \tag{2.19}$$

The meaning of $\nabla \bullet \boldsymbol{\tau}$ is discussed in Appendix A3. From Equation (2.13) we have

$$\begin{aligned} \nabla \bullet \boldsymbol{\tau} &= \lambda \nabla \bullet \left[(\nabla \bullet \mathbf{u}) \mathrm{I} \right] + \mu \left[\nabla \bullet \nabla \mathbf{u} + \nabla \bullet (\nabla \mathbf{u})^T \right] \\ &= (\lambda + 2\mu) \nabla (\nabla \bullet \mathbf{u}) - \mu \nabla \times \nabla \times \mathbf{u} \end{aligned} \tag{2.20}$$

where use is made of the vector identities given in Equations (A5.1) and (A5.2) of Appendix A5. In vector notation the final equation of motion is therefore

$$(\lambda + 2\mu)\nabla(\nabla \bullet \mathbf{u}) - \mu\nabla \times \nabla \times \mathbf{u} = \rho\ddot{\mathbf{u}} \tag{2.21}$$

Equation (2.21) describes the propagation of rotational (shear) and dilatational (pressure) waves in the medium. For purely rotational waves $\nabla \bullet \mathbf{u} = 0$ so that we have the wave equation

$$\ddot{\mathbf{u}} = -\left(\frac{\mu}{\rho}\right)\nabla \times \nabla \times \mathbf{u} \tag{2.22}$$

Shear waves are seen to propagate at a velocity given by

$$v_s = (\mu / \rho)^{\frac{1}{2}} \tag{2.23}$$

For purely dilatational waves $\nabla \times \mathbf{u} = \mathbf{0}$ and we have the wave equation

$$\ddot{\mathbf{u}} = \left(\frac{\lambda + 2\mu}{\rho}\right)\nabla(\nabla \bullet \mathbf{u}) \tag{2.24}$$

Pressure waves propagate at a higher velocity given by

$$v_p = \left[(\lambda + 2\mu) / \rho\right]^{\frac{1}{2}} \tag{2.25}$$

2.2.3 Boundary conditions

For two solids in welded contact all three components of displacement have to be continuous across the boundary. This leads to the boundary condition

$$\mathbf{u}_1 - \mathbf{u}_2 = \mathbf{0} \tag{2.26}$$

Continuity of traction across the interface requires that

$$\mathbf{n} \bullet (\tau_1 - \tau_2) = \mathbf{0} \tag{2.27}$$

where **n** is the unit vector normal to the interface.

2.2.4 Elastic constants

Although Lamé's constants are convenient at times, other elastic coefficients are also used. For a medium under hydrostatic pressure P, the stress components become

$\tau_{[ii]} = \tau_{[jj]} = \tau_{[kk]} = -P$ and $\tau_{ij} = 0$ for $i \neq j$. Under these conditions Hooke's law may be used to obtain the ratio of the applied pressure to the compression (e_{kk}<0)

$$K = \frac{-P}{e_{kk}} = \lambda + \frac{2}{3}\mu \tag{2.28}$$

where K is the *bulk modulus* of the medium. *Young's modulus* (E) is defined as the ratio between the normal stress applied to a medium and the strain that results from the stress. For normal stress applied in the i direction Young's modulus is given by

$$E = \frac{\tau_{[ii]}}{e_{[ii]}} = \frac{\mu(3\lambda + 2\mu)}{\lambda + \mu} \tag{2.29}$$

Poisson's ratio gives the ratio of the fractional transverse contraction (or extension) to the fractional normal extension (or contraction) when normal traction (or stress) is applied to a medium. For normal traction (or stress) in the i direction it is defined as

$$\nu = \frac{-e_{[jj]}}{e_{[ii]}} = \frac{\lambda}{2(\lambda + \mu)} \tag{2.30}$$

2.3 The propagation of mechanical disturbances in fluid-saturated porous media (Biot theory)

Maurice A. Biot presents a theory for the propagation of elastic waves in fluid-saturated porous solids in a series of classical papers (Biot, 1956a, 1956b, 1962a, 1962b). Biot considered the stress components acting on both the solid and liquid phases of the medium and obtained an expressions for the total stress tensor, given in vector notation by

$$\tau = \lambda^*(\nabla \bullet \mathbf{u})\mathrm{I} + \mu^*\left[\nabla\mathbf{u} + (\nabla\mathbf{u})^T\right] + C(\nabla \bullet \mathbf{w})\mathrm{I} \tag{2.31}$$

and the fluid pressure

$$-P = C(\nabla \bullet \mathbf{u}) + M(\nabla \bullet \mathbf{w}) \tag{2.32}$$

where $\mathbf{u}$ is the displacement vector of the solid frame and $\mathbf{w}$ is the relative fluid-solid displacement multiplied by the porosity. The equation of motion for a fluid-saturated porous medium as derived by Biot is given in vector notation as

$$\nabla \bullet \tau = \rho\ddot{\mathbf{u}} + \rho_f\ddot{\mathbf{w}} \tag{2.33}$$

where ρ is the mass density of the bulk material (the bulk density) given by

$$\rho = \rho_s(1-\phi) + \rho_f\phi \tag{2.34}$$

where ρ_s and ρ_f are the mass densities of the solid and fluid, respectively. Equation (2.33) is the fluid-saturated porous medium equivalent of Equation (2.19). Biot further derives the following relation between the pressure gradient and the second and first time-derivatives of **u** and **w**, respectively

$$-\nabla P = \rho_f\ddot{\mathbf{u}} + \frac{\eta}{k}\dot{\mathbf{w}} \tag{2.35}$$

where k is the dynamic permeability and η is the fluid viscosity. Equations (2.31), (2.32), (2.33) and (2.35) form a set of four equations commonly known as *Biot's Equations*.

Comparison of Equation (2.31) with Equation (2.13) shows that Biot's expression for the total stress tensor is similar to the stress tensor obtained from Hooke's law for an isotropic continuum, but that it contains an additional term containing the dilatation of the relative flow. The Lamé constants are also modified. The coefficient μ* now represents the shear modulus of the solid frame while λ* is the Lamé constant of the porous material under conditions of constant pore pressure. The quantities C and M are elastic constants relating the dilatation of solid and the divergence of the relative flow to the fluid pressure and to the total stress tensor.

In the literature Equation (2.31) is often written in one of the following equivalent forms

$$\tau = (H-2G)(\nabla \bullet \mathbf{u})\mathrm{I} + G\left[\nabla\mathbf{u} + (\nabla\mathbf{u})^T\right] + C(\nabla \bullet \mathbf{w})\mathrm{I} \tag{2.36}$$

or

$$\tau = \left[K(\nabla \bullet \mathbf{u}) + C(\nabla \bullet \mathbf{w})\right]\mathrm{I} + G\left[\nabla\mathbf{u} + (\nabla\mathbf{u})^T - \frac{2}{3}(\nabla \bullet \mathbf{u})\mathrm{I}\right] \tag{2.37}$$

where the G is the shear modulus of the porous frame (identical to μ*), K is the bulk modulus of the fluid-saturated porous medium defined similarly to Equation (2.28) as

$$K = \lambda^* + \frac{2}{3}\mu^* = \lambda^* + \frac{2}{3}G \tag{2.38}$$

and H is a stiffness coefficient defined by Biot (1962a) as

$$H = \lambda^* + 2G = K + 4G/3 \tag{2.39}$$

In terms of the bulk modulus of the dry porous frame (K_{fr}), the bulk modulus of the pore fluid (K_f), the bulk modulus of the solid material making up the porous frame (K_s) and the porosity (ϕ) of the rock, the elastic constants are given as (Ranada Shaw *et al.*, 2000)

$$K = \frac{K_f\left(K_s - K_{fr}\right) + \phi K_{fr}\left(K_s - K_f\right)}{K_f\left(1 - \phi - K_{fr}/K_s\right) + \phi K_s} \tag{2.40}$$

$$C = \frac{K_f\left(K_s - K_{fr}\right)}{K_f\left(1 - \phi - K_{fr}/K_s\right) + \phi K_s} \tag{2.41}$$

$$M = \frac{K_f K_s}{K_f\left(1 - \phi - K_{fr}/K_s\right) + \phi K_s} \tag{2.42}$$

Equation (2.40), also derived by Gassmann (1951), is often referred to in the literature as the *Gassmann's equation.*

The fluid-saturated porous medium equivalents of the elastic constants defined in Equations (2.29) and (2.30) may be defined as

$$E^* = \frac{G\left(3\lambda^* + 2G\right)}{\lambda^* + G} \tag{2.43}$$

$$\nu^* = \frac{\lambda^*}{2\left(\lambda^* + G\right)} \tag{2.44}$$

2.3.1 Plane wave solutions of Biot's equations in a homogeneous and isotropic whole-space

Following the methodology of Haartsen (1995) and Pride and Haartsen (1996), plane wave solutions to Biot's equations may be found by considering pure harmonic waves with $\exp(-i\omega t)$ time-dependence in homogeneous and isotropic media. The complete set of Biot's equations may be reduced to two vector equations as follows:

Combining Equations (2.33) and (2.36) yields

$$\left[(H - G)\nabla\nabla + \left(G\nabla^2 + \omega^2\rho\right)\mathbf{I}\right] \bullet \mathbf{u} + \left[C\nabla\nabla + \omega^2\rho_f\mathbf{I}\right] \bullet \mathbf{w} = \mathbf{0} \tag{2.45}$$

Combining Equations (2.32) and (2.35) gives

$$\left[C\nabla\nabla + \omega^2 \rho_f \mathbf{I}\right] \bullet \mathbf{u} + \left[M\nabla\nabla + \omega^2 \tilde{\rho} \mathbf{I}\right] \bullet \mathbf{w} = \mathbf{0} \tag{2.46}$$

where $\tilde{\rho}$ is a complex and frequency-dependent effective density defined as

$$\tilde{\rho} = \frac{i\eta}{\omega\, k} \tag{2.47}$$

Plane-wave representations of $\mathbf{u}$, and $\mathbf{w}$ are given by

$$\mathbf{u} = U \exp[i(\mathbf{k} \bullet \mathbf{r} - \omega t)]\, \hat{\mathbf{u}} \tag{2.48}$$

$$\mathbf{w} = W \exp[i(\mathbf{k} \bullet \mathbf{r} - \omega t)]\, \hat{\mathbf{w}} \tag{2.49}$$

where $\mathbf{k} = \omega s \hat{\mathbf{k}}$ is the propagation vector and s is the frequency-dependent complex phase slowness of the wave. The reason for working with slownesses instead of velocities is discussed in Appendix C. With these plane-wave representations Biot's equations may be written in matrix form as

$$\begin{bmatrix} (H-G)s^2\left(\hat{\mathbf{k}} \bullet \hat{\mathbf{u}}\right)\hat{\mathbf{k}} - \left(\rho - Gs^2\right)\hat{\mathbf{u}} & Cs^2\left(\hat{\mathbf{k}} \bullet \hat{\mathbf{w}}\right)\hat{\mathbf{k}} - \rho_f \hat{\mathbf{w}} \\ Cs^2\left(\hat{\mathbf{k}} \bullet \hat{\mathbf{u}}\right)\hat{\mathbf{k}} - \rho_f \hat{\mathbf{u}} & Ms^2\left(\hat{\mathbf{k}} \bullet \hat{\mathbf{w}}\right)\hat{\mathbf{k}} - \tilde{\rho}\hat{\mathbf{w}} \end{bmatrix} \begin{bmatrix} U \\ W \end{bmatrix} = \begin{bmatrix} \mathbf{0} \\ \mathbf{0} \end{bmatrix} \tag{2.50}$$

Equation (2.50) can be used to examine the longitudinal and transverse plane-waves propagating in the porous continuum. A transverse mode is one for which the material response is perpendicular to the direction of propagation ($\hat{\mathbf{k}} \bullet \hat{\mathbf{u}} = \hat{\mathbf{k}} \bullet \hat{\mathbf{w}} = 0$), while a longitudinal mode corresponds to the material response being parallel to the direction of propagation ($\hat{\mathbf{k}} \bullet \hat{\mathbf{u}} = \hat{\mathbf{k}} \bullet \hat{\mathbf{w}} = 1$). From Equation (2.50) it can be shown that wave modes with mixed responses lead to the trivial solution $U = W = 0$, and thus do not exist. It can furthermore be shown that for both longitudinal and transversal modes $\hat{\mathbf{u}} = \hat{\mathbf{w}}$.

2.3.1.1 Transverse modes

Setting $\hat{\mathbf{k}} \bullet \hat{\mathbf{u}} = \hat{\mathbf{k}} \bullet \hat{\mathbf{w}} = 0$ and $\hat{\mathbf{u}} = \hat{\mathbf{w}}$, Equation (2.50) becomes

$$\begin{bmatrix} \left(\rho - Gs^2\right) & \rho_f \\ \rho_f & \tilde{\rho} \end{bmatrix} \begin{bmatrix} U \\ W \end{bmatrix} = \begin{bmatrix} 0 \\ 0 \end{bmatrix} \tag{2.51}$$

Non-trivial solutions for U, and W exist only if the determinant of the matrix vanishes, in which case the complex transverse wave slowness is found

$$s = \left(\rho_t / G\right)^{1/2} \tag{2.52}$$

where ρ_t is a complex density defined as

$$\rho_t = \rho - \rho_f^2 / \tilde{\rho} \tag{2.53}$$

Equation (2.52) is the fluid-saturated porous medium equivalent of Equation (2.23). The slowness given in Equation (2.52) corresponds exactly to the velocity of transverse waves in fluid-saturated porous media as derived by Biot (1956a). From Equation (2.51) the relation between the wave amplitudes is found to be

$$W = \frac{G}{\rho_f}\left(s^2 - \frac{\rho}{G}\right)U \tag{2.54}$$

Plane transverse waves may have one of two different polarisations. For a plane wave propagating in the *x-z* plane of a Cartesian system (x, y, z) the one polarisation corresponds to $\hat{\mathbf{u}} = \hat{\mathbf{w}} = \hat{\mathbf{y}}$. This polarisation is referred to as the *SH* (Shear Horizontal) mode since it corresponds to displacements in a horizontal direction. The other polarisation corresponds to $\hat{\mathbf{u}} = \hat{\mathbf{w}} = \hat{\mathbf{y}} \times \hat{\mathbf{k}}$ and is referred to as the *SV* (Shear Vertical) mode since it deals with displacements in a vertical plane.

2.3.1.2 Longitudinal modes

Setting $\hat{\mathbf{k}} \bullet \hat{\mathbf{u}} = \hat{\mathbf{k}} \bullet \hat{\mathbf{w}} = 1$ and $\hat{\mathbf{u}} = \hat{\mathbf{w}}$ Equation (2.50) becomes

$$\begin{bmatrix} Hs^2 - \rho & Cs^2 - \rho_f \\ Cs^2 - \rho_f & Ms^2 - \tilde{\rho} \end{bmatrix} \begin{bmatrix} U \\ W \end{bmatrix} = \begin{bmatrix} 0 \\ 0 \end{bmatrix} \tag{2.55}$$

Setting the determinant to zero gives two distinct longitudinal wave slownesses

$$2s_{pf,ps}^2 = \gamma \mp \left\{\gamma^2 - \frac{4\tilde{\rho}\rho_t}{\Delta}\right\}^{1/2} \tag{2.56}$$

with

$$\gamma = \frac{\rho M + \tilde{\rho} H - 2\rho_f C}{\Delta} \tag{2.57}$$

and

$$\Delta = MH - C^2 \tag{2.58}$$

The negative sign in front of the radical in Equation (2.56) corresponds to the slowness (s_{pf}) of the Biot fast pressure wave, while the positive sign corresponds to the slowness (s_{ps}) of the Biot slow pressure wave. These slownesses correspond exactly to the longitudinal wave velocities derived by Biot (1956a). In terms of amplitude we have

$$W = \beta_{pf,ps}\, U \tag{2.59}$$

with

$$\beta_{pf,ps} = -\left(\frac{Hs_{pf,ps}^2 - \rho}{Cs_{pf,ps}^2 - \rho_f} \right) \tag{2.60}$$

The longitudinal wave modes are hereafter referred to as the *Pf–Ps* (Pressure fast – Pressure slow) modes.

2.3.2 Boundary conditions

The following boundary conditions have to be satisfied at a conformal interface between two dissimilar fluid-saturated porous media:

$$\mathbf{u}_1 - \mathbf{u}_2 = \mathbf{0} \tag{2.61}$$

$$\mathbf{n} \bullet \left[\tau_1 - \tau_2 \right] = \mathbf{0} \tag{2.62}$$

$$\mathbf{n} \bullet \left[\mathbf{w}_1 - \mathbf{w}_2 \right] = 0 \tag{2.63}$$

$$P_1 - P_2 = 0 \tag{2.64}$$

where **n** is a unit vector normal to the interface. These boundary conditions express the continuity in the solid displacement, momentum flux, fluid flux and fluid pressure across the interface.

2.4 Governing equations for electroseismic phenomena

Pride (1994) uses volume-averaging arguments to derive a set of equations that govern the coupled seismic and electromagnetic wave-fields in fluid-saturated porous material. In the time-domain in the absence of sources these equations are

$$\nabla \bullet \tau = \rho \ddot{\mathbf{u}} + \rho_f \ddot{\mathbf{w}} \tag{2.65}$$

$$\tau = (H - 2G)(\nabla \bullet \mathbf{u})\mathrm{I} + G\left[\nabla \mathbf{u} + (\nabla \mathbf{u})^T\right] + C(\nabla \bullet \mathbf{w})\mathrm{I} \tag{2.66}$$

$$-P = C(\nabla \bullet \mathbf{u}) + M(\nabla \bullet \mathbf{w}) \tag{2.67}$$

$$\dot{\mathbf{w}} = L\mathbf{E} + \frac{k}{\eta}\left[-\nabla P - \rho_f \ddot{\mathbf{u}}\right] \tag{2.68}$$

$$\mathbf{J} = \sigma \mathbf{E} + L\left[-\nabla P - \rho_f \ddot{\mathbf{u}}\right] \tag{2.69}$$

$$\nabla \times \mathbf{E} = -\dot{\mathbf{B}} \tag{2.70}$$

$$\nabla \times \mathbf{H} = \mathbf{J} + \dot{\mathbf{D}} \tag{2.71}$$

$$\mathbf{D} = \epsilon \mathbf{E} \tag{2.72}$$

$$\mathbf{B} = \mu \mathbf{H} \tag{2.73}$$

where **E** is the electric field, **H** the magnetic field, **B** the magnetic induction field and **D** the displacement current density. The parameter ϵ is the dielectrical permittivity of the porous medium, μ is the magnetic permeability, σ is the electrical conductivity and L is the electrokinetic coupling coefficient. The parameter k is the dynamic permeability and η is the fluid viscosity.

The governing equations are seen to consist of Biot's equations coupled to Maxwell's equations through two transport equations (Equations (2.68) and (2.69)). If L is set to zero the mechanical (Biot) and electromagnetic (Maxwell) equations decouple completely. In the absence of coupling ($L = 0$), and for a stationary solid ($\ddot{\mathbf{u}} = \dot{\mathbf{u}} = \mathbf{0}$), Equations (2.68) and (2.69) reduce to Darcy's law for saturated flow of a viscous fluid through a porous medium ($\dot{\mathbf{w}}$ is the Darcy filtration velocity) and Ohm's law for electric current flow, respectively. Pride (1994) derives complex and frequency-dependent expressions for σ, L and k. These expressions are given in Appendix B.

A number of assumptions were made in the derivation of the above electroseismic governing equations, namely:

1) Only linear disturbances obeying the principle of superposition are considered.

2) The fluid is assumed to be an ideal electrolyte, thus restricting salt concentrations to less than one mole per litre.

3) Both the solid grains and the macroscopic-constitutive laws are assumed to be isotropic.

4) All wave-induced diffusion effects are neglected.

5) No wave scattering from the individual grains of the porous material is allowed for.

In order for the 4th assumption to be valid at pore and grain scale, two conditions must be fulfilled: a) the dielectric constant of the grains must be much less than the dielectric constant of the electrolyte (by a factor of ten or more), and b) the thickness of the EDL should be much less than the radii of curvature of the solid grains (Pride, 1994). For water-saturated sedimentary rocks these conditions are generally met. The 5th assumption restricts the upper frequency of validity to a value in the order 10^6 Hz. This frequency is at least 3 orders of magnitude higher then the frequencies routinely employed in seismic methods.

2.4.1 Plane wave solutions in a homogeneous and isotropic whole-space

Haartsen (1995) and Pride and Haartsen (1996) obtain plane wave solutions to the set of equations that govern electroseismic waves by considering pure harmonic waves (with $\exp(-i\omega t)$ time-dependence) in homogeneous and isotropic media. The complete set of governing equations may be reduced to three vector equations as follows: Combining Equations (2.65) and (2.66) yields

$$\left[(H-G)\nabla\nabla + \left(G\nabla^2 + \omega^2\rho\right)\mathbf{I}\right] \bullet \mathbf{u} + \left[C\nabla\nabla + \omega^2\rho_f\mathbf{I}\right] \bullet \mathbf{w} = \mathbf{0} \tag{2.74}$$

Combining Equations (2.67) and (2.68) gives

$$\left[C\nabla\nabla + \omega^2\rho_f\mathbf{I}\right] \bullet \mathbf{u} + \left[M\nabla\nabla + \omega^2\rho\mathbf{I}\right] \bullet \mathbf{w} - i\omega\tilde{\rho}L\mathbf{E} = \mathbf{0} \tag{2.75}$$

where $\tilde{\rho}$ is a complex and frequency-dependent effective density defined in Equation (2.47). Finally, combining Equations (2.68) and (2.69) and using Equations (2.70) to (2.73) yield

$$\left[\nabla\nabla - \left(\nabla^2 + \omega^2\mu\tilde{\varepsilon}\right)\mathbf{I}\right] \bullet \mathbf{E} + i\omega^3\mu\tilde{\rho}L\mathbf{w} = \mathbf{0} \tag{2.76}$$

where $\tilde{\epsilon}$ is the complex and frequency-dependent electrical permittivity of the porous continuum defined as

$$\tilde{\epsilon} = \epsilon + \frac{i}{\omega}\sigma - \tilde{\rho}L^2 \tag{2.77}$$

As in Section 2.3.1 plane-wave representations of **u**, **w** and **E** are given by

$$\mathbf{u} = U\exp[i(\mathbf{k}\bullet\mathbf{r} - \omega t)]\,\hat{\mathbf{u}} \tag{2.78}$$

$$\mathbf{w} = W\exp[i(\mathbf{k}\bullet\mathbf{r} - \omega t)]\,\hat{\mathbf{w}} \tag{2.79}$$

$$\mathbf{E} = E\exp[i(\mathbf{k}\bullet\mathbf{r} - \omega t)]\,\hat{\mathbf{e}} \tag{2.80}$$

With these plane-wave representations the governing equations (Equations (2.74), (2.75) and (2.76)) may be written in matrix form as

$$\begin{bmatrix} (H-G)s^2\left(\hat{\mathbf{k}}\bullet\hat{\mathbf{u}}\right)\hat{\mathbf{k}} - \left(\rho - Gs^2\right)\hat{\mathbf{u}} & Cs^2\left(\hat{\mathbf{k}}\bullet\hat{\mathbf{w}}\right)\hat{\mathbf{k}} - \rho_f\hat{\mathbf{w}} & 0 \\ Cs^2\left(\hat{\mathbf{k}}\bullet\hat{\mathbf{u}}\right)\hat{\mathbf{k}} - \rho_f\hat{\mathbf{u}} & Ms^2\left(\hat{\mathbf{k}}\bullet\hat{\mathbf{w}}\right)\hat{\mathbf{k}} - \tilde{\rho}\hat{\mathbf{w}} & \frac{i}{\omega}\tilde{\rho}L\hat{\mathbf{e}} \\ 0 & -i\omega\mu\tilde{\rho}L\hat{\mathbf{w}} & s^2\left(\hat{\mathbf{k}}\bullet\hat{\mathbf{e}}\right)\hat{\mathbf{k}} + \left(\tilde{\epsilon}\mu - s^2\right)\hat{\mathbf{e}} \end{bmatrix} \begin{bmatrix} U \\ W \\ E \end{bmatrix} = \begin{bmatrix} \mathbf{0} \\ \mathbf{0} \\ \mathbf{0} \end{bmatrix}$$

(2.81)

Equation (2.81) can be used to investigate the longitudinal and transverse plane-waves propagating in the porous continuum. As before, a transverse mode corresponds to $\hat{\mathbf{k}}\bullet\hat{\mathbf{u}} = \hat{\mathbf{k}}\bullet\hat{\mathbf{w}} = \hat{\mathbf{k}}\bullet\hat{\mathbf{e}} = 0$, while a longitudinal mode corresponds to $\hat{\mathbf{k}}\bullet\hat{\mathbf{u}} = \hat{\mathbf{k}}\bullet\hat{\mathbf{w}} = \hat{\mathbf{k}}\bullet\hat{\mathbf{e}} = 1$. Wave modes with mixed responses again lead to the trivial solution $U = W = E = 0$, and do therefore not exist. It can be shown that for both longitudinal and transversal modes $\hat{\mathbf{u}} = \hat{\mathbf{w}} = \hat{\mathbf{e}}$.

2.4.1.1 Transverse modes

Setting $\hat{\mathbf{k}}\bullet\hat{\mathbf{u}} = \hat{\mathbf{k}}\bullet\hat{\mathbf{w}} = \hat{\mathbf{k}}\bullet\hat{\mathbf{e}} = 0$ and $\hat{\mathbf{u}} = \hat{\mathbf{w}} = \hat{\mathbf{e}}$ Equation (2.81) becomes

$$\begin{bmatrix} \left(\rho - Gs^2\right) & \rho_f & 0 \\ \rho_f & \tilde{\rho} & -\frac{i}{\omega}\tilde{\rho}L \\ 0 & -i\omega\mu\tilde{\rho}L & \left(\tilde{\epsilon}\mu - s^2\right) \end{bmatrix} \begin{bmatrix} U \\ W \\ E \end{bmatrix} = \begin{bmatrix} 0 \\ 0 \\ 0 \end{bmatrix} \tag{2.82}$$

Non-trivial solutions for U, W and E exist only if the determinant of the matrix vanishes, in which case two distinct complex transverse wave slownesses are found

$$2s_{s,em}^2 = \frac{\rho_t}{G} + \mu\tilde{\epsilon}\left(1 + \frac{\tilde{\rho}L^2}{\tilde{\epsilon}}\right) \pm \left\{\left[\frac{\rho_t}{G} - \mu\tilde{\epsilon}\left(1 + \frac{\tilde{\rho}L^2}{\tilde{\epsilon}}\right)\right]^2 - 4\mu\frac{\rho_f^2 L^2}{G}\right\}^{1/2} \tag{2.83}$$

where ρ_t is a complex density defined in Equation (2.53). The positive sign in front of the radical in Equation (2.83) corresponds to the mechanical shear-wave slowness s_s, while the negative sign corresponds to the slowness of the electromagnetic wave. This can be seen by setting $L = 0$ in which case the slownesses reduce to the familiar expressions $s_s^2 = \rho_t / G$ and $s_{em}^2 = \mu\tilde{\epsilon}$ for the wave slownesses of shear waves and electromagnetic waves, respectively.

From Equation (2.82) the relation between the wave amplitudes are found to be

$$W = \frac{G}{\rho_f}\left(s_{s,em}^2 - \frac{\rho}{G}\right)U \tag{2.84}$$

$$E = i\omega\mu\tilde{\rho}L\frac{G}{\rho_f}\beta_{s,em}\, U \tag{2.85}$$

with

$$\beta_{s,em} = -\left(\frac{s_{s,em}^2 - \rho / G}{s_{s,em}^2 - \mu\tilde{\epsilon}}\right) \tag{2.86}$$

Plane transverse waves may have one of two different polarisations. For a plane wave propagating in the *x-z* plane of a Cartesian system (x, y, z) the one polarisation corresponds to $\hat{\mathbf{u}} = \hat{\mathbf{w}} = \hat{\mathbf{e}} = \hat{\mathbf{y}}$. This polarisation is referred to as the *SH–TE* (Shear Horizontal − Transverse Electric) mode since it corresponds to displacements in a horizontal direction and transverse electric fields. The other polarisation corresponds to $\hat{\mathbf{u}} = \hat{\mathbf{w}} = \hat{\mathbf{e}} = \hat{\mathbf{y}} \times \hat{\mathbf{k}}$ and is referred to as the *SV–TM* (Shear Vertical − Transverse Magnetic) mode since it corresponds to displacements in a vertical plane and horizontally polarised magnetic fields.

2.4.1.2 Longitudinal modes

Setting $\hat{\mathbf{k}} \bullet \hat{\mathbf{u}} = \hat{\mathbf{k}} \bullet \hat{\mathbf{w}} = \hat{\mathbf{k}} \bullet \hat{\mathbf{e}} = 1$ and $\hat{\mathbf{u}} = \hat{\mathbf{w}} = \hat{\mathbf{e}}$ Equation (2.81) becomes

$$\begin{bmatrix} \left(Hs^2 - \rho\right) & Cs^2 - \rho_f & 0 \\ Cs^2 - \rho_f & Ms^2 - \tilde{\rho} & \dfrac{i}{\omega}\tilde{\rho}L \\ 0 & i\omega\mu\tilde{\rho}L & -\tilde{\epsilon}\mu \end{bmatrix} \begin{bmatrix} U \\ W \\ E \end{bmatrix} = \begin{bmatrix} 0 \\ 0 \\ 0 \end{bmatrix} \tag{2.87}$$

Setting the determinant to zero gives two distinct longitudinal wave slownesses

$$2s_{pf,ps}^2 = \gamma \mp \left\{ \gamma^2 - \frac{4\tilde{\rho}\rho}{\Delta}\left(\frac{\rho_t}{\rho} + \frac{\tilde{\rho}L^2}{\tilde{\epsilon}} \right) \right\}^{1/2} \tag{2.88}$$

with

$$\gamma = \frac{\rho M + \tilde{\rho}H\left(1 + \tilde{\rho}L^2/\tilde{\epsilon}\right) - 2\rho_f C}{\Delta} \tag{2.89}$$

and Δ defined in Equation (2.58). The negative sign in front of the radical in Equation (2.88) corresponds to the slowness (s_{pf}) of the Biot fast pressure wave, while the positive sign corresponds to the slowness (s_{ps}) of the Biot slow pressure wave. With $L = 0$ these slownesses agree exactly with the slownesses derived by Biot (1956a).

In terms of amplitude we have

$$W = \beta_{pf,ps}\, U \tag{2.90}$$

$$E = \frac{i\omega\tilde{\rho}L}{\tilde{\epsilon}}\beta_{pf,ps}\, U \tag{2.91}$$

with $\beta_{pf,ps}$ defined in Equation (2.60).

2.4.2 The electroseismic eigen response

Pride and Haartsen (1996) obtain the eigen responses of the longitudinal and transverse wave modes. In a homogeneous, isotropic medium any direction corresponds to a principal direction of the system. The eigen response of the system can therefore be found by considering the response in an arbitrary direction. Consider a plane wave propagating in the *x*-*z* plane of a Cartesian system. The direction of propagation is given by

$$\hat{\mathbf{k}} = [p/s, \quad 0, \quad q/s]^T \tag{2.92}$$

where s and q are the phase slowness and vertical phase slowness of the plane wave under consideration (for example, $s = s_{pf}$ and $q = q_{pf}$ when considering the fast pressure wave) and p is the horizontal phase slowness (which, according to Snell's law, is conserved upon reflection and refraction).

2.4.2.1 SH-TE *and* SV-TM *eigen response*

Assuming horizontal displacement of the solid (in the direction $\hat{\mathbf{y}}$) and by using Equations (2.66), (2.67), (2.70), (2.73), (2.84) and (2.85) the *SH–TE* eigen response is found to be

$$\mathbf{u} = U\exp(i\mathbf{k}\bullet\mathbf{r})\hat{\mathbf{y}} \tag{2.93}$$

$$\mathbf{w} = \frac{G}{\rho_f}\left(s_{s,em}^2 - \frac{\rho}{G}\right) U\exp(i\mathbf{k}\bullet\mathbf{r})\,\hat{\mathbf{y}} \tag{2.94}$$

$$\tau = i\omega s_{s,em} G\, U\exp(i\mathbf{k}\bullet\mathbf{r})\left[\hat{\mathbf{k}}\hat{\mathbf{y}} + \hat{\mathbf{y}}\hat{\mathbf{k}}\right] \tag{2.95}$$

$$P = 0 \tag{2.96}$$

$$\mathbf{E} = i\omega\mu\frac{\tilde{\rho}}{\rho_f} LG\beta_{s,em} \;\; U\exp(i\mathbf{k}\bullet\mathbf{r})\hat{\mathbf{y}} \tag{2.97}$$

$$\mathbf{H} = i\omega s_{s,em}\frac{\tilde{\rho}}{\rho_f} LG\beta_{s,em} \;\; U\exp(i\mathbf{k}\bullet\mathbf{r})\left(\hat{\mathbf{k}}\times\hat{\mathbf{y}}\right) \tag{2.98}$$

where use is made of the dyadic notation to give

$$\hat{\mathbf{k}}\hat{\mathbf{y}} + \hat{\mathbf{y}}\hat{\mathbf{k}} = \begin{bmatrix} 0 & p/s_{s,em} & 0 \\ p/s_{s,em} & 0 & q/s_{s,em} \\ 0 & q/s_{s,em} & 0 \end{bmatrix} \tag{2.99}$$

In a similar way the *SV-TM* eigen response (solid displacement in the $\hat{\mathbf{y}}\times\hat{\mathbf{k}}$ direction) is found to be

$$\mathbf{u} = U\exp(i\mathbf{k}\bullet\mathbf{r})\left(\hat{\mathbf{y}}\times\hat{\mathbf{k}}\right) \tag{2.100}$$

$$\mathbf{w} = \frac{G}{\rho_f}\left(s_{s,em}^2 - \frac{\rho}{G} \right) \; U \exp(i\mathbf{k} \bullet \mathbf{r}) \left(\hat{\mathbf{y}} \times \hat{\mathbf{k}} \right) \tag{2.101}$$

$$\tau = i\omega s_{s,em} G \, U \exp(i\mathbf{k} \bullet \mathbf{r}) \left[\hat{\mathbf{k}}\left(\hat{\mathbf{y}} \times \hat{\mathbf{k}} \right) + \left(\hat{\mathbf{y}} \times \hat{\mathbf{k}} \right)\hat{\mathbf{k}} \right] \tag{2.102}$$

$$P = 0 \tag{2.103}$$

$$\mathbf{E} = i\omega\mu \frac{\tilde{\rho}}{\rho_f} LG\beta_{s,em} \;\; U \exp(i\mathbf{k} \bullet \mathbf{r}) \left(\hat{\mathbf{y}} \times \hat{\mathbf{k}} \right) \tag{2.104}$$

$$\mathbf{H} = i\omega s_{s,em} \frac{\tilde{\rho}}{\rho_f} LG\beta_{s,em} \;\; U \exp(i\mathbf{k} \bullet \mathbf{r}) \, \hat{\mathbf{y}} \tag{2.105}$$

where

$$\hat{\mathbf{k}}\left(\hat{\mathbf{y}} \times \hat{\mathbf{k}} \right) + \left(\hat{\mathbf{y}} \times \hat{\mathbf{k}} \right)\hat{\mathbf{k}} = \begin{bmatrix} 2pq / s_{s,em}^2 & 0 & (q^2 - p^2) / s_{s,em}^2 \\ 0 & 0 & 0 \\ (q^2 - p^2) / s_{s,em}^2 & q / s & -2pq / s_{s,em}^2 \end{bmatrix} \tag{2.106}$$

For both polarisations of shear waves no changes in the fluid pressure are induced ($P = 0$). Relative flow is therefore the result of grain acceleration only. The relative flow results in a streaming current that produces the magnetic field **H** which, in turn, induces a small electric field **E**. The **E** and **H** fields are carried along with the shear wave and have no extent outside of it. This shows that in homogeneous media no electromagnetic (EM) wave is generated by shear waves.

2.4.2.2 Pf-Ps *eigen response*

From Equations (2.66), (2.67), (2.70), (2.73), (2.90) and (2.91) the longitudinal *Pf-Ps* eigen response is found to be

$$\mathbf{u} = U \exp(i\mathbf{k} \bullet \mathbf{r}) \, \hat{\mathbf{k}} \tag{2.107}$$

$$\mathbf{w} = \beta_{pf,ps} \;\; U \exp(i\mathbf{k} \bullet \mathbf{r}) \, \hat{\mathbf{k}} \tag{2.108}$$

$$\tau = i\omega s_{pf,ps} \; U \exp(i\mathbf{k} \bullet \mathbf{r}) \left[\left(H - 2G + C\beta_{pf,ps} \right) \mathrm{I} + 2G\hat{\mathbf{k}}\hat{\mathbf{k}} \right] \tag{2.109}$$

$$-P = i\omega s_{pf,ps} \left(C + M\beta_{pf,ps} \right) U \exp(i\mathbf{k} \bullet \mathbf{r}) \tag{2.110}$$

$$\mathbf{E} = i\omega \frac{\tilde{\rho} L}{\tilde{\epsilon}} \beta_{pf,ps} \ \ U \exp(i\mathbf{k} \bullet \mathbf{r})\, \hat{\mathbf{k}} \tag{2.111}$$

$$\mathbf{H} = \mathbf{0} \tag{2.112}$$

where the dyadic term in Equation (2.109) is given by

$$\hat{\mathbf{k}}\hat{\mathbf{k}} = \begin{bmatrix} p^2 / s_{pf,ps}^2 & 0 & pq / s_{pf,ps}^2 \\ 0 & 0 & 0 \\ pq / s_{pf,ps}^2 & q / s & q^2 / s_{pf,ps}^2 \end{bmatrix} \tag{2.113}$$

The fact that **H = 0** shows that there is no net electrical current inside the compressional waves. This implies that the streaming current is exactly balanced by an equal and opposite conduction current. The electric field **E** is due entirely to the accumulation and depletion of charges within the compressions and rarefactions of the pressure waves. This electric field is carried along with the pressure waves and has no extent outside of the waves. In homogeneous isotropic media compressional waves do therefore not lead to the radiation of EM waves.

2.4.3 Boundary conditions

Pride and Haartsen (1996) establish the boundary conditions that have to be satisfied at a conformal interface between two dissimilar fluid-saturated porous media. These conditions are

$$\mathbf{u}_1 - \mathbf{u}_2 = \mathbf{0} \tag{2.114}$$

$$\mathbf{n} \times [\mathbf{E}_1 - \mathbf{E}_2] = \mathbf{0} \tag{2.115}$$

$$\mathbf{n} \times [\mathbf{H}_1 - \mathbf{H}_2] = \mathbf{0} \tag{2.116}$$

$$\mathbf{n} \bullet [\tau_1 - \tau_2] = \mathbf{0} \tag{2.117}$$

$$\mathbf{n} \bullet [\mathbf{w}_1 - \mathbf{w}_2] = 0 \tag{2.118}$$

$$P_1 - P_2 = 0 \tag{2.119}$$

where **n** is the unit vector normal to the interface. These boundary conditions express the continuity in the solid displacement, the tangential components of **E** and **H,** momentum flux, fluid flux and fluid pressure across the interface.

CHAPTER 3 RESOLUTION OF SURFACE ELECTROSEISMIC DATA

The ability of surface electroseismic techniques to detect and/or resolve thin imbedded fluid-saturated layers depends on the resolution of surface ES data. In this chapter the various criteria for lateral and vertical resolution and detection of such thin layers are discussed. Since electroseismic methods have much in common with seismic methods, concepts from seismic resolution criteria are borrowed and adapted to be applicable to electroseismic methods.

3.1 Lateral resolution of surface electroseismic data

As in seismics, the Fresnel zone concept may be used to estimate the lateral resolution of ES data. Since the Fresnel zone concept has its origin in optics, optical Fresnel zones are first briefly discussed.

3.1.1 Fresnel zones in optics

In optics the term *Fresnel zone* is defined in the context of light diffraction. Consider a circular hole in a screen, with radius r, between a light source and an observation point as in Figure 3.1.1, where the centre of the circular hole, the light source (S) and the observation point (M) lie along a straight line.

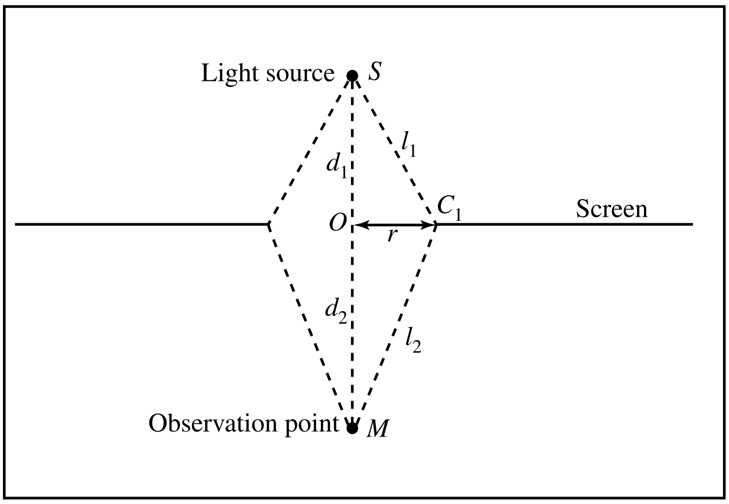

Figure 3.1.1. Fresnel zones in optics.

The phase difference between the light wave components reaching the observation point directly along path *SOM* and the diffracted wave components travelling along the path SC_1M, is given by

$$\begin{aligned}\Delta\phi &= k(l_1 + l_2) - k(d_1 + d_2) \\ &= \frac{2\pi}{\lambda}\left[(l_1 + l_2) - (d_1 + d_2)\right]\end{aligned} \tag{3.1}$$

where $k = 2\pi/\lambda$ is the propagation constant and λ is the wavelength of the light wave. The phase difference $\Delta\phi$ attains a value of π when $(l_1 + l_2) - (d_1 + d_2) = \lambda/2$. Values of r for which $(l_1 + l_2) - (d_1 + d_2) \leq \lambda/2$ result in wave arrivals at the observation point that are out of phase by π radians or less. These wave arrivals therefore contribute constructively to the total energy reaching the observation point. The radius of the first Fresnel zone in optics is defined as the radius r_1 for which $(l_1 + l_2) - (d_1 + d_2) = \lambda/2$. If the light source and observation point are at equal distances from the screen ($l_1 = l_2 = d_1 + \lambda/4$) this radius may be calculated from

$$r_1 = \left((d + \lambda/4)^2 - d^2\right)^{1/2} \tag{3.2}$$

The radius of the n^{th} Fresnel zone in optics is similarly defined as

$$r_n = \left((d + n\lambda/4)^2 - d^2\right)^{1/2} \tag{3.3}$$

3.1.2 Fresnel zones in seismics

In seismic reflection investigations the term *Fresnel zone* is defined in the context of the *reflection* of seismic energy and thus differs from the definition in optics where the *diffraction* of light is considered. Seismic Fresnel zones are therefore not Fresnel zones in the truest sense, but since the phase considerations are equivalent to those in optical diffraction, the term has been in wide use over the last 30 years. The first seismic Fresnel zone is often defined as the area of the reflector that contributes energy (constructively) to the total reflection energy that reaches the observation point (Brühl *et al.*, 1996). Consider a monochromatic seismic source above a horizontal reflector situated at a depth of d units, as in Figure 3.1.2.

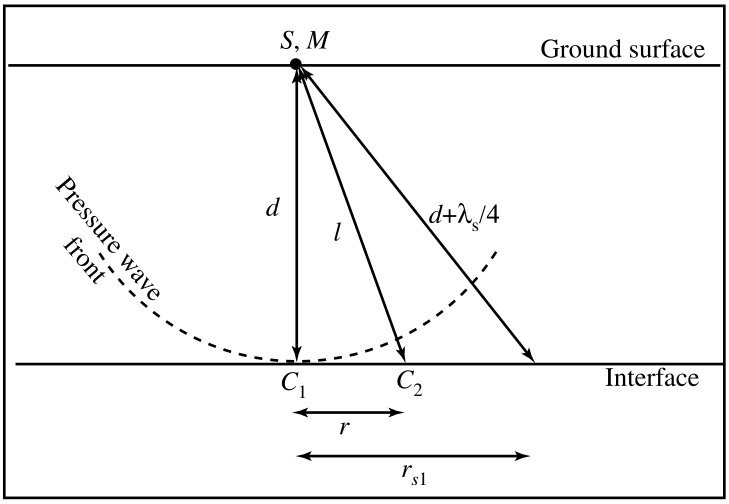

Figure 3.1.2. Seismic Fresnel zones.

Assume for the sake of argument that the observation point M and the source position S coincide. The phase difference between the seismic wave components reaching the observation point reflected from a point C_1 vertically below the seismic source and from a point C_2 horizontally displaced by a distance r, is given by

$$\begin{aligned} \Delta\phi &= k_s(2l) - k_s(2d) \\ &= \frac{4\pi}{\lambda_s}(l-d) \end{aligned} \tag{3.4}$$

where $k_s = 2\pi/\lambda_s$ is the propagation constant and λ_s is the wavelength of the seismic wave. The phase difference $\Delta\phi$ attains a value of π when $(l - d) = \lambda_s/4$. All positions on the reflector for which $(l - d) \leq \lambda_s/4$ result in wave arrivals at the observation point that are out of phase by π radians or less. These wave arrivals therefore contribute constructively to the total energy reaching the observation point. The radius of the first seismic Fresnel zone for monochromatic excitation is defined as

$$r_{s1} = \left(\left(d + \lambda_s/4\right)^2 - d^2\right)^{1/2} \tag{3.5}$$

The radius of the n^{th} seismic Fresnel zone from monochromatic excitation is similarly defined as

$$r_{sn} = \left(\left(d + n\lambda_s/4\right)^2 - d^2\right)^{1/2} \tag{3.6}$$

3.1.3 Fresnel zones in electroseismics

The ES Fresnel zones may be defined analogously to the seismic Fresnel zones. In Figure 3.1.3 a monochromatic seismic source (S) is located above a horizontal interface between media of different electrokinetic properties. The spherically spreading seismic wave intersects the interface and causes fluid flow across the interface. Due to the streaming current imbalance at the interface, electric dipole sources oscillating in phase with the seismic wave are created on the interface. EM waves are radiated from the dipole sources and are recorded at the observation point (M).

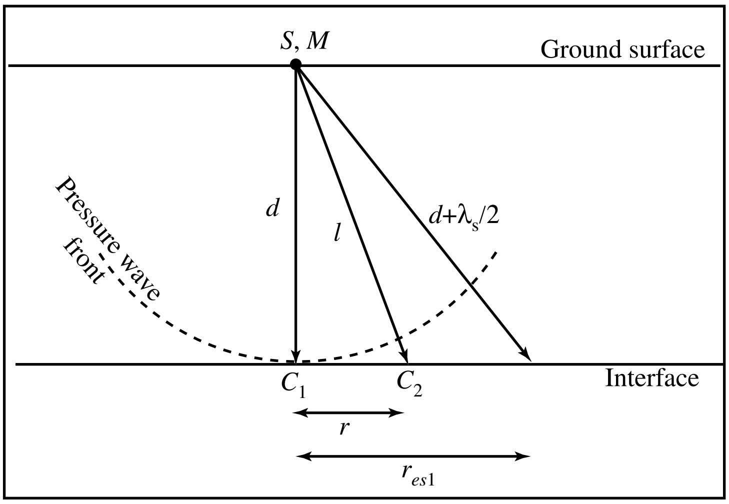

Figure 3.1.3. ES Fresnel zones.

The phase difference between the EM wave components reaching the observation radiated from a point C_1 vertically below the seismic source and from a point C_2 horizontally displaced by a distance r, is given by

$$\begin{aligned}\Delta\phi &= \left[k_s l + k_{em} l\right] - \left[k_s d + k_{em} d\right] \\ &= k_s(l-d) + k_{em}(l-d)\end{aligned} \tag{3.7}$$

Where $k_s = 2\pi/\lambda_s$ is the propagation constant of the seismic wave with a wavelength $\lambda_s = v_s/f$, where v_s is the speed of propagation of the seismic wave and f is the source frequency. Similarly $k_{em} = 2\pi/\lambda_{em}$ is the propagation constant of the EM wave with a wavelength $\lambda_{em} = v_{em}/f$, where v_{em} is the speed of propagation of the EM wave. Since the speed of propagation of seismic and EM waves in earth material differ by 2 to 3 orders of magnitude, we have $k_{em} << k_s$ and Equation (3.7) simplifies to

$$\Delta\phi \approx k_s(l-d) = \frac{2\pi}{\lambda_s}(l-d) \tag{3.8}$$

Again the radius of the first ES Fresnel zone corresponds to positions on the interface for which $\Delta\phi = \pi$, that is where $(l - d) = \lambda_s/2$. The radius of the first ES Fresnel zone due to monochromatic excitation is consequently given by

$$r_{es1} = \left((d + \lambda_s/2)^2 - d^2 \right)^{1/2} \tag{3.9}$$

The radius of the n^{th} ES Fresnel zone from monochromatic excitation is given by

$$r_{esn} = \left((d + n\lambda_s/2)^2 - d^2 \right)^{1/2} \tag{3.10}$$

Comparison of Equations (3.6) and (3.10) shows that the ES Fresnel zones are larger than their seismic equivalents. For interfaces that are deep relative to the seismic wavelength ($d >> \lambda_s$), the area of the ES Fresnel zones are seen to be approximately twice as large as the area of the corresponding seismic Fresnel zones ($r_{esn} \approx \sqrt{2} \times r_{sn}$). This indicates that the lateral resolution of surface ES data is relatively poor when compared with the lateral resolution of surface seismic data.

It is interesting to note that apart from the difference in size between seismic and ES Fresnel zones, there is also a difference in shape when the source and observation points are separated. For a horizontal interface the ES Fresnel zones are, to a close approximation, circular and centred directly beneath the shot-point, whereas the seismic Fresnel zones are ellipses centred halfway between the shot-point and measurement position. This observation is a direct consequence of the fact that $k_{em} << k_s$.

Figure 3.1.4 shows how the radius of the first ES Fresnel zone depends on the velocity at which the pressure wave propagates in the medium above the interface and the interfacial depth. As an example, a frequency of 75 Hz and a seismic wave velocity of 2 000 m s^{-1} result in a radius of 38.9 m for the first ES Fresnel zone at an interface located at a depth of 50 m. The corresponding first seismic Fresnel zone has a radius of 26.7 m, showing that the lateral resolution of surface ES data is relatively poor.

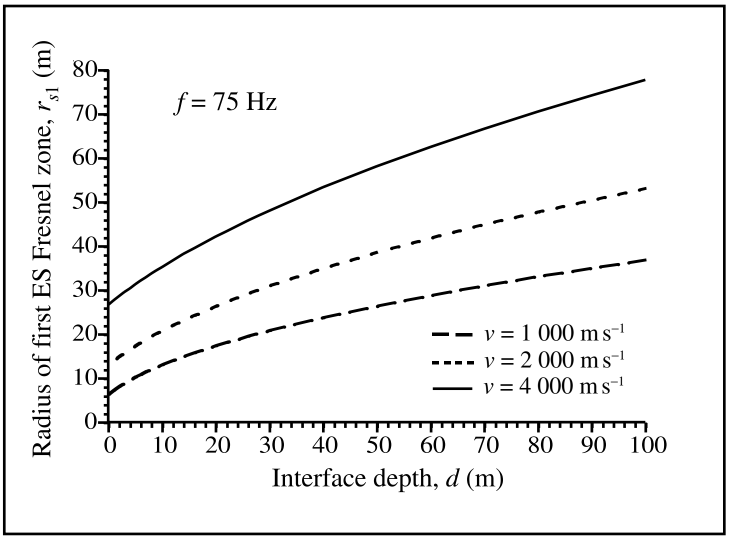

Figure 3.1.4. The radius of the first ES Fresnel zone as a function of pressure wave velocity and interface depth.

The seismic velocities of real earth materials generally increase with depth (Telford *et al.*, 1990). In Figure 3.1.5 the phase of a spherical pressure wave at an interfacial position directly beneath the shot-point is compared with the phase at a specific interfacial position removed by a fixed distance R. The phase differences in two velocity models are examined. In Model A the interface is overlain by a single homogeneous medium with seismic velocity v_1, whereas in Model B two layers overlie the interface with the velocity of the deeper layer higher than that of the shallow layer ($v_2 > v_1$). The phase difference between the two interfacial positions in Model A is given by $\Delta\phi_A = k_1(l - d)$, while the phase difference in Model B is $\Delta\phi_B = k_1(l_1 - d_1) + k_2(l_2 - d_2)$, with $k_1 = \omega / v_1$ and $k_2 = \omega / v_2$ the propagation constants of the seismic waves in the low and high velocity media, respectively. The ratio of the phase differences in the two models is given by

$$\frac{\Delta\phi_B}{\Delta\phi_A} = \frac{l_1 - d_1}{l - d} + \frac{v_1}{v_2}\frac{l_2 - d_2}{l - d} \tag{3.11}$$

This ratio is always less than unity if $v_1 < v_2$, that is $\Delta\phi_B < \Delta\phi_A$. When $\Delta\phi_A = \pi$ the distance R corresponds to the radius of the first ES Fresnel zone in Model A. In Model B, however, we have $\Delta\phi_B < \pi$ and R is still smaller than the radius of the first ES Fresnel zone. ES Fresnel zones are larger in the model that displays a velocity increase with depth and that velocity increases with depth therefore impact negatively on the lateral resolution of surface ES data.

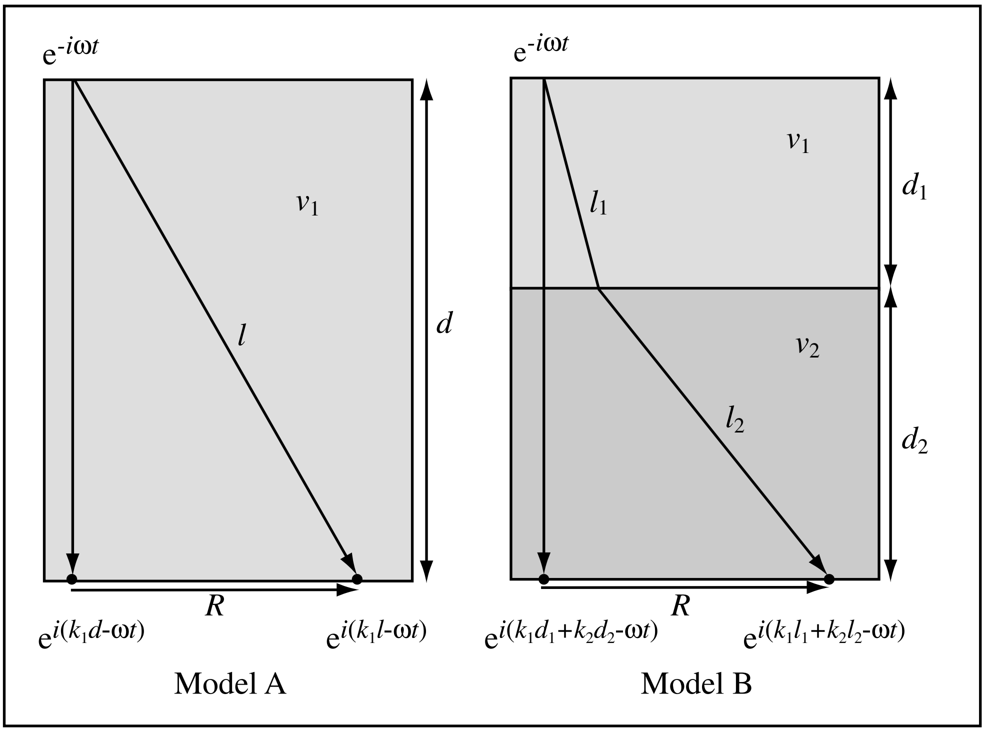

Figure 3.1.5. Model used to investigate the influence of velocity increases with depth on the ES Fresnel zones.

Thus far the discussion on seismic and ES Fresnel zones has focussed on scenarios with monochromatic seismic sources. For broadband sources Equations (3.6) and (3.10) are no longer valid. The ES Fresnel zones from broadband excitation are considered in Section 3.1.5.1.

3.1.4 A simplified model to investigate the lateral resolution of surface electroseismic data

Although an ES record is usually dominated by the electric fields accompanying seismic pressure waves (Garambois and Dietrich, 2001), the model developed here examines only the effects of radiated EM waves generated at interfaces in the subsurface (the interface response), since only these waves contain information about medium properties at depth. The radiated waves result in near-simultaneous arrivals at an array of surface antennæ, and may therefore be removed from the other wave arrivals by means of *f*-*k* dip-filtering. Garambois and Dietrich (2001) show that the radiated waves have a different frequency content from the other wave arrivals and may therefore also be separated by frequency filtering.

The model developed here neglects radiated EM waves from critically refracted shear waves with vertical polarisation and takes only the interface response into account, since Haartsen (1995) showed that the conversion to electromagnetic waves of mechanical waves traversing boundaries is mainly due to pressure gradients generated by pressure waves across the interface. Consider a horizontal interface between two different fluid-saturated media, as shown in Figure 3.1.6. Suppose that only a specific interfacial zone of limited extent exhibits properties that are suitable for ES energy conversion generating independent EM waves. The interfacial zone where ES energy conversion takes place is hereafter referred to as the *conversion zone*. Represent the conversion zone by oscillating electric dipoles spread over its surface area. Point O is the origin of the coordinate system, S is the seismic source position and M is the measurement position. The interface on which the conversion zone occurs is located at a depth of d units. All relevant position vectors are shown in Figure 3.1.6.

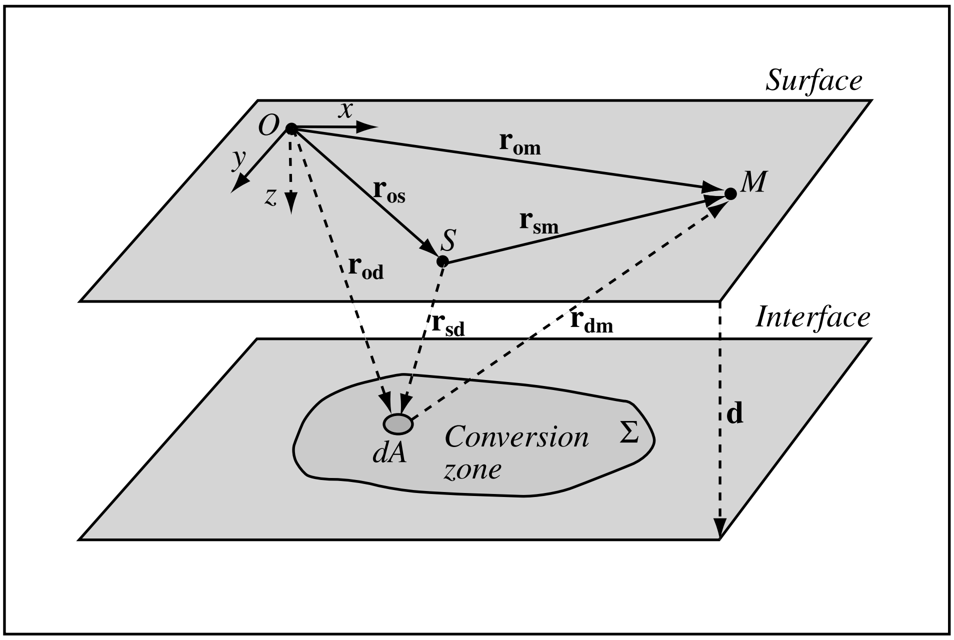

Figure 3.1.6. Model geometry.

From EM theory we know that the skin depth is a measure of the depth of penetration of an EM wave into a conductive medium. It is defined as

$$\delta = \sqrt{\frac{2}{\mu\sigma\omega}} \tag{3.12}$$

where μ and σ are the magnetic permeability and electrical conductivity of the medium, respectively, and ω is the angular frequency of the EM wave. For electric dipoles oscillating at seismic frequencies and with the conductivities of real earth materials the skin depth has a value of a few hundred metres. Since we are generally interested in the responses from interfaces at depths much shallower than the skin depth, we are working in the EM near zone ($r_{dm} << \delta$) and only the low frequency (quasi-static) dipole terms need to be considered.

Patra and Mallick (1980) give the near zone electric field components due to an electric dipole in an unbounded homogeneous, isotropic, conductive medium. The corresponding electric potential may be written in the form

$$\varphi \propto \frac{\mathbf{P} \bullet \mathbf{r}_{dm}}{r_{dm}^{\;3}} \tag{3.13}$$

where $\mathbf{P}$ is the electric dipole moment and $\mathbf{r}_{dm}$ is the displacement vector from the dipole to the measurement position. We are, however, not dealing with unbounded media, and it is appropriate to investigate the effect of boundaries on the electric potential at surface. Figure 3.1.7 is a graphical representation of a two-layered earth in contact with the air. The electric potential at a measurement position M is calculated for a steady current I introduced to Medium 1 at position C. Following Telford *et al.* (1990) the total electric potential may be found by means of the method of images. The total electric potential is written as the sum of the *direct* and *reflected* contributions. The reflected contributions are considered by means of image current sources. Positions C' and C'' in Figure 3.1.7 correspond to the positions of the image current sources for a reflection from the interface between the two conductive media and a reflection from the surface, respectively. An infinite number of additional image sources are required to deal with multiple reflections between the interface and the surface.

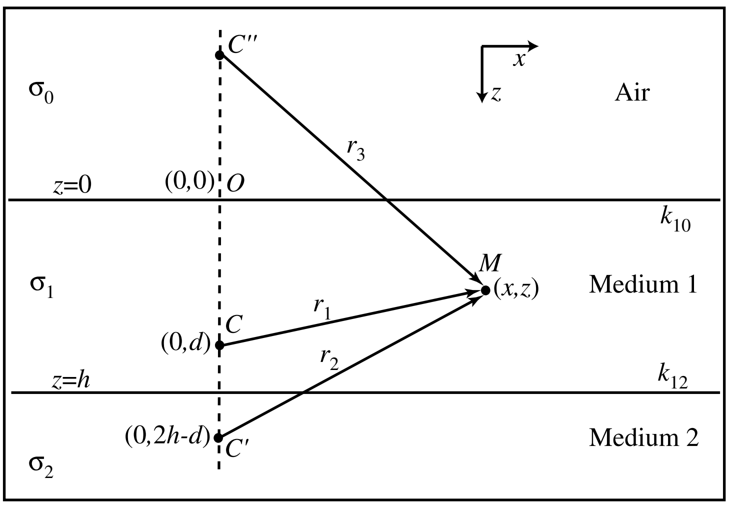

Figure 3.1.7. Model geometry for the calculation of the electric potential due to current injection in a bounded conductive medium.

If k_{10} is the reflection coefficient for currents flowing from Medium 1 to the air, and k_{12} is the reflection coefficient for currents flowing from Medium 1 to Medium 2, the total electric potential may be written as

$$\varphi = \frac{I}{4\pi\sigma_1}\left[\frac{1}{r_1} + \frac{k_{12}}{r_2} + \frac{k_{10}}{r_3}\right] + \left(\begin{array}{c} \textit{contributions from} \\ \textit{multiple reflections} \end{array}\right) \tag{3.14}$$

with

$$k_{ij} = \frac{\sigma_i - \sigma_j}{\sigma_i + \sigma_j} \tag{3.15}$$

When the current source occurs on the interface between the two media ($d = h$), and when the measurement position M is on the surface ($z = 0$), the total electric potential is given by

$$\varphi = \frac{I}{4\pi\sigma_1}\left[\left(1 + k_{10} + k_{12} + k_{10}k_{12}\right)\sum_{n=0}^{\infty}\left\{\left(k_{10}k_{12}\right)^n\left(x^2 + (2n+1)h^2\right)^{-\frac{1}{2}}\right\}\right] \tag{3.16}$$

The conductivity of free air (σ_0) is zero and the value of k_{10} is therefore unity. The total electric potential may therefore be written as

$$\varphi = \frac{I}{2\pi\sigma_1}\left[\left(1 + k_{12}\right)\sum_{n=0}^{\infty}\left\{k_{12}{}^n\left(x^2 + (2n+1)h^2\right)^{-\frac{1}{2}}\right\}\right] \tag{3.17}$$

This series is convergent because $|k_{12}| < 1$. Figure 3.1.8 shows graphs of the normalized surface electric potential calculated for different conductivity contrasts between the two conductive media. The summation in Equation (3.17) is taken over the first hundred terms, although far fewer terms are needed to attain acceptable convergence. σ_1 is kept constant at a value of 30 mS m^{-1} while σ_2 is varied from 10 to 50 mS m^{-1}. Also plotted is the normalized electric potential calculated for an unbounded homogeneous medium ($\sigma_0 = \sigma_1 = \sigma_2$). When the conductivity contrast between the two media is zero (σ_2 = 30 mS m^{-1}) the normalized surface potential agrees exactly with the normalized potential calculated for the unbounded medium (called the *normal potential*), and the two graphs are indistinguishable.

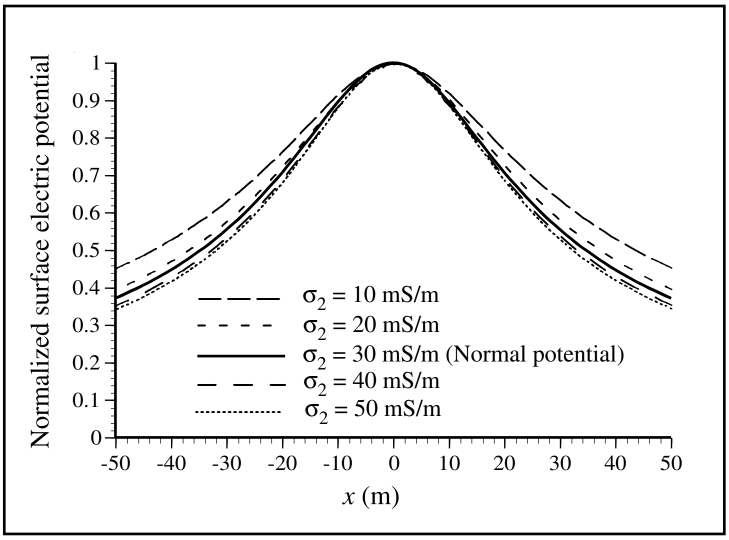

Figure 3.1.8. The normalized surface electric potential for different values of σ_2 (σ_1 = 30 mS m^{-1})

From Figure 3.1.8 it is clear that larger conductivity contrasts result in larger deviations from the normal potential, but that conductivity increases with depth lead to less severe deviation from the normal potential than conductivity decreases with depth. These observations show that for small conductivity contrasts the surface electric potential in bounded media such as in Figure 3.1.7 is approximately directly proportional to the electric potential for an unbounded medium. Under these conditions Equation (3.13) is therefore also approximately valid for bounded media.

Returning to Figure 3.1.6, let **p** be the electric dipole moment per unit area of the conversion zone. The electric potential at a surface position $\mathbf{r}_{om}$ due to a surface element dA of the conversion zone may be calculated from

$$d\varphi \propto \frac{\mathbf{p} \bullet \mathbf{r}_{dm}}{r_{dm}^{\;3}} dA \tag{3.18}$$

Assume that the magnitude of the dipole moment created on the interface is directly proportional to the streaming current imbalance caused when a spherical pressure wave intersects the interface at depth d. Following Haartsen (1995) we insert Equation (2.68) into Equation (2.69) to obtain an expression for the total electric current density in terms of the conductive- and streaming current densities.

$$\begin{aligned} \mathbf{J} &= \sigma\mathbf{E} + \frac{L\eta}{k}[\dot{\mathbf{w}} - L\mathbf{E}] \\ &= \mathbf{J}_c + \mathbf{J}_s \end{aligned} \tag{3.19}$$

where $\mathbf{J}_c$ is the conduction current density and $\mathbf{J}_s$ is the streaming current density. The electrically induced part of the streaming current is second order in the electrokinetic coupling coefficient (L) and may therefore be neglected. The mechanical part of the streaming current is given by

$$\mathbf{J}_{sm} = \frac{L\eta}{k}\dot{\mathbf{w}} \tag{3.20}$$

From Equations (2.107) and (2.108) we see that in homogeneous media the relative fluid-solid displacement (**w**) is directly proportional to the displacement of the solid grains (**u**). The mechanical part of the streaming current may therefore be written as

$$\mathbf{J}_{sm} \propto \dot{\mathbf{u}} \tag{3.21}$$

With these assumptions the dipole moment on the interface at a distance r_{sd} from the seismic source may be written in the form

$$\mathbf{p} \propto \frac{\dot{\mathbf{u}}(t - r_{sd} / v)}{4\pi\sigma\, r_{sd}} = \frac{\dot{u}(t - r_{sd} / v)}{4\pi\sigma\, r_{sd}}\mathbf{e_{sd}} \tag{3.22}$$

where **u**(t) is the displacement of the solid at the source location, with magnitude u. The term $1/r_{sd}$ represents amplitude loss due the spherical spreading of the pressure wave, v is the velocity at which the pressure wave propagates in the medium overlying the interface and may be complex and frequency-dependent to allow for attenuation and dispersion, σ is the conductivity of the medium above the interface and $\mathbf{e}_{sd}$ is a unit vector pointing from the seismic source to the dipole location. Since only fluid flow across the interfacial conversion zone will give rise to radiated EM waves, the dipole moment may be modified by taking only the vertical components of fluid flow into account. For the purpose of simplicity it is assumed that the flow across the interface can be represented by considering only the vertical component of relative fluid-solid flow associated with the pressure wave incident on the interface, so that

$$\mathbf{p} \propto \frac{d}{4\pi\sigma r_{sd}^{\;2}}\,\dot{u}(t - r_{sd} / v)\,\mathbf{e_z} \tag{3.23}$$

The above assumption is rather crude since the angle of incidence and the angle of transmission of the pressure wave will generally be different and depend on the velocities at which the waves propagate in the media above and below the interface. In addition, the amplitude of the transmitted pressure wave will generally differ from the amplitude of the incident pressure wave. Due to the difference in velocities of the Biot fast and slow waves one would expect different flow patterns across the interface for these two types of waves

– something which the simplified modelling scheme presented here does not take into account. Regardless of these limitations the modelling scheme still provides a simple way to obtain insight into the responses that could be expected from localized interfacial zones of ES energy conversion.

From Equation (3.18) the electric potential due to the entire conversion zone may be written as follows

$$\varphi(\mathbf{r}_{om},t) \propto \frac{d^2}{4\pi\sigma} \iint_{\Sigma} \frac{\dot{u}(t - r_{sd}/v)}{r_{sd}^{\;2} r_{dm}^{\;3}} dA \tag{3.24}$$

By considering the simplest case of a monochromatic seismic source with solid displacement $u(t) = \exp(-i\omega t)$, Equation (3.24) becomes

$$\varphi(\mathbf{r}_{om},t) \propto \frac{-i\omega d^2}{4\pi\sigma} e^{-i\omega t} \iint_{\Sigma} \frac{e^{ikr_{sd}}}{r_{sd}^{\;2} r_{dm}^{\;3}} dA \tag{3.25}$$

where ω is the angular frequency of the source and k the propagation constant, which may be complex and frequency-dependent. Since the effects of dispersion is very slight in the seismic frequency range (D'Arnaud Gerkens, 1989), k is assumed to be frequency-independent.

An analytical expression for the surface electric potential may be found for the case where both the seismic source and observation position occur vertically above the centre of a circular conversion zone. By employing a cylindrical coordinate system, as in Figure 3.1.9, Equation (3.25) may be written as

$$\varphi(\mathbf{r}_{om},t) \propto \frac{-i\omega d^2}{4\pi\sigma} e^{-i\omega t} \int_0^{2\pi} \int_0^{R} \frac{e^{ikr_{sd}}}{r_{sd}^{\;2} r_{dm}^{\;3}} \, \rho \, d\rho \, d\theta \tag{3.26}$$

If the source and observation positions are identical and are settled on the normal to the conversion zone passing through its centre, then $r_{sd} = r_{dm}$ and the integrand becomes independent of θ. We therefore have

$$\varphi(\mathbf{r}_{om},t) \propto \frac{-i\omega d^2}{2\sigma} e^{-i\omega t} \int_0^{R} \frac{\rho \, e^{ikr_{sd}}}{r_{sd}^{5}} \, d\rho \tag{3.27}$$

Writing the integral in terms of r_{sd} and making the substitution $\gamma = kr_{sd}$ yields

$$\varphi(\mathbf{r}_{om},t) \propto \frac{-i\omega d^2 k^3}{2\sigma} e^{-i\omega t} \int_{kD}^{kR_{sd}} \frac{e^{i\gamma}}{\gamma^4} \, d\gamma \tag{3.28}$$

The integral in Equation (3.28) can be evaluated analytically by noting that

$$\int_A^B \frac{e^{i\gamma}}{\gamma^4}\,d\gamma = -\frac{1}{3}\left[\left\{\frac{1}{\gamma^3}+\frac{i}{2\gamma^2}-\frac{1}{2\gamma}\right\}e^{i\gamma}\right]_A^B - \frac{i}{6}\left[Ei(iB)-Ei(iA)\right] \tag{3.29}$$

where Ei is the exponential integral function defined as

$$Ei(ix) = -\int_x^{\infty}\frac{e^{it}}{t}\,dt \tag{3.30}$$

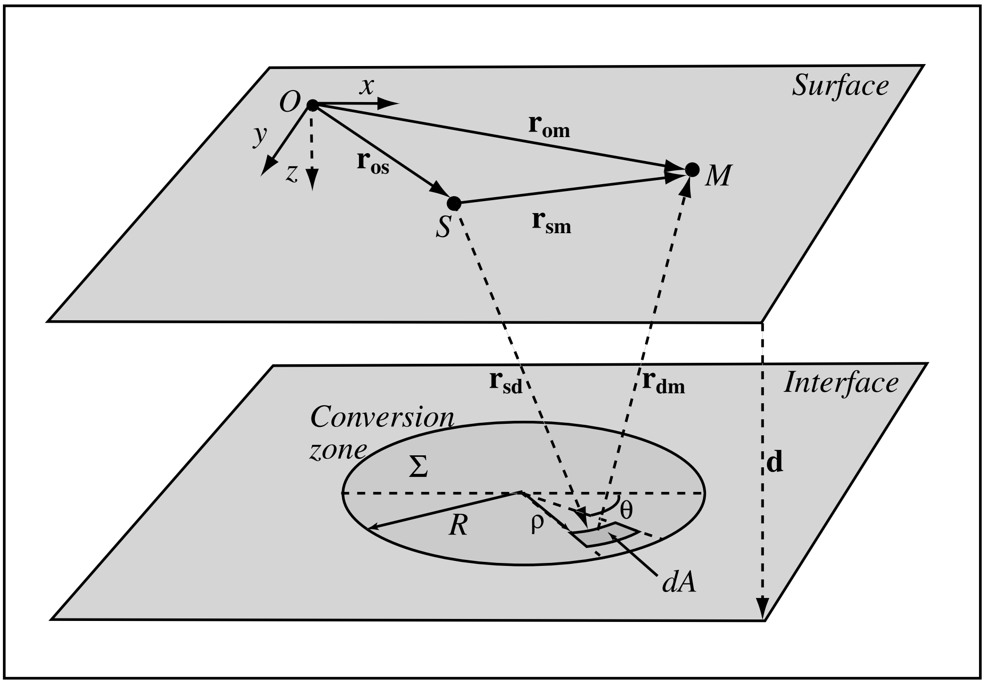

Figure 3.1.9. Model geometry for circular conversion zone.

3.1.5 Model results

In the models that follow the surface electric potentials resulting from broadband excitation were calculated numerically from Equation (3.24). For computational efficiency the electric potentials due to monochromatic seismic sources were calculated numerically from Equation (3.25). A Fortran code based on Simpson's method of numerical integration was developed to perform the calculations. The effects of wave attenuation were disregarded so that the propagation constant k was assumed to be real. Since only scaled outputs from the models were investigated, the value of the conductivity σ was arbitrary.

For broadband excitation both a zero-phase Ricker wavelet and an impulsive (Delta) wavelet were employed. The Ricker wavelet is of the form

$$u(t) = (1 - 2p)\exp(-p), \quad p = (\pi f_0 t)^2 \tag{3.31}$$

with f_0 the dominant frequency (the frequency component with the largest amplitude) of the wavelet. Although the seismic frequency band for land surveys spans frequencies from around 10 to 500 Hz (Sengbush, 1983), the dominant frequencies typically have values of less than 200 Hz (Telford *et al.*, 1990).

Impulsive excitation was modelled by means of a function of the form

$$u(t) = (1 + n^2 t^2)^{-1} \quad (n = 1\,000) \tag{3.32}$$

to yield a wavelet with a halfwidth of 2 ms.

3.1.5.1 Model 1 – ES Fresnel zone radii

Consider a circular conversion zone on an interface between two dissimilar media. The seismic source is located above the centre of the conversion zone, as shown in Figure 3.1.10. The surface electric potential due to a monochromatic seismic source of 75 Hz is compared with the responses from an impulsive source and two Ricker wavelets with dominant frequencies of 75 Hz and 65 Hz, respectively. The model parameters are listed in Table 3.1.1.

Table 3.1.1. Model parameters for Model 1.

Monochromatic source frequency	75 Hz
Ricker wavelet frequencies	65 Hz, 75 Hz
Interface depth (d)	20 m
Pressure wave velocity (v)	1 000 m s^{-1}

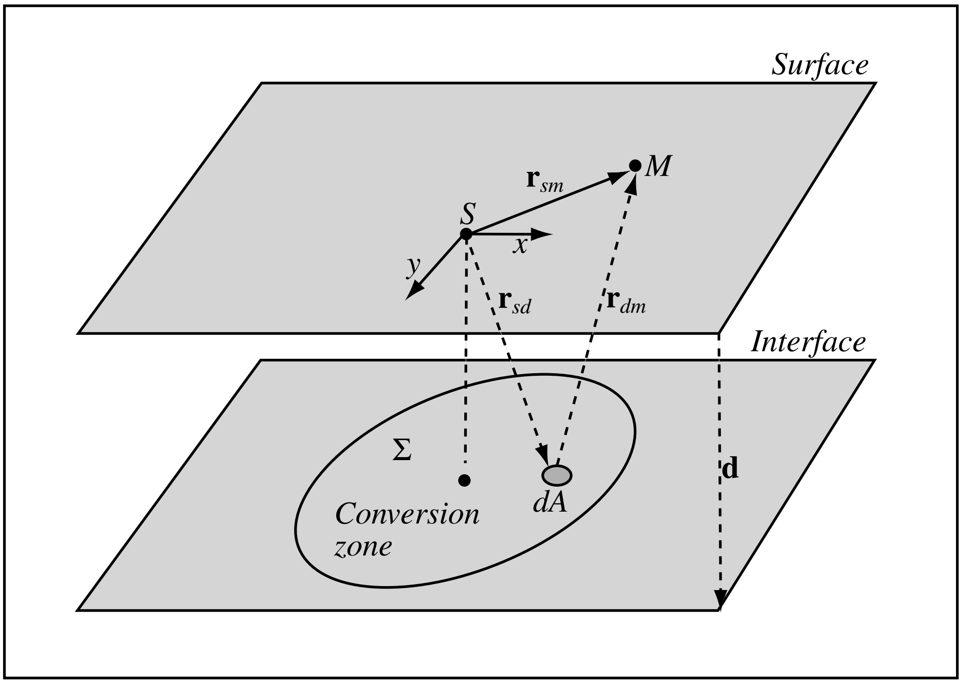

Figure 3.1.10. Geometry of Model 1.

The surface electric potential at the shot-point for monochromatic and broadband excitation is shown in Figure 3.1.11 as a function of conversion zone radius. Scaling of the responses was performed to allow easy comparison of the individual graphs. For the monochromatic source the radii of the consecutive Fresnel zones are clearly seen as the maxima and minima of the graph. Brühl *et al.* (1996) generalize the Fresnel zone concept in seismics to include broadband excitation. They show that only the first seismic Fresnel zone can, in general, be identified for broadband signals and that the radius of the Fresnel zone corresponds to the radius on the reflector that results in maximum energy build-up at the measurement position. From Figure 3.1.11 it is clear that this observation also applies to the ES Fresnel zones. For both the 65 Hz and 75 Hz Ricker wavelets only single ES Fresnel zones can be identified at the maxima of the respective graphs. For this reason the adjective "first" may be dropped when referring to the Fresnel zone from broadband excitation.

Brühl *et al.* (1996) further state that radius of the seismic Fresnel zone is determined mainly by the dominant frequency of the wavelet, but depends on the bandwidth of the signal. In Figure 3.1.11 the radius of the ES Fresnel zone from the 75 Hz Ricker wavelet is seen to be smaller than the first Fresnel zone of the 75 Hz monochromatic source (14.2 m compared to 16.1 m). The Fresnel zone from the 65 Hz Ricker wavelet has an intermediate radius (15.4 m). This observation shows that the lateral resolution of surface ES methods depends on both the dominant frequency and the bandwidth of the seismic source. Higher dominant frequencies (shorter dominant wavelengths) and a broader bandwidth result in higher resolution. As expected, no Fresnel zones are observed for impulsive excitation due to the absence of a strong dominant frequency.

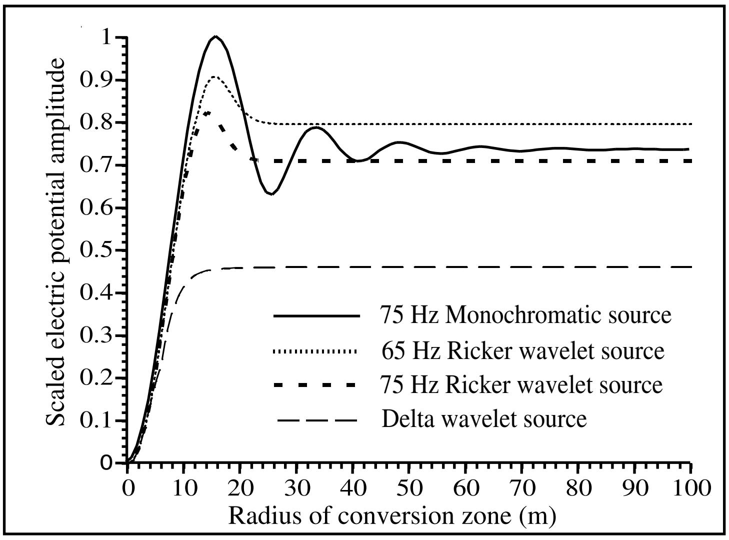

Figure 3.1.11. Scaled surface electric potential amplitude as a function of conversion zone radius.

Table 3.1.2 compares the monochromatic Fresnel zone radii observed in the model results with the radii calculated from Equation (3.10). Due to the fact that Equation (3.10) is based on geometric considerations only and that amplitude losses due to spherical spreading are not taken into account, the observed model Fresnel zone radii are slightly smaller than predicted.

Table 3.1.2. Comparison of the geometric and model ES Fresnel zone radii.

	n^{th} ES Fresnel zone radius (m)	
n	*Geometric*	*Model*
1	17.6	16.1
2	26.7	25.8
3	34.6	33.9
4	42.2	41.4
5	49.4	48.7
6	56.6	55.9
7	63.6	62.9
8	70.6	69.9

3.1.5.2 Model 2 – Ring-shaped conversion zone

To examine the effects of an inactive zone where no energy conversion takes place within a larger active zone, consider a ring-shaped conversion zone, as shown in Figure 3.1.12. The model parameters are listed in Table 3.1.3.

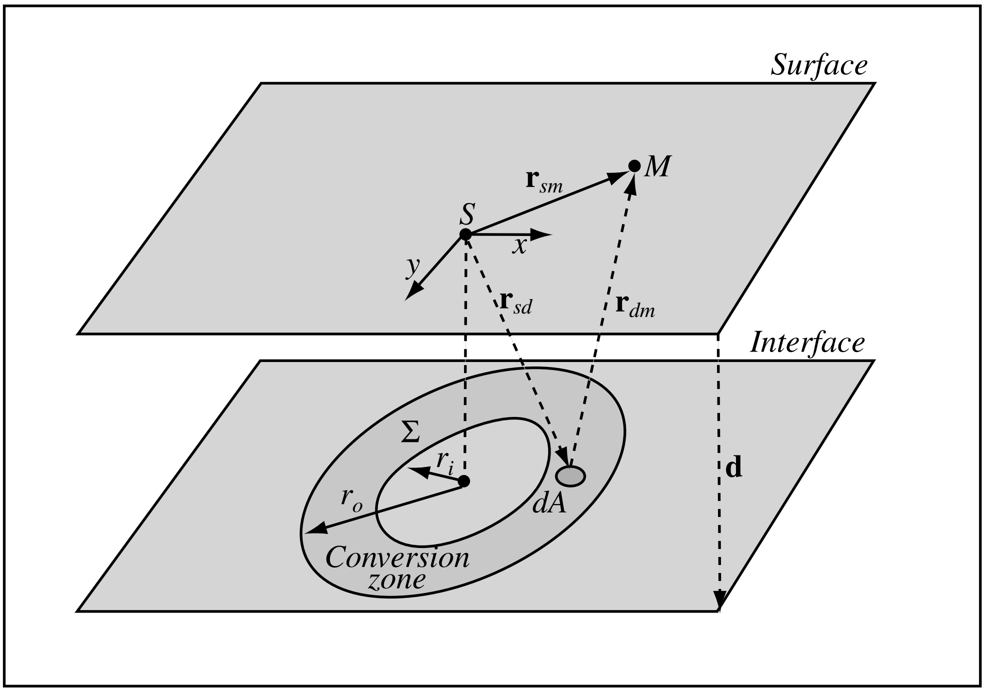

Figure 3.1.12. Geometry of Model 2.

Table 3.1.3. Model parameters for Model 2.

Monochromatic source frequency	120 Hz
Ricker wavelet frequency	120 Hz
Interface depth (d)	40 m
Pressure wave velocity (v)	800 m s^{-1}
Outer radius (r_o)	20 m

The surface electric potential at the seismic source is shown in Figure 3.1.13 as a function of the inner radius (r_i) of the conversion zone. Scaling of the calculated potentials was again performed to allow easy comparison of the individual responses. While the electric potential due to impulsive excitation decreases monotonically for increasing r_i, the electric potential due to monochromatic excitation increases as r_i increases, reaches a maximum value when r_i reaches a value of 9.0 m and decreases to zero as r_i approaches the outer radius of the conversion zone. For Ricker wavelet excitation the electric potential exhibits a maximum for an inner radius of approximately 11.2 m.

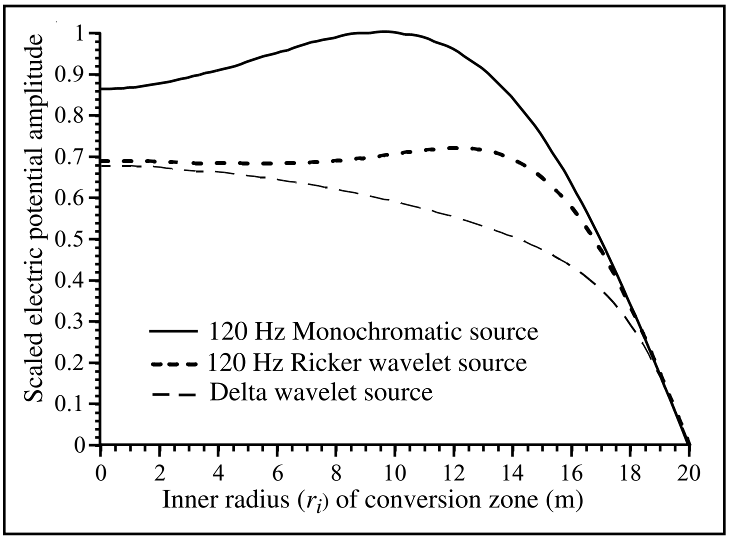

Figure 3.1.13. Scaled surface electric potential amplitude due to a ring-shaped conversion zone.

These observations imply that larger electric potentials may be generated from conversion zones with smaller surface areas. The equivalent observation in optics is that the irradiance at an observation point may be increased through the insertion of a Fresnel zone plate between the light source and the observation point (Hecht and Zajac, 1974). Figure 3.1.13 shows that the electric potential recorded vertically above a zone where no ES energy conversion occurs may be larger than the potential vertically above a zone where energy conversion does take place. The implication for groundwater exploration in fractured Karoo rock is that the lateral resolution of surface ES data may be insufficient to resolve the presence of large unfractured areas within fractured areas, and possibly result in the siting of low-yielding boreholes in the vicinity of an existing fracture.

3.2 Vertical electroseismic resolution

In seismics vertical resolution has two common definitions. The first relates to the position of a reflector in space (the thick-bed response), while the second deals with the ability to separate two features that are close together (the thin-bed response) (Knapp, 1990). Kallweit and Wood (1982) point out that, when working with thin beds, resolution and detection are two different concepts. Detection deals with the recording of a composite reflection regardless of whether the composite reflection can be resolved into its constituent wavelets. Resolution deals with the identification of individual reflections from the top and bottom of a thin bed. Vertical ES resolution is dealt with in this section, while the detection of a thin fluid-saturated layer imbedded in a half-space is considered in the Section 3.3.

3.2.1 Vertical electroseismic resolution criteria

Kallweit and Wood (1982) give a thorough description of the limits of resolution of zero-phase Ricker wavelets. Figure 3.2.1 graphically represents two different resolution criteria. The Rayleigh criterion for temporal resolution of equal-amplitude wavelets with the same polarity is to define the peak-to-trough separation (or *tuning thickness*, $b/2$) as the limit of resolution. Objects that are separated by less than $b/2$ are said to be unresolved. Kallweit and Wood (1982) define the *peak frequency* of the wavelet as the frequency component most strongly present in the wavelet, corresponding to the term *dominant frequency* (f_0) used in this thesis, and the *predominant frequency* (f_{pr}) as the inverse of the trough-to-trough separation ($1/b$). The tuning thickness, $b/2$, may be found by equating the first time-derivative of the Ricker-wavelet (given in Equation (3.31)) to zero. One finds that

$$\frac{b}{2} = \frac{\sqrt{1.5}}{\pi f_0} \approx \frac{1}{2.6 f_0} \tag{3.33}$$

The Ricker criterion for temporal resolution of equal-amplitude wavelets with the same polarity takes the limit of resolvability to be that separation where the composite waveform has a curvature of zero (a "flat spot") at its central maximum. This separation corresponds to the separation (T_R, called *temporal resolution*) between the inflexion point on the main peak of the wavelet. T_R may be found by equating the second time-derivative of the Ricker-wavelet to zero. The four solutions are $\pm(1/\pi f_0)\sqrt{\left(3-\sqrt{6}\right)/2}, \quad \pm(1/\pi f_0)\sqrt{\left(3+\sqrt{6}\right)/2}$. The temporal resolution corresponds to the time difference between the two solutions closest to zero, that is

$$T_R = \frac{2}{\pi f_0}\sqrt{\frac{3-\sqrt{6}}{2}} \approx \frac{1}{3.0 f_0} \tag{3.34}$$

We see that both the Ricker and Rayleigh criteria depend solely on the peak frequency of the Ricker wavelet. Kallweit and Wood (1982) further show that Ricker's zero-curvature criterion for resolution can also be applied to the case of equal amplitude and opposite polarity wavelets. They indicate that the temporal resolution corresponds to limiting bed thicknesses of $\lambda_{pr}/4.62$ at temporal resolution whereas tuning thickness corresponds to a limiting bed thickness of $\lambda_{pr}/4$, where $\lambda_{pr} = v/f_{pr}$ is the predominant wavelength through a bed with interval velocity v. In practice the Rayleigh criterion is often used as the resolution limit and beds thinner than $\lambda/4$, where λ is the dominant (or peak) wavelength, are deemed to be unresolvable (Sheriff, 1999).

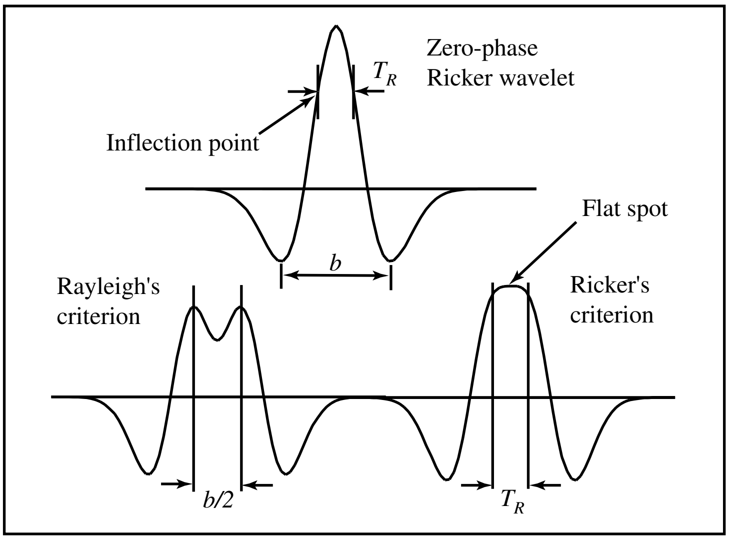

Figure 3.2.1. The resolution criteria of Rayleigh and Ricker.

The Ricker and Rayleigh criteria of temporal resolution were developed for seismic reflection data and are based on the two-way travel time of a seismic wave through a thin bed. In ES data only the one-way travel-time of the seismic wave is relevant, since the generated EM waves travel at speeds that are at least two orders of magnitude higher. The implication is that the temporal separation of the ES responses from the top and bottom interfaces is half as large as for seismic reflection data. The vertical resolution of surface ES data can therefore be no better than $\lambda/2$. For ES phenomena there are, however, two dominant wavelengths to consider – those of the slow and fast pressure waves. The respective wavelengths can be found from the velocities with which the slow and fast waves propagate through the medium.

3.2.2 Estimation of the pressure wave velocities in fluid-saturated Karoo rocks

Equation (2.88) may be used (along with the macroscopic transport coefficients defined in Appendix B) to calculate the complex phase slownesses (s) of both the fast and slow pressure waves in fluid-saturated Karoo rocks. The real phase velocity (v), and the real attenuation coefficient (α) are calculated from

$$v = 1 / \mathrm{Re}\{s\} \tag{3.35}$$

$$\alpha = \omega \, \mathrm{Im}\{s\} \tag{3.36}$$

To evaluate Equation (2.88), information on various physical and chemical properties of these rocks, and the fluids that saturate them, is required.

3.2.2.1 Elastic properties of Karoo rocks

Limited information on the elastic properties of Karoo rocks is available. Brink (1983) reports a few values for the Young's modulus (E) and Poisson's ratio (ν) of sandstones of the Beaufort and Ecca Groups as well as for the sandstones of the Clarens Formation. Geertsema (2000) also gives a few values of E and ν of sandstones, mudstones and siltstones of the Karoo Supergroup.

The most comprehensive list of elastic parameter values for Karoo rocks is, however, given by Olivier (1976) in his study of engineering-geological aspects of tunnel construction between the Orange and Fish rivers. The rocks in the area of study form part of the Beaufort Group of the Karoo Supergroup and consist predominantly of sandstones, mudstones and shales. Olivier gives both the secant and tangent values of Young's modulus measured for the various sedimentary rocks encountered during tunnel construction. The secant Young's modulus is given by the slope of the line from the origin to a point on the stress:strain curve at 50% of the ultimate strength, that is, the stress value at which rock failure occurs (see Figure 3.2.2). The tangent Young's modulus is given by the slope of the tangent of the stress:strain curve at some fixed point on the curve, usually at 50% of the ultimate strength.

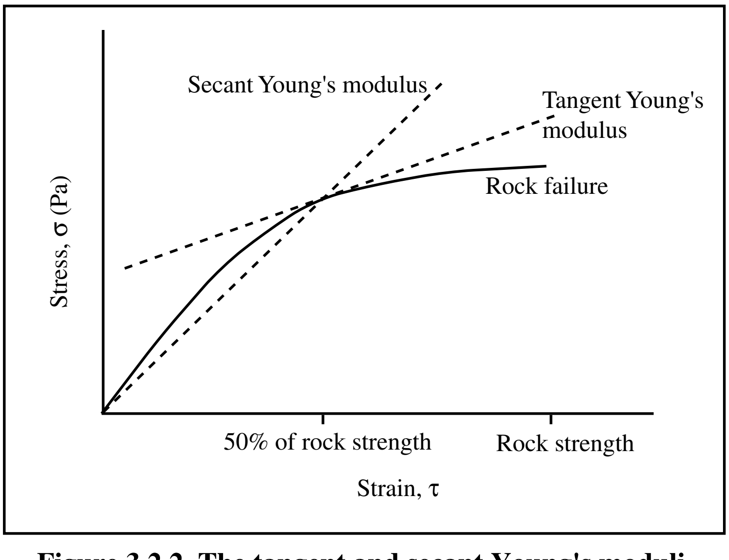

Figure 3.2.2. The tangent and secant Young's moduli.

The strains associated with the propagation of seismic waves in earth materials are adequately small so that a linear relation between stress and strain is generally assumed (Hooke's law, Equation (2.8)), except possibly near the seismic source (see for example Aki and Richards (1980)). From Figure 3.2.2 we see that the Young's modulus of small strains agrees more closely with the secant Young's modulus than with the tangent

Young's modulus. In the present study we will therefore use the values of the secant Young's modulus, as obtained by Olivier, to estimate the elastic properties of Karoo rocks. Table 3.2.1 and Table 3.2.2 list Olivier's values for the secant Young's modulus and Poisson's ratio obtained for oven-dried samples of the various sedimentary rocks, that is, for the dry frames of these rocks.

Table 3.2.1. Young's modulus for Karoo rocks.

Rock type	Young's modulus for dry rocks, E_{fr} ($\times 10^{10}$ Pa)			Number of samples	Std Deviation ($\times 10^{10}$ Pa)
	Minimum	*Maximum*	*Average*		
Sandstones	1.01	3.09	2.19	10	0.63
Mudstones	1.29	2.60	1.86	9	0.51
Siltstones	1.20	4.16	2.28	19	0.77

Table 3.2.2. Poisson's ratio for Karoo rocks.

Rock type	Poisson's ratio for the dry rocks, ν_{fr}			Number of samples	Std Deviation
	Minimum	*Maximum*	*Average*		
Sandstones	0.06	0.16	0.10	10	0.03
Mudstones	0.04	0.13	0.09	9	0.03
Siltstones	0.05	0.17	0.10	19	0.04

To estimate the velocities at which seismic waves propagate in different Karoo rock types, Young's moduli of 2.20, 1.90 and 2.30 and Poisson's ratios of 0.10, 0.09 and 0.10 will be taken for dry sandstones, mudstones and siltstones, respectively. The dry porous frame equivalents of Equations (2.38), (2.43) and (2.44) are

$$K_{fr} = \lambda^{**} + \frac{2}{3}G \tag{3.37}$$

$$E_{fr} = \frac{G\left(3\lambda^{**} + 2G\right)}{\lambda^{**} + G} \tag{3.38}$$

$$\nu_{fr} = \frac{\lambda^{**}}{2\left(\lambda^{**} + G\right)} \tag{3.39}$$

where λ^{**} is the Lamé constant of the dry porous material. With the Young's moduli and Poisson's ratios listed in Table 3.2.1 and Table 3.2.2, Equations (3.37), (3.38) and (3.39) may be used to find the bulk and shear moduli of the dry frames of the different rock types from

$$G = \frac{E_{fr}}{2(\nu_{fr} + 1)} \tag{3.40}$$

$$K_{fr} = \frac{E_{fr}}{3(1 - 2\nu_{fr})} \tag{3.41}$$

These values are listed in Table 3.2.3. Since ν_{fr}<0.125 we find that K_{fr}<G for all the rock types, that is, the frames of the rocks are more resistant to shearing than to volume changes.

Table 3.2.3. Bulk and shear moduli of dry Karoo rocks.

Rock type	K_{fr} ($\times 10^{10}$ Pa)	G ($\times 10^{10}$ Pa)
Sandstones	0.92	1.00
Mudstones	0.77	0.87
Siltstones	0.96	1.05

3.2.2.2 Hydraulic properties of Karoo rocks

The porosities of Karoo sedimentary rocks are generally very low (<0.10) (Rowsell and De Swardt, 1976). The estimate of the porosity of the sandstones used here (0.08) is of a similar magnitude to that obtained by Van der Voort (2001) on the Campus Test Site at the University of the Free State and by Beukes (1969) for sandstones of the Clarens Formation.

The permeabilities of the different rock types are estimated by using values obtained with double-packer tests by Botha *et al.* (1998) for the horizontal hydraulic conductivity (K_h) of Karoo sedimentary rocks on the Campus Test Site at the University of the Free State, and using the relation

$$k_0 = \frac{\eta K_h}{\rho_f g} \tag{3.42}$$

where g is the gravitational acceleration and all other symbols have their meanings as previously defined. For water of low salinity Equation (3.42) becomes $k_0 \approx 10^{-7} \times K_h$ and we obtain permeabilities of 5.0×10^{-12} m^2 for the sandstones, 3.6×10^{-13} m^2 for the mudstones and 1.0×10^{-13} m^2 for the siltstones.

Berryman (1980) gives a relation between the tortuosity (α_∞) and porosity of porous media with spherical grains

$$\alpha_\infty = 0.5\left(\phi^{-1} + 1\right) \tag{3.43}$$

This definition of the tortuosity has the properties that $\underset{\phi\to 0}{\alpha_\infty} \to \infty$ and $\underset{\phi\to 1}{\alpha_\infty} = 1$. Note that the tortuosity defined in this way should be interpreted as the inverse of the definition given by Bear (1988). With the porosity values assumed for the sandstone, mudstone and siltstone, one finds tortuosity values of 6.75 for the sandstones and 13 for the mudstones and siltstones.

3.2.2.3 *Solid properties*

It is assumed that the grains forming the different sedimentary rocks are of the same material (quartz) and that the density of the solid material (ρ_s) is the same for all rock types. The density of quartz is approximately 2.7×10^3 kg m^{-3} while the dielectric constants for quartz is approximately 4 (Telford *et al.*, 1990), so that $\epsilon_s \approx 4\,\epsilon_0$, where ϵ_0 is the dielectric permittivity of free space.

No universal law relating the elastic moduli to porosity exists (Pride *et al.*, 2002). Nolen-Hoeksema (2000) summarises the modulus-porosity relations of two-phase media often used in literature. The bulk modulus of the saturated porous material may be written as the sum of the bulk moduli of the porous frame and the fluid-saturated pores, while the shear modulus of the saturated porous material equals the shear modulus of the porous frame since the shear modulus of a fluid is zero, that is

$$K = K_{fr} + K_{pore} \tag{3.44}$$

$$G = G_{fr} \tag{3.45}$$

The Reuss isostress relations (Reuss, 1929) assume that the grain framework becomes disaggregated. Reuss' relation corresponds to the Wood equation (Wood, 1930) and the Hashin-Shtrikman lower bound (Hashin and Shtrikman, 1963). According to the Reuss relation the bulk and shear moduli of the porous frame become zero, and Equations (3.44) and (3.45) become

$$K = 0 + \left[\frac{\phi}{K_f} + \frac{(1-\phi)}{K_s}\right]^{-1} \tag{3.46}$$

$$G = 0 \tag{3.47}$$

Where K_f and K_s are the bulk moduli of the fluid and solid, respectively. The Voigt isostrain conditions give upper bounds for the saturated bulk moduli K and G (Voigt, 1928).

$$K = (1 - \phi)K_s + \phi K_f \tag{3.48}$$

$$G = (1 - \phi)\, G_s \tag{3.49}$$

Where G_s is the shear modulus of the material forming the solid grains. The Hashin-Shtrikman upper bounds for K and G (Hashin and Shtrikman, 1963) are lower than the Voigt bounds. The modulus porosity relations for the Hashin-Shtrikman upper bounds are

$$K = \left(1-\alpha_K^{HS}\right)K_s + \left(\alpha_K^{HS}\right)^2\left[\frac{\phi}{K_f} + \frac{\left(\alpha_K^{HS} - \phi\right)}{K_s}\right]^{-1} \tag{3.50}$$

$$G = \left(1-\alpha_G^{HS}\right)G_s \tag{3.51}$$

with

$$\alpha_K^{HS} = \frac{\left(4G_s + 3K_s\right)\phi}{4G_s + 3K_s\phi} \tag{3.52}$$

$$\alpha_G^{HS} = \frac{5\left(4G_s + 3K_s\right)\phi}{\left(8G_s + 9K_s\right) + \left(12G_s + 6K_s\right)\phi} \tag{3.53}$$

Both the Hashin-Shtrikman upper bounds and the Voigt bounds may be modified to incorporate the concept of critical porosity as described by Nur *et al.* (1998). The critical porosity is the porosity ϕ_c above which the frame moduli are zero. It separates the cohesive regime from the disaggregated regime. The Modified Voigt and Modified Hashin-Shtrikman relations require the replacement of ϕ with ϕ/ϕ_c in Equations (3.48), (3.49), (3.50), (3.52) and (3.53).

Pride *et al.* (2002) propose relations between the frame and solid moduli of the form

$$K_{fr} = K_s \frac{1-\phi}{1+a\phi} \tag{3.54}$$

$$G = G_s \frac{1-\phi}{1+b\phi} \tag{3.55}$$

where a and b are factors varying with lithology. These relations have the required properties $\underset{\phi\to 1}{K_{fr}} = 0$, $\underset{\phi\to 0}{K_{fr}} = K_s$ and $\underset{\phi\to 1}{G} = 0$, $\underset{\phi\to 0}{G} = G_s$. For consolidated sandstones b ranges between 2 and 20, 2 being well consolidated and 20 poorly consolidated. Pride *et al.* (2002) further state that $a = 2b/3$ is a reasonable assumption for consolidated sediments. Figure 3.2.3 and Figure 3.2.4 illustrate the various modulus-porosity relations by plotting K_{fr} and G as a function of ϕ.

The relations of Pride (Equations (3.54) and (3.55)) are seen to fall within the upper bounds and resemble the Hashin-Shtrikman relations. Due to the simplicity of Pride's relations they are henceforth assumed to describe the relations between K_{fr}, G and ϕ. Due to the fact that the Karoo sediments were subject to long periods of burial at great depths (see Section 1.2) it is henceforth assumed that the Karoo sedimentary rocks are well consolidated and b and a are (somewhat arbitrarily) chosen to be equal to 4 and 2.3, respectively. With these values and the values of K_{fr} and G estimated for sandstones in Section 3.2.2.1, as well as the porosity estimate for sandstone given in Section 3.2.2.2, Equations (3.54) and (3.55) may be used to estimate the K_s and G_s. One finds that $K_s \approx 1.2\times10^{10}$ Pa and $G_s \approx 1.4\times10^{10}$ Pa. These values differ from the corresponding values for pure quartz (3.6×10^{10} Pa and 3.1×10^{10} Pa) due to the fact that various clay minerals, feldspaths, micas and iron minerals also form part of the solid matrix in Karoo sedimentary rocks. In addition, imperfections in the quartz crystals could also contribute to lowering the bulk and shear moduli. It is henceforth assumed that $K_s = 1.2\times10^{10}$ Pa and $G_s = 1.4\times10^{10}$ Pa.

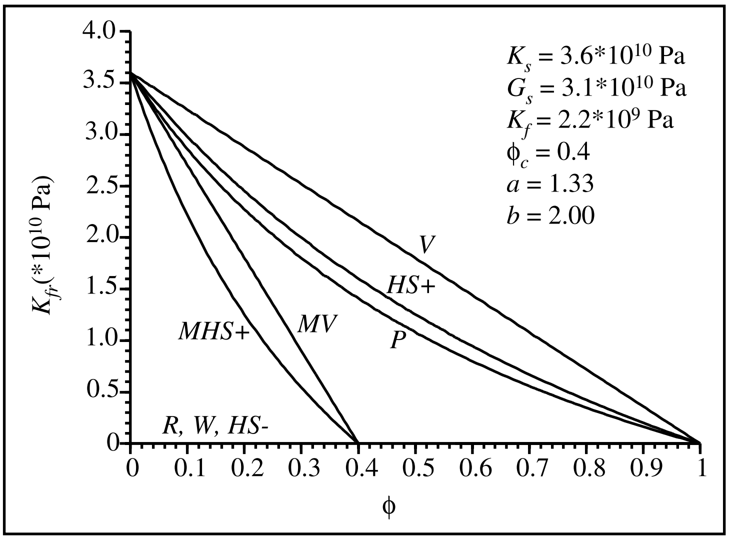

Figure 3.2.3. Relation between the bulk modulus of the porous frame and the porosity as given by the Voigt relation (*V*), the Hashin-Shtrikman upper bound (*HS*+), Pride's relations (*P*), the Modified Voigt relation (*MV*), the Modified Hashin-Shtrikman upper bound (*MHS*+) and the Reuss (*R, W, HS*−) relation.

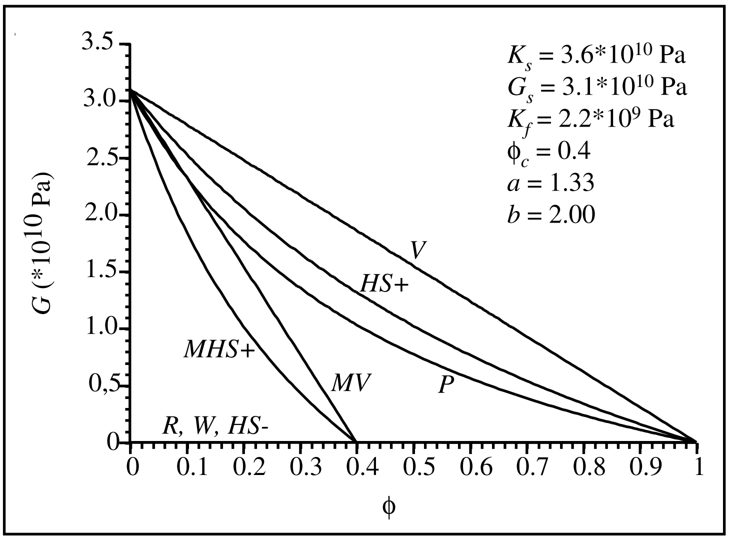

Figure 3.2.4. Relation between the shear modulus of the porous frame and the porosity as given by the Voigt relation (*V*), the Hashin-Shtrikman upper bound (*HS*+), Pride's relations (*P*), the Modified Voigt relation (*MV*), the Modified Hashin-Shtrikman upper bound (*MHS*+) and the Reuss (*R, W, HS*−) relation.

3.2.2.4 Fluid properties

A fluid conductivity of 70 mS m^{-1} is used in accordance with the value measured on the Campus Test Site (Van Wyk *et al.*, 2001). If the assumption is made that NaCl is the dominant salt then this conductivity corresponds to a salinity (C) of approximately 0.0055 mol L^{-1} and a TDS (Total Dissolved Solids) value of approximately 320 mg L^{-1}.

(The true TDS value on the Campus Test Site is $500 - 600\ \mathrm{mg\ L^{-1}}$, indicating the presence of other, heavier salts.) For such a low salinity the density (ρ_f), viscosity (η), and dielectric permittivity (ϵ_f) of the fluid is assumed to differ negligibly from that of pure water. A fluid density of 1 000 kg m^{-3} and a viscosity of 1.0×10^{-3} Pa s are consequently assumed. The dielectric constant of pure water is approximately 80 (Telford *et al.*, 1990), so that we have $\epsilon_f \approx 80\,\epsilon_0$ where ϵ_0 is the dielectric permittivity of free space ($8.854\times10^{-12}\ \mathrm{C^2\ N^{-1}\ m^{-2}}$). The bulk modulus ($K_f$) of pure water ($2.2\times10^9$ Pa) is assumed.

3.2.2.5 Electrical properties of Karoo rocks

The bulk conductivity of the sandstone is taken as $30\ \mathrm{mS\ m^{-1}}$, while the bulk conductivities of the mudstone and siltstone are taken as $15\ \mathrm{mS\ m^{-1}}$. These values are consistent with known values for the conductivities of Karoo rocks (Fourie, 2000).

The bulk dielectric permittivity is taken as the volume average of the dielectric permittivities of the solid and the fluid

$$\epsilon = \phi\epsilon_f + (1-\phi)\epsilon_s \tag{3.56}$$

Table 3.2.4 gives a summary of the model parameters, estimated for fluid-saturated Karoo sedimentary rocks, used to calculate the complex phase slownesses, velocities, attenuation coefficients and wavelengths of the fast and slow pressure waves.

The results of the velocity calculations are given in Table 3.2.5. A source frequency of 100 Hz is assumed. The fast pressure waves are seen to propagate at velocities that are typical for pressure waves in sedimentary rocks. The slow pressure waves, on the other hand, have velocities that are approximately 15, 48 and 85 times slower than the fast waves in the sandstones, mudstones and siltstones, respectively. The wavelengths of the slow waves are also correspondingly shorter.

Table 3.2.4. Model parameters used to calculate the complex phase slownesses, velocities, attenuation coefficients and wavelengths of pressure waves propagating in Karoo rocks.

Parameter	Sandstone	Mudstone	Siltstone
Solid material			
Bulk modulus of solid, K_s [Pa]	1.2E10	1.2E10	1.2E10
Shear modulus of solid, G_s [Pa]	1.4E10	1.4E10	1.4E10
Density of solid, ρ_s [kg m^{-3}]	2.7E03	2.7E03	2.7E03
Fluid			
Bulk modulus of fluid, K_f [Pa]	2.2E09	2.2E09	2.2E09
Salinity, C [mol L^{-1}]	5.5E-03	5.5E-03	5.5E-03
Fluid conductivity, σ_f [S m^{-1}]	7.0E-02	7.0E-02	7.0E-02
Density of fluid, ρ_f [kg m^{-3}]	1.0E03	1.0E03	1.0E03
Fluid viscosity, η [Pa s]	1.0E-03	1.0E-03	1.0E-03
Porous frame			
Bulk modulus of frame, K_{fr} [Pa]	9.2E09	7.7E09	9.6E09
Shear modulus of frame, G [Pa]	1.0E10	8.7E09	1.1E10
Porosity, ϕ	8.0E-02	4.0E-02	4.0E-02
Permeability, k_0 [m^2]	5.0E-12	3.6E-13	1.0E-13
Tortuosity, α_∞	6.75	13	13
Bulk			
Bulk permittivity, ε [C^2 N^{-1} m^{-2}]	1.0E-10	5.0E-11	5.0E-11
Bulk electrical conductivity, σ_0 [S m^{-1}]	3.0E-02	1.5E-02	1.5E-02

Model studies by Haartsen and Pride (1997) confirm that for sedimentary earth materials the slow pressure wave may have a velocity two orders lower than the fast pressure wave. The dominant wavelength of the slow pressure wave is therefore, theoretically, the limiting factor when considering the vertical resolution of surface ES data. From Table 3.2.5 the limiting bed thickness ($\lambda/2$) for the estimated parameters of Karoo sandstones, mudstones and siltstones are approximately 1.18 m, 0.38 m and 0.23 m, respectively, when considering the wavelengths of the slow waves. The magnitudes of the attenuation coefficients of the slow waves in the sedimentary rocks indicate that these waves are strongly dissipative. It is also interesting to note that the slow wave with the highest resolution (shortest wavelength) is subject to the strongest attenuation. Slow waves are therefore expected to die out rapidly from the interfaces where they are created, and may therefore be of less practical use in defining the vertical resolution of ES field data.

Table 3.2.5. Calculated complex phase slownesses, velocities, attenuation coefficients and wavelengths of fast and slow pressure waves propagating in Karoo rocks.

	Complex slowness, s [s m^{-1}]	Velocity, v [m s^{-1}]	Att. coeff., α [m^{-1}]	Wavelength, λ [m]
Sandstones				
Slow wave	(3.40E-3, 2.40E-3)	294.5	1.51	2.95
Fast wave	(3.29E-4, 4.28E-8)	3 036.7	2.68E-5	30.37
Mudstones				
Slow wave	(1.12E-2, 1.01E-2)	89.4	6.37	0.89
Fast wave	(3.45E-4, 0.00E0)	2 902.4	0.00	29.02
Siltstones				
Slow wave	(1.64E-2, 1.60E-2)	60.7	10.1	0.61
Fast wave	(3.21E-4, 0.00E0)	3 114.8	0.00	31.15

3.3 Electroseismic detection of a thin fluid-saturated layer imbedded in a half-space

In seismics a thin layer is defined as a layer with a thickness less than a quarter of the dominant wavelength (Sheriff, 1999). As was shown in Section 3.2.1, the equivalent condition in electroseismics requires a thickness of less than half the dominant wavelength. Assuming that there is a sufficiently large contrast in electrokinetic properties between an imbedded thin layer and the half-space to allow the generation of detectable EM waves, the study of the conditions under which the imbedded layer becomes detectable is essentially a study of the conditions under which constructive interference of the signals generated at the top and bottom interfaces occurs.

3.3.1 Approximate model

The model developed here examines the conditions for constructive interference between the signals generated at the upper and lower interface of an imbedded thin layer. Since the influence of each pressure wave type is considered separately, the model gives only an approximation of the true thin layer response. In reality, mode conversion between the various wave modes occurs at the interfaces and the combined influence of all the various wave modes should be considered to get a more realistic result (this is done in Section 3.3.2). The approximate model developed here does, however, provide insight into the thickness criteria for a thin layer to be detectable.

As in seismics, the response of a thin layer may be investigated by considering plane waves normally incident on horizontal interfaces (Koefoed and de Voogd, 1980, Kallweit and Wood, 1982, de Voogd and den Rooijen, 1983). Due to reasons of symmetry, a plane wave normally incident on an interface between two dissimilar fluid-saturated porous media will give rise to zero electric field on any surface parallel to the interface. The electric potential will, however, be non-zero on such surfaces and may be used to investigate the detection criteria.

Consider a plane pressure wave normally incident on a horizontal fluid-saturated layer imbedded in a fluid-saturated half-space as in Figure 3.3.1. Suppose the displacement of the solid in a plane pressure wave has the form $u_s = u(t)$ at the surface. At the top interface of the imbedded layer at a depth z_0, the displacement of the solid is of the form $u_{10} = u(t - q_0 z_0)$, where q_0 is the (vertical) phase slowness of the plane pressure wave in the half-space, given by $q_0 = k_0 / \omega$, where k_0 is the (vertical) propagation constant of the pressure wave. Since k_0 is in general a complex quantity to allow for wave attenuation, q_0 is also complex. Similarly, at the bottom interface of the imbedded layer with thickness z_1 the displacement of the solid is of the form $u_{12} = u(t - q_0 z_0 - q_1 z_1)$.

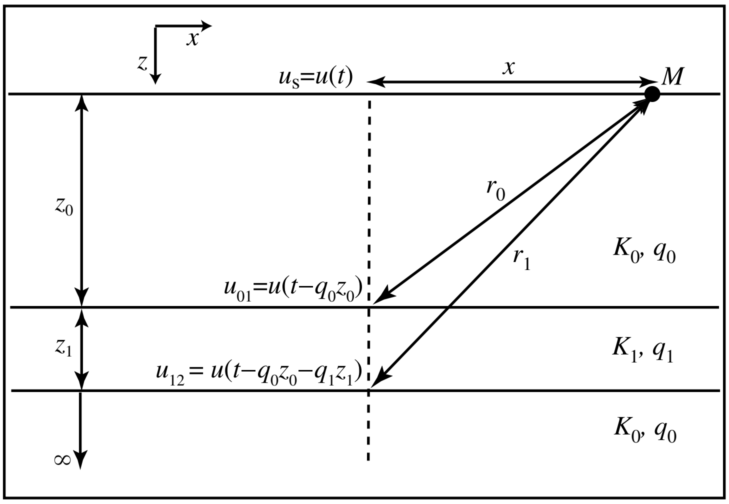

Figure 3.3.1. Model geometry used for investigating the conditions under which an imbedded thin layer becomes detectable.

Assume, as before, that the streaming current in each medium is directly proportional to the first time-derivative of the displacement of the solid grains. Let K_0 and K_1 be the proportionality constants relating the streaming current to the time-derivative of the displacement of the solid in the half-space and imbedded layer, respectively. If the assumption is again made that the electric dipole moment per unit area generated on the interface is directly proportional to the streaming current imbalance, then the magnitude of the dipole moment on the top interface is of the form

$$p_{01} \propto (K_1 - K_0)\, \dot{u}_{01} = (K_1 - K_0)\, \dot{u}(t - q_0 z_0) \tag{3.57}$$

Similarly the magnitude of the dipole moment per unit area on the bottom interface is of the form

$$p_{12} \propto \left(K_0 - K_1\right) \dot{u}_{12} = \left(K_0 - K_1\right) \dot{u}\left(t - q_0 z_0 - q_1 z_1\right) \tag{3.58}$$

From symmetry the electric dipole moments generated on the interfaces have only vertical components, so that $\mathbf{p}_{01} = p_{01}\,\mathbf{e}_z$, and $\mathbf{p}_{12} = p_{12}\,\mathbf{e}_z$. Consider for the moment only the contributions to the total electric potential of electric dipoles located at positions on the top and bottom interfaces along a vertical axis horizontally removed from the observation point M by a distance x, as in Figure 3.3.1. For small conductivity contrasts between the half-space and the imbedded layer, the electric potential due to the electric dipoles may be written as

$$\begin{aligned} d\varphi &= \frac{1}{4\pi\sigma}\left[\frac{\mathbf{p}_{01} \bullet \mathbf{r}_0}{r_0^{\,3}} + \frac{\mathbf{p}_{12} \bullet \mathbf{r}_1}{r_1^{\,3}}\right] dA \\ &= \frac{(K_0 - K_1)}{4\pi\sigma}\left[\frac{\dot{u}_{01}\; z_0}{r_0^{\,3}} - \frac{\dot{u}_{12}\;(z_1 + z_0)}{r_1^{\,3}}\right] dA \end{aligned} \tag{3.59}$$

where σ is the electrical conductivity of the half-space. If the thickness of the imbedded layer (z_1) is much smaller than the depth to the top interface (z_0), we have

$$\begin{aligned} d\varphi &\approx \frac{(K_0 - K_1) z_0}{4\pi\sigma r_0^{\,3}}\left[\dot{u}_{01} - \dot{u}_{12}\right] dA \\ &= \frac{(K_0 - K_1) z_0}{4\pi\sigma r_0^{\,3}}\left[\dot{u}(t - q_0 z_0) - \dot{u}(t - q_0 z_0 - q_1 z_1)\right] dA \end{aligned} \tag{3.60}$$

We see that the electric potential is directly proportional to the difference in the speeds of the solid grains at the two interfaces. To evaluate the behaviour of the electric potential as a function of the imbedded layer thickness, take the partial derivative of $d\varphi$ with respect to z_1

$$\frac{\partial}{\partial z_1}\left[d\varphi\right] = \frac{(K_1 - K_0) z_0}{4\pi\sigma r_0^{\,3}}\left[\frac{\partial}{\partial z_1}\left[\dot{u}(t - q_0 z_0 - q_1 z_1)\right]\right] dA \tag{3.61}$$

The zeros of Equation (3.61) are independent of x, showing that electric dipoles anywhere on the interfaces will result in the same dependence of $d\varphi$ on z_1. After integration over the surfaces of the interfaces to include the contributions from all the electric dipoles, Equation (3.61) is of the form

$$\frac{\partial \varphi}{\partial z_1} \propto \frac{\partial}{\partial z_1}\left[\dot{u}(t - q_0 z_0 - q_1 z_1)\right] \tag{3.62}$$

3.3.1.1 Monochromatic source

Consider a harmonic plane pressure wave in which the displacement of the solid at surface is of the form $u_s = u(t) = \exp(-i\omega t)$. Equations (3.60) and (3.62) respectively become

$$d\varphi = \frac{-i\omega(K_0 - K_1)z_0}{4\pi\sigma r_0^{\ 3}}\left[1 - \exp(i\omega q_1 z_1)\right]\exp(-i\omega(t - q_0 z_0))\, dA \tag{3.63}$$

and

$$\frac{\partial \varphi}{\partial z_1} \propto \left[i\omega q_1 \exp(i\omega q_1 z_1)\right]\exp(-i\omega(t - q_0 z_0)) \tag{3.64}$$

For arbitrary time t, the electric potential attains maximum (and minimum) values at the zeros of Equation (3.64), that is where

$$i\omega q_1 \exp(i\omega q_1 z_1) = 0 \tag{3.65}$$

By writing q_1 as the sum of its real and imaginary parts ($q_1 = q_{1R} + iq_{1I}$), we obtain two equations corresponding to the real and imaginary parts of Equation (3.65). The solutions of the imaginary part of Equation (3.65) yield values of z_1 for which the electric potential attains only local maxima and minima, corresponding to scenarios of maximum signal generation at one of the interfaces and zero signal generation at the other, as is explained in Figure 3.3.2.

Solving for z_1 in the real part of Equation (3.65) gives

$$z_1 = \frac{1}{\omega q_{1R}}\tan^{-1}\left(\frac{-q_{1I}}{q_{1R}}\right) \tag{3.66}$$

As before, the real phase velocity of the pressure wave is given by $v = 1/q_{1R}$, while the real attenuation coefficient is given by $\alpha = \omega q_{1I}$.

For the model parameters estimated for Karoo sandstones, mudstone and siltstone listed in Table 3.2.4, the real and imaginary parts of the phase slownesses are listed in Table 3.2.5. From Table 3.2.5 we see that for fast pressure waves propagating through fluid-saturated Karoo sedimentary rocks, little attenuation occurs, and that q_{1R} dominates over q_{1I}. Solving Equation (3.66) for fast pressure waves gives $z_1 = n\pi/\omega q_{1R} = n\lambda/2$, with

$n = 0, \pm 1, \pm 2\ldots$ Positive uneven values of n correspond to constructive interference from the top and bottom interfaces of the imbedded layer, while positive even values of n correspond to destructive interference. For $n = 1$ the first non-negative, non-trivial value of z_1 occurs at $z_1 = 0.5\ \lambda$.

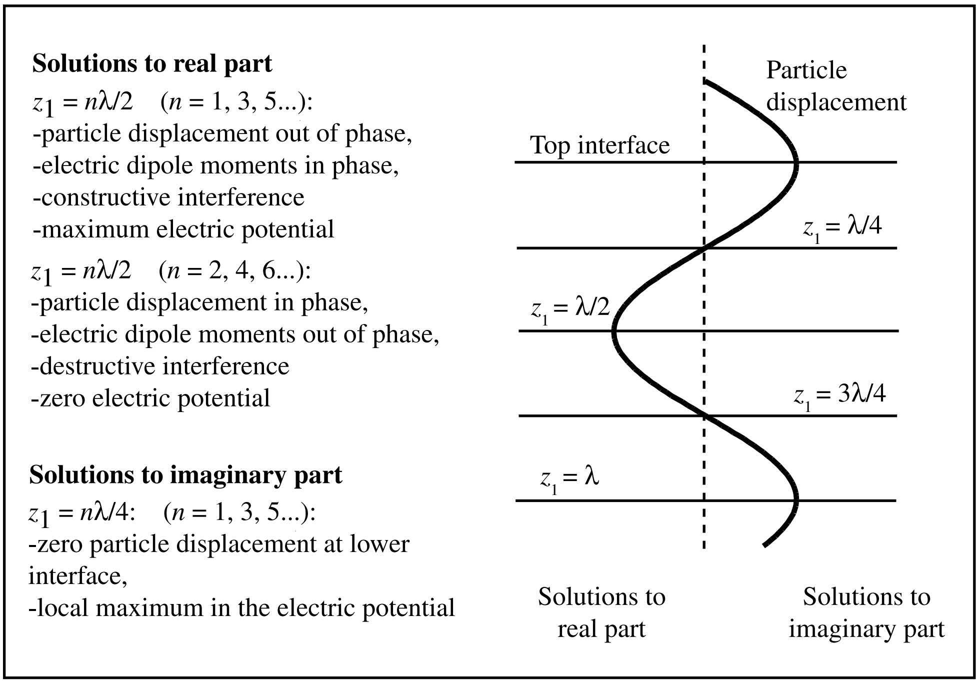

Figure 3.3.2. A graphical representation of the solutions to the real and imaginary part of Equation (3.65).

Solving Equation (3.66) for slow pressure waves in sandstones we get $z_1 = (n\pi - 0.78\pi/4)\,/\,\omega q_{1R} = (4n - 0.78)\lambda/8$, with $n = 0, \pm 1, \pm 2\ldots$ Similarly, for slow pressure waves in mudstones and siltstones we respectively get $z_1 = (4n - 0.93)\lambda/8$ and $z_1 = (4n - 0.98)\lambda/8$, with $n = 0, \pm 1, \pm 2\ldots$The first non-negative, non-trivial values of z_1 occur when $n = 1$. For the sandstone, mudstone and siltstone we get $z_1 \approx 0.40\lambda$, $z_1 \approx 0.38\lambda$ and $z_1 \approx 0.38\lambda$, respectively. With the values of the wavelengths of the slow pressure waves taken from Table 3.2.5, we see that for slow waves in sandstones, mudstones and siltstones these values correspond to thicknesses of 1.18 m, 0.34 m and 0.23 m, respectively. These thicknesses are much larger than the apertures of the fractures of concern – an observation which shows that signal enhancement due to constructive interference from the top and bottom interfaces of the fractures in Karoo rocks is unlikely.

Figure 3.3.3 shows graphs corresponding to the fast and slow pressure waves in Karoo sedimentary rocks of the real part of the $[1 - \exp(i\omega q_1 z_1)]$ term contained in the equation describing the surface electric potential (Equation (3.63)) as a function of the bed thickness scaled by the wavelength. For the fast waves the electric potential is zero at zero bed thickness and reaches a maximum value equal to twice the response from a single interface when the bed thickness equals $\lambda/2$. For a bed thicknesses of $n\lambda/4$ ($n = 1, 3, 5\ldots$) the total response from the upper and lower interfaces is equal to the response from a single interface.

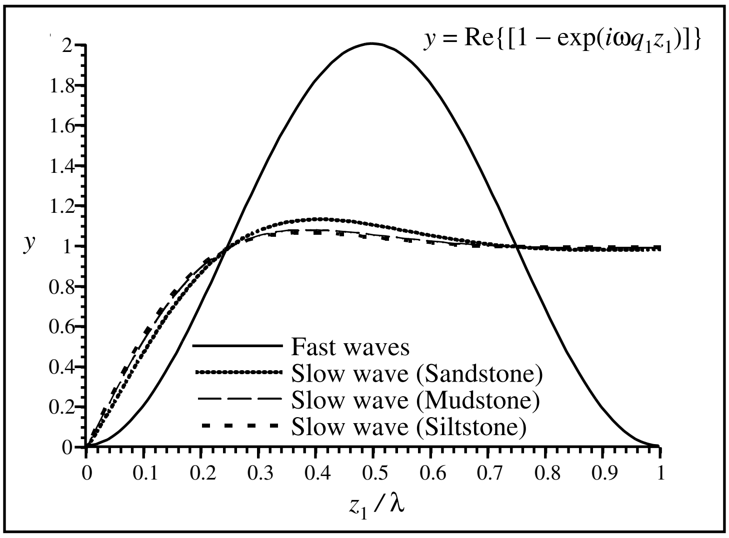

Figure 3.3.3. Graphs showing the influence of the embedded layer thickness on the surface electric potential. Excitation is by means of a monochromatic source, and the time-dependent nature of the source is neglected.

For the slow waves in sandstone the term $[1 - \exp(i\omega q_1 z_1)]$ is zero for zero bed thickness and reaches a maximum value for a bed thickness of 0.40λ. At this bed thickness it attains a value of approximately 1.14 times its value when only a single interface is responsible for signal generation (that is, when $z_1 \to \infty$). Similar behaviour is exhibited for the slow waves in mudstone and siltstone, but maximum values of 1.08 and 1.07 are reached at a bed thickness of 0.38λ. This observation suggests that, even when constructive interference from the signal generated at the top and bottom interfaces occurs, the total signal due to slow waves is only 7-14% stronger than the signal from a single interface. For an imbedded thin layer to be detected by means of a slow wave it is therefore necessary that the contrast in the electrokinetic properties between the thin layer and the half-space be sufficiently large so that signal generated at one interface alone will be strong enough for detection at ground surface.

The total response from the top and bottom interfaces is again equal to the individual response from the upper interface when the bed thickness equals $n\lambda/4$ ($n = 1, 3, 5\ldots$), but due to wave attenuation the difference between the total and individual responses becomes negligible for thicknesses larger than $3\lambda/4$.

These observations suggest that, for both the fast and slow pressure waves, a bed thickness of less than a quarter of a wavelength will cause the total ES signal to be smaller than the response from a single interface. With the values of the calculated slow wave wavelengths as given in Table 3.2.5, $\lambda/4$ corresponds to bed thicknesses of approximately 0.74 m, 0.22 m and 0.15 m for sandstones, mudstones and siltstones, respectively. The aperture widths of fractures in Karoo rocks are much smaller than 0.15 m and the detection of these fractures with surface ES methods is therefore very unlikely, even when higher source frequencies are employed.

It is, however, appropriate to take the time-dependence of the source into account when investigating the amplitude of the total electric potential generated at the two interfaces. This may be done by evaluating Equation (3.63) for incremental time-steps and finding the maximum electric potential amplitude for each bed thickness z_1. The maximum electric potential amplitude, scaled by the amplitude of the response from a single interface, is shown in Figure 3.3.4 as a function of the bed thickness scaled by the wavelength.

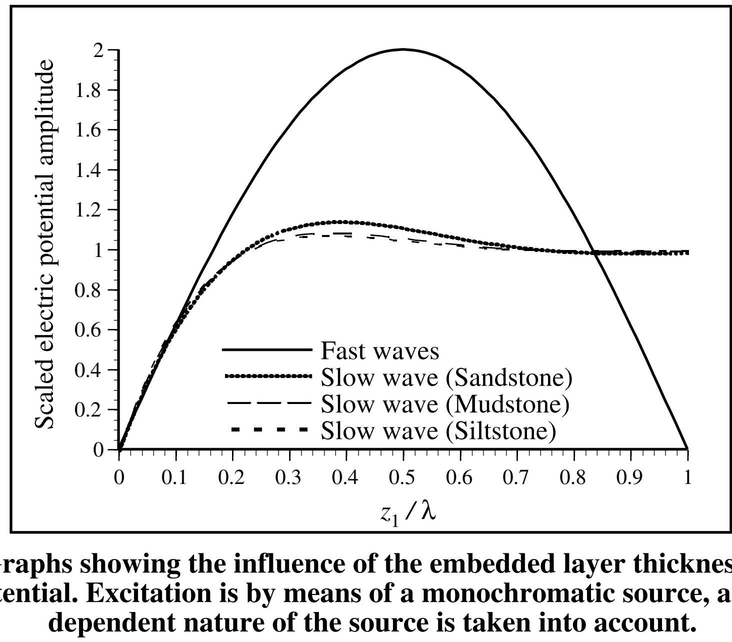

Figure 3.3.4. Graphs showing the influence of the embedded layer thickness on the surface electric potential. Excitation is by means of a monochromatic source, and the time-dependent nature of the source is taken into account.

From Figure 3.3.4 it can be seen that constructive interference due to the fast pressure wave does indeed occur at a bed thickness of $\lambda/2$. The thin-layer responses due to the slow waves are also very similar to the responses shown in Figure 3.3.3. It may therefore be concluded that the detection of fractures in Karoo rocks with surface ES techniques is very unlikely.

3.3.1.2 *Broad-band source*

Consider a plane pressure wave in which the displacement of the solid at surface is of the form of a Ricker-wavelet given by Equation (3.31). For the sake of simplicity assume for the moment that no wave attenuation occurs so that the wave slownesses of both the fast and slow pressure waves in the two media are real. For the Ricker wavelet source Equations (3.60) and (3.62) respectively become

$$d\varphi = \frac{\pi f_0 (K_0 - K_1) z_0}{4\pi\sigma r_0^{\ 3}} \left[\left(4\zeta^3 - 6\zeta\right)\exp\left(-\zeta^2\right) - \left(4\xi^3 - 6\xi\right)\exp\left(-\xi^2\right) \right] dA \tag{3.67}$$

$$\frac{\partial\varphi}{\partial z_1} \propto -2\pi^2 f_0^2 q_1 \left[-4\xi^4 + 12\xi^2 - 3\right]\exp\left(-\xi^2\right) \tag{3.68}$$

with $\zeta = \pi f_0 \left(t - q_0 z_0\right)$ and $\xi = \pi f_0 \left(t - q_0 z_0 - q_1 z_1\right)$. The electric potential attains maximum (and minimum) values at the zeros of Equation (3.68), that is where

$$-4\xi^4 + 12\xi^2 - 3 = 0 \tag{3.69}$$

The solutions of Equation (3.69) are $\xi = \pm\sqrt{\left(3 - \sqrt{6}\right)/2}, \quad \pm\sqrt{\left(3 + \sqrt{6}\right)/2}$. Comparing the first two solutions with Equation (3.34) shows that these solutions are related to the temporal resolution (T_R) as defined earlier. Figure 3.3.5 is the equivalent of Figure 3.3.2 showing the condition under which maximum constructive interference from the signals generated at the top and bottom interfaces occurs. This happens when the two larger peaks of the time-derivative of the Ricker-wavelet fall on the interfaces. In Figure 3.3.5 the wavelet is shown at a time $t = q_0 z_0 + T_R /2$ when the second (later in time) maximum peak falls on the top interface. For the first peak of the wavelet to fall on the bottom interface one requires that $z_1 = T_R / q_1$. Expressed in terms of the dominant wavelength of the wavelet this condition becomes

$$z_1 = \frac{2\lambda_0}{\pi}\sqrt{\frac{3 - \sqrt{6}}{2}} \approx \frac{\lambda_0}{3} \tag{3.70}$$

Maximum constructive interference thus occurs for an imbedded layer thickness corresponding to a third of the dominant wavelength.

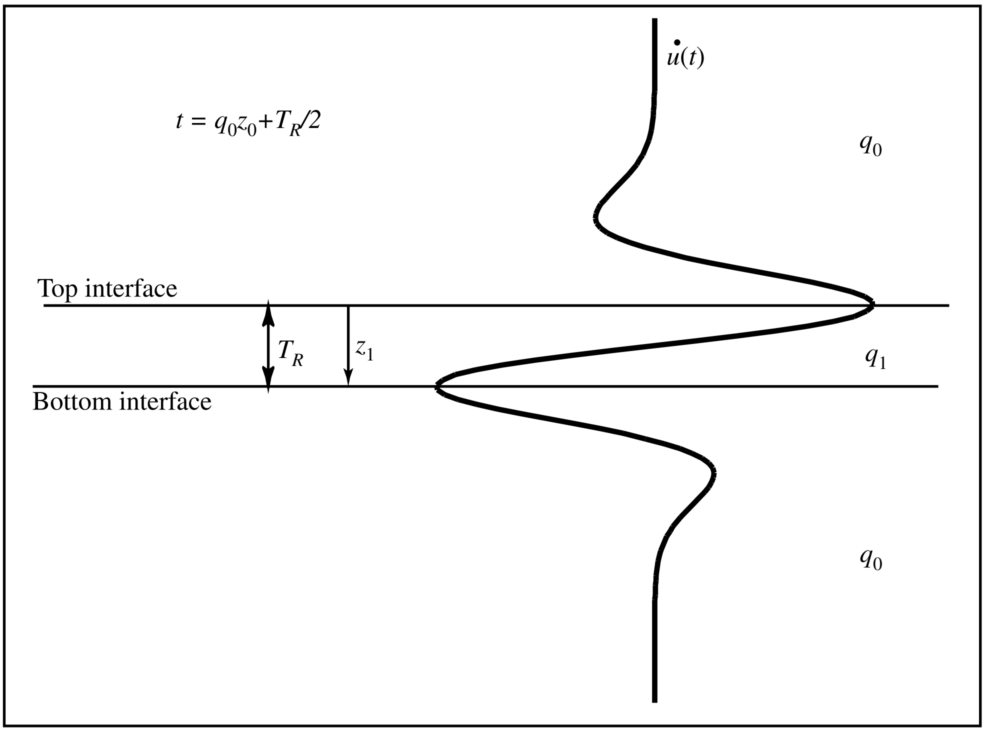

Figure 3.3.5. A graphical representation of the condition under which maximum constructive interference occurs for Ricker-wavelet excitation.

Since wave attenuation is strong for the slow pressure waves, it should not be neglected. The attenuation coefficient given in Equation (3.36) is seen to be frequency-dependent and each frequency-component of the Ricker-wavelet is subject to its own attenuation. If the assumption is, however, made that the attenuation of the wavelet may be described by the attenuation coefficient belonging to the dominant frequency then Equation (3.67) can be modified so that

$$d\varphi = \frac{\pi f_0(K_0 - K_1)z_0}{4\pi\sigma r_0^3}\Big[\left(4\zeta^3 - 6\zeta\right)\exp\left(-\zeta^2\right)\exp\left(-\omega q_{0I}z_0\right) \\ -\left(4\xi^3 - 6\xi\right)\exp\left(-\xi^2\right)\exp\left(-\omega q_{1I}z_1\right)\Big]\,dA \tag{3.71}$$

With the time $t = q_0z_0 + T_R/2$, one obtains $\zeta = \sqrt{\left(3-\sqrt{6}\right)/2}$ and $\xi = \sqrt{\left(3-\sqrt{6}\right)/2} - \pi z_1/\lambda_0$. Figure 3.3.6 is the Ricker-wavelet equivalent of Figure 3.3.3.

The term $\left[1-\left(4\xi^3-6\xi\right)\exp\left(-\xi^2\right)\exp\left(-\omega q_{1I}z_1\right)\left\{\left(4\zeta^3-6\zeta\right)\exp\left(-\zeta^2\right)\exp\left(-\omega q_{0I}z_0\right)\right\}^{-1}\right]$ is plotted as a function of the dimensionless thickness z_1/λ_0. The slownesses listed in Table 3.2.5 are used in the calculations.

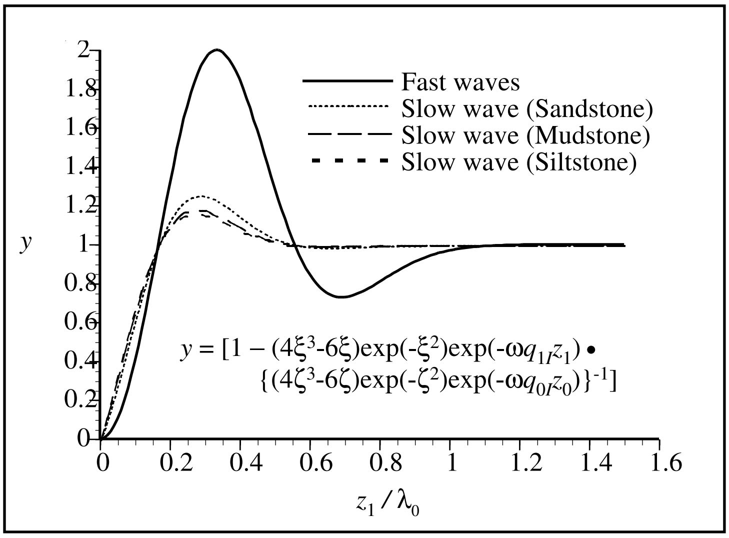

Figure 3.3.6. Graphs showing the influence of the embedded layer thickness on the surface electric potential. Excitation is by means of a Ricker wavelet source.

For the fast pressure waves the electric potential is zero at zero bed thickness and reaches a maximum value equal to twice the response from a single interface when the bed thickness equals approximately $\lambda_0/3$. For the slow pressure waves in sandstone, mudstone and siltstone, maxima are reached for bed thicknesses of approximately $0.28\lambda_0$, $0.27\lambda_0$, and $0.27\lambda_0$, respectively. The electric potentials corresponding to these maxima are approximately 1.25, 1.18 and 1.16 times higher than the electric potential generated from only a single interface (that is, when $z_1 \to \infty$). This observation suggests that even when constructive interference from the signal generated at the top and bottom interfaces occurs, the total signal due to slow waves is only 16-25% stronger than the signal from a single interface. For an imbedded thin layer to be detected it is therefore necessary that the contrast in the electrokinetic properties between the thin layer and the half-space be sufficiently large so that signal generated at one interface alone will be strong enough for detection at ground surface.

For both the fast and slow pressure waves the total response from the top and bottom interfaces is equal to the individual response from the upper interface when $4\xi^3 - 6\xi = 0$. This condition is satisfied when $z_1 = (\lambda_0/\pi)\sqrt{(3-\sqrt{6})/2} \approx \lambda_0/6$ (and when $z_1 = (\lambda_0/\pi)\left[\sqrt{3/2} + \sqrt{(3-\sqrt{6})/2}\right] \approx 9\lambda_0/5$).

From these observations it is clear that for both the fast and slow pressure waves, a bed thickness of less than a sixth of the dominant wavelength causes the total ES signal to be smaller than the response from a single interface. With the values of the calculated slow wave wavelengths as given in Table 3.2.5, $\lambda_0/6$ corresponds to bed thicknesses of approximately 0.49 m, 0.15 m and 0.10 m for sandstones, mudstones and siltstones, respectively. The aperture widths of fractures in Karoo rocks are much smaller than 0.10 m and the detection of these fractures with surface ES methods is therefore unlikely, even when higher seismic source frequencies are employed.

Again it is appropriate to take the temporal nature of the source into account. As before, this may be done by using incremental time-steps to evaluate the maximum electric potential by means of Equation (3.71) for different bed thicknesses, z_1. The maximum electric potential amplitude, scaled by the amplitude of the response from a single interface, is shown in Figure 3.3.7 as a function of the bed thickness scaled by the wavelength.

From Figure 3.3.7 it can be seen that, for Ricker wavelet excitation, constructive interference due to the fast pressure wave does indeed occur at a bed thickness of $\lambda_0/3$. The thin-layer responses due to the slow waves are also very similar to the responses shown in Figure 3.3.6, and it may be concluded that the detection of fractures in Karoo rocks with surface ES techniques, is unlikely.

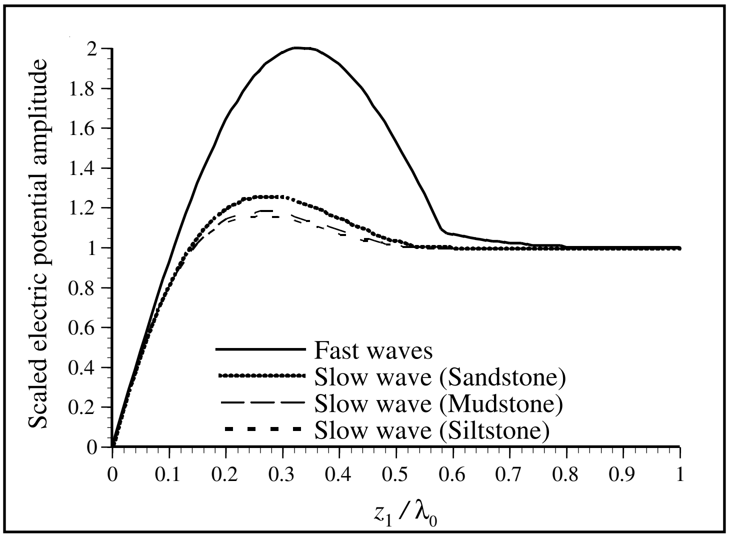

Figure 3.3.7. Graphs showing the influence of the embedded layer thickness on the surface electric potential. Excitation is by means of a Ricker wavelet source, and the time-dependent nature of the source is taken into account.

3.3.2 Matrix method for evaluating the electroseismic response from a thin bed

In this section the ES response from a thin sandstone layer imbedded in mudstone is investigated by means of a matrix method discussed in Appendix C. To implement this method, information on the boundary conditions, eigenvectors and eigenvalues of the waves modes is required. In Section 2.4.3 the electroseismic boundary conditions as obtained by Pride and Haartsen (1996) were given. These conditions are

$$\mathbf{u}_1 - \mathbf{u}_2 = \mathbf{0} \tag{2.114}$$

$$\mathbf{n} \times [\mathbf{E}_1 - \mathbf{E}_2] = \mathbf{0} \tag{2.115}$$

$$\mathbf{n} \times [\mathbf{H}_1 - \mathbf{H}_2] = \mathbf{0} \tag{2.116}$$

$$\mathbf{n} \bullet [\tau_1 - \tau_2] = \mathbf{0} \tag{2.117}$$

$$\mathbf{n} \bullet [\mathbf{w}_1 - \mathbf{w}_2] = 0 \tag{2.118}$$

$$P_1 - P_2 = 0 \tag{2.119}$$

where **n** is the unit vector normal to the interface. For plane waves propagating in the *x-z* plane the non-trivial physical quantities in the *PSVTM* mode that are continuous across the welded interface are u_x, u_z, w_z, τ_{zx}, τ_{zz}, P, E_x and H_y.

According to the matrix method discussed in Appendix C, the problem of electroseismic plane waves may be studied by means of an equation of the form

$$\frac{\partial \mathbf{h}}{\partial z} = \mathbf{A}\mathbf{h} \tag{C1.1}$$

Using the ordering for the vector **h** as employed by Ranada Shaw *et al.* (2000) ($\mathbf{h} = \left[u_z, w_z, \tau_{zx}, H_y, E_x, \tau_{zz}, -P, u_x\right]^T$) and the notations of Ranada Shaw *et al.* (2000) and Haartsen and Pride (1997), gives

$$\frac{\partial}{\partial z}\mathbf{f} = \begin{bmatrix} \mathbf{0}_{4\times4} & \mathbf{A}_1 \\ \mathbf{A}_2 & \mathbf{0}_{4\times4} \end{bmatrix}\mathbf{f} \tag{3.72}$$

where

$$\mathbf{A}_1 = \begin{bmatrix} 0 & M/\Delta & -C/\Delta & -i\omega p\alpha_1 \\ pL & -C/\Delta & H/\Delta - p^2/\tilde{\rho} & i\omega p\alpha_2 \\ -i\omega\rho_f L & -i\omega p\alpha_1 & i\omega p\alpha_2 & -\omega^2\left[\rho_t - 2p^2G(1+\alpha_1)\right] \\ i\omega\tilde{\epsilon}\left(1+\dfrac{\tilde{\rho}L^2}{\tilde{\epsilon}}\right) & 0 & -i\omega\rho L & -\omega^2\rho_f L \end{bmatrix} \tag{3.73}$$

$$\mathbf{A}_2 = \begin{bmatrix} 0 & -\omega^2 p\tilde{\rho}\dfrac{L}{\tilde{\epsilon}} & 0 & i\omega\mu\left(1-\dfrac{p^2}{\mu\tilde{\epsilon}}\right) \\ -\omega^2\rho & -\omega^2\rho_f & -i\omega p & 0 \\ -\omega^2\rho_f & -\omega^2\tilde{\rho}\left(1+\dfrac{\tilde{\rho}L^2}{\tilde{\epsilon}}\right) & 0 & -i\omega p\tilde{\rho}\dfrac{L}{\tilde{\epsilon}} \\ -i\omega p & 0 & 1/G & 0 \end{bmatrix} \tag{3.74}$$

and where $\mathbf{f}$ is a column vector giving the depth-dependencies of the physical quantities in vector $\mathbf{h}$. The matrix $\mathbf{0}_{4\times4}$ is a square matrices containing only zeros. The parameters α_1 and α_2 are defined as

$$\alpha_1 = 1 - 2GM/\Delta \tag{3.75}$$

$$\alpha_2 = \rho_f/\tilde{\rho} - 2GC/\Delta \tag{3.76}$$

All other parameters have been defined earlier in this thesis. To apply the matrix method one needs to find the eigenvectors of the matrix $\mathbf{A}$. Setting up and solving the characteristic equation for the eigenvalues of the 8×8 matrix $\mathbf{A}$, proves to be an arduous task. Instead the eigenvectors may be found directly from the electroseismic eigenresponse as derived by Haartsen (1995) and Pride and Haartsen (1996) (see Section 2.4.2). The longitudinal eigenvectors for the fast and slow pressure waves can be found from Equations (2.93) to (2.98). For a unit solid displacement they are

$$\mathbf{b}_{pf}^{\mp} = \begin{bmatrix} \pm\left(q_{pf}/s_{pf}\right) \\ \pm\beta_{pf}\left(q_{pf}/s_{pf}\right) \\ \pm 2i\omega Gp\left(q_{pf}/s_{pf}\right) \\ 0 \\ i\omega\left(\tilde{\rho}L/\tilde{\epsilon}\right)\beta_{pf}\left(p/s_{pf}\right) \\ i\omega s_{pf}\left(H - 2G\left(p^2/s_{pf}^2\right) + \beta_{pf}C\right) \\ i\omega s_{pf}\left(C + \beta_{pf}M\right) \\ p/s_{pf} \end{bmatrix} \tag{3.77}$$

$$\mathbf{b}_{ps}^{\mp} = \begin{bmatrix} \pm\left(q_{ps}/s_{ps}\right) \\ \pm\beta_{ps}\left(q_{ps}/s_{ps}\right) \\ \pm 2i\omega Gp\left(q_{ps}/s_{ps}\right) \\ 0 \\ i\omega\left(\tilde{\rho}L/\tilde{\epsilon}\right)\beta_{ps}\left(p/s_{ps}\right) \\ i\omega s_{ps}\left(H - 2G\left(p^2/s_{ps}^2\right) + \beta_{ps}C\right) \\ i\omega s_{ps}\left(C + \beta_{ps}M\right) \\ p/s_{ps} \end{bmatrix} \tag{3.78}$$

where the minus sign corresponds to down-going waves and the plus sign to up-going waves. The transverse wavefield eigenvectors can be found from Equations (2.100) to (2.105). For a unit solid displacement they are

$$\mathbf{b}_{sv}^{\mp} = \begin{bmatrix} -\left(p/s_{sv}\right) \\ -\left(G/\rho_f\right)\left(s_{sv}^2 - \rho/G\right)\left(p/s_{sv}\right) \\ i\omega G\left(q_{sv}^2 - p^2\right)/s_{sv} \\ i\omega s_{sv}\left(\tilde{\rho}/\rho_f\right)LG\beta_{sv} \\ \pm i\omega\mu\left(\tilde{\rho}/\rho_f\right)LG\beta_{sv}\left(q_{sv}/s_{sv}\right) \\ \mp 2i\omega Gp\left(q_{sv}/s_{sv}\right) \\ 0 \\ \pm q_{sv}/s_{sv} \end{bmatrix} \tag{3.79}$$

$$\mathbf{b}_{tm}^{\mp} = \begin{bmatrix} -\left(p/s_{tm}\right) \\ -\left(G/\rho_f\right)\left(s_{tm}^2 - \rho/G\right)\left(p/s_{tm}\right) \\ i\omega G\left(q_{tm}^2 - p^2\right)/s_{tm} \\ i\omega s_{tm}\left(\tilde{\rho}/\rho_f\right)LG\beta_{tm} \\ \pm i\omega\mu\left(\tilde{\rho}/\rho_f\right)LG\beta_{tm}\left(q_{tm}/s_{tm}\right) \\ \mp 2i\omega Gp\left(q_{tm}/s_{tm}\right) \\ 0 \\ \pm q_{tm}/s_{tm} \end{bmatrix} \tag{3.80}$$

These vectors are easily confirmed to be eigenvectors of **A** by direct substitution into the eigenequation $\mathbf{Ab} = \lambda\mathbf{b}$, in which case the eigenvalues corresponding to $\mathbf{b}_{pf}^{-}$, $\mathbf{b}_{ps}^{-}$, $\mathbf{b}_{sv}^{-}$, $\mathbf{b}_{tm}^{-}$, $\mathbf{b}_{pf}^{+}$, $\mathbf{b}_{ps}^{+}$, $\mathbf{b}_{svf}^{+}$ and $\mathbf{b}_{tm}^{+}$ are found to be $i\omega q_{pf}$, $i\omega q_{ps}$, $i\omega q_{sv}$, $i\omega q_{tm}$, $-i\omega q_{pf}$, $-i\omega q_{ps}$, $-i\omega q_{sv}$, and $-i\omega q_{tm}$. The matrix containing the eigenvectors as columns is given by

$$\mathbf{E} = \begin{bmatrix} | & | & | & | & | & | & | & | \\ \mathbf{b}_{pf}^{-} & \mathbf{b}_{ps}^{-} & \mathbf{b}_{sv}^{-} & \mathbf{b}_{tm}^{-} & \mathbf{b}_{pf}^{+} & \mathbf{b}_{ps}^{+} & \mathbf{b}_{sv}^{+} & \mathbf{b}_{tm}^{+} \\ | & | & | & | & | & | & | & | \end{bmatrix} \tag{3.81}$$

As is illustrated in Appendix C.3, the thin layer response may now be investigated by evaluating an equation of the form

$$\mathbf{w}_1 = \mathbf{A}^{-1}\mathbf{B}\mathbf{C}^{-1}\mathbf{D}\,\mathbf{w}_3 = \mathbf{M}\,\mathbf{w}_3 \tag{C3.6}$$

where the matrices $\mathbf{A}$, $\mathbf{B}$, $\mathbf{C}$ and $\mathbf{D}$ are formed from the products of the matrices containing the electroseismic eigenvectors in the different media and the matrices containing the vertical phase factors of the various wave types in each medium. To investigate the electroseismic thin layer response due to pressure wave excitation the weighting vectors should be chosen as follows

$$\mathbf{w}_1 = \left(1,\quad 0,\quad 0,\quad 0,\quad w_{15},\quad w_{16},\quad w_{17},\quad w_{18}\right)^T \tag{3.82}$$

$$\mathbf{w}_3 = \left(w_{31},\quad w_{32},\quad w_{33},\quad w_{34},\quad 0,\quad 0,\quad 0,\quad 0\right)^T \tag{3.83}$$

With these choices for the weighting vectors, Equation (C3.6) may be rearranged to obtain

$$\begin{aligned} &\left(w_{31},\quad w_{32},\quad w_{33},\quad w_{34},\quad w_{15},\quad w_{16},\quad w_{17},\quad w_{18}\right)^T \\ &\quad = \left(\begin{array}{ccc|c} m_{11} & \cdots & m_{14} & 0_{4\times4} \\ \vdots & & \vdots & -- \\ m_{81} & \cdots & m_{84} & -\mathbf{I}_{4\times4} \end{array}\right)^{-1} \left(1,\quad 0,\quad 0,\quad 0,\quad 0,\quad 0,\quad 0,\quad 0\right)^T \end{aligned} \tag{3.84}$$

where m_{ij} is the entry in the i^{th} row and j^{th} column of matrix $\mathbf{M}$. The amplitude of the EM wave that is reflected from the thin layer may now be found by solving Equation (3.84) and by examining the coefficient w_{18}.

Using the estimated parameter values of a Karoo sandstone and mudstone listed in Table 3.2.4, the thin bed response due to fast pressure wave excitation is now examined. Since normal incidence of a plane pressure wave on a horizontal interface does not give rise to an electric field at surface, the responses from incidence angles of 5° and 10° are examined. These results are shown in Figure 3.3.8 where the surface electric field, scaled by the field due to only one interface, is plotted against the thin layer thickness scaled by the wavelength of the fast pressure wave. Also shown is the scaled surface electric potential for fast wave excitation as obtained from the approximate model (Section 3.3.1.1, Figure 3.3.4).

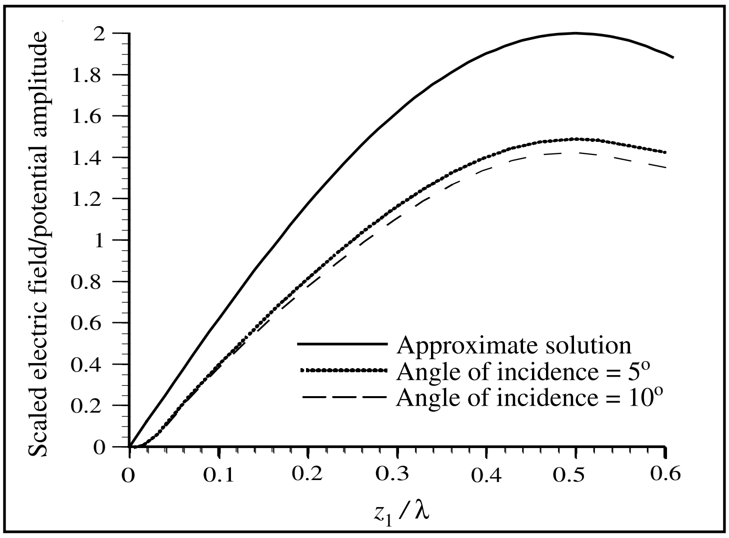

Figure 3.3.8. Graphs showing the influence of the embedded layer thickness on the surface electric field. Results of the approximate solution are compared with the results obtained from the matrix method for plane waves with 5° and 10° incidence.

In Figure 3.3.8 it is observed that, although the approximate solution over-estimates the maximum response, it is in agreement with the solutions of obtained from the matrix method regarding the thickness of the thin layer ($z_1 = \lambda/2$) that results in maximum response. Since the approximate model neglected mode conversion between the various wave types, it is to be expected that it would over-estimate the maximum response. The fact that larger angles of incidence lead to smaller maximum electric field amplitudes can be understood by noting that more *P-SV* mode conversion occurs as the angle of incidence increases from zero (this will be seen in Section 5.1 where ES reflection and refraction in Karoo rocks will be discussed).

Since the matrix method simultaneously considers all the ES wave components, an important observation can be made from Figure 3.3.8. It is clear that the wavelength of the fast pressure wave is the determining factor when considering the conditions for the detection of an imbedded thin layer. The influence of the slow pressure wave seems to be negligible.

3.4 Discussion

The models used in this chapter to investigate the conditions under which a thin imbedded layer becomes detectable assumes that the thin layer consists of consolidated porous material that is saturated with a fluid. The response from this thin layer is then used to evaluate the conditions of detection of fractures in Karoo rocks.

However, studies by Botha *et al*. (1998) has shown that the apertures of the fractures of interest in Karoo aquifers are usually only a few millimetres wide and filled with mud or clay particles. The unconsolidated nature of the material that fills the fractures and the high porosities expected for these materials cause the velocities for the slow pressure wave to be high compared to the velocity in the low porosity consolidated rock hosting the fracture. For example, with a value of 20 for the consolidation factor *b* in Equation (3.55) and a porosity of 0.30, and using the parameter values estimated for Karoo mudstones listed in Table 3.2.4, the slow wave velocity is calculated to be approximately 1 267 m s^{-1}. This high velocity implies a relatively large wavelength for the slow pressure wave in the unconsolidated material. Fractures filled with unconsolidated material will therefore be more difficult to detect than thin layers consisting of consolidated material.

An open fracture has a porosity approaching unity, and wave propagation in a water-filled fracture differs dramatically from wave propagation in a water-saturated porous medium. Only a single pressure wave (and no shear waves) propagates through water at a velocity of approximately 1 500 m s^{-1}. The wavelength of this pressure wave is again much larger than that of the slow pressure wave in a water-saturated porous solid. This implies that an open water-saturated fracture will be more difficult to detect than a thin water-saturated porous layer, even though the electrokinetic contrast between the open fracture and the hosting rock is likely to be high.

Studies on fractured aquifers in Karoo rocks (Riemann and Van Tonder, 2001) indicate that fractured zones may be formed between two closely-separated bedding-plane fractures and that the porosity in this fractured zone may be as high as 0.49. The observed thicknesses of the fractured zones range between 0.1 and 0.2 m. Although no observable surface ES responses from the individual bedding-plane fractures are expected, the thickness of the fractured zone is of a similar magnitude to 1/4 of the estimated wavelength of the slow pressure wave in Karoo sedimentary rocks. Although the conditions under which a thin layer becomes detectable seem to be determined by the wavelength of the fast pressure wave, it could be possible that such a fractured zone may give rise to a surface detectable ES signal if a large enough contrast with the host rock exists.

CHAPTER 4 INFORMATION ON AQUIFER ELASTIC PARAMETERS AND AQUIFER DEFORMATION FROM THE ANALYSES OF ELECTROSEISMIC DATA

Rock deformations caused by stresses can significantly decrease the apertures of fractures in the rock, with magnitudes that depend on the strength of the rock hosting the fractures (Makurat, 2001, Botha and Cloot, 2002). Although fracture deformation decreases dramatically with increasing rock strength, fractures in hard rocks are more prone to deform permanently than fractures in soft rocks, with a corresponding decrease in permeability. Since ES energy conversion in fluid-saturated porous rocks depends on the properties of both the fluid and the solid matrix, ES techniques may provide a non-invasive means of obtaining information on the elastic properties of the rock matrix and, consequently, on the deformability of fractures in the rock. This possibility is examined in this chapter.

4.1 Electroseismic and magnetoseismic transfer functions

Garambois and Dietrich (2001) derived electroseismic and magnetoseismic transfer functions that describe the relations between the amplitudes of the solid displacements due to pressure and shear waves propagating in fluid-saturated porous media, and the induced electric and magnetic fields. These transfer functions were obtained by approximating the frequency-dependent complex transport coefficients derived by Pride (1994) (listed in Appendix B) by their low-frequency equivalents. The frequency content of seismic waves generally ranges from a few Hertz to a couple of hundred Hertz. In Equation (B1.4) the transition (angular) frequency present in the expressions for the dynamic permeability, electrokinetic coupling coefficient and electric conductivity is given by

$$\omega_t = \frac{\phi}{\alpha_\infty k_0}\frac{\eta}{\rho_f} \tag{B1.4}$$

For fluid-saturated eath material this transition angular frequency corresponds to a frequency in the order of several kilohertz to tens of kilohertz, so that the frequency of seismic waves in earth material is several orders lower than the transition frequency. With the assumption that $\omega << \omega_t$ and for realistic rock and fluid parameters, Garambois and

Dietrich (2001) show that Equations (B1.1), (B1.2), (B1.3), (2.47) and (2.77) respectively become

$$k(\omega) \approx k_0 \tag{4.1}$$

$$L(\omega) \approx -\frac{\phi}{\alpha_\infty k_0} \frac{\epsilon_f \zeta}{\eta} \tag{4.2}$$

$$\sigma(\omega) \approx \frac{\phi \sigma_f}{\alpha_\infty} \tag{4.3}$$

$$\tilde{\rho}(\omega) \approx \frac{i}{\omega} \frac{\eta}{k_0} \tag{4.4}$$

$$\tilde{\epsilon}(\omega) \approx \frac{i}{\omega} \frac{\phi \sigma_f}{\alpha_\infty} \tag{4.5}$$

4.1.1 Electroseismic transfer functions for compressional waves

From Equations (2.107) and (2.111) we see that

$$\mathbf{E} = i\omega \frac{\tilde{\rho} L}{\tilde{\epsilon}} \beta_{pf,ps} \mathbf{u} \tag{4.6}$$

By using the results of Dutta and Odé (1979), Garambois and Dietrich (2001) show that

$$\beta_{pf}(\omega) \approx \frac{\rho_f}{\tilde{\rho}(\omega)} \left(1 - \frac{\rho}{\rho_f} \frac{C}{H} \right) \tag{4.7}$$

$$\beta_{ps} \approx -\frac{H}{C} \tag{4.8}$$

Substituting Equations (2.60), (4.2), (4.4), (4.5), (4.7) and (4.8) into Equation (4.6) yields

$$\begin{aligned} \mathbf{E}_{pf} &= \frac{-\omega^2}{\sigma_f} \frac{\epsilon_f \rho_f \zeta}{\eta} \left(1 - \frac{\rho}{\rho_f} \frac{C}{H} \right) \mathbf{u}_{pf} \\ &= \frac{1}{\sigma_f} \frac{\epsilon_f \rho_f \zeta}{\eta} \left(1 - \frac{\rho}{\rho_f} \frac{C}{H} \right) \ddot{\mathbf{u}}_{pf} \\ &= L_{pf} \, \ddot{\mathbf{u}}_{pf} \end{aligned} \tag{4.9}$$

$$
\begin{aligned}
\mathbf{E}_{ps} &= -i\omega\left(\frac{\epsilon_f \zeta}{k_0 \sigma_f}\right)\frac{H}{C}\mathbf{u}_{ps} \\
&= \left(\frac{\epsilon_f \zeta}{k_0 \sigma_f}\right)\frac{H}{C}\dot{\mathbf{u}}_{ps} \\
&= L_{ps}\ \dot{\mathbf{u}}_{ps}
\end{aligned}
\tag{4.10}
$$

where use is made of the fact that $\dot{\mathbf{u}} = -i\omega\mathbf{u}$ and $\ddot{\mathbf{u}} = -\omega^2\mathbf{u}$ for a harmonic time-dependence, exp(-$i\omega t$), and where the displacement field $\mathbf{u}$ is decomposed into the fast and slow Biot wave components, that is

$$\mathbf{u} = \mathbf{u}_{pf} + \mathbf{u}_{ps} \tag{4.11}$$

Equations (4.9) and (4.10) give linear relations between the solid displacement of the fast and slow Biot waves and the co-seismic electric fields, with proportionality constants L_{pf} and L_{ps}, respectively. The electroseismic transfer functions may be defined as follows

$$\frac{\left|\mathbf{E}_{pf}\right|}{\left|\ddot{\mathbf{u}}_{pf}\right|} = L_{pf} \tag{4.12}$$

$$\frac{\left|\mathbf{E}_{ps}\right|}{\left|\dot{\mathbf{u}}_{ps}\right|} = L_{ps} \tag{4.13}$$

(These definitions are the inverses of the transfer functions as defined by Garambois and Dietrich (2001).)

4.1.2 Magnetoseismic transfer function for transverse waves

From Equations (2.93) and (2.98) we see that

$$\left|\mathbf{H}\right| = \left| i\omega s_s \frac{\tilde{\rho}L}{\rho_f} G\beta_s \right| \left|\mathbf{u}\right| \tag{4.14}$$

Garambois and Dietrich (2001) show that for real earth materials at seismic frequencies the following approximations are relevant

$$\rho_t(\omega) \approx \rho \tag{4.15}$$

$$s_s \approx \left[\rho/G\right]^{1/2} \tag{4.16}$$

$$\beta_s(\omega) \approx \frac{\rho_f^2}{\tilde{\rho}(\omega)\rho} \tag{4.17}$$

Substituting Equations (4.2), (4.16) and (4.17) into Equation (4.14) gives

$$\begin{aligned} |\mathbf{H}| &= -i\omega \frac{\phi}{\alpha_\infty} \frac{\epsilon_f \rho_f |\zeta|}{\eta} [G/\rho]^{1/2} \, |\mathbf{u}| \\ &= \frac{\phi}{\alpha_\infty} \frac{\epsilon_f \rho_f |\zeta|}{\eta} [G/\rho]^{1/2} \, |\dot{\mathbf{u}}| \\ &= T\, |\dot{\mathbf{u}}| \end{aligned} \tag{4.18}$$

where use is made of the property $\dot{\mathbf{u}} = -i\omega\mathbf{u}$, and T is a proportionality constant defined implicitly in Equation (4.18). The magnetoseismic transfer function may be defined as

$$\frac{|\mathbf{H}|}{|\dot{\mathbf{u}}|} = T \tag{4.19}$$

(This definition is again the inverse of the transfer function as defined by Garambois and Dietrich (2001).)

4.2 Aquifer elastic parameter estimation

Equations (4.9), (4.10) and (4.18) give linear relations between the solid displacement **u** (or its time-derivatives) and the associated electric and magnetic fields in homogeneous porous media. The electric fields associated with both the Biot fast and slow waves are seen to depend on the elastic parameters C and H, while the magnitude of the magnetic field is seen to depend on the elastic parameter G. The possibility therefore exists that information on aquifer elastic parameters may be obtained from the analyses of the electroseismic- and magnetoseismic transfer functions.

4.2.1 Information from the electroseismic transfer function associated with the fast pressure waves

Consider a borehole intersecting an aquifer, as in Figure 4.2.1. Suppose that a seismic source generating spherically spreading pressure waves is located near the borehole. Apart from the pressure wave propagating past a position on the borehole wall, surface waves, called Stoneley or tube waves, will be generated at the fluid-solid interface of the borehole wall. These waves have propagation velocities lower than both the propagation velocities of the pressure wave in the fluid and the shear wave in the solid matrix (D'Arnaud Gerkens, 1989). Due to this difference it is henceforth assumed that the solid displacement due to the Stoneley wave can be separated from the displacement due to the fast pressure wave.

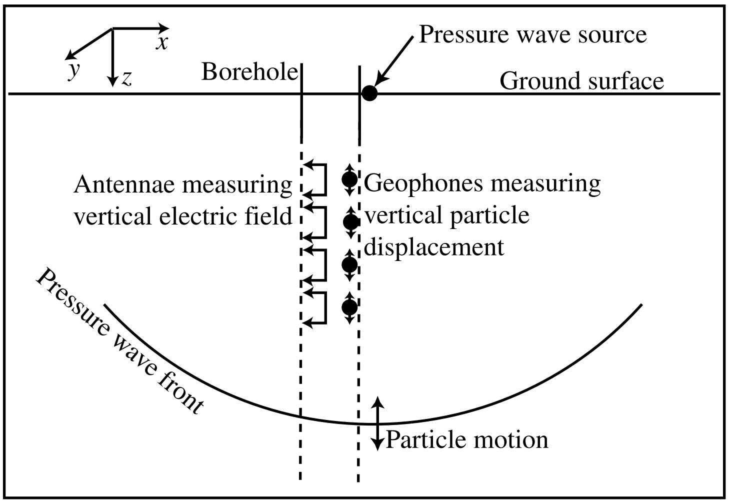

Figure 4.2.1. Model to evaluate the information on aquifer elastic parameters obtained from the electroseismic transfer function associated with the fast pressure wave.

The pressure wave propagating past an observation point located inside the borehole will cause approximately vertical displacements of the solid near the borehole wall. Suppose that geophones and electrodes respectively measuring the vertical (z-) component of the solid displacement and electric field can be attached to the borehole wall. For this wave geometry the electroseismic transfer function for the fast pressure wave given in Equation (4.12), becomes

$$L_{pf} = -E_{pf_z} / \ddot{u}_{pf_z} \tag{4.20}$$

From Equation (4.9) it can be seen that, apart from the ratio H/C, L_{pf} also depends on the fluid parameters ϵ_f, σ_f, η, and ρ_f as well as the zeta-potential and the bulk density ρ, which is in turn a function of ρ_f, ρ_s and ϕ. The fluid parameters can be accurately determined from *in situ* or laboratory analyses of groundwater samples. The porosity ϕ may be estimated from hydraulic investigations, for example by means of tracer tests. Fairly accurate estimation of the mass density of the solid material ρ_s is also possible by consideration of the densities of the minerals forming the solid grains. There are, however, as yet no non-invasive methods for the routine and accurate determination of the zeta-potential. This implies that the ratio H/C can at present not be determined unambiguously from the analyses of the electroseismic transfer function associated with the fast pressure wave.

4.2.2 Information from the electroseismic transfer function associated with the slow pressure waves

Equation (4.10) suggests that information on aquifer elastic properties may be obtained by considering the solid displacement due to the Biot slow wave and the associated electric field. This would, however, require the separation of the fast and slow Biot wave components from the total solid displacement. In addition, the Biot slow wave is strongly dissipative and dies out rapidly from the interfaces where it is created. Measurements of the solid displacement and electric field should therefore be done near such interfaces. However, near the interfaces the distinction between the Biot fast and slow wave components will be more difficult since insufficient time will have elapsed to allow spatial separation of these waves. The amplitude of the transmitted Biot slow wave is significantly smaller than that of the Biot fast wave, as will be shown in Chapter 5 where electroseismic reflection and transmission coefficients for interfaces between Karoo rocks are calculated. These observations show that great difficulty can be expected in separating the displacement due to the Biot slow wave from the total displacement.

Suppose for the moment that it is possible to separate the slow and fast wave components of the solid displacement near an interface. Consider a borehole intersecting an aquifer, as in Figure 4.2.2 and assume that a seismic source generating spherically spreading pressure waves is located near the borehole. The pressure wave propagating past an observation point located inside the borehole will cause approximately vertical displacements of the solid near the borehole wall.

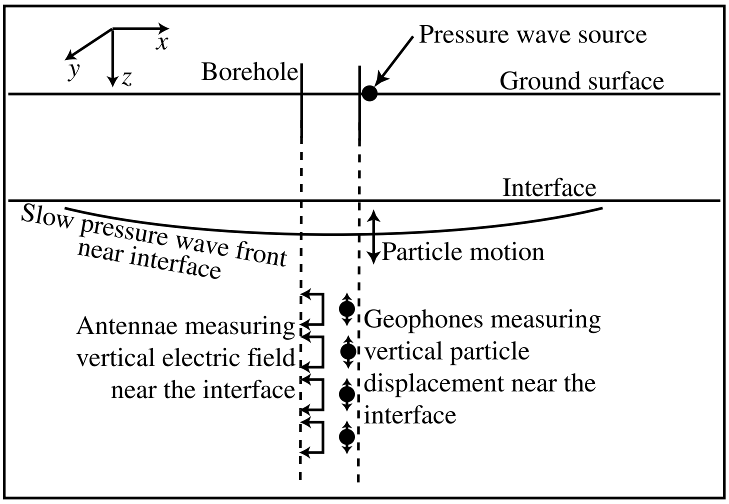

Figure 4.2.2. Model to evaluate the information on aquifer elastic parameters obtained from the electroseismic transfer function associated with the slow pressure wave.

Suppose that geophones and electrodes respectively measuring the vertical component of the solid displacement and electric field can be attached to the borehole wall close enough to aquifer boundaries to measure the effects of the slow pressure wave. For this wave geometry the electroseismic transfer function for the slow pressure wave given in Equation (4.13), becomes

$$L_{ps} = -E_{ps_z} / u_{ps_z} \tag{4.21}$$

From Equation (4.10) it can be seen that, apart from the ratio C/H, L_{ps} depends on the fluid parameters ϵ_f, and σ_f, as well as the permeability k_0, the zeta-potential ζ and the bulk density ρ, which is in turn a function of ρ_f, ρ_s and ϕ. As before, the fluid parameters may be found from the analyses of groundwater samples, ρ_s may estimated from the mineral densities and k_0 and ϕ may be estimated from hydraulic tests. The zeta-potential is again the only parameter that cannot be determined by non-invasive means and the ratio C/H can therefore not be determined unambiguously from the analyses of the electroseismic transfer function associated with the slow pressure wave.

4.2.3 Information from the magnetoseismic transfer function associated with the shear waves

Equation (4.18) suggests that information on the shear modulus (G) of the solid frame may be obtained by measuring the total solid displacement (**u**) and the magnitude of the associated magnetic field. To investigate this possibility, consider a borehole penetrating an aquifer, as in Figure 4.2.3. Suppose that a seismic source, generating spherically propagating shear waves, occurs at surface near the borehole. Assume, as before, that the shear wave components can be separated from the Stoneley wave. This assumptions is reasonable since the shear wave causes solid displacements that are perpendicular to the solid displacements of the Stoneley wave. The shear waves propagating past an observation point inside the borehole will therefore have approximately horizontal polarisations.

Assume further that geophones measuring the one horizontal component (say the x-component) of the solid displacement can be attached to the side of the borehole, and that magnetometers measuring the perpendicular horizontal component (the y-component) of the magnetic field are suspended near the geophones.

From Equation (4.18) the magnetoseismic transfer function may be estimated by noting that for this wave geometry

$$T = H_y / \dot{u}_x \tag{4.22}$$

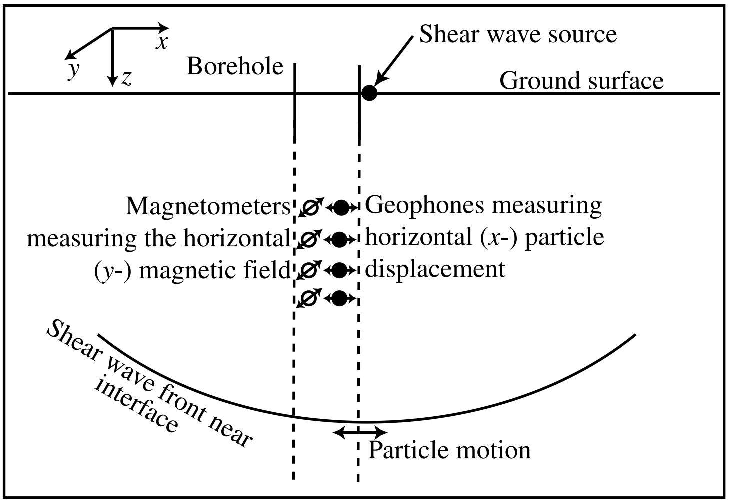

Figure 4.2.3. Model to evaluate the information on aquifer elastic parameters obtained from the magnetoseismic transfer function associated with shear waves.

From Equation (4.18) it can be seen that, apart from the elastic parameter G, the magnetoseismic transfer function depends on a number of other system parameters. The fluid properties may be found from the analyses of groundwater samples, the porosity and tortuosity (α_∞) of the solid medium may be accurately estimated from tracer tests and the solid density may be estimated from the densities of the minerals forming the solid grains. The zeta-potential is again the only parameter that remains unknown and the elastic parameter G cannot be obtained unambiguously. It should also be noted that the magnitude of the magnetic field is proportional to the square root of the shear modulus G, whereas it is directly proportional to the parameters ϵ_f, ρ_f and $|\zeta|$. A change of 10% in one of these parameters will have the same effect on the magnitude of the magnetic field as a change of 21% in the shear modulus. The fact that the magnetic field is more sensitive to these parameters than to the shear modulus suggests that it will be difficult to obtain reliable estimates of the shear modulus, unless the other parameters are well known.

4.3 Aquifer elastic parameter estimation from the analyses of wave velocities

Since the velocities at which fast and slow Biot waves and shear waves propagate in fluid-saturated porous media are dependent on the elastic properties of the media, the possibility exists that information on the aquifer elastic parameters may be obtained by analysing these velocities.

The velocities of the shear waves and fast and slow pressure waves may be found from Equations (2.83) and (2.88), respectively. For earth materials saturated with groundwater the electrokinetic coupling coefficient (L) is of the order 10^{-9} to 10^{-10} (see Chapter 5) and the influence of electroseismic coupling on the phase velocities of the shear wave and fast pressure wave becomes negligible. These velocities may consequently be closely approximated by the "true" Biot velocities that may be found from Equations (2.52) and (2.56). The velocity of the Biot fast wave depends on the elastic parameters H, C and M defined in Equations (2.39) to (2.42). These elastic parameters are in turn functions of the bulk and shear moduli (K_{fr} and G) of the porous frame. Since the only elastic parameter that influences the velocity of the shear wave is the shear modulus of the porous frame, information on the shear modulus may more readily be obtained.

From Equations (2.47), (2.53) and (3.35), Equation (2.52) may be written in terms of the shear wave velocity (v_s) as

$$v_s^2 = \mathrm{Re}\left\{\frac{G}{\rho_t}\right\} = \frac{G\rho}{\rho^2 + \left(\omega k \rho_f^2 / \eta\right)^2} \tag{4.23}$$

For real earth materials at seismic frequencies the first term in the denominator is seven to nine orders of magnitude larger than the second term. To a very close approximation we therefore have

$$G = \rho v_s^2 = \left[\phi \rho_f + (1-\phi)\rho_s\right] v_s^2 \tag{4.24}$$

G can therefore be determined if the porosity of the material and the mass densities of the fluid and solid constituents are known. The salt concentrations in groundwater are in general adequately low so that the mass density differs negligibly from that of pure water. The fluid density ρ_f may therefore be taken as 1 000 kg m^{-3} without loss of accuracy. The mass density of the solid material may be estimated by considering the mass densities of the minerals forming the solid grains. The sedimentary rocks of the Karoo Supergroup predominantly consist of quartz and the clay mineral illite (Brink, 1983). The quartz content of Karoo sandstones varies between 50 and 70%, while mudstones and shales contain around 30% quartz and 60% clay minerals. Minor to trace amounts of feldspar, montmorillonite, chlorite, vermiculite and kaolinite are also generally present in these rocks. Table 4.3.1 lists the average mass densities of these minerals (http://webminerals.com, http://www.tydex.ru/materials2, http://mineral.galleries.com).

The mass densities of the minerals forming the solid grains of Karoo sedimentary rocks are seen to differ by less than 13%. If the assumption is made that quartz and illite make up 90% of the volume of the solid grains then the mass density of the solid material in Karoo sandstones varies between 2 623 and 2 681 kg m^{-3} while the mass density of the solid grains in Karoo mudstones and siltstones varies between 2 635 and 2 669 kg m^{-3}. If the mass density of the solid grains of Karoo sedimentary rocks is therefore estimated at 2650 kg m^{-3} the error in the estimation will be less than two percent.

Table 4.3.1. Average mass densities of the minerals in Karoo rocks.

Mineral	Mass density [kg m^{-3}]
Quartz	2 625
Illite	2 750
Orthoclase	2 560
Plagioclase	2 685
Chlorite	2 420
Vermiculite	2 500
Kaolinite	2 600

The estimates of ρ_f and ρ_s thus obtained may be used along with information on the porosity to estimate the bulk mass density ρ and to obtain an estimate of the shear modulus G by means of Equation (4.24), if the shear wave velocity is known. Note that G is directly proportional to ρ but proportional to the square of v_s. An error of 5% in the estimated value of ρ will therefore have the same effect on the accuracy of the estimate of G as an error of 2.4% in the measurement of v_s. This sensitivity of G with respect to v_s implies that accurate measurement of the shear wave velocity is required for accurate estimation of G.

Once estimates of the shear modulus, G, of Karoo sedimentary rocks have been obtained it is possible to estimate the bulk modulus of the porous frame K_{fr}. In Figure 4.3.1 the elastic moduli of Karoo sedimentary rocks as obtained by Olivier (1976) are plotted with K_{fr} on the vertical axis and G on the horizontal axis. From Figure 4.3.1 it can be seen that an approximate linear relation between K_{fr} and G exists. The equation describing the least squares fit of a straight line through the data is

$$K_{fr} = 1.16G - 0.21\times10^{10} \quad [\mathrm{Pa}] \tag{4.25}$$

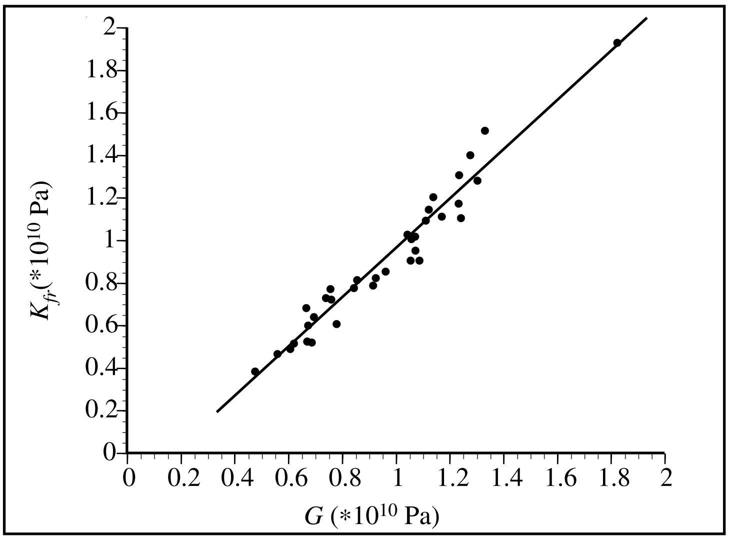

Figure 4.3.1. K_{fr} plotted against G for Karoo sedimentary rocks.

4.4 Information on aquifer deformation

Although the elastic parameters H/C (or C/H) and G cannot be determined unambiguously from the analyses of the electroseismic and magnetoseismic transfer functions, the possibility exists that changes in the transfer functions due to aquifer deformation may be detected. Aquifer deformation will have no effect on the fluid parameters, nor on the zeta-potential. It is assumed that aquifer deformation has negligible effects on the density of the solid grains.

The parameters that are likely to be affected by aquifer deformation are the porosity ϕ, as well as all porosity-dependent parameters such as α_∞, K_{fr}, G and k_0. The porosity-dependences of α_∞, K_{fr} and G may be expressed through Equations (3.43), (3.54) and (3.55), respectively. The Kozeny-Carman equation gives a relation between the permeability k_0 and porosity of porous media in which the pores are formed by capillary tubes (Bear, 1988). Although the capillary tube model is a rather crude approximation of porous media, the Kozeny-Carman equation it is still the most frequently used expression for the permeability of a porous medium (Koponen *et al.*, 1997). It is of the form

$$k_0 \propto \frac{\phi^3}{(1-\phi)^2} \tag{4.26}$$

Equations (2.34), (2.39), (2.40), (2.41), (3.43), (3.54), (3.55) and (4.26) allow us to find expressions for the electroseismic and magnetoseismic transfer functions in terms of porosity

$$L_{pf} \propto 1-\left[\frac{\rho_s(1-\phi)+\rho_f\phi}{\rho_f}\right]\left[\frac{(1+a)K_f K_s}{\Gamma}\right] \tag{4.27}$$

$$L_{ps} \propto \left[\frac{(1-\phi)^2}{\phi^3}\right]\left[\frac{\Gamma}{(1+a)K_f K_s}\right] \tag{4.28}$$

$$T \propto \frac{2\phi^2}{(1+\phi)}\left(\frac{(1-\phi)G_s}{(1+b\phi)\left[\rho_s(1-\phi)+\rho_f\phi\right]}\right)^{1/2} \tag{4.29}$$

with

$$\begin{aligned}\Gamma = {} & (a+\phi)K_f K_s+(1-\phi)K_s^{\ 2} \quad + \\ & \frac{4}{3}G_s\left[a(1-\phi)^2 K_f+(1-\phi)(1+a\phi)K_s\right](1+b\phi)^{-1}\end{aligned} \tag{4.30}$$

Figure 4.4.1 gives graphs of L_{pf} as a function of porosity for porosity values ranging from 0.01 to 1.00. Graphs for three values of b corresponding to three degrees of consolidation are shown. The values of K_s, G_s, K_f, ρ_s and ρ_f are taken from Table 3.2.4. The graphs are normalized with respect to the maximum values of L_{pf} obtained at a porosity of 0.01. Since no ES energy conversion can take place in media consisting of only solid material or only fluid, one would expect L_{pf} to tend to zero as the porosity approaches zero and unity. From Figure 4.4.1 it is clear that L_{pf} indeed goes to zero as the porosity approaches unity but that does not meet this requirement when porosity tends to zero. The reason for this lies in the fact that Biot theory and the theory of electroseismics were derived for media with finite porosities. Gassmann (1951) also stresses that the theory of the elasticity of fluid-saturated porous media is based on the assumption that the pore size of the porous medium is large enough so that the volume of adsorped water is small compared to the volume of solid material making up the frame of the porous medium. For media with small pores or for fine-grained media the volume of adsorped water may become significant. In addition, capillary effects will also start to play a role. It should therefore be stressed that Equation (4.27) gives a poor representation of the reality for porosity values that approach zero.

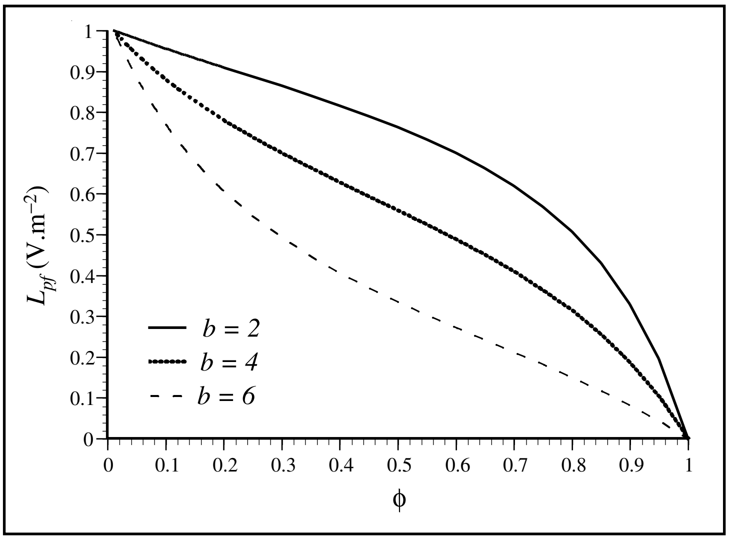

Figure 4.4.1. Graphs of the normalized values of L_{pf} as a function of porosity.

In the study of Karoo rocks we are generally dealing with effective porosity values lower than 0.20. Although the porosities of Karoo rocks (particularly shales and mudstones) may be small enough to cause significant adsorption and capillary effects, it is henceforth assumed that Equation (4.27) is valid for the porosity range of concern for this study ($0.01 < \phi < 0.20$).

For highly consolidated media ($b = 2$, $b = 4$) L_{pf} is to a close approximation linearly dependent on ϕ across the porosity range of interest. An important observation is that an extremely weak dependence of L_{pf} on ϕ exists for highly consolidated media. For a consolidation factors $b = 2$, $b = 4$ and $b = 6$, a 10% change in porosity from 0.10 to 0.11 leads to a change of only 0.5%, 1.3% and 2.5% in L_{pf}, respectively. The above observations indicate the unlikelihood of obtaining information on aquifer deformation in consolidated rocks from the fast pressure wave.

Figure 4.4.2 gives graphs of L_{ps} as a function of porosity for porosity values that range from 0.01 to 0.98. Graphs for three values of b corresponding to three degrees of consolidation are shown. The values of K_s, K_f, ρ_s and ρ_f are taken from Table 3.2.4. The graphs are normalised with respect to the maximum values of L_{ps} obtained at a porosity of 0.01.

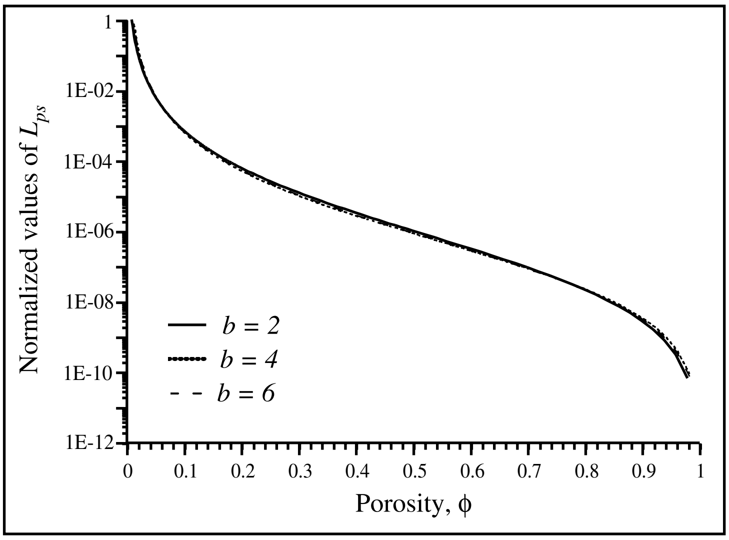

Figure 4.4.2. Graphs of the normalized values of L_{ps} as a function of porosity.

Since no ES energy conversion can take place in single-phase media, one would expect L_{ps} to tend to zero as the porosity approaches zero and unity. From Figure 4.4.2 it is clear that L_{ps} indeed goes to zero as the porosity approaches unity, but not as the porosity tends to zero. Again the reason for this observation lies in the fact that Biot theory and electroseismic theory are only valid for media with finite porosities. For all three degrees of consolidation the dependence of L_{ps} on ϕ is seen to be very strong. This sensitivity of L_{ps} to porosity changes suggests that, if the slow pressure wave can be separated from the fast pressure wave, valuable information on aquifer deformation may be gained by evaluating the slow pressure wave electroseismic transfer function.

Figure 4.4.3 shows graphs of T as a function of porosity for three different values of b. The graphs are normalised with respect to the maximum values of T. The values of G_s, ρ_s and ρ_f are taken from Table 3.2.4. Since no ES energy conversion can take place in single-phase media, one would expect T to tend to zero as the porosity approaches zero and unity. From Figure 4.4.3 it is clear that Equation (4.29) satisfies these requirements. The dependence of T on ϕ is seen to be strong for most porosity values. For a consolidated medium ($b = 2$) a 10% change in porosity from 0.10 to 0.11 results in a change of almost 19% in T. This observation suggests that evaluation of the magnetoseismic transfer function may yield valuable information on aquifer deformation.

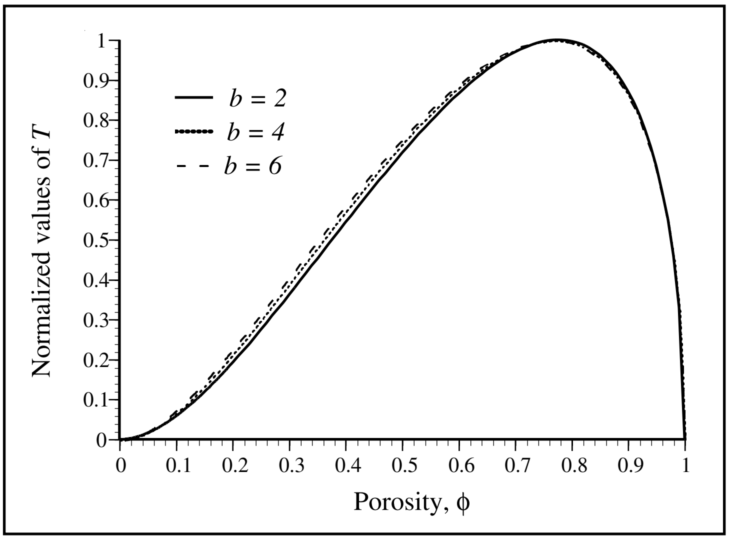

Figure 4.4.3. Graphs of the normalized values of *T* as a function of porosity.

4.5 Summary

In this chapter electroseismic and magnetoseismic transfer functions were given. These transfer functions are seen to be dependent on various physical and chemical parameters, including the elastic properties of the solid porous matrix. It is therefore concluded that none of these parameters can be determined unambiguously from the evaluation of the different transfer functions. The aquifer elastic parameters can therefore not be obtained without prior knowledge of other parameters such as the porosity, mass density and tortuosity of the solid medium, the dielectric permittivity, mass density, electrical conductivity and viscosity of the fluid, and the zeta potential. Some of these parameters, such as the electrical conductivity, density, viscosity and dielectric permittivity of the fluid, can be determined by either *in situ* or laboratory measurements. Other parameters, such as the porosity and tortuosity, may be estimated through hydraulic investigations, for example by means of tracer tests. There are, however, as yet no methods for the routine determination of zeta potential. The measurement of this parameter would, at present, require the removal of a specimen of the porous material to be analysed in a laboratory.

The shear modulus of the porous frame may be estimated from measurements of the shear wave velocity in a fluid-saturated porous system. Since an approximately linear relation exists between the shear and bulk moduli of the porous frame, the bulk modulus may be estimated once the shear modulus is known.

It is demonstrated that the possibility exists that porosity changes due to aquifer deformation may lead to changes in the transfer functions. As such, determination of the transfer functions could serve as a means of measuring aquifer deformation. The porosity dependencies of the various transfer functions were obtained by assuming certain relations for the porosity-dependent parameters contained in the transfer functions (for example, the Kozeny-Carman relation between permeability and porosity). As such, the accuracy with which Equations (4.27), (4.28) and (4.29) describe reality is limited by the accuracy of the assumed porosity dependencies of the various parameters. Both the expression for the transfer function of the fast pressure wave and the expression for the transfer function of the slow pressure wave are shown to give poor representations of the reality for porosities that approach zero. These equations should therefore only be seen as indications of the degree to which the transfer functions are porosity-dependent.

The electroseismic transfer function of the fast pressure wave (Equation (4.27)) is shown to be insensitive to porosity changes in consolidated material. The electroseismic transfer function of the slow pressure wave (Equation (4.28)), on the other hand, is shown to be very sensitive to porosity changes. However, due to the dispersive nature of the slow waves, they exist only near interfaces. At such positions the slow and fast waves co-exist, but due to the small amplitudes of the solid displacement in the slow pressure waves, the total displacement of the solid is dominated by the displacement of the fast pressure wave. Separation of the slow wave from the fast wave is therefore likely to proof very difficult.

The magnetoseismic transfer function (Equation (4.29)) is shown to be sensitive to porosity changes. It correctly predicts zero ES energy conversion for porosities of zero and unity. The magnetoseismic transfer function is associated with solid displacement due to a shear wave which can easily be distinguished and separated from both the slow and fast pressure waves, as well as from the Stoneley wave.

The above observations suggest that, of the three transfer functions, the magnetoseismic transfer function associated with the shear wave is likely to yield the most useful information on aquifer deformation.

CHAPTER 5 INFLUENCE OF POROSITY/PERMEABILITY CONTRASTS ON ELECTROSEISMIC REFLECTION IN KAROO ROCKS

The reflection and transmission of seismic and (electroseismically converted) electromagnetic energy at an interface depend on the properties of the media above and below the interface. In this chapter the influence of porosity and/or permeability contrasts of Karoo rocks on the electroseismic reflection and transmission coefficients are examined. The reflection (*R*) and transmission (*T*) coefficients are obtained my means of the matrix method described in Appendix C.

In the present study we are interested in understanding the electroseismic energy conversion that takes place when a fast pressure wave is incident on a boundary between two porous media. The *R* and *T* coefficients are therefore only calculated for incident fast pressure waves, but a similar approach can be taken to determine the *R* and *T* coefficients for slow pressure waves, horizontally and vertically polarised shear waves and electromagnetic waves.

Consider the interface between two fluid-saturated porous media. Following the method described in Appendix C2, the ES reflection and transmission coefficients may be found by evaluating the matrix equation

$$\begin{aligned}&\left(T_{pfpf}, T_{pfps}, T_{pfsv}, T_{pftm}, R_{pfpf}, R_{pfps}, R_{pfsv}, R_{pftm}\right)^T \\ &\qquad = \mathbf{D}^{-1}\left(F_{11}, F_{21}, F_{31}, F_{41}, F_{51}, F_{61}, F_{71}, F_{81}\right)^T\end{aligned} \tag{5.1}$$

where **D** is an 8×8 matrix given by

$$\mathbf{D} = \begin{pmatrix} G_{11} & \cdots & G_{14} & -F_{15} & \cdots & -F_{18} \\ \vdots & & \vdots & \vdots & & \vdots \\ G_{81} & \cdots & G_{84} & -F_{85} & \cdots & -F_{88} \end{pmatrix} \tag{5.2}$$

The F_{ij} and G_{ij} entries in matrix **D** are formed from the electroseismic eigenvectors in the media above and below the interface, as explained in Appendix C. These eigenvectors are given in Equations (3.77) to (3.80).

Calculation of the reflection and transmission coefficients by means of Equation (5.1) is computationally intensive since it requires the inversion of an 8×8 matrix with complex entries.

5.1 ES reflection and refraction at a Karoo mudstone-sandstone interface

Consider a Karoo mudstone overlying a Karoo sandstone as shown in Figure 5.1.1. A fast pressure wave is incident on the interface between the two media, generating reflected and refracted fast pressure (*Pf*-) waves, slow pressure (*Ps*-) waves, shear (*SV*-) waves and electromagnetic waves in which the magnetic field is transversally polarised (*TM*-waves).

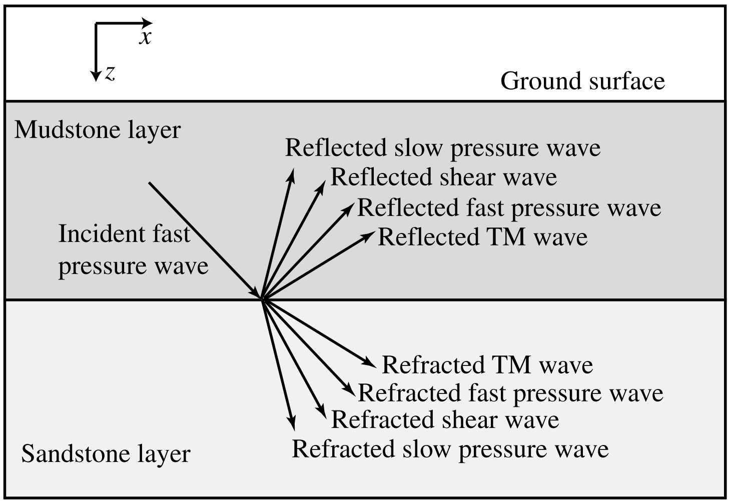

Figure 5.1.1. Model used to investigate ES reflection and refraction in saturated Karoo rocks.

Using the matrix method described above and the mudstone and sandstone parameter estimates listed in Table 3.2.4, the ES reflection and transmission coefficients at the interface may now be calculated as a function of the incidence angle. Although in ES surveys we are primarily concerned with the R_{pftm} coefficient, the moduli of all the reflection and transmission coefficients are shown in Figure 5.1.2.

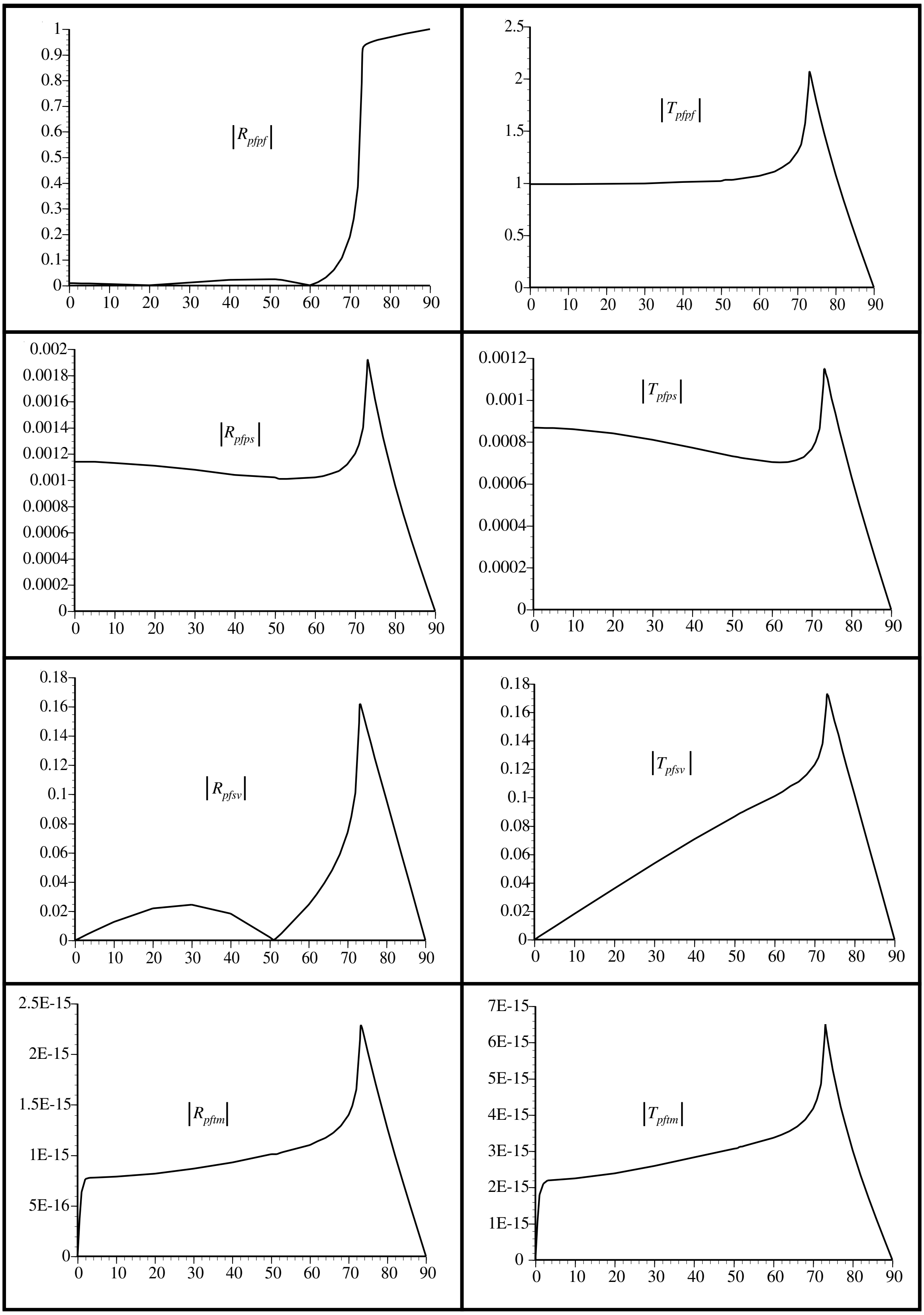

Figure 5.1.2. The reflection and transmission coefficients at the mudstone/sandstone interface. Horizontal axes give the angle of incidence (in degrees) of the fast pressure wave, while vertical axes give the numeric values of the reflection and transmission coefficients.

5.1.1 Discussion

From Equations (2.83), (2.88) and (3.35) the parameter values listed in Table 3.2.4, the wave velocities in the mudstone and sandstone may be calculated. The results of the calculations are presented in Table 5.1.1.

Table 5.1.1. Seismic and electromagnetic wave velocities in the sandstone and mudstone.

Wave type	Wave velocity [m s^{-1}]	
	Mudstone	Sandstone
Fast pressure (v_{pf})	2 908.61	3 040.89
Slow pressure (v_{ps})	93.35	346.88
Shear (v_{sv})	1 818.10	1 974.88
Electromagnetic (v_{tm})	258 153	182 589

Since the wave velocity of the incident fast pressure wave in the mudstone (v_{pf1}) is lower than that of the fast pressure wave in the sandstone (v_{pf2}), a critical angle for *Pf-Pf* refraction may be found, namely $\theta_{pfpf} = \sin^{-1}\left(v_{pf1}/v_{pf2}\right)$. With the wave velocities listed in Table 5.1.1 the critical angle is found to be 73.04°. The effect of critical *Pf-Pf* refraction is clearly seen in the behaviour of all the reflection and refraction coefficients shown in Figure 5.1.2. As the incidence angle approaches θ_{pfpf} all the reflection and transmission coefficients display changes in character.

Beyond the critical angle $|R_{pfpf}|$ tends to unity as total internal reflection occurs while $|T_{pfpf}|$ dies off to zero as the refracted wave becomes evanescent. The observation that $|R_{pfpf}|$ is very small for most incidence angles while $|T_{pfpf}|$ is approximately unity, is due to the fact that the mudstone and sandstone properties listed in Table 3.2.4 result in a small contrast in seismic impedance (density × velocity). This does, however, not imply that one should expect poor fast wave reflection from all mudstone/sandstone interfaces in Karoo rocks since the properties listed in Table 3.2.4 are only estimates obtained using averaged values for the properties of Karoo sandstones and mudstones.

Note that apart from θ_{pfpf} two other critical angles exist. The one is for *Pf-TM* refraction and the other for *Pf-TM* reflection. From the wave velocities in Table 5.1.1 these critical angles are found to be 0.91° and 0.65°, respectively. Near these critical angles all the reflection and refraction coefficients display changes in character, although these changes are not visible on the scales employed in Figure 5.1.2.

For normal incidence no reflected or refracted shear waves are generated. Similarly no reflected or refracted EM waves are generated. This can be understood by noting that for a plane pressure wave normally incident on a horizontal interface, the symmetry implies that we have uniform vertical solid displacements and electric fields over the interface. Both the solid displacement and electric field are therefore rotation free and neither shear waves nor magnetic fields can be generated.

Note that since the reflection and transmission coefficients are dimensionless, their numeric values give the ratios between the amplitudes of the solid displacements associated with each wave type and the amplitude of the solid displacement of the incident wave. $|R_{pftm}|$ therefore gives the ratio between the amplitude of the solid displacement due the reflected EM wave and the amplitude of the solid displacement due the incident fast pressure wave. Equation (2.85) should in this case be employed if one wishes to convert from solid displacement amplitude to electric field amplitude.

5.2 Electroseismic reflection as a function of sandstone porosity

To investigate the influence of aquifer porosity on ES reflection all the physical parameters of the mudstone layer are kept constant while the porosity of the sandstone layer is varied. The porosity-dependence of the permeability (k), tortuosity (α_∞), bulk permittivity (ε), bulk electrical conductivity (σ_0), bulk modulus of the solid frame (K_{fr}) and shear modulus of the solid frame (G) is incorporated into the investigation. The permeability of the sandstone layer is assumed to be a function of porosity given by the Kozeny-Carman equation

$$k_0 = \frac{1}{5M_s^2} \frac{\phi^3}{(1-\phi)^2} \tag{5.3}$$

where M_s is the specific surface of porous material defined as the total interstitial surface of the pores per unit volume of solid material (Bear, 1988). If the assumption is made that the solid grains are uniformly spherical with radius r, then $M_s = 3/r$, and Equation (5.3) becomes

$$k_0 = \frac{r^2}{45} \frac{\phi^3}{(1-\phi)^2} \tag{5.4}$$

Using the estimates for the porosity and permeability of sandstone in Table 3.2.4 gives a radius $r = 0.6$ mm for the sandstone grains. The diameter of 1.2 mm obtained is seen to fall outside the known range of grain sizes (0.03 to 0.25 mm in diameter) for sandstones measured on the Campus Test Site (Botha *et al.*, 1998). The discrepancy could be attributed to the fact that the Kozeny-Carman equation was developed from the restrictive assumption that the pores of the medium consists of capillary tubes. To allow agreement with the observed sandstone permeability given in Table 3.2.4, a value of 0.6 mm is henceforth assumed for the radius of the sandstone grains in Equation (5.4).

The porosity-dependencies of the bulk density, tortuosity and bulk dielectrical permittivity are assumed to be given by Equations (2.34), (3.43) and (3.56), respectively. The porosity-dependence of the electrical conductivity of the water-saturated bulk material may be described by Archie's emperical law (Telford *et al.*, 1990)

$$\sigma = a\phi^m \sigma_f \tag{5.5}$$

where a and m are constants depending on the rock properties. Archie's law is only valid for a conductive phase saturating a non-conductive matrix (Glover *et al.*, 2000). It should also be noted that Archie's law is not valid when the porosity approaches zero or unity. For zero porosity Archie's law predicts zero conductivity instead of the conductivity σ_s of the solid material. For a porosity of unity Archie's law predicts a conductivity of $a\sigma_f$ which agrees with the conductivity σ_f of the fluid only if $a = 1.0$.

Alternatively the porosity-dependence of the electrical conductivity may be expressed by combining Equations (3.43) and (B1.10) to obtain

$$\sigma = 2\frac{\phi^2}{1+\phi}\sigma_f \tag{5.6}$$

At low porosities Equation (5.6) is approximately equivalent to Equation (5.5) with $a = 2$ and $m = 2$. Equation (5.6) gives the desired property that $\underset{\phi\to 1}{\sigma_0} = \sigma_f$, but like Equation (5.5) predicts zero bulk conductivity for zero porosity.

Glover *et al.* (2000) modify Archie's law to obtain a law that is can be used for two conductive phases of any conductivity and porosity. This law is given by

$$\sigma = \sigma_f \phi^n + \sigma_s (1-\phi)^m \tag{5.7}$$

with

$$n = \log\left(1-(1-\phi)^m\right) / \log\phi \tag{5.8}$$

where *m* is a measure of the connectivity of fluid phase. Equation (5.7) is seen to satisfy both the required properties $\underset{\phi \to 0}{\sigma} = \sigma_s$ and $\underset{\phi \to 1}{\sigma} = \sigma_f$. A fluid conductivity of 70 mS m^{-1} is used in accordance with the value measured on the Campus Test Site (Van Wyk *et al.*, 2001). For a porous frame consisting predominantly of quartz, the conductivity of the solid phase is in the order of 10^{-8} mS m^{-1} or less (Telford *et al.*, 1990), and is therefore negligible compared with the fluid conductivity. Equation (5.7) then becomes

$$\sigma \approx \sigma_f \phi^n \tag{5.9}$$

Using the porosity of 0.08 and the bulk conductivity of 30 mS m^{-1} given in Table 3.2.4 for Karoo sandstones allows one to obtain an estimate of 6.71 for the connectivity *m*. This value is henceforth used in Equations (5.8) and (5.9) to describe the porosity-dependence of the bulk conductivity.

As in Section 3.2.2.3 the bulk and shear moduli of the solid frame are assumed to be given by (3.54) and (3.55) with $a = 2.3$ and $b = 4$.

Table 5.2.1 lists the relevant model parameters for the two layers under consideration. (Porosity-independent information is taken from Table 3.2.4.)

Figure 5.2.1 shows graphs of $|R_{pftm}|$ for a sandstone porosity of 0.080, as well as for sandstone porosities of 0.064 and 0.096, corresponding to a 20% porosity decrease and increase, respectively. Critical angles for *Pf-Pf* refraction corresponding to sandstone porosity of 0.064, 0.080 and 0.096 occur at 69.60°, 73.04° and 77.23°, respectively. An important observation to be made from Figure 5.2.1 is that for most angles of incidence higher sandstone porosity leads to increases in $|R_{pftm}|$. Only near the critical angles could the opposite be true. One should, however, take into account the fact that $|R_{pftm}|$ was obtained by considering plane waves incident on horizontal interfaces. In practice the seismic source creates a wave that propagates radially away from the source. Due to shorter travel distances to positions on the interface that occur at small angles of incidence, less wave attenuation due to spherical spreading and other loss mechanisms is incurred. As a result reflection from small angles of incidence generally dominates over reflection from large angles of incidence. As was shown in Section 3.1, the first ES Fresnel zone on the interface makes the largest contribution to the total generated signal. For the model parameters in Table 5.2.1 the first ES Fresnel zone corresponds to incidence angles of less than 55° for interfaces at depths greater than 20m, and the graphs in Figure 5.2.1 therefore show that stronger reflection can be expected for increasing sandstone porosity.

The stronger reflection with increasing sandstone porosity can be explained in terms of the electrokinetic contrast between the mudstone and sandstone layers. The electrokinetic coupling coefficients of these layers may be calculated from Equations (4.2) and (B1.9) and the parameter values listed in Table 5.2.1. The mudstone layer has an electrokinetic coupling coefficient of 1.10×10^{-10} A s^2 kg^{-1}. For porosities of 0.064, 0.080 and 0.096 the sandstone layer has electrokinetic coupling coefficients of 2.76×10^{-10}, 4.25×10^{-10} and 6.04×10^{-10} A s^2 kg^{-1}, respectively. Sandstones of increasing porosity therefore lead to increasing electrokinetic contrasts between the sandstone and mudstone layers and, as a consequence, stronger reflection.

Table 5.2.1. Model parameters used to investigate ES reflection in Karoo rocks.

Parameter	Sandstone	Mudstone
Solid material		
Bulk modulus of solid, K_s [Pa]	1.2E10	1.2E10
Shear modulus of solid, G_s [Pa]	1.4E10	1.4E10
Density of solid, ρ_s [kg m^{-3}]	2.7E03	2.7E03
Fluid		
Bulk modulus of fluid, K_f [Pa]	2.2E09	2.2E09
Salinity, C [mol L^{-1}]	5.5E-03	5.5E-03
Fluid conductivity, σ_f [S m^{-1}]	7.0E-02	7.0E-02
Fluid density, ρ_f [kg m^{-3}]	1.0E03	1.0E03
Fluid viscosity, η [Pa s]	1.0E-03	1.0E-03
Porous frame		
Bulk modulus of frame, K_{fr} [Pa]	varied	7.7E09
Shear modulus of frame, G [Pa]	varied	8.7E09
Porosity, ϕ	varied	4.0E-02
Permeability, k_0 [m^2]	varied	3.6E-13
Tortuosity, α_∞	varied	13
Bulk		
Bulk electrical conductivity, σ_0 [S m^{-1}]	varied	1.5E-02
Bulk permittivity, ε [C^2 N^{-1} m^{-2}]	varied	5.0E-11

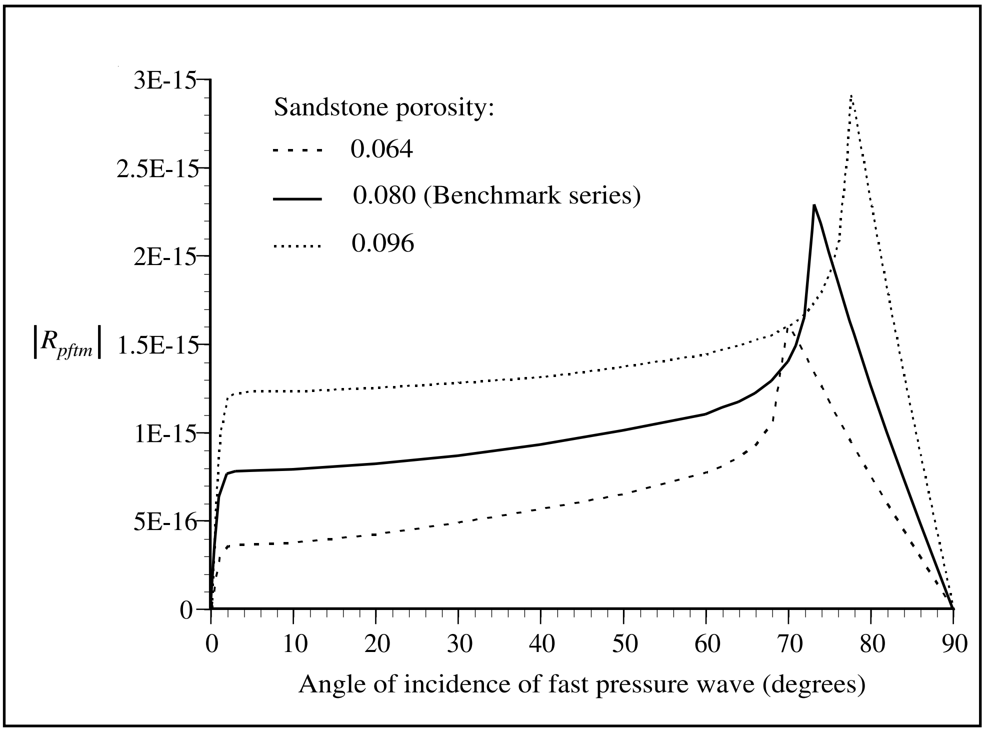

Figure 5.2.1. $|R_{pftm}|$ at the mudstone/sandstone interface for different sandstone porosities as a function of the angle of incidence of the fast pressure wave.

The results obtained above suggest that ES techniques may be used as a tool to distinguish between zones of low and high sandstone porosity/permeability in a certain geological environment. Since zones of high porosity/permeability could be considered targets during groundwater exploration, ES techniques may play an important role in future groundwater exploration programs.

It should, however, be appreciated that ES reflection from an interface depends on the electrokinetic contrast between the two media in contact. Lateral changes in the properties of either medium may affect the magnitude of the reflected EM wave. ES techniques are therefore likely to be useful as a means of mapping the physical/chemical contrast between two saturated geological formations but further interpretation of these contrast maps in terms the geological/geohydrological environment will still be necessary. For this interpretation additional information on the geological and/or groundwater conditions may be required.

5.3 Sensitivity investigation

In Section 5.2 it was shown how changes in the sandstone porosity affect ES reflection. The sandstone porosity is however not the only parameter that affects ES reflection. In this section the influence that different parameters have on ES reflection is examined in order to determine which physical/chemical parameters have the strongest effects. The sensitivity of ES reflection with respect to changes in porosity, fluid salinity, the zeta potential and the elastic parameters of the porous frame is examined. The same model geometry as in Figure 5.1.1 is used to calculate $|R_{pftm}|$. The parameter values listed in Table 3.2.4 are used as a benchmark series against which all results are compared.

Changes in the sandstone porosity

The influence of a 20% increase and decrease in the sandstone porosity on $|R_{pftm}|$ is discussed in Section 5.2 and shown in Figure 5.2.1.

Changes in the mudstone porosity

The effects of a 20% increase and decrease in the mudstone porosity on $|R_{pftm}|$ is shown in Figure 5.3.1. All porosity-dependent parameters are again adjusted according to Equations (2.34), (3.43), (3.54), (3.55), (3.56), (5.4) and (5.9). To allow for agreement with the parameters values listed in Table 3.2.4 the constants *a* and *b* in Equations (3.54) and (3.55) are taken as 12.4 and 13.6, respectively, the grain radius *r* in Equation (5.4) is taken as 0.48 mm, and the connectivity *m* in Equation (5.8) is taken as 5.91.

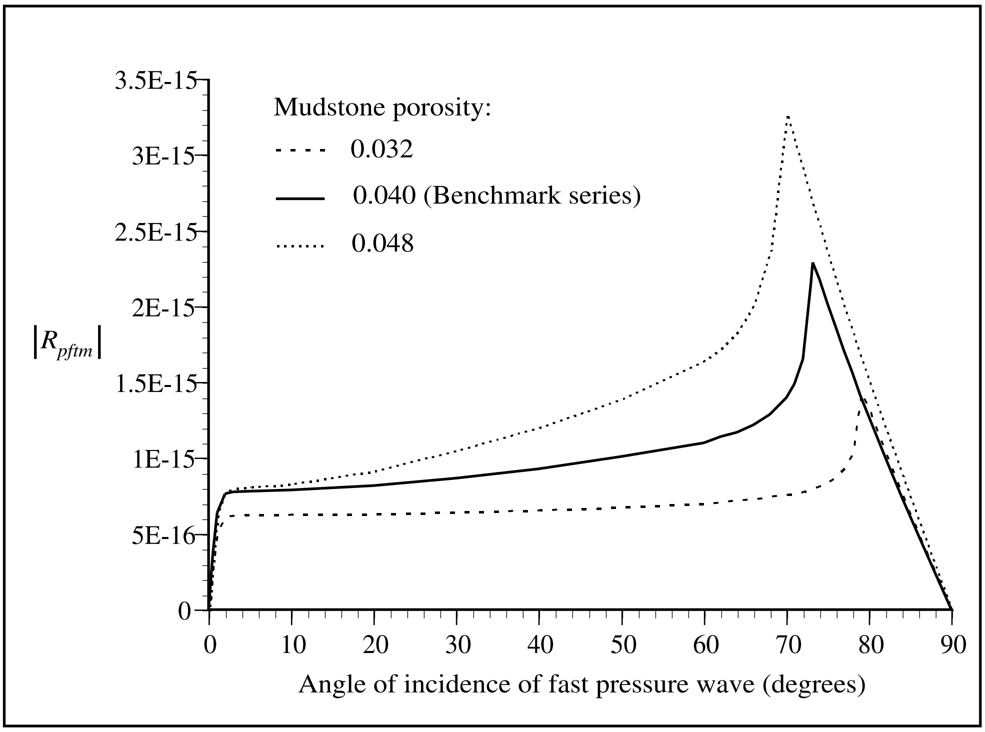

Figure 5.3.1. $|R_{pftm}|$ at the mudstone/sandstone interface for different mudstone porosities as a function of the angle of incidence of the fast pressure wave.

The angle of critical refraction for *Pf-Pf* waves are found to occur at 78.92°, 73.04° and 69.08° for mudstone porosities of 0.032, 0.040 and 0.048, respectively. Comparison of the

$|R_{pftm}|$ coefficients at small angles of incidence in Figure 5.3.1 and Figure 5.2.1 reveals that ES reflection at the mudstone/sandstone interface is less sensitive to changes in the porosity of the lower porosity medium. In addition, porosity increases in the mudstone have less impact on $|R_{pftm}|$ than porosity decreases.

Changes in the fluid salinity (in sandstone and mudstone)

Figure 5.3.2 shows the influence of a 20% salinity increase and decrease on ES reflection. The salinity in both the sandstone and the mudstone is changed from 0.0055 mol L^{-1} to 0.0044 mol L^{-1} and 0.0066 mol L^{-1}. All salinity-dependent chemical parameters are adjusted accordingly. Comparison of the $|R_{pftm}|$ coefficients at small angles of incidence in Figure 5.3.2 and Figure 5.2.1 reveals that ES reflection at the mudstone/sandstone interface is much less sensitive to salinity changes than to changes in the sandstone porosity. The salinity changes have negligible influence on the fast wave velocities in the two media so that the critical angle of *Pf*-*Pf* refraction remains constant at 73.04°.

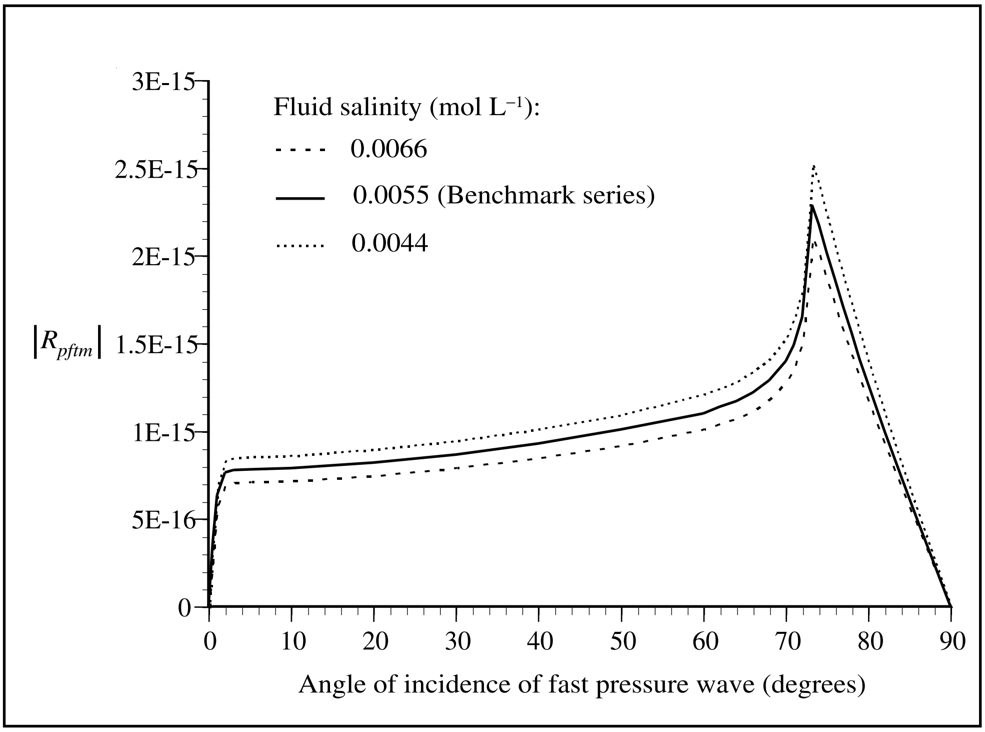

Figure 5.3.2. $|R_{pftm}|$ at the mudstone/sandstone interface for different fluid salinities as a function of the angle of incidence of the fast pressure wave.

Changes in the fluid salinity (in the sandstone only)

The effects of 20% salinity increases and decreases of the groundwater saturating the sandstone layer, while the salinity of the groundwater in the mudstone layer is kept constant, are illustrated in Figure 5.3.3. The changes in $|R_{pftm}|$ are of similar magnitude to the changes due to salinity increases in both the sandstone and mudstone, as shown in Figure 5.3.2.

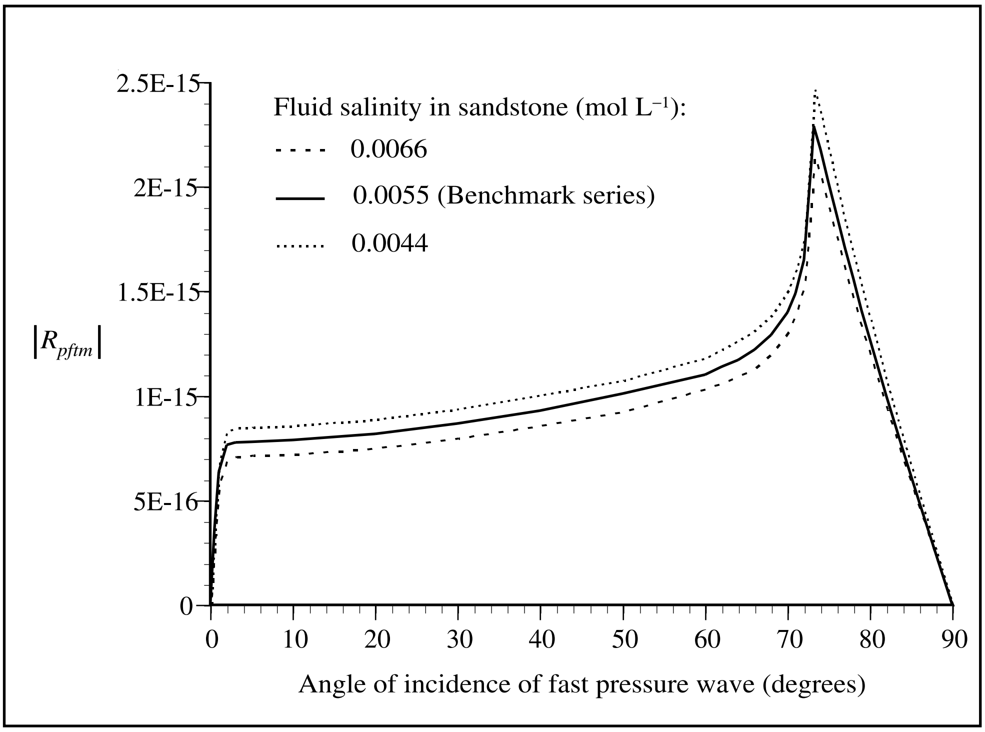

Figure 5.3.3. $|R_{pftm}|$ at the mudstone/sandstone interface for different fluid salinities in the sandstone as a function of the angle of incidence of the fast pressure wave.

Changes in the fluid salinity (in mudstone only)

The effects of 20% salinity increases and decreases of the groundwater saturating the mudstone layer, while the salinity of the groundwater in the sandstone layer is kept constant, are illustrated in Figure 5.3.4. Very small changes in $|R_{pftm}|$ are observed. Comparison of Figure 5.3.2, Figure 5.3.3 and Figure 5.3.4 suggests that the salinity of the higher porosity medium has a much stronger effect on ES reflection than the salinity of the low porosity medium.

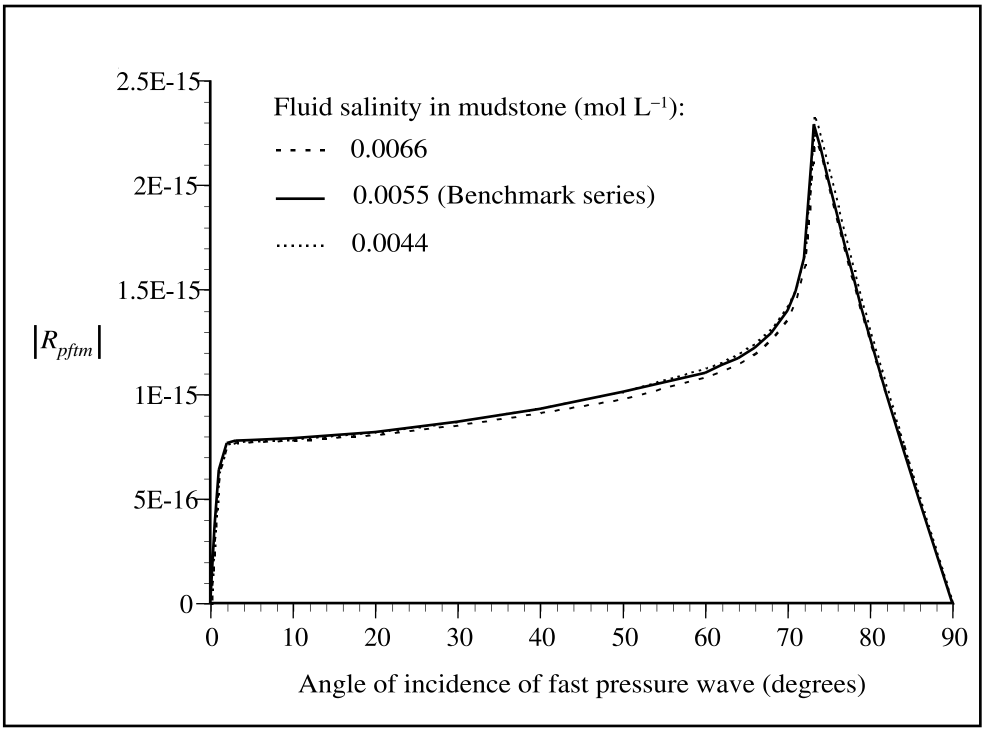

Figure 5.3.4. $|R_{pftm}|$ at the mudstone/sandstone interface for different fluid salinities in the mudstone as a function of the angle of incidence of the fast pressure wave.

Changes in the zeta potential of sandstone

A 20% increase and decrease in the zeta potential of the sandstone from the benchmark value of –50.7 mV to –60.8 mV and –40.5 mV affect the $|R_{pftm}|$ coefficient as illustrated in Figure 5.3.5. ES reflection is seen to be sensitive to changes in the zeta potential of the sandstone, although comparison with Figure 5.2.1 reveals that the sensitivity is less than the sensitivity with respect to sandstone porosity. Changes in zeta potential of the sandstone have negligible influence on the fast wave velocities in the two media so that the critical angle of *Pf-Pf* refraction remains constant at 73.04°

Changes in the zeta potential of the mudstone

Figure 5.3.6 shows the influence of a 20% increase and decrease in the zeta potential of the mudstone on ES reflection. The influence is seen to be much smaller than similar increases and decreases in the zeta potential of the sandstone. This observation again suggests that ES reflection is more sensitive to the properties of the higher porosity medium.

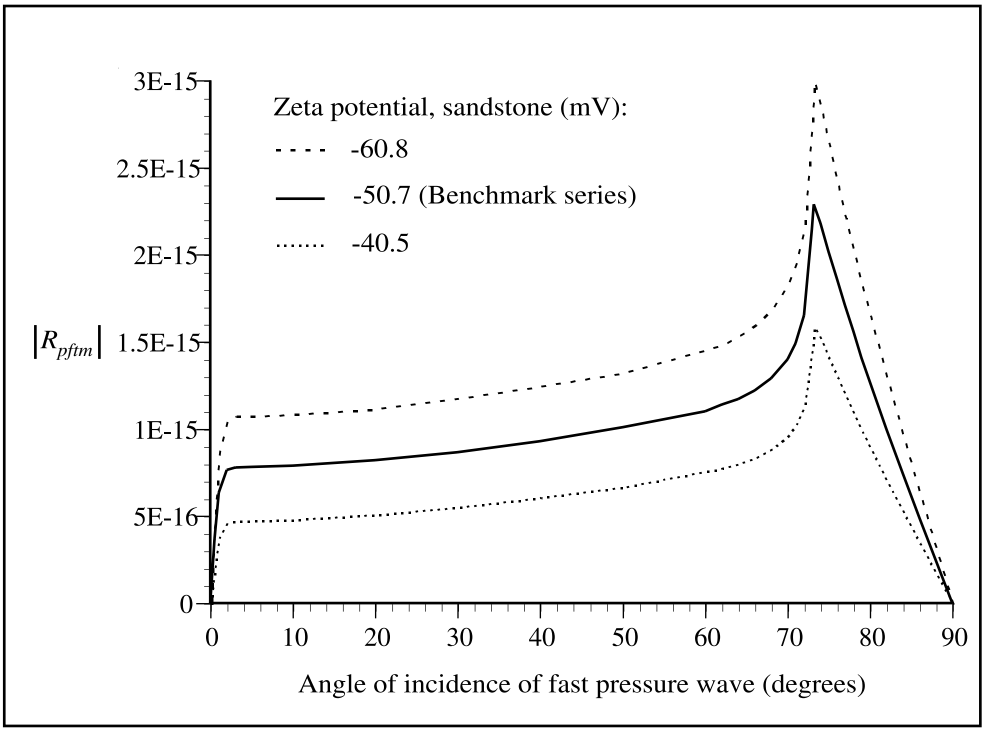

Figure 5.3.5. $|R_{pftm}|$ at the mudstone/sandstone interface for different values of the zeta potential at the solid/fluid contacts in the sandstone as a function of the angle of incidence of the fast pressure wave.

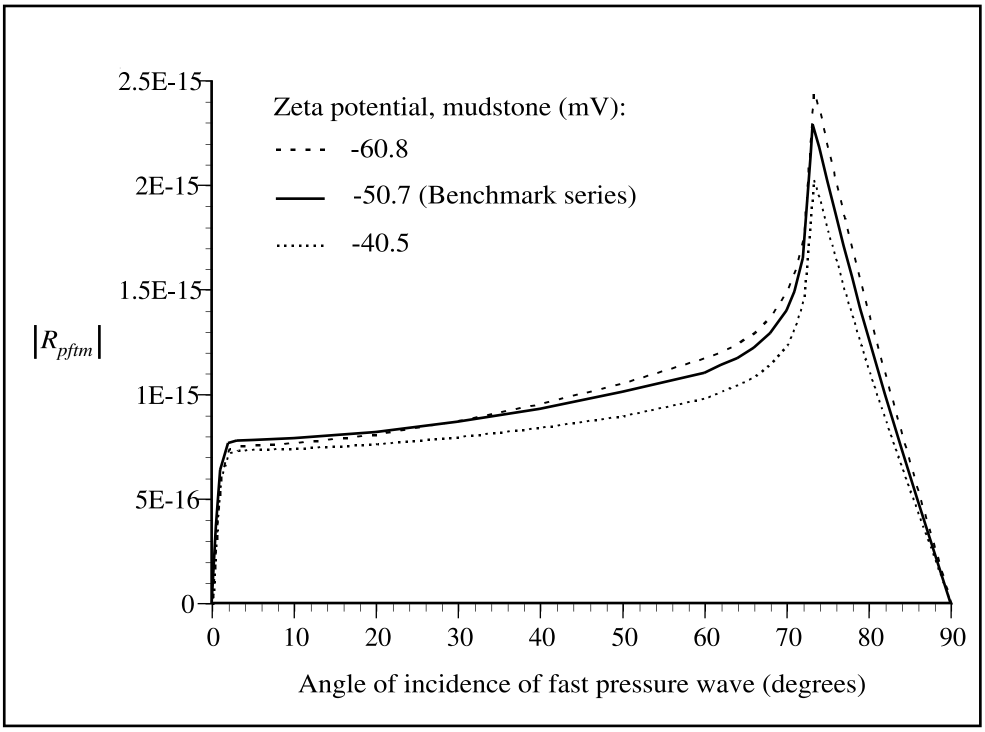

Figure 5.3.6. $|R_{pftm}|$ at the mudstone/sandstone interface for different values of the zeta potential at the solid/fluid contacts in the mudstone as a function of the angle of incidence of the fast pressure wave.

Changes in the elastic parameters of the sandstone

The sensitivity of ES reflection with respect to changes in the elastic parameters of the sandstone is investigated by considering the influence of 20% increases and decreases in the values of both the bulk and shear moduli of the porous sandstone frame, while all other parameters are kept constant. The results are shown in Figure 5.3.7. The large differences in the $|R_{pftm}|$ coefficient at small angles of incidence show that ES reflection is very sensitive to changes in elastic parameters of the sandstone. Note that for 20% decreases in the sandstone porosity the fast pressure wave velocity in the sandstone is lower than in the mudstone and that no *Pf-Pf* critical angle thus exists.

Changes in the elastic parameters of the mudstone

20% changes in the elastic parameters of the low porosity medium have a much less significant effect on the $|R_{pftm}|$ coefficient at small angles of incidence than similar changes in the elastic parameters of the high porosity medium, as can be seen in Figure 5.3.8. For 20% increases in the mudstone porosity no *Pf-Pf* critical angle exists.

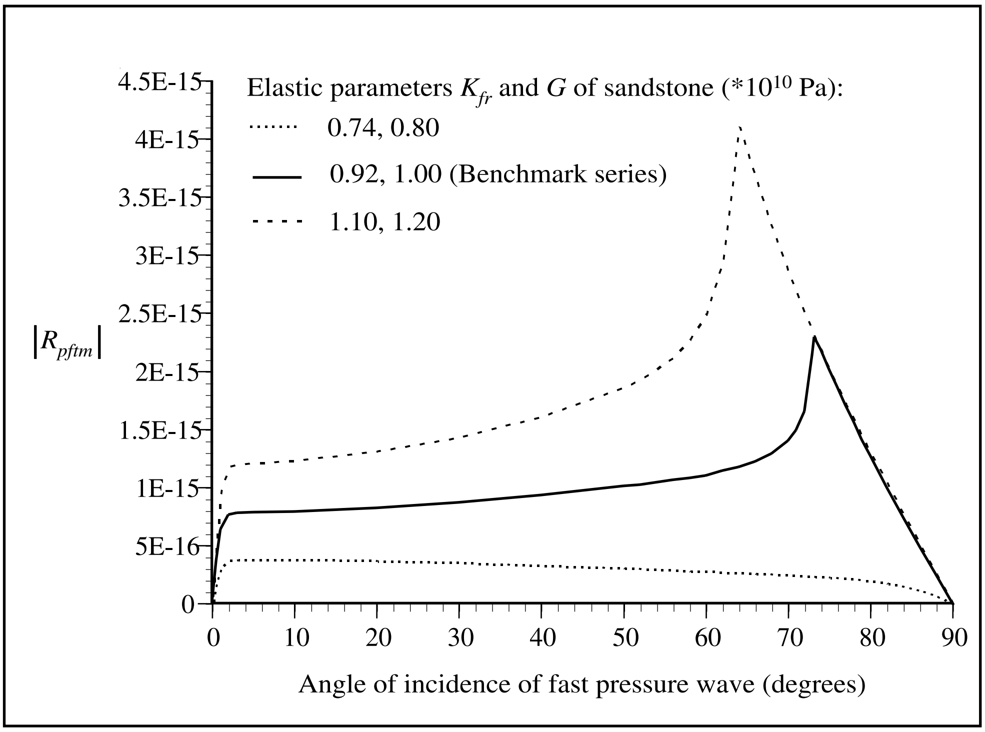

Figure 5.3.7. $|R_{pftm}|$ at the mudstone/sandstone interface for different sandstone elastic parameters as a function of the angle of incidence of the fast pressure wave.

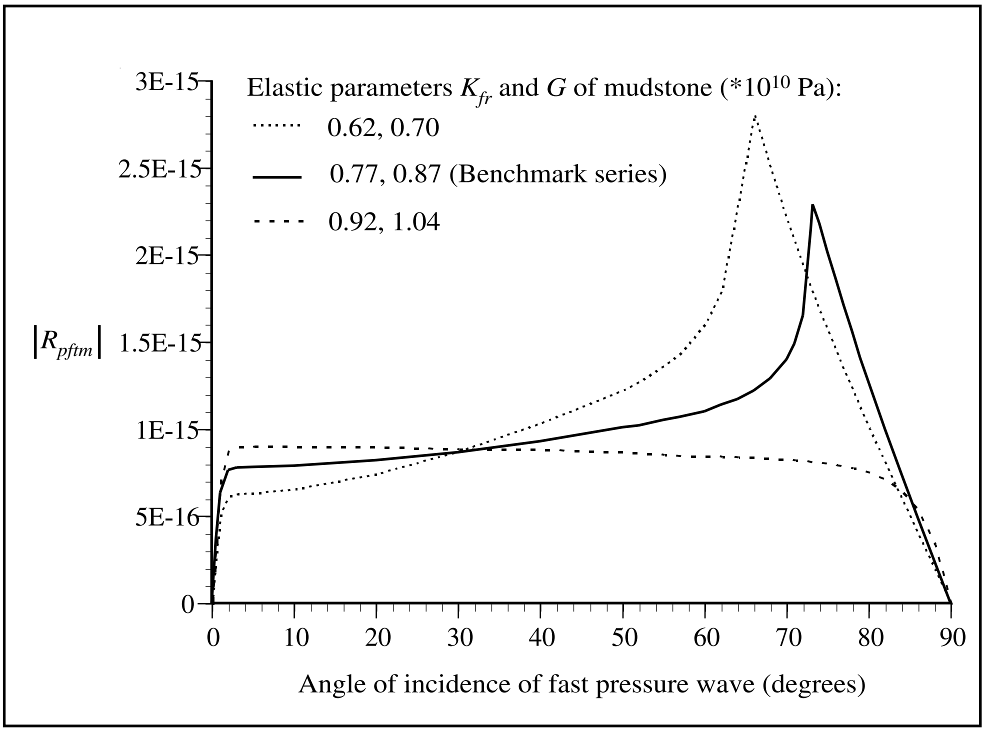

Figure 5.3.8. $|R_{pftm}|$ at the mudstone/sandstone interface for different mudstone elastic parameters as a function of the angle of incidence of the fast pressure wave.

5.3.1 Discussion

The results of the sensitivity investigations shown in Figure 5.2.1 and Figure 5.3.1 to Figure 5.3.8 indicate that ES reflection is more sensitive to changes in the high permeability medium (the sandstone) than to changes in the low permeability medium (the mudstone). This observation holds favourable implications for groundwater exploration where the properties of the medium of high permeability are more important than that of the surrounding host media. ES reflection is found to be mostly sensitive to the elastic parameters and the porosity of the sandstone, and to a lesser degree to the zeta potential and fluid salinity in the sandstone.

The question remains as to the magnitude of the changes in the various parameters that can be expected for real saturated earth materials. Although ES reflection is much less sensitive to fluid salinity than to the elastic parameters and porosity of the sandstone, large changes in fluid salinity could occur if, for example, contaminants occur in the groundwater.

Little is at present known about the zeta potential at the fluid-solid interface and the factors that affect it. Preferential deposition of secondary minerals at certain locations in the aquifer could affect the charge balance at the fluid-solid interface and thus alter the zeta potential. The magnitude of these possible changes in the zeta potential is at present unknown.

The sensitivity of ES reflection with respect to the elastic parameters was considered by changing these parameters while all other parameters, including the porosity, was kept constant. From Equations (3.54) and (3.55) we see that such porosity-independent changes in the elastic parameters should be attributed to changes in the consolidation factors a and b. Localized changes in the degree of consolidation at constant porosity imply localized changes in the cementation of the solid grains. Such localized changes would require changes in the chemical nature of the cementing material, possibly through preferential deposition of secondary minerals. However, it seems highly unlikely that the deposition of secondary minerals onto the solid grain surfaces would result in large changes in the elastic parameters of the sedimentary rocks.

The above observations suggest that porosity changes in sedimentary rocks saturated with uncontaminated groundwater is likely to have the strongest influence on ES reflection, although the magnitude of changes in the zeta potential that can be expected in earth materials is at present unknown. Such changes could possibly strongly influence ES reflection and could lead to erroneous interpretation of ES data if the assumption is made that changes in the $|R_{pftm}|$ coefficient is the result of porosity changes.

CHAPTER 6 ELECTROSEISMIC FIELD SURVEY RESULTS AND DISCUSSION

6.1 Introduction

In this chapter the results of a field survey conducted on the Campus Test Site at the University of the Free State are presented and discussed. Apart from the localised presence of horizontal bedding plane fractures, the geology over much of the Campus Test Site is relatively uniform, as will be discussed in Section 6.2. The aim of the field survey is to compare the surface ES data recorded at a position vertically above a known horizontal fracture occurrence with the data recorded at a position laterally removed from the known fracture occurrence. Comparison of the data recorded at the two positions should reveal whether the presence of the fracture leads to the generation of ES signal that is detectable at surface. Because the theoretical results presented in Chapter 3 suggest that the lateral and vertical resolution of surface ES data are insufficient for the detection of these fractures, the field results may be seen as a test to confirm the results predicted by the theory.

The equipment used in the field survey is the commercial system developed by the company Groundflow Ltd. The system employs two antennæ, each consisting of two grounded electrodes, situated symmetrically on either side of the seismic source. With this geometry Groundflow claims that surveying may be done in a sounding mode whereby the recorded signal may be related to condition vertically below the seismic source. The Groundflow Ltd system and the assumptions on which it operates are discussed in greater detail in Section 6.3.2..

6.2 Geology and geohydrology of the Campus Test Site

The information in this section is taken from a comprehensive discription of the geological and geohydrological conditions on the Campus Test Site, as given by Botha *et al*. (1998). The test site is located on the property of the University of the Free State and covers an area of approximately 180×192 m^2. It was originally intended as a test site for postgraduate students. The positions of 30 percussion and seven core-boreholes that had been drilled on the site by 2003 are shown in Figure 6.2.1. The test site is partially situated on a basal outcrop of the Spitskop Sandstone, but mainly on the underlying Campus Sandstone. The southern border of the test site is formed by a dolerite sill.

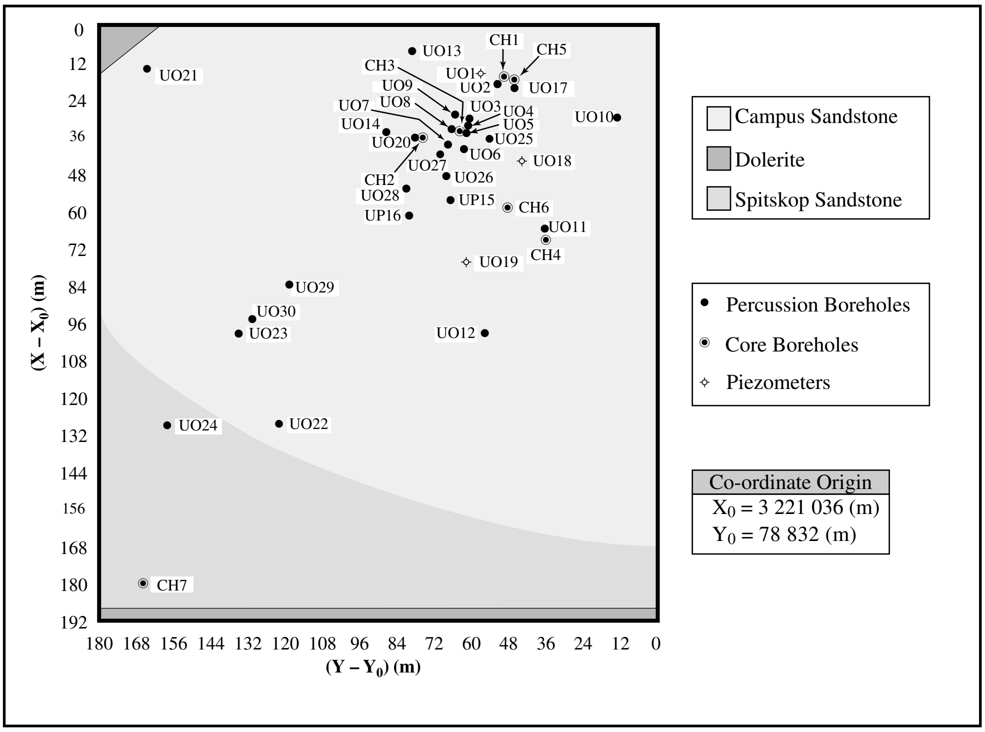

Figure 6.2.1. Plan view of the borehole locations and surface geology at the Campus Test Site.

The geological column as revealed from percussion- and core drilling shows a remarkable uniformity across the Campus Test Site. This can be seen in Figure 6.2.2 and Figure 6.2.3 where the geological profiles of two inclined core-boreholes (CH5 and CH6) and three vertical core-boreholes (CH2, CH3 and CH4) are shown. From the geological column five easily recognisable lithofacies can be identified (Botha e*t al.*, 1998), namely mudstone facies, a cross-laminated rhythmite (siltstone-mudstone) sequence, cross-bedded sandstone facies, cross-laminated mudstone and siltstone facies and a carbonaceous shale layer. These facies are numbered 1 to 5 in Figure 6.2.3. Comparison of the core-boreholes shows that the geological units have shallow dips on the test site.

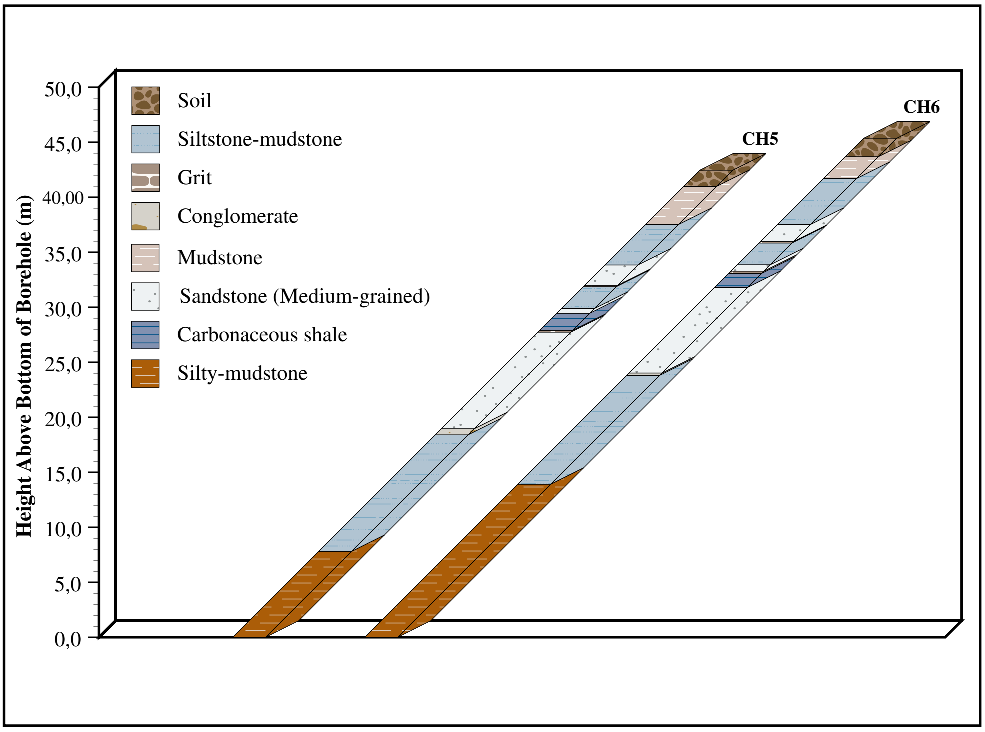

Figure 6.2.2. Geological profiles of two inclined boreholes drilled on the Campus Test Site (taken from Botha *et al*. (1998)).

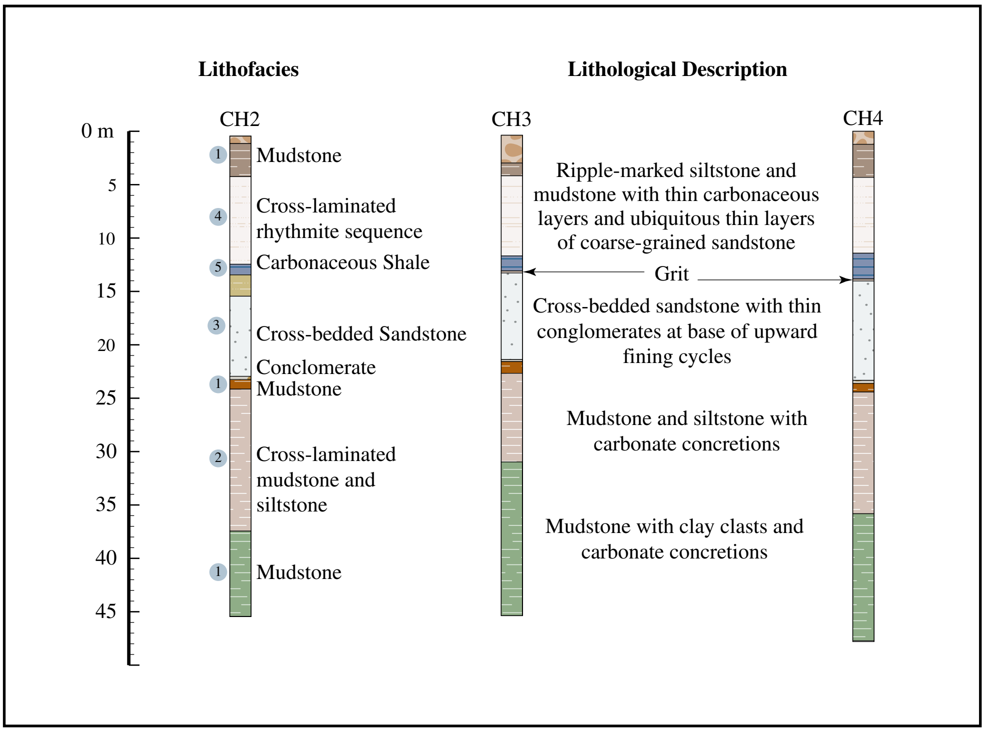

Figure 6.2.3. Lithological description of drill-core data from three core boreholes drilled on the Campus Test Site (adapted from Botha *et al*. (1998)).

From the core samples, Botha *et al.* (1998) identified a prominent bedding-plane fracture, with aperture ranging from 0.5 to10.0 mm, situated in the sandstone facies. Although the fracture has an estimated areal extent of 5 000 m^2, its occurrence is very localised. Acoustic scanner images taken in the high-yielding percussion borehole UO5 in 1996 and borehole video images taken in borehole UO23 in 2000 confirmed the presence of the bedding plane fracture at a depth of between 20.9 and 23.3 m. The borehole video images indicated that the aperture of the fracture may at some positions reach values in the centimetre range.

6.2.1 Geometry of the Campus Test Site aquifer system

Three aquifers have been identified on the Campus Test Site (Botha *et al.*, 1998). Figure 6.2.4 is a schematic diagram of the different aquifers present on the Campus Test Site.

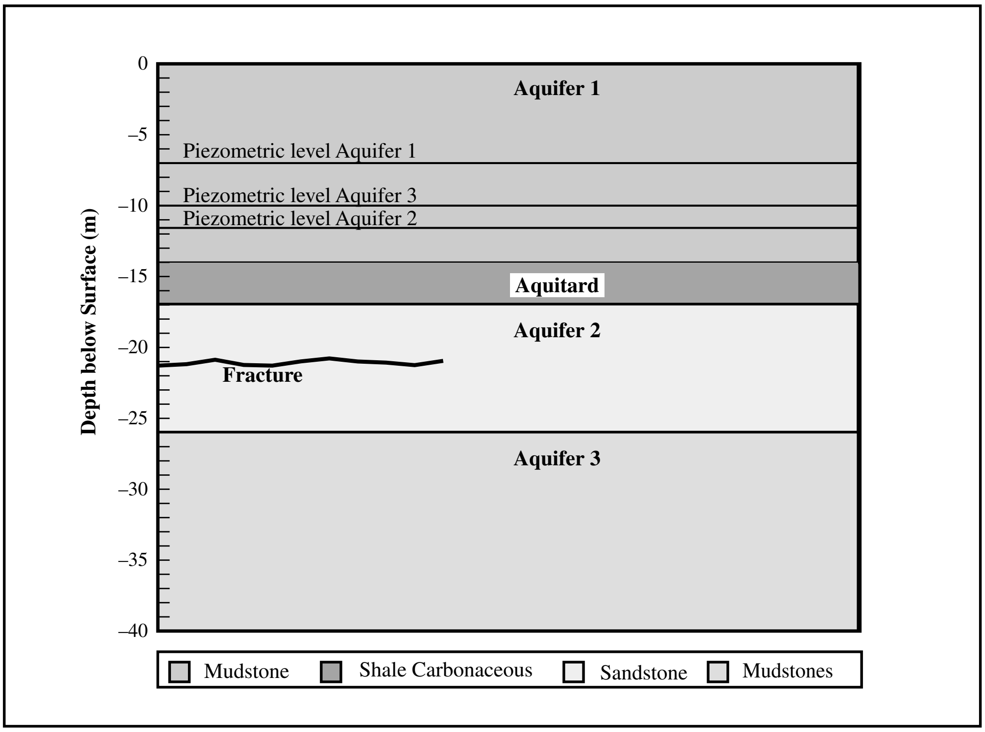

Figure 6.2.4. Schematic diagram of the different geological formations and aquifers present on the Campus Test Site (taken from Botha *et al.* (1998)).

The top-most aquifer is a phreatic aquifer that occurs in a laminated alteration of mudstone and siltstone (6-9 m thick) and a fine-grained, cross-laminated rhythmite sequence (1-6 m thick). The second and main aquifer is separated from the overlying aquifer by a carbonaceous shale layer whose thickness ranges between 0.5 and 4 m. The main aquifer is confined and occurs in the Campus Sandstone layer. A third aquifer, also confined, occurs in a succession of interbedded mudstone, siltstone and fine-grained sandstone.

An important observation made by Botha *et al*. (1998) is that the yield of the boreholes on the Campus Test Site depends on the presence or absence of the prominent bedding-plane fracture. All the high-yielding and none of the low-yielding boreholes intersect this fracture. In Figure 6.2.5 the positions of the percussion boreholes that intersect the fracture (all high-yielding boreholes) are indicated with filled circles. The positions of boreholes that do not intersect the fracture are indicated by crosses while the boreholes that showed indications of poorly developed fracturing are indicated by empty circles. The area in which the fracture was encountered during percussion drilling is roughly indicated by a dashed line.

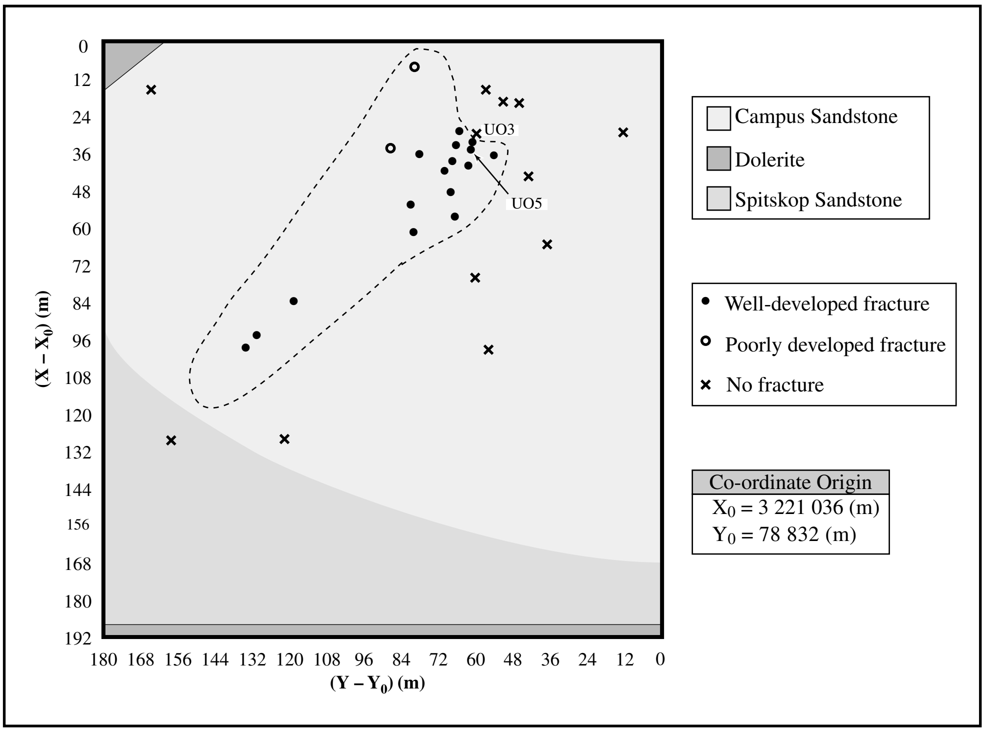

Figure 6.2.5. Plan view of the Campus Test Site indicating the positions of boreholes that intersect the bedding-plane fracture where it is well developed, poorly developed and where it is absent. The area of known fracture occurrence is roughly outlined in a dashed line.

From Figure 6.2.5 it is clear that the occurrence of the prominent bedding-plane fracture is very localised, and that the fracture seems to extend in a Northeast-Southwest direction on the test site. Although boreholes UO3 and UO5, for example, are separated by a distance of only 5 m, only UO5 displays the prominent fracture. The blow yields of UO5 and UO3 were 30 and 0.5 $m^3.h^{-1}$, respectively (Botha *et al.*, 1998), confirming the importance of the fracture for high-yielding boreholes.

Van der Voort and Van Tonder (2000) analysed the data from pumping tests performed on boreholes UO26, UO28 and UO29 (see Figure 6.2.1) by means of the Barker method. Their results showed that the prominent fracture on the Campus Test Site has a fractal dimension of approximately 1.5. Figure 6.2.6 shows one possible geometry of the prominent fracture if a fractal dimension of 1.5 is assigned to it. Two important observations that may be made are that the occurrence of the fracture is likely to be very localised and that fracturing may be present at positions removed from the area of known fracture occurrence, as outlined in Figure 6.2.5.

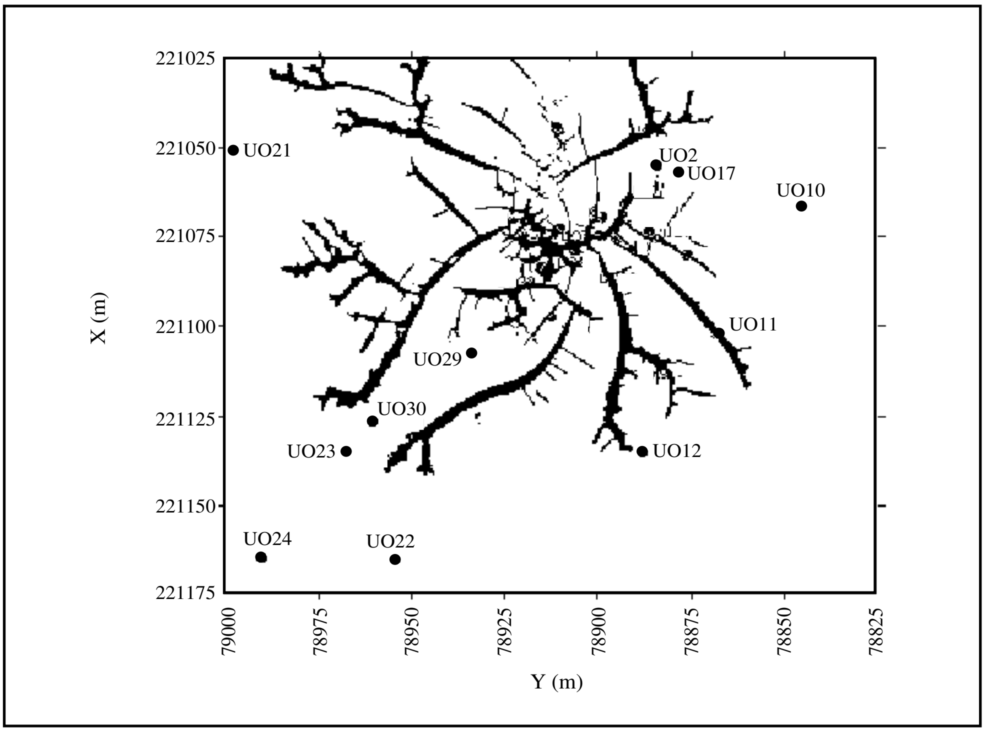

Figure 6.2.6. A fractal representation of the geometry of the prominent fracture on the Campus Test Site (from Van der Voort and Van Tonder (2000)).

6.3 Field Survey

6.3.1 Aim of the survey

The study conducted into the lateral and vertical resolution of surface ES data conducted in Chapter 3 indicates that the resolution is insufficient to detect the presence of fractures with apertures in the millimetre to a few centimetre range. The aim of the field survey is to confirm the theoretical results presented in Chapter 3. By comparing the spatial and temporal ES data recorded at a position above a known fracture occurrence with the data recorded at a position where no known fracture occurs, it may be possible to see if the presence of the fracture leads to additional ES energy reaching the surface. The lack of such additional energy in the recorded data may be seen as a confirmation of the theoretical results.

6.3.2 Equipment and survey geometry

The equipment used during the field survey was the commercially available Groundflow1000 system manufactured by the company Groundflow Ltd in Marlborough, UK. The Groundflow1000 system is a two-channel system that employs a survey geometry in which the antennæ, each consisting of a pair of grounded electrodes, are located symmetrically on either side of the seismic source at positions of small offset (0.25 m for the inner electrode). Data is recorded for 400 ms after triggering at a sampling interval of 50 µs. The sampling frequency is therefore 20 kHz while the highest frequency that can be accurately captured in the data (the Nyquist frequency) is 10 kHz. These frequencies are at least an order of magnitude higher than the frequency range expected during ES surveys, but the high sampling frequency is employed to allow robust digital data filtering procedures in which data records may be truncated.

The claimed advantages of using two small offset antennæ are:

- Surface waves exhibit radial symmetry on the interfaces between homogeneous media. Due to this symmetry surface waves travelling along a horizontal interface rapidly contribute less signal once they pass beneath the positions of the surface antennæ.
- Calculations performed by Beamish (1999) to evaluate the electric field associated with a buried vertical electric dipole indicate a field that is sharply focused above the position of the dipole. A rapid spatial decay of signal amplitude can therefore be expected. Using antennæ located close to the seismic source allows larger signal-to-noise ratios.
- For the Fresnel zone coupling mechanism, the total ES signal has its origin mainly within the first ES Fresnel zone. Groundflow Ltd assumes that by working with small offset antennæ the 3D problem is essentially reduced to a 1D problem so that measurements may be taken in a sounding mode whereby the recorded ES signal can be attributed to positions vertically below the seismic source.
- The use of two electrode pairs situated on either side of the shot-point allows data to be recorded on two channels, which allows distinction to be made between electroseismic signal and incoherent noise.

For the above reasons, Groundflow Ltd calls the ES technique using small offset antennæ the *Electrokinetic Sounding* (EKS) technique.

In Sections 3.1.3 and 3.1.5.1 the ES Fresnel zones from monochromatic and broadband excitation were discussed. It was shown that the ES Fresnel zones are larger than their seismic equivalents and that the lateral resolution of surface ES data is consequently poor than surface seismic data. The example given in Section 3.1.3 shows that a source frequency of 75 Hz and a seismic velocity of 2 000 m s^{-1} result in a radius of 38.9 m for the first ES Fresnel of an interface located at a depth of 50 m. Lateral variations in the properties of the fluid-saturated rock may thus be expressed in the recorded ES signal. The above observations cast considerable doubt on Groundflow Ltd's assumption that the 3D problem may be reduced to a 1D problem. In addition, the use of only two channels is clearly not discriminatory in terms of describing the complete spatial and temporal nature of all the ES signals generated in the subsurface (Beamish and Peart, 1998). To distinguish between the signals generated by the various wave types, as well as between co-seismic energy and the interface responses, multi-channel systems are required.

Although the Groundflow1000 system only provides two channels for recording, the system may be used in a somewhat unconventional (and time-consuming) mode to obtain data similar to the data from multi-channel systems. This is illustrated in Figure 6.3.1 where the conventional stationary multi-channel geometry, such as used during seismic surveys, is compared with the unconventional geometry.

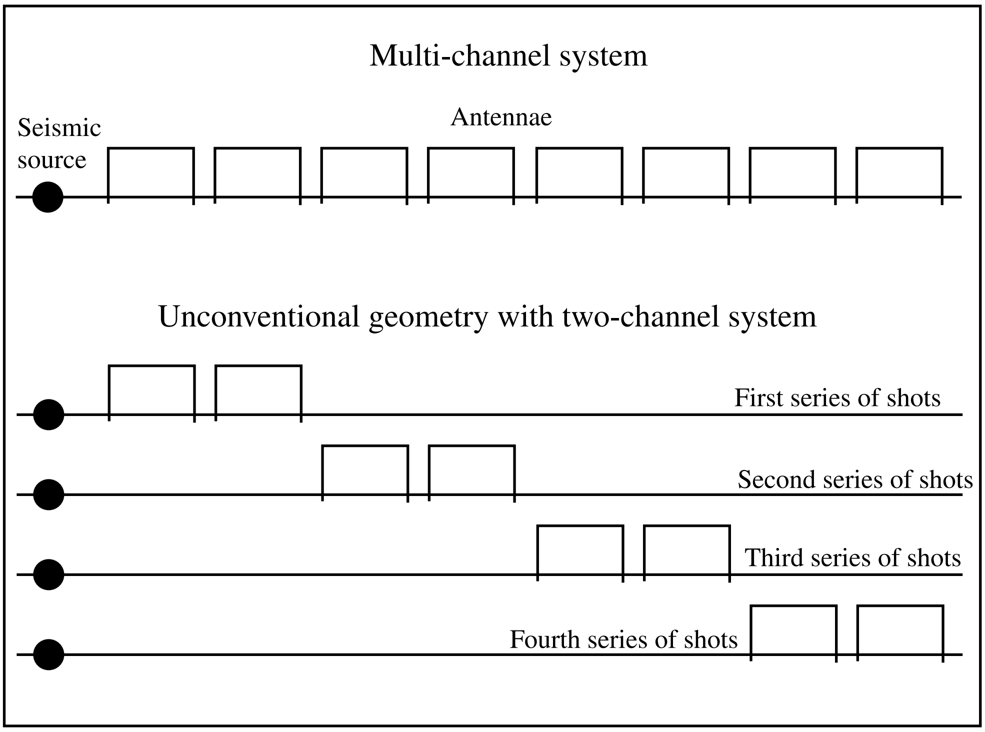

Figure 6.3.1. Comparison of the conventional multi-channel geometry with the unconventional geometry used during this study.

Multi-channel systems simultaneously record data on all the available channels. During stationary multi-channel surveys (surveys in which the source and receiver locations remain fixed) a number of seismic disturbances ("shots") are generated at the source position and the responses are simultaneously recorded on all the available channels over a selected period of time. These temporal responses are called traces. The traces recorded on each channel for the various shots are averaged ("stacked") to enhance the signal-to-noise (S/N) ratio, since coherent energy is enhanced while incoherent energy is suppressed in the averaging process. The number of shots fired depends on the required S/N ratio – more shots lead to a better S/N ratio. Seismic surveys typically employ 8- or 12-fold stacking, that is to say, eight or 12 traces are averaged.

The unconventional geometry used with the Groundflow1000 system requires that the two antennæ be moved to the different receiver positions on the surface to be able to record data in a multi-channel mode. Since only two channels can be recorded at once, more seismic shots have to be fired to attain the same fold as with multi-channel systems. For example, recording 40-fold data on a normal multi-channel system with 16 channels requires only 40 shots. To obtain the same fold on 16 channels with the unconventional geometry requires 40×8 seismic shots. Apart from being more laborious and time-consuming, the unconventional geometry has the added disadvantage that the various traces recorded are not due to the same excitation of the earth during each seismic shot fired.

The two positions chosen for the field survey are indicated in Figure 6.3.2 Source position A is laterally displaced from the known fracture occurrence while source position B is located above the horizontal bedding-plane fracture, as indicated by core- and percussion borehole information. The lines along which the antennæ were laid out (the survey lines) are also shown. The antennæ consisted of electrode pairs with a separation of 2 m. Data were recorded on 16 channels with the positions of the inner electrodes at offsets of 1, 4, 7, 10, 13, 16, 19, 22, 25, 28, 31, 34, 37, 40, 43 and 46 m. The choices of source locations and survey line direction were strongly influenced by the presence of existing boreholes lined with steel casings. Cased boreholes are likely to be sources of seismic and EM noise due to: 1) scattering of seismic energy from the casing and borehole walls, 2) streaming current imbalances at the casing and borehole walls and 3) electrical eddy currents induced in the conductive casing.

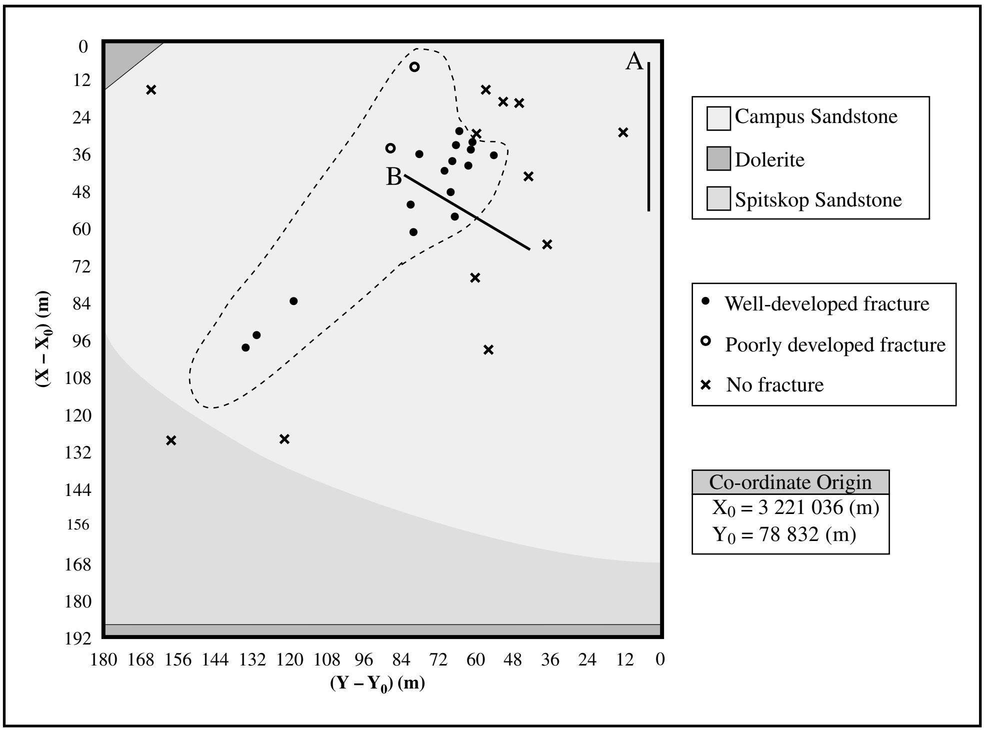

Figure 6.3.2. The positions of the seismic sources A and B, and the orientation of the survey lines during the survey on the Campus Test Site.

Due to the large number of boreholes on the Campus Test Site, especially in the vicinity of the known fracture occurrence, a strong noise component can be expected in the data recorded along survey line B (see Figure 6.3.2). To minimise this noise component, source B is located at a position in-between boreholes that all intersect the fracture, and at least 5 m away from the nearest borehole. The possible directions of the survey lines were limited by the presence of local infrastructure (fences, paved walkways) on the Campus Test Site.

6.4 Field survey results

Throughout this section the data recorded along line A (laterally removed from the known fracture) is compared with the data recorded along line B (with the seismic source vertically above the known fracture zone). Both sets of data are subjected to the same processing procedures to allow comparison of the results and to see whether any additional energy arrivals on line B may be due to the presence of the bedding-plane fracture.

6.4.1 Data processing

Both sets of data are subjected to the following steps of processing:

- Removal of the 50 Hz powerline noise and its harmonics by a subtraction procedure;
- Stacking;
- The application of gain and frequency filtering.

6.4.1.1 Removal of 50 Hz powerline noise

The 50 Hz powerline noise and its harmonics are removed by a simple subtraction procedure. The ES data was recorded for a total time of 400 ms. The reasonable assumption is made that after 200 ms no ES signal generated in the earth is detectable and that this part of the data contains only coherent noise. Subtraction of the latter half of the record from the first 200 ms will thereby suppress the 50 Hz noise component in the data.

Figure 6.4.1 shows the time traces recorded from five different hammer blows. Even though the equipment used to record the ES signal allows some reduction of the 50 Hz noise component by means of an adjustable electronic notch filter, the recorded data is severely contaminated by 50 Hz powerline noise with an amplitude of approximately 0.4 mV. Only during the first 30 ms of the traces the ES data is seen to have amplitudes adequately large to be recognisable above the coherent noise.

The amplitude spectra of the five data traces are shown in Figure 6.4.2. The 50 Hz noise component is clearly seen as a sharp peak that dominates the rest of the frequency components. Also seen are amplitude peaks at 150 and 450 Hz, corresponding to the 3rd and 9th harmonics of the powerline noise.

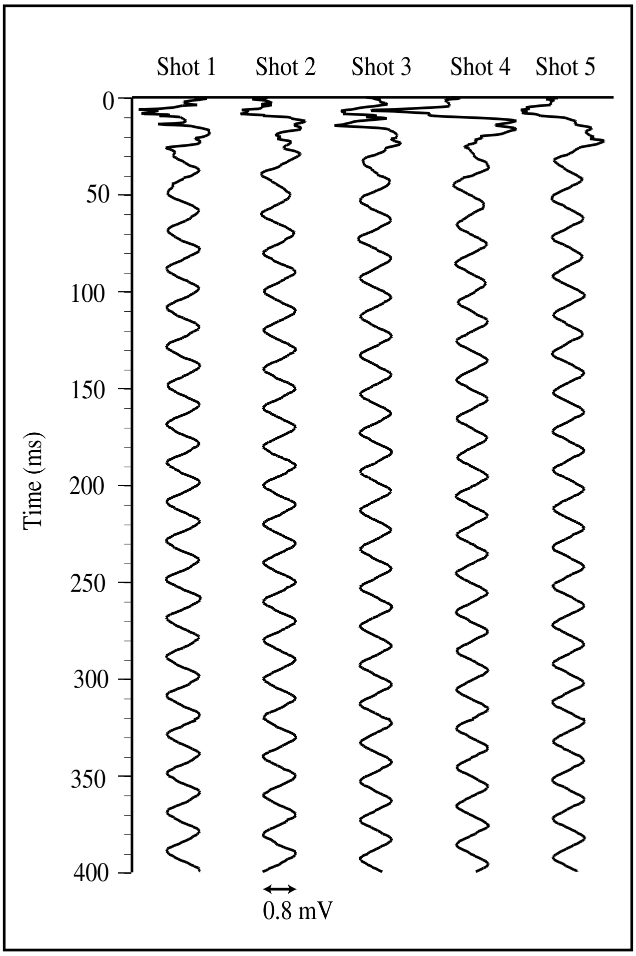

Figure 6.4.1. Examples of raw data recorded on the Campus Test Site.

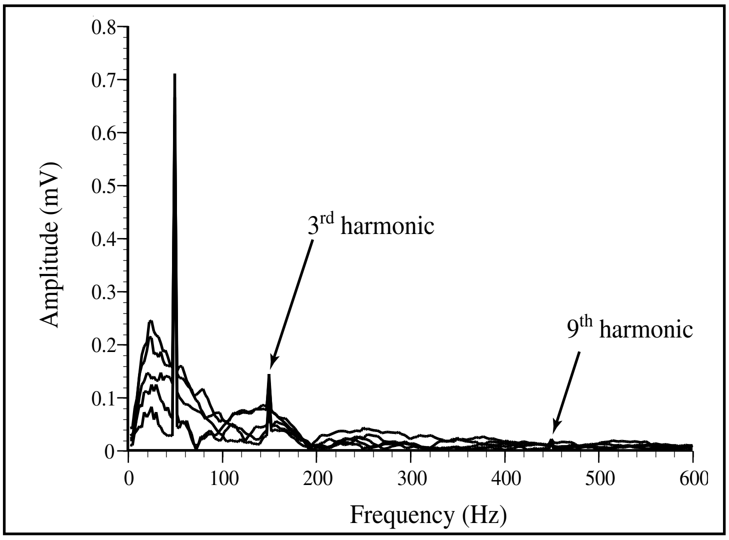

Figure 6.4.2. Amplitude spectra of the raw data recorded on the Campus Test Site.

The five data traces and their amplitude spectra are respectively shown in Figure 6.4.3 and Figure 6.4.4 after powerline noise removal by means of the subtraction procedure.

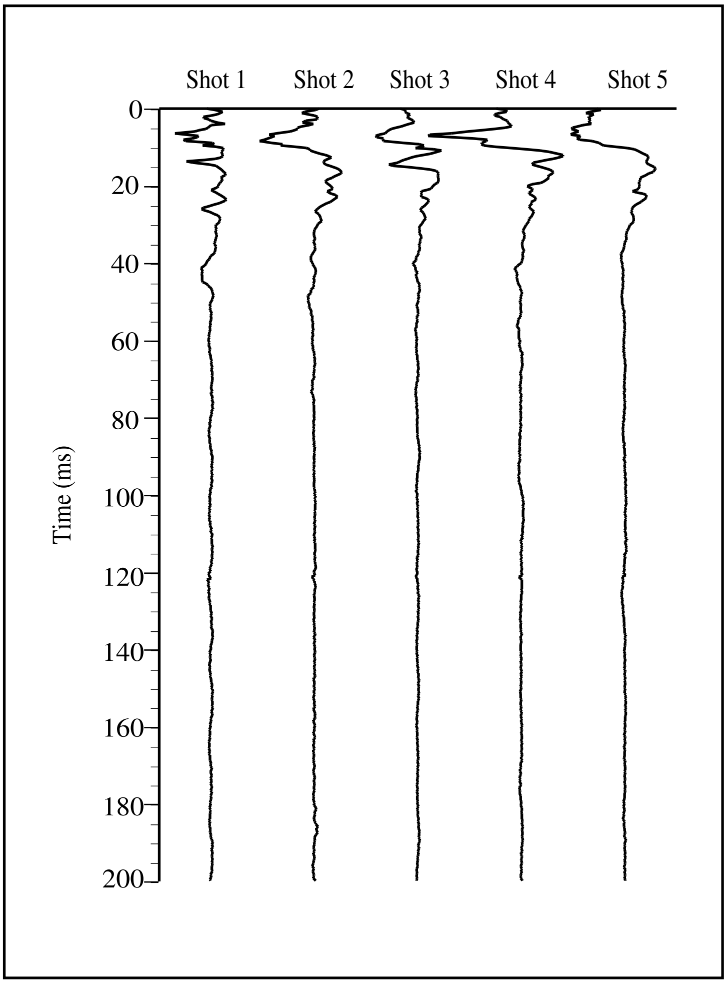

Figure 6.4.3. Example of raw data traces after removal of powerline noise.

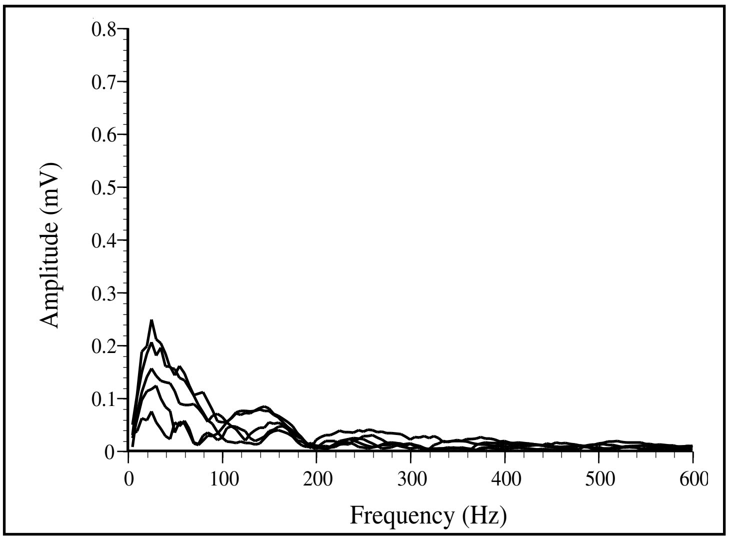

Figure 6.4.4. Amplitude spectra after powerline noise removal.

From Figure 6.4.3 and Figure 6.4.4 it is clear that the subtraction procedure is successful in removing the 50 Hz noise component and its harmonics. The low repeatability of the data in the five traces shown in Figure 6.4.3 suggests that the data quality is generally low.

6.4.1.2 Stacking

To improve data quality, stacking of the recorded data is done by averaging the response measured after a number of seismic excitation events. Forty data traces, corresponding to 40 blows with the hammer, were recorded for each electrode pair position. Forty-fold stacking of the data was done by obtaining the averages of the 40 traces for each recording position. The results of stacking of the data recorded on line A (away from the known fracture occurrence) and line B (seismic source located above the fracture) are displayed in Figure 6.4.5.

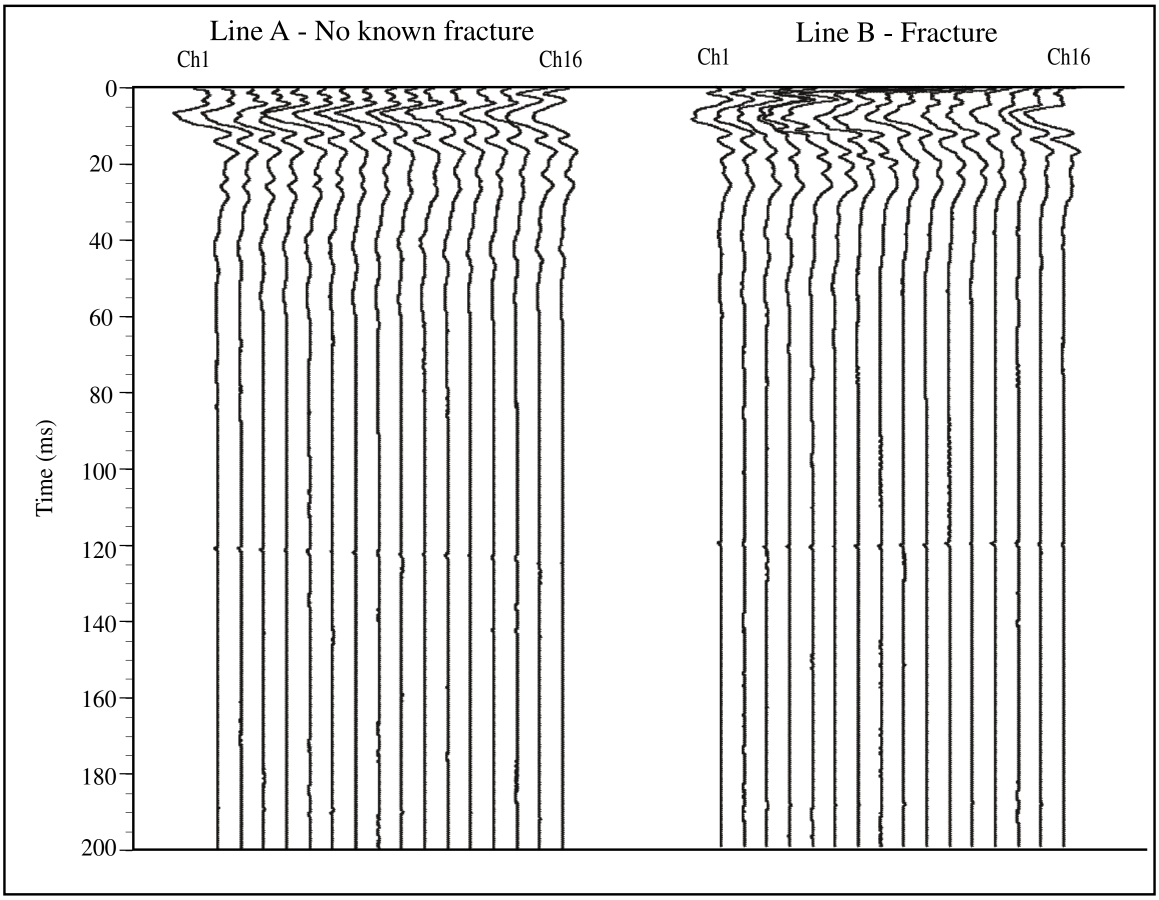

Figure 6.4.5. Forty-fold stacked data recorded on the Campus Test Site.

From Figure 6.4.5 a number of observations can be made:

- The high repeatability from trace to trace shows that stacking led to a marked improvement in the data quality. This is especially true for the data recorded along line A.
- The data recorded along line B is more noisy than that recorded along line A. This is most probably due to source B's proximity to the cased boreholes.
- All energy arrivals are virtually instantaneous across the electrode arrays and no move-out is observed. This observation suggests that the interface response dominates over the response from surface waves at the Campus Test Site. The reason for the absence of co-seismic energy is in all likelihood due to the fact that the ES survey on the Campus Test Site was conducted during the dry winter months. The absence of fluids in the near-surface does not allow for a streaming current to be generated, and no electric fields are therefore observed when the seismic waves traverse these dry upper layers.
- During the first 20 ms a number of energy arrivals are observed. These arrivals may exhibit large overlap of signals generated at different horizons and it is difficult to identify the separate arrivals and to determine their times of arrival.
- Energy arrivals are observed at times of around 25 and 45 ms on line A. These arrivals also occur on line B but are weaker and slightly displaced in time.
- The high-frequency arrival observed on both lines at a time of around 120 ms is not due to true ES signal, but is an artefact of the system employed for the recording of the data, as will be shown in the discussions that follow.

Figure 6.4.6 shows the average amplitude spectra recorded for both lines A and B.

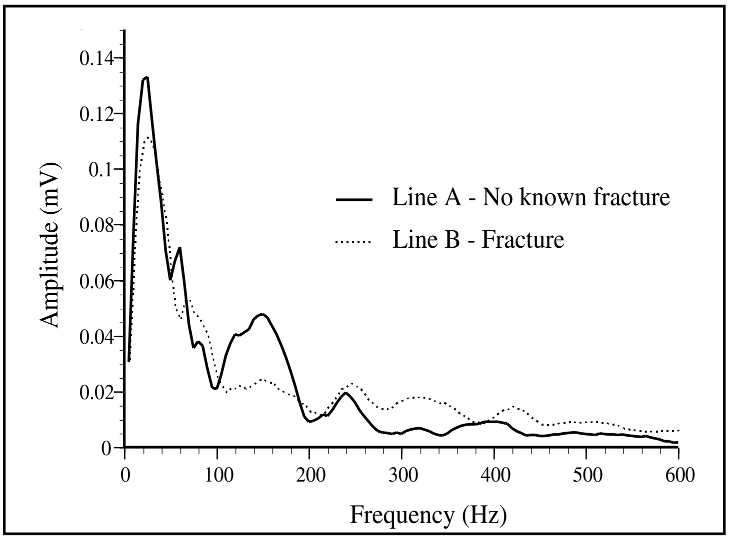

Figure 6.4.6. Average amplitude spectra recorded on line A and line B.

Frequencies lower than 100 Hz are seen to dominate the data from both locations. On line A energy with frequencies between 100 and 200 Hz is evident. This energy is not observed in the data from line B. The data from line B does, however, have a stronger high frequency component, possibly due to the noise associated with the cased boreholes.

6.4.1.3 Gain

Figure 6.4.7 shows the data recorded along lines A and B after the application of a linear gain function to enhance the signal recorded at later times.

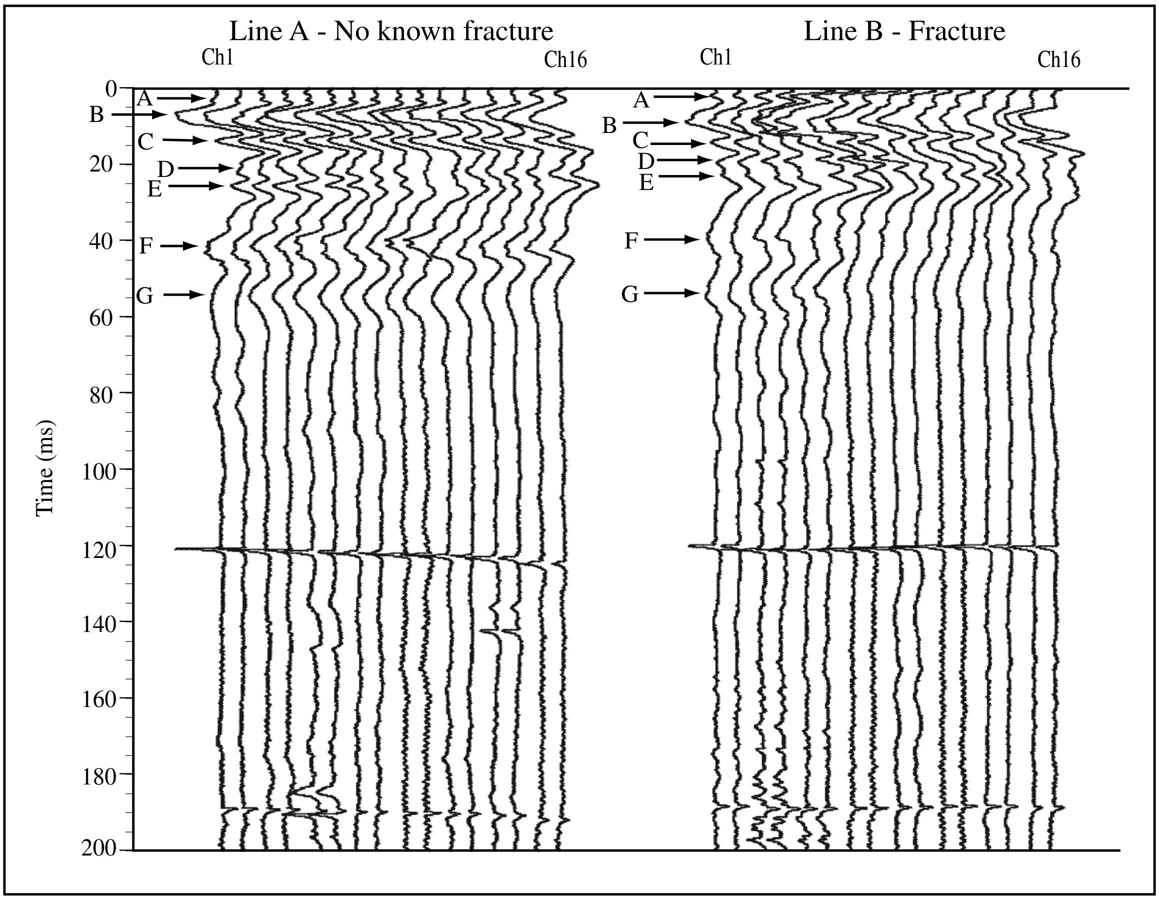

Figure 6.4.7. Results of the application of linear gain to the data recorded on the Campus Test Site.

From Figure 6.4.7 the following observations can be made:

- Although data recorded on line B are noisier than the data recorded along line A, the general temporal behaviour of the signals are similar. Seven marker horizons (marked A to G) corresponding to negative peaks in the data sets are shown. These horizons are visible on both sets of data, although they are slightly displaced in time and are not always evident on all the traces. Some horizons also exhibit stronger/weaker amplitudes in the two data sets.

- The application of linear gain enhanced the high-frequency horizon at around 120 ms, and brought out an additional high-frequency horizon at around 190 ms.

To investigate whether the two high-frequency energy arrivals at 120 and 190 ms were indeed due to ES signal, fifty measurements of the 50 Hz powerline noise were made on the Campus Test Site, and the data was consequently stacked. The results of stacking are shown in Figure 6.4.8. The presence of "anomalous" peaks in the stacked noise at times of around 120 and 190 ms shows that the peaks observed at these times in the field data (Figure 6.4.5 and Figure 6.4.7) are not true energy arrivals but are artefacts of the system used to record the data.

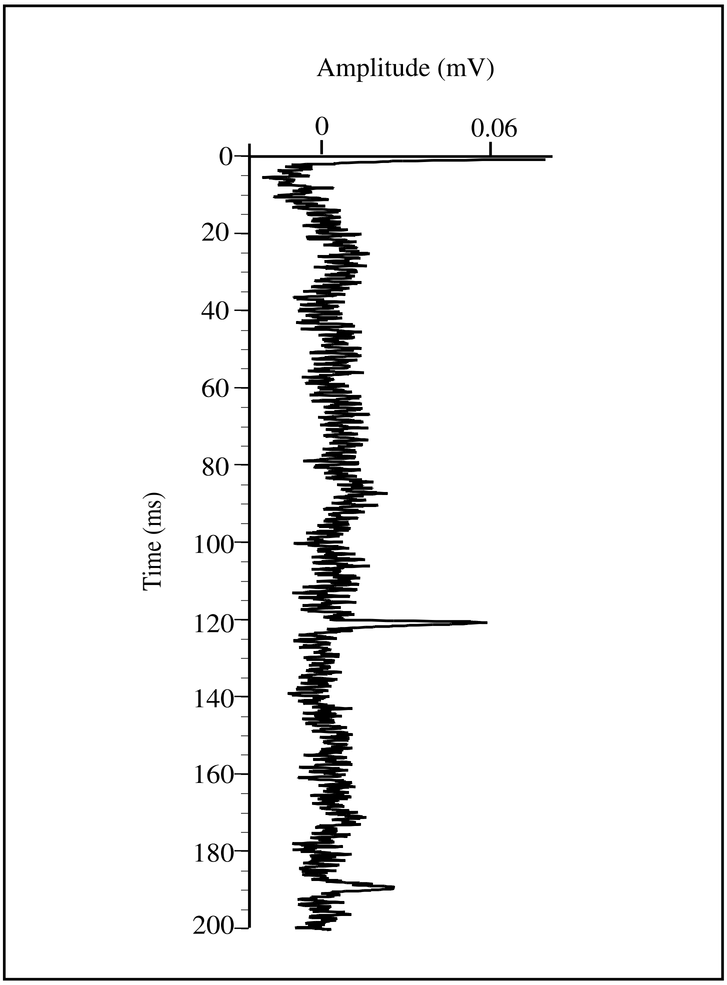

Figure 6.4.8. Fifty-fold stack of the powerline noise.

6.4.1.4 Frequency filtering

Frequency filtering by means of band-pass and high-pass filters was done to investigate the frequency content of the observed energy arrivals. As seen in Figure 6.4.6, frequencies lower than 100 Hz dominate the data at both locations. On line A energy with frequencies between 100 and 200 Hz is evident which is not observed in the data from line B. The data from line B has a stronger high frequency component. The following filters were applied to both data sets:

- A 100 Hz high-pass filter,
- A 200 Hz high-pass filter, and
- A 100-200 Hz band-pass filter.

The results of applying the 100 Hz high-pass filter are shown in Figure 6.4.9.

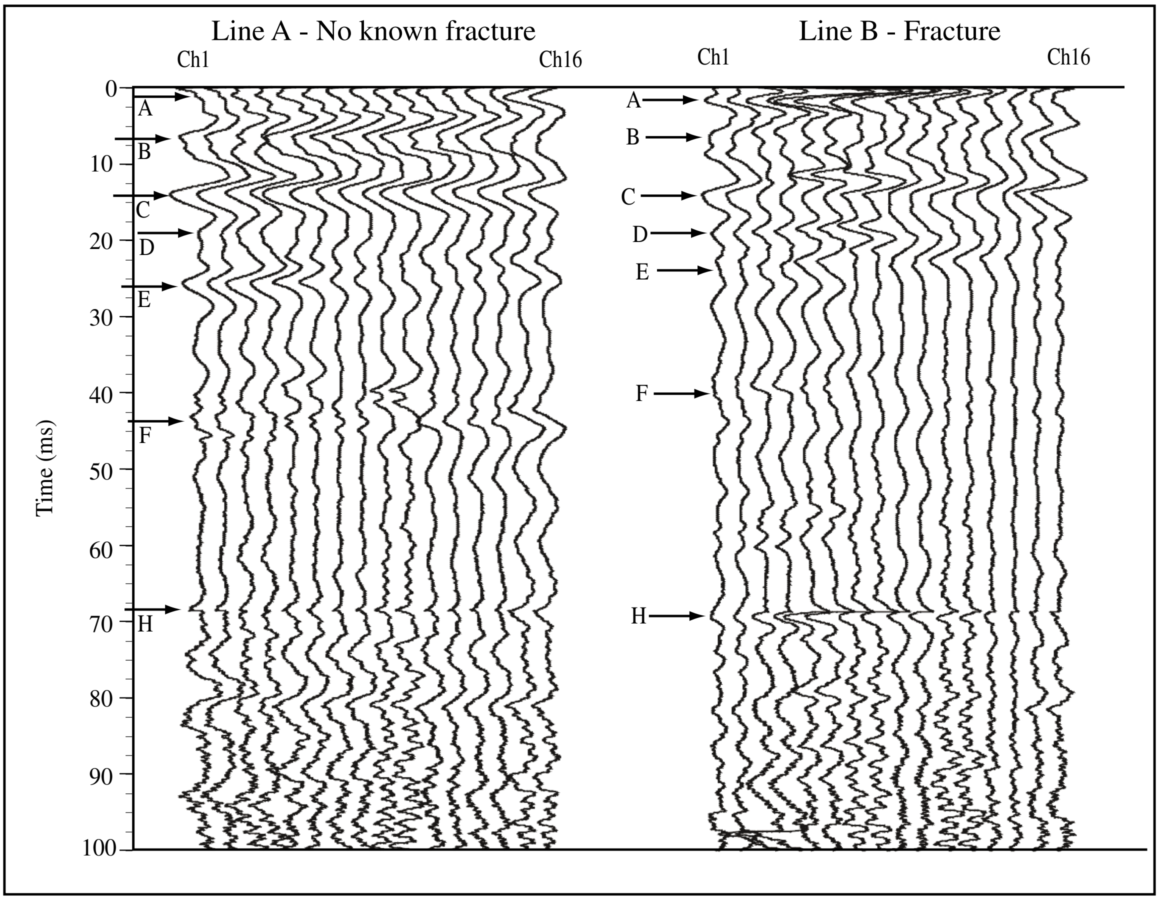

Figure 6.4.9. Results of the application of a 100 Hz high-pass filter and exponential gain to the data recorded on the Campus Test Site.

The horizons corresponding to those indicated in Figure 6.4.7 are shown in Figure 6.4.9. From this figure the higher quality of the data from line A is apparent. Horizons B, C, E and F are much more clearly defined in the data of line A than in the data of line B, although horizon F does not display high repeatability form trace to trace. Horizon D is, however, better defined in the data of line B. This may be due to a local higher contrast in medium properties between the fluid-saturated porous media. Note that in both data sets a new high-frequency energy arrival is observed at a time of around 68 ms. This energy arrival is due to true ES signal and is not an artefact, since it is not observed in the processed powerline noise data. This shows that surface ES techniques do have the ability to image contrasts in medium properties at depth. (A conservative estimate of 2000 m s^{-1} for the average seismic velocity of the overlying layers yields a depth of approximately 140 m for the interface where signal generation occurs.)

Similar observations can be made from the 200 Hz high-pass filtered data (with exponential gain) shown in Figure 6.4.10. The same horizons as before may again be identified. Again it is clear that the data of line A is of a higher quality that that of line B. Note how filtering of the data revealed additional horizons between horizons B and C, and D and E. Although characterised by low repeatability from trace to trace, horizon F is much more clearly defined on line A than on line B.

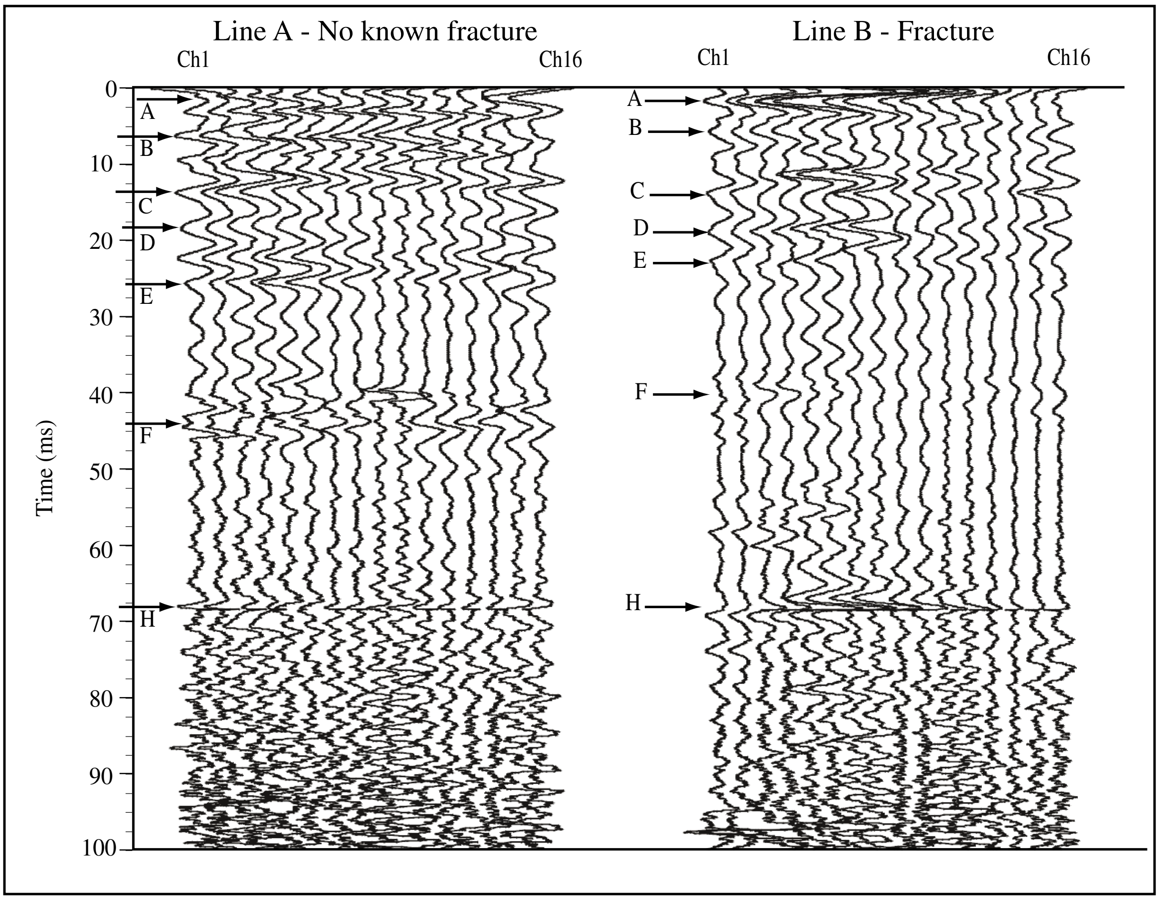

Figure 6.4.10. Results of the application of a 200 Hz high-pass filter and exponential gain to the data recorded on the Campus Test Site.

To investigate the origin of the 100-200 Hz energy observed in the amplitude spectrum of line A but absent in the amplitude spectrum of line B (see Figure 6.4.6), a 100-200 Hz band-pass filter was applied to both data sets. The results are shown in Figure 6.4.11.

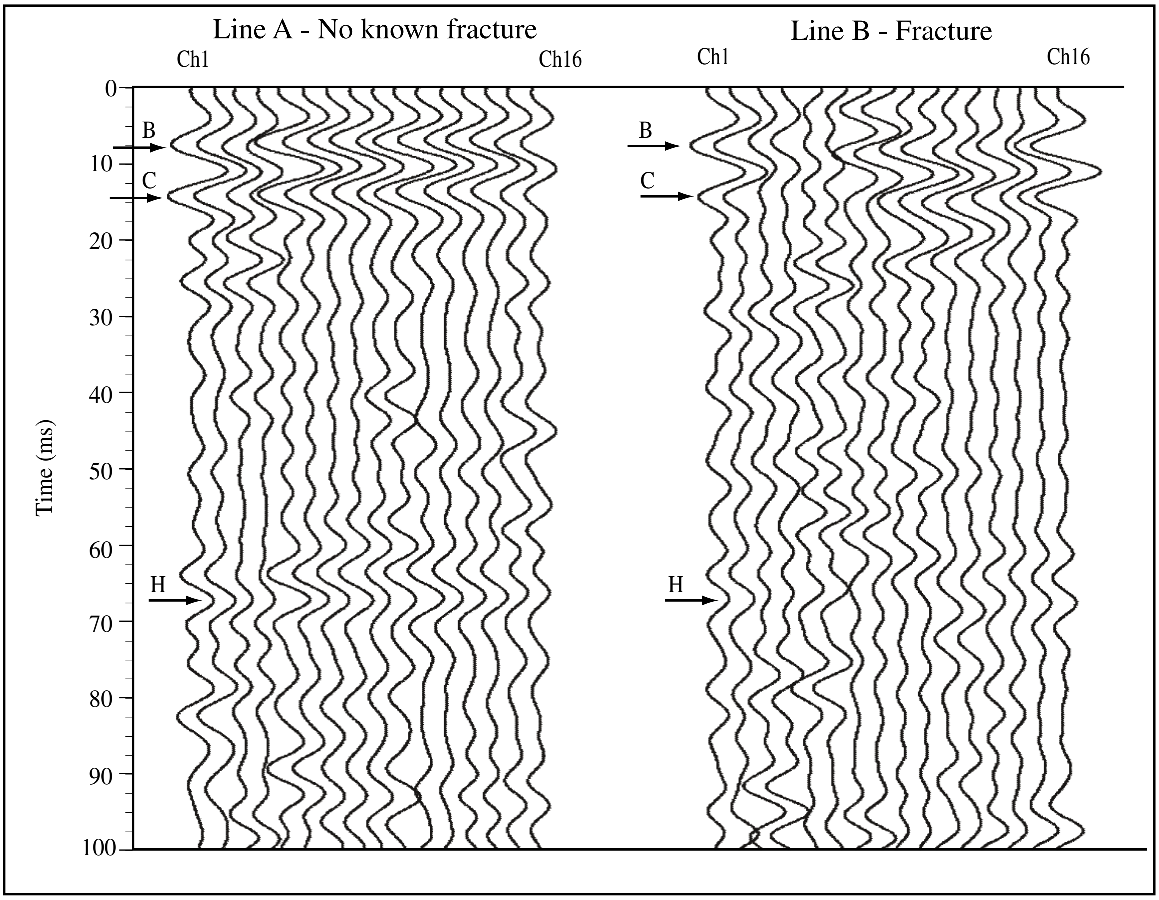

Figure 6.4.11. Results of the application of a 100-200 Hz band-pass filter and exponential gain to the data recorded on the Campus Test Site.

Only the most prominent horizons are shown in Figure 6.4.11. Note how well defined horizons B, C and H are on line A compared to line B. This is the most pronounced difference between the two data sets and it therefore seems that the 100-200 Hz energy observed in the data from line A may be attributed to the ES signals generated at interfaces at depths corresponding to these horizons.

6.4.2 Interpretation

The aim of the field survey was to compare the ES data recorded at a position above a known fracture occurrence with the data recorded at a position where no fracture is thought to exist. Energy arrivals present in the data from the fracture position that are absent in the data from the position laterally removed from the fracture would indicate that such a fracture may indeed be detected with surface ES methods. From the results presented in Figure 6.4.7, Figure 6.4.9, Figure 6.4.10 and Figure 6.4.11 it is, however, clear that no prominent energy arrival is observed in the data of line B that is not observed in the data from line A. This observation suggests that the vertical ES resolution is insufficient to detect such fractures, and seems to confirm the results of the investigation into the vertical resolution of surface ES data, presented in Chapter 3.

For the present study the interpretation of the recorded signal in terms of the known geology is of lesser importance and will only be discussed briefly and generally. In Figure 6.4.12 the geological logs of three percussion borehole in the vicinity of the seismic sources on lines A and B are shown. Borehole UO10 is the nearest borehole to source A, while source B was located at a position between boreholes UP16 and UO20.

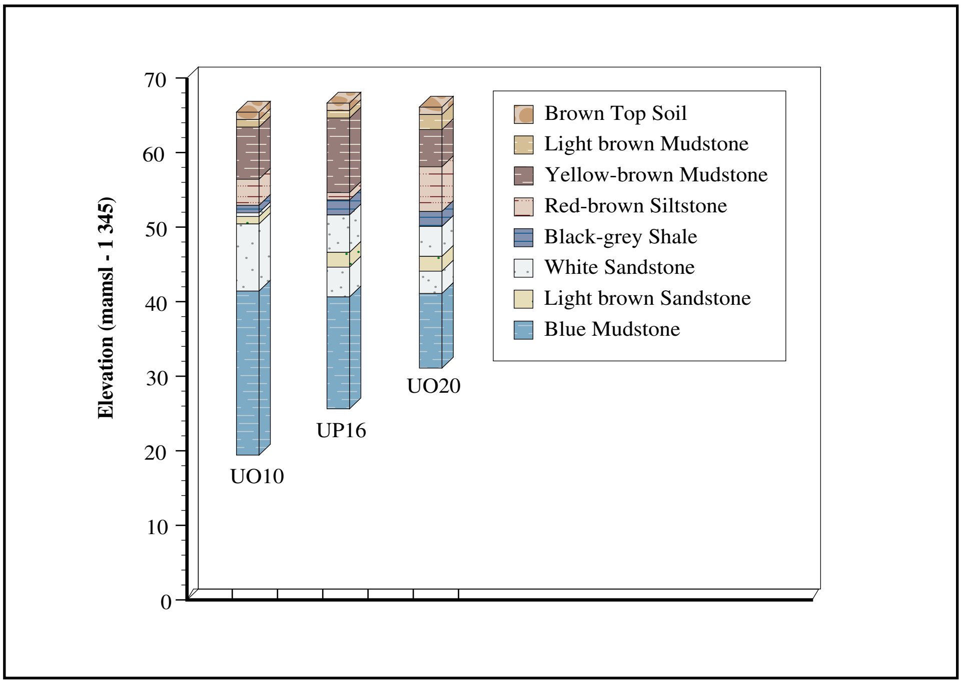

Figure 6.4.12. Geological logs of boreholes near the seismic source positions of line A and line B (adapted from Botha *et al* . (1998)).

From the borehole logs shown in Figure 6.4.12, the following observations can be made in terms of the expected electroseismic contrasts and responses from the interfaces between the various rock units:

- The brown topsoil is only approximately one metre thick on the Campus Test Site. This layer is also unsaturated and no ES response is therefore expected from this layer.
- The light brown mudstone underlying the topsoil has a thickness of between one and two metres in the three boreholes shown in Figure 6.4.12. From Figure 6.2.4 we see that the groundwater table and piezometric levels of the different aquifers at the

Campus Tests Site occur at depths that lie within the yellow-brown mudstone layer underlying the light brown mudstone layer. Since the light brown mudstone layer is not saturated, no generation of streaming current can occur within this layer and no ES response is expected from this layer.

- The top interface of the yellow-brown mudstone layer also lies above the groundwater table, and no ES response can therefore be generated at this interface.
- The groundwater table (and piezometric levels of the confined aquifers) lies within the yellow-brown mudstone at a depth of around 5 m. Since streaming current can only be created in the saturated parts of this mudstone, any mechanical disturbance that causes motion of the groundwater table will give rise to unbalanced current flow in the vicinity of the groundwater table. EM radiation is therefore expected and a surface measurable ES response is therefore likely.
- The red-brown siltstone underlying the yellow-brown mudstone has a thickness of around 4, 1 and 6 m at boreholes UO10, UP16 and UO20, respectively. Taking a very conservative estimate of the seismic velocity for this layer as 1 000 m s^{-1}, frequencies of 50 to 100 Hz result in wavelengths of 10 to 20 m. The layer thicknesses are therefore small compared to the expected seismic wavelengths and destructive interference from the signals generated at the top and bottom interfaces is therefore expected. If the difference in the seismic contrasts between the red-brown siltstone and the yellow-brown mudstone, and the red-brown siltstone and the underlying black-grey shale is large enough, surface measurable ES responses could result.
- Similar observations can be made about the black-grey shale layer. In all three boreholes it has a thickness of two metres or less. Only very large differences in the electroseismic contrast at the top and bottom interfaces will result in surface detectable ES signal. Due to the small thickness of the shale layer compared to the expected seismic wavelengths, this does, however, seem unlikely.
- As stated above, the thicknesses of the red-brown siltstone and the black-grey shale are so small that surface-detectable ES signal generation from these layers is unlikely. Although the yellow-brown mudstone is not in physical contact with the white sandstone (and the imbedded light brown sandstone) the effective electroseismic contrast between these layers is likely to be high due to large differences in the permeability. Although the thickness of the sandstone layer (approximately 10 m) may be insufficient to allow resolution of the two separate EM "reflections" from the two interfaces, its thickness is likely to be large enough to allow detection of the composite signal from the two interfaces.

The above observations suggest that, in the first 25 m of the subsurface, surface-detectable ES signal generation is likely to occur at the groundwater table and in the vicinity of the upper and lower contacts of the white sandstone. Since the depths at which signal generation is expected to occur differ by distances that are small compared to the expected wavelengths, considerable temporal overlap of signal generated at different depths is expected. The first energy arrival (horizon A in Figure 6.4.7, Figure 6.4.9 and Figure 6.4.10) is likely to be due to the signal generated at the groundwater table.

Using an estimate for the seismic wave velocity in the upper weathered layers and taking the minimum velocities of pressure wave propagation in unweathered sandstone and siltstone into account (> 1 500 m s^{-1}) (Telford *et al.*, 1990), all the depths of signal generation should correspond to times earlier than 20 ms. Only the first 20 ms of the records shown in Figure 6.4.5, Figure 6.4.7, Figure 6.4.9, Figure 6.4.10 and Figure 6.4.11 can therefore be related to the known geology as shown in Figure 6.4.12. The energy arrivals observed at later times are therefore due to ES contrasts at depths exceeding those of the percussion boreholes on the test site, and no information exists to allow interpretation of these arrivals.

To obtain reliable estimates of the depths of the interfaces responsible for signal generation, information on the seismic velocities of the various rock units on the Campus Test Site is required. No such information was, however, available at the time of the current study. In seismics, velocity analyses is often performed on the seismic time sections. On a time-distance graph, direct arrivals (and surface waves such as Rayleigh and Love waves) display linear trends that pass through the origin (Telford *et al.*, 1990). Refracted arrivals also have linear trends, while reflected arrivals exhibit hyperbolic curves (normal moveout). From the slopes of the straight lines associated with the direct and refracted arrivals, as well as from the shapes of the hyperbola due the reflected arrivals, estimates of the seismic velocities of the various rock layers may be found.

Velocity analyses on the ES data recorded on the Campus Test Site is more difficult to perform for two reasons. Firstly, the dry surface layer at the time of recording eliminated all co-seismic energy from the recorded data. No direct or refracted arrivals were therefore recorded. Secondly, since the ES interface response leads to energy arrivals that are virtually instantaneous (negligible moveout) on a seismic time-scale, the velocities could also not be estimated by examining the normal moveout curves.

To obtain only first order estimates of the depths of the interfaces responsible for signal generation, four different seismic velocity models for the Campus Test Site were assumed and the time section shown in Figure 6.4.10 was converted to four depth sections corresponding to the four velocity models. Since the weathered surface layers on the

Campus Test Site are expected to exhibit low seismic velocities, a velocity of 800 m s^{-1} was assumed for the upper two metres, while a seismic velocity of 1 500 m s^{-1} was assumed for the rock material occurring at depths of between two and 10 metres. In Section 3.2.2 (Table 3.2.5) the pressure wave velocities in consolidated Karoo sedimentary rocks were estimated by assuming averaged values for the physical parameters of these rocks. The fast pressure wave velocities in the sandstone, siltstone and mudstone were all found to be approximately 3 000 m s^{-1}. To allow for uncertainty in the seismic velocities of the consolidated sedimentary rocks, four values for the average seismic velocity of the layers at depths greater than 10 m were assumed, namely 2 000, 2 500, 3 000 and 3 500 m s^{-1}. These velocities are in agreement with known pressure wave velocities in sandstones and shales (Telford *et al.*, 1990). The depth sections for the four velocity models are shown in Figure 6.4.13 to Figure 6.4.16.

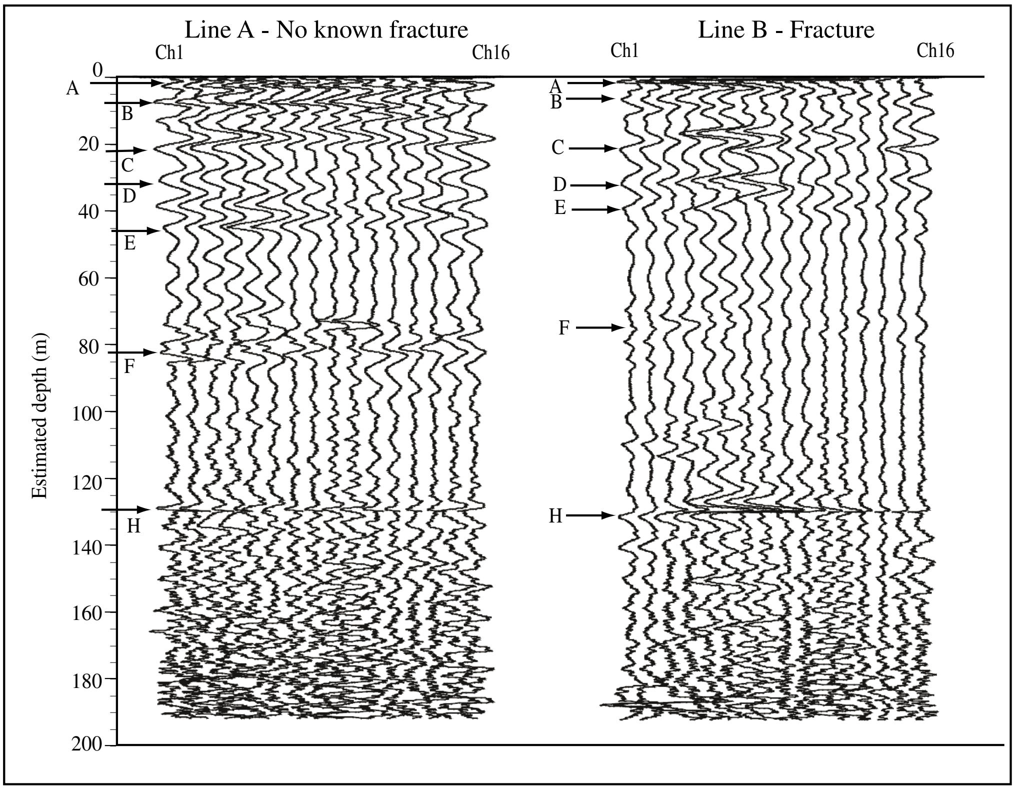

Figure 6.4.13. Depth section derived from the data recorded on the Campus Test Site. (Velocity model: 0-2 m ⇒ 800 m s^{-1}, 2-10 m ⇒ 1 500 m s^{-1}, >10 m ⇒ 2 000 m s^{-1})

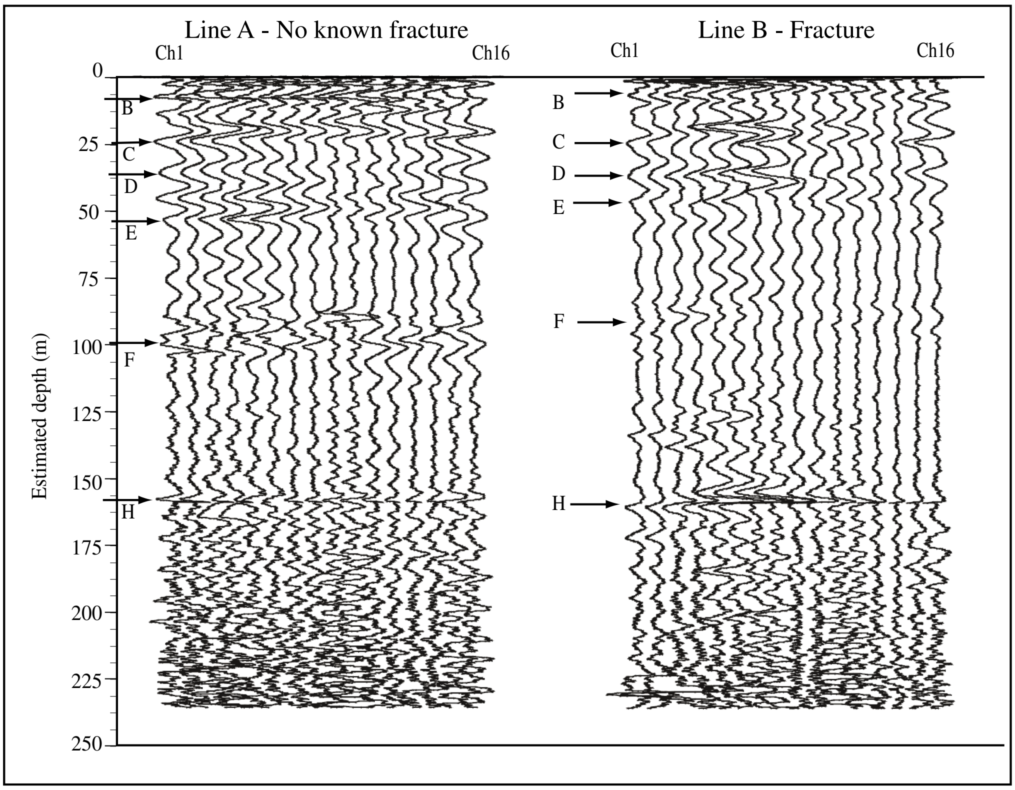

Figure 6.4.14. Depth section derived from the data recorded on the Campus Test Site. (Velocity model: 0-2 m ⇒ 800 m s^{-1}, 2-10 m ⇒ 1 500 m s^{-1}, >10 m ⇒ 2 500 m s^{-1})

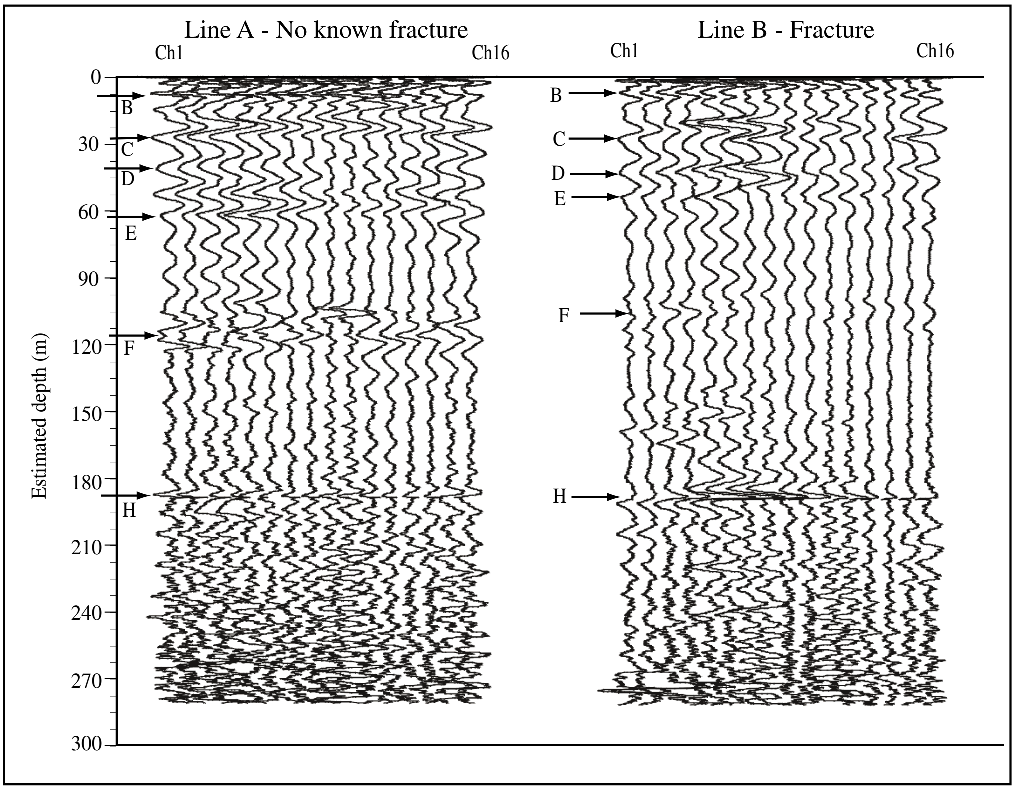

Figure 6.4.15. Depth section derived from the data recorded on the Campus Test Site. (Velocity model: 0-2 m ⇒ 800 m s^{-1}, 2-10 m ⇒ 1 500 m s^{-1}, >10 m ⇒ 3 000 m s^{-1})

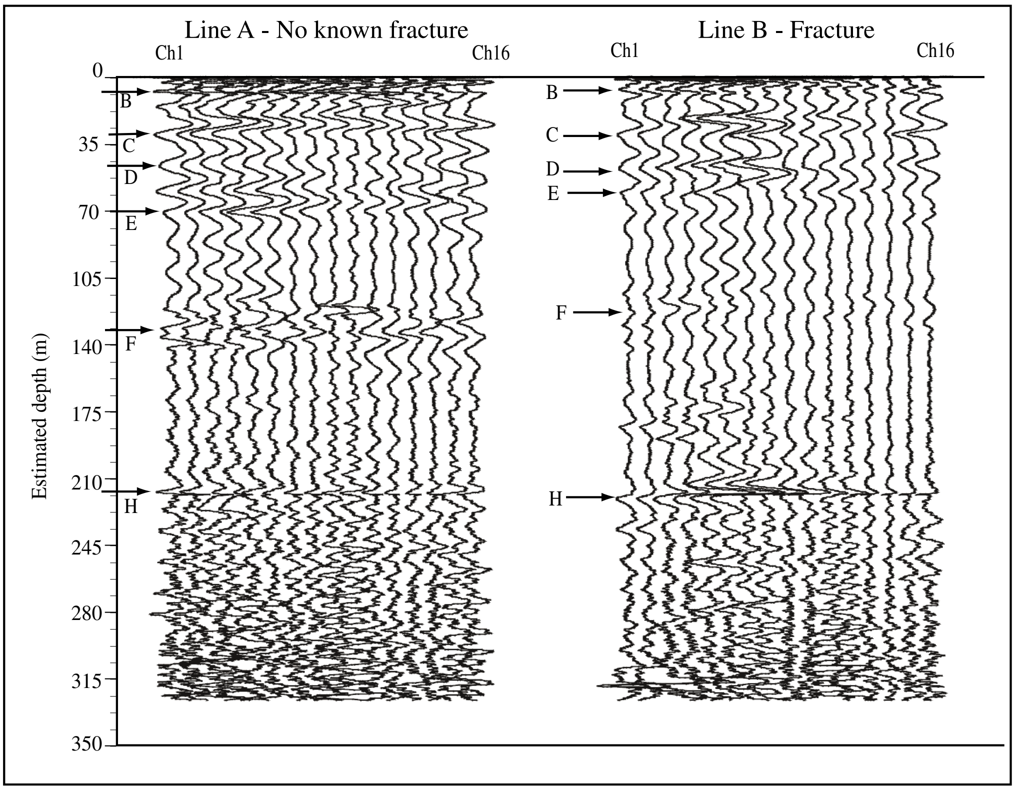

Figure 6.4.16. Depth section derived from the data recorded on the Campus Test Site. (Velocity model: 0-2 m ⇒ 800 m s^{-1}, 2-10 m ⇒ 1 500 m s^{-1}, >10 m ⇒ 3 500 m s^{-1})

The estimated depth sections shown in Figure 6.4.13 to Figure 6.4.16 emphasise the need for reliable estimates of the seismic velocities of the various rock units if accurate estimates of the depths of the interfaces responsible for signal generation are to be found. In these figures the estimated depth of the interface responsible for energy arrival F ranges from 80 to 131 m, while energy arrival H corresponds to an interface depth of between 130 and 217 m. This observation suggests that, for the purpose of velocity analyses, seismic data should also be recorded when performing ES surveys if reliable depth estimates are to be obtained.

6.5 Discussion

The results of the investigation into the vertical resolution of surface ES data (Chapter 3) indicated that the resolution is inadequate to detect the horizontal bedding-plane fracture present on at the Campus Test Site. To test this result, a field survey was performed and the data recorded above a known fracture was compared to the data recorded at a position laterally displaced from the known fracture occurrence. Since no additional energy arrivals could be identified in the data from the fracture location, it seems reasonable to conclude that the fracture is not detectable by surface ES methods and that the results of Chapter 3 are confirmed.

There are, however, three important aspects of the survey and the recorded data that need to be taken into account. Firstly, the data recorded above the fracture have a much higher noise component due to the proximity of cased boreholes. This noise component may have resulted in the masking of an energy arrival from the fracture.

Secondly, the fracture occurs at a shallow depth compared to the seismic wavelength and within 5 m from other interfaces at which ES signal generation may occur. Significant temporal overlap of signals generated at the various interfaces is therefore expected, and the identification of any energy arrival from the fracture is thereby made more difficult.

Thirdly, although the boreholes intersecting the well developed fracture seem to occur in a specific zone on the Campus Test Site, the fractal geometry of the fracture implies that localised occurrences of the fracture may be present beyond the zone outlined in Figure 6.2.5. Results of core-drilling have also indicated that the areal extent of the fracture may be larger than was initially thought, even though the fracture may be very poorly developed in areas removed from the zone where the well-developed fracture is known to occur. Therefore, although source position A was used during the survey on the Campus Test Site as a position laterally removed from the known fracture occurrence, it is quite possible that fracturing may be present at this position, albeit poorly developed. Comparison of the data recorded along line B with the data recorded along line A does therefore not constitute a definite comparison of data recorded above a fracture with data recorded at a position where fracturing is absent.

These three aspects of the field survey on the Campus Test Site need to be taken into consideration when comparing the theoretical results of Chapter 3 with the results of the field survey presented in this chapter. It can therefore be concluded that the field data only suggest, but do not conclusively proof, that the fracture cannot be detected by surface ES methods. Further investigations that could involve the drilling of boreholes at locations removed from known fractures may be required to obtain more certainty about the possibility of using surface ES techniques for the detection of fractures.

CHAPTER 7 CONCLUSIONS

The main objectives of this study were two-fold: to investigate the possibility of using surface ES methods for groundwater exploration in Karoo rocks, and to investigate the possibility of obtaining information on the aquifer elastic parameters by the analyses of ES data.

Groundwater exploration

The investigation focussed on two aspects of groundwater exploration in Karoo rocks, namely, the possibility of detecting fractures with limited lateral extent and small apertures by means of surface ES methods, and the possibility of mapping contrasts in the porosity/permeability of saturated Karoo rocks.

Since fractures play an integral role in the determination of borehole yield in Karoo rocks, the possibility of detecting such fractures was investigated by examining the lateral and vertical resolution criteria of surface ES data and the ES thin bed response. As in seismics, the Fresnel zone concept was used to investigate the lateral resolution of surface ES data. The following results were obtained:

- Geometric considerations showed that the ES Fresnel zones are larger than their seismic equivalents and the lateral resolution of surface ES data is consequently poorer than that of surface seismic data. For deep interfaces at depths much larger than the seismic wavelength, the ES Fresnel zones are twice as large in surface area than the seismic Fresnel zones, and the lateral resolution is twice as poor.
- When the source and receiver locations are separated, the seismic Fresnel zones are elliptical in shape, but the ES Fresnel zones are, to a very good approximation, circular and centred below the seismic source.
- Seismic velocity increases with depth result in increases in the radii of the ES Fresnel zones and result in poorer lateral resolution.
- For broadband excitation, only a single ES Fresnel zone is, in general, observed. This observation is in agreement with similar observations in seismics.
- As in seismics, the lateral resolution of surface ES data is predominantly determined by the dominant frequency of the source, but bandwidth also influences the resolution. Higher dominant frequencies and broader bandwidth lead to better lateral resolution.

- The surface electric potential vertically above a zone where no ES energy conversion occurs may be larger than the potential vertically above a zone where energy conversion does take place. The implication for groundwater exploration in fractured Karoo rock is that the lateral resolution of surface ES data may be insufficient to resolve the presence of large unfractured areas within fractured zones, and possibly result in the siting of low-yielding boreholes in the vicinity of an existing fracture.

Vertical resolution of surface ES data was studied by considering the resolution criteria commonly used in seismics and adapting these criteria to be applicable to ES surveys. The following observations were made:

- Rayleigh's criterion for vertical resolution applied to of surface ES data requires that the imbedded layer should have a thickness of at least $\lambda/2$ to be deemed resolvable. This thickness is twice as large as the equivalent criterion in seismics where a bed with a thickness of $\lambda/4$ is considered resolvable.

- There are, however, two wavelengths to take into account when considering vertical resolution: the wavelengths of the Biot slow and fast waves. Since the Biot slow wave may have a wavelength that is a couple of orders of magnitude smaller than the Biot fast wave, the theoretical limits of resolution are determined by the slow wave wavelength. The slow wave is, however, strongly dissipative and quickly decays, so that the practical limits of resolution seem to depend more strongly on the wavelength of the fast pressure wave. This observation suggests that the vertical resolution of surface ES data is indeed twice as poor as that of surface seismic data.

The thin bed response of surface ES data was studied by means of a simplified approach which separately considered the interface response due to excitement by Biot fast and slow waves, and by a full waveform approach that took all converted wave modes into account and considered the combined influence of all wave types. The following observations were made:

- The simplified approach showed that for monochromatic excitation the fast pressure wave results in maximum surface response, equal to twice the response from a single interface, when the imbedded thin layer has a thickness of $\lambda/2$, where λ is the wavelength of the fast pressure wave. Similar observations in seismics show that the maximum surface response occurs when the imbedded thin layer has a thickness of $\lambda/4$. In seismics beds with thicknesses less than $\lambda/4$ are labelled "thin beds". This observation suggests that, in ES, a bed may be defined as thin if it has a thickness of less than $\lambda/2$.

- Although the slow pressure wave exhibits maxima at much smaller bed thicknesses for both monochromatic and broadband excitation, the response at surface is less than 25% stronger than the response from a single interface. This observation again suggests that the fast pressure wave may have a stronger influence on the detectability limits of an imbedded thin layer.
- The full waveform approach which included the combined influence of the fast and slow pressure waves showed that maximum ES signal at surface does indeed occur at a bed thickness of $\lambda/2$, where λ is the wavelength of the fast pressure wave. It therefore seems that the fast pressure wave plays the dominant role in the determination of both the resolution and detection criteria.

The investigation into the lateral and vertical resolution of surface ES data therefore indicates that surface ES methods are unlikely to detect fractures with apertures much smaller than the wavelength of the fast pressure wave. Even if a surface-detectable signal is generated at such fractures, the lateral resolution of the data is likely to be insufficient to resolve the localised occurrence of the fractures. Groundwater exploration by means of the detection at surface of single fractures therefore seem highly unlikely. Fractures zones, may however, have thicknesses that are adequately large to allow detection.

In an attempt to confirm the results of the investigation into the resolution criteria and the thin bed response, a surface ES survey was conducted on the Campus Test Site at the University of the Free State. ES measurements were taken at two positions: one vertically above a known fracture, and one laterally removed from the fracture. Any energy arrivals at surface that were detectable in the data from the position above the fracture, but absent in the data from the other position, could have indicated that the fracture does indeed give rise to surface-detectable signal. However, no such energy arrivals were observed. It therefore seems that the response from the fracture is insufficient to allow detection at surface. It should, however, be noted that, due to the presence of cased boreholes in the vicinity of the fracture and the shallow depth of the fracture compared to the seismic wavelength, the results of the field survey cannot be seen as conclusive proof that the fracture does not generate a surface-detectable signal.

The influence of porosity contrasts on ES reflection was studied by examining the change in the magnitude of the reflection coefficients when varying the porosity (and all porosity-dependent parameters, such as permeability) of a Karoo sandstone overlain by a Karoo mudstone. Increases in the sandstone porosity resulted in larger reflection coefficients, and consequently, stronger reflection. The possibility therefore exists to map porosity contrasts in a certain geological environment and thus identify zones more likely to be suitable as aquifers. Since only contrasts may be mapped, it should be remembered that changes in the properties of either of the two media in contact may result in changes in the reflection amplitude. Additional geological and/or geohydrological information may be required in the interpretation of the contrast maps.

Information on aquifer elastic parameters and aquifer deformation

Since ES energy conversion in fluid-saturated porous rocks depends on the properties of both the fluid and the solid matrix, ES techniques could potentially provide a non-invasive means of obtaining information on the elastic properties of the rock matrix and, consequently, on the deformability of fractures in the rock. This possibility was investigated by examining the electroseismic and magnetoseismic transfer functions at positions in boreholes. The investigation indicated that:

- The transfer functions are dependent on various physical and chemical parameters, including the elastic properties of the solid porous matrix. None of these parameters can therefore be determined unambiguously from the evaluation of the different transfer functions. Consequently, the aquifer elastic parameters cannot be obtained without prior knowledge of other parameters such as the porosity, mass density and tortuosity of the solid medium, the dielectric permittivity, mass density, electrical conductivity and viscosity of the fluid, and the zeta potential. Some of the parameters, such as the electrical conductivity, density, viscosity and dielectric permittivity of the fluid, can be determined by either *in situ* or laboratory measurements. Other parameters, such as the porosity and tortuosity, may be estimated through hydraulic investigations, for example by means of tracer tests. There are, however, as yet no methods for the routine determination of zeta potential. The measurement of this parameter would, at present, require the removal of a specimen of the porous material to be analysed in a laboratory.
- The shear modulus of the porous frame may be estimated from measurements of the shear wave velocity in a fluid-saturated porous system. Since an approximate linear relation exists between the shear and bulk moduli of the porous frame, the bulk modulus may be estimated once the shear modulus is known.
- It is demonstrated that the possibility exists that porosity changes due to aquifer deformation may lead to changes in the transfer functions. As such, determination of the transfer functions could serve as a means of measuring aquifer deformation. The porosity dependencies of the various transfer functions were obtained by assuming relations for the porosity-dependent parameters contained in the transfer functions. Both the expression for the transfer function of the fast pressure wave and the expression for the transfer function of the slow pressure wave are shown to give poor representations of the reality for porosities that approach zero. These equations

should therefore only be seen as indications of the degree to which the transfer functions are porosity-dependent.

- The electroseismic transfer function of the fast pressure wave is shown to be insensitive to porosity changes in consolidated material. The electroseismic transfer function of the slow pressure wave, on the other hand, is shown to be very sensitive to porosity changes. However, due to the dissipative nature of the slow waves, they exist only near interfaces. At such positions the slow and fast waves co-exist, but due to the small amplitudes of the solid displacement in the slow pressure waves, the total displacement of the solid is dominated by the displacement of the fast pressure wave. Separation of the slow wave from the fast wave is therefore likely to proof very difficult.
- The magnetoseismic transfer function is shown to be sensitive to porosity changes. It correctly predicts zero ES energy conversion for porosities of zero and unity. The magnetoseismic transfer function is associated with solid displacement due to a shear wave that can easily be distinguished and separated from both the slow and fast pressure waves, as well as from the Stoneley wave.
- The magnetoseismic transfer function associated with the shear wave is likely to yield the most useful information on aquifer deformation.

Recommendations for future work

In future research on electroseismics, the following approaches could be considered:

- In examining the lateral resolution of surface ES data by means of the Fresnel zone concept (Section 3.1), it was assumed that all positions on the interface may contribute (constructively or destructively) to the total signal recorded at the measurement position. This is indeed the case when employing grounded electrode pairs as antennæ, as is usually done in ES surveys. It may, however, be possible to use directional antennæ focussing on positions vertically below the seismic source, thus improving the lateral resolution capabilities of ES techniques. There will, however, be a trade-off between enhanced lateral resolution and reduced signal strength if only a portion of the (first) Fresnel zone is allowed to contribute to the recorded signal.
- Attention should be paid to the possibility of using magnetometers or induction loops instead of grounded electrode pairs as receivers. This would offer the advantage of less cumbersome and time-consuming acquisition of data. It should,

however, be kept in mind that the EM waves in ES surveys have frequencies in the seismic frequency range. These low frequencies may require the development of specialised recording instruments.

- The possibility exists that the use of surface ES techniques over aquifers being subjected to pumping may yield enhanced signal generation in the subsurface due to larger flow across interfaces being induced. The possibility that other benefits may result from the simultaneous use of ES techniques and pumping tests should also be investigated.
- In Section 6.4.2 it was shown that velocity analyses on ES time sections may be much more difficult to perform than velocity analyses on seismic time sections, especially under conditions of dry surface layers that effectively eliminate the co-seismic electric fields from the recorded data. This observation suggests that the seismic response should also be recorded when performing ES surveys if the recorded ES time section is to be converted into a realistic depth section. Comparison of seismic and ES depth sections may also indicate which energy arrivals in the ES data are due to mechanical contrasts and which may be due to contrasts in the fluid properties. Other advantages of the simultaneous analyses of ES and seismic data could include the identification and removal of multiples in the two data sets.

References

Aki, K. and Richards, P. G. (1980) *Quantitative Seismology, Theory and Methods, vol. 1*. W.H. Freeman and Company, New York.

Arfken, G. (1970). *Mathematical methods for physicists (2 ed).* Academic Press. New York.

Beamish, D. and Peart, R. J. (1998) Electrokinetic geophysics - a review. *Terra Nova.* **10**, 48-55.

Beamish, D. (1999) Characteristics of near-surface electrokinetic coupling. *Geophysical Journal International.* **137**, 231-242.

Bear, J. (1988) *Dynamics of Fluids in Porous Media.* American Elsevier Publishing Company, New York.

Berryman, J. G. (1980) Confirmation of Biot's theory. *Applied Physics Letters.* **37**, 382-384.

Beukes, G. N. (1969) *Die Sedimentologie van die Etage Holkranssandsteen, Sisteem Karoo.* Unpublished M.Sc. Thesis. Departement of Geology, University of the Free State. Bloemfontein.

Biot, M. A. (1956a) Theory of propagation of elastic waves in a fluid-saturated porous solid. I. Low frequency range. *Journal of the Acoustical Society of America.* **28** (2), 168–178.

Biot, M. A. (1956b) Theory of propagation of elastic waves in a fluid-saturated porous solid. II. Higher frequency range. *Journal of the Acoustical Society of America.* **28** (2), 179-191.

Biot, M. A. (1962a) Generalized theory of acoustic propagation in porous dissipative media. *Journal of the Acoustical Society of America.* **34** (9), 1254-1264.

Biot, M. A. (1962b) Mechanics of deformation and acoustic propagation in porous media. *Journal of Applied Physics.* **33** (4), 1482-1498.

Blau, L. W. and Statham, L. (1936) Method and apparatus for seismic-electric prospecting. *U.S Patent 2054067.*

Botha, J. F., Verwey, J. P., Van der Voort, I., Vivier, J. J. P., Colliston, W. P. and Loock, J. C. (1998) *Karoo Aquifers. Their Geology, Geometry and Physical Behaviour*. Report to the Water Research Commission, P.O. Box 824, Pretoria 0001. WRC 487/1/98.

Botha, J. F., Cloot, A. (2002) *Karoo Aquifers. Deformation, Hydraulic and Mechanical Properties*. Report to the Water Research Commission, P.O. Box 824, Pretoria 0001. In press.

Brink, A. B. A. (1983) *Engineering Geology of Southern Africa.* Vol. 3: The Karoo Sequence. Building Publications.

Brühl, M., Vermeer, G. J. O. and Kiehn, M. (1996) Fresnel zones for broadband data. *Geophysics.* **61** (2), 600-604.

Butler, K. E., Russell, R. D. and Kepic, A. W. (1996) Measurement of the seismoelectric response from a shallow boundary. *Geophysics.* **61** (5), 1769-1778.

D'Arnaud Gerkens, J. C. (1989) *Foundation of exploration geophysics*. Methods in Geophysics and Geochemistry. Vol. 25. Elsevier, Amsterdam.

de Voogd, N. and den Rooijen, H. (1983) Thin-layer response and spectral bandwidth. *Geophysics*. **48** (1), 12-18.

Dutta, N. C. and Odé, H. (1979) Attenuation and dispersion of compressional waves in fluid-filled porous rocks with partial gas saturation (White Model) - Part I: Biot theory. *Geophysics.* **44**, 1777-1788.

Fitterman, D. V. (1978) Electrokinetic and magnetic anomalies associated with dilatant regions in a layered earth. *Journal of Geophysical Research.* **83** (B12), 5923–5928.

Fourie, F. D. (2000) *An Introduction to Geophysics for Geohydrologists*. Unpublished lecture notes. Institute for Groundwater Studies, University of the Orange Free State, P.O. Box 339, Bloemfontein 9300.

Frenkel, J. (1944) On the theory of seismic and seismoelectric phenomena in moist soil. *Journal of Physics (Soviet).* 230-241.

Garambois, S. and Dietrich, M. (2001) Seismo-electric wave conversion in porous media: Field measurements and transfer function analysis. *Geophysics.* **66** (5), 1414-1430.

Gassmann, F. (1951) Uber die elastizitat poroser medien. *Viertaljahrschr. Naturforsch. Ges.* **96**, 1-23.

Geertsema, A. J. (2000) *The Engineering Characteristics of Important Southern African Rock Types With Emphasis on Shear Strength of Concrete Dam Foundations*. Water Research Commission Report Number 433/1/00.

Geertsma, J. and Smit, D. C. (1961) Some aspects of elastic wave propagation in fluid-saturated porous solids. *Geophysics.* **26** (2), 168-181.

Glover, W. J., Hole, M. J. and Pous, J. (2000) A modified Archie's law for two conducting phases. *Earth and Planetary Science Letters.* **180**, 369-383.

Haartsen, M. W. (1995) *Coupled electromagnetic and acoustic wavefield modeling in poro-elastic media and its application in geophysical exploration*. Unpublished Ph.D. Thesis. Massachusetts Institute of Technology, Cambridge.

Haartsen, M. W. and Pride, S. R. (1997) Electroseismic waves from point sources in layered media. *Journal of Geophysical Research.* **102** (B11), 24745-24769.

Haartsen, M. W., Dong, W. and Toksöz, M. N. (1998) Dynamic streaming currents from seismic point sources in homogeneous poroelastic media. *Geophysical Journal International.* **132**, 256-274.

Haines, S., Pride, S. and Klemperer, S. (2001) Development of Experimental Methods in Electroseismic Research. *Transactions of the American Geophysical Union.* **82** (47).

Hashin, Z. and Shtrikman, S. (1963) A variational approach to the theory of the elastic behaviour of multiphase materials. *J. Mech. Phys. Solids.* **11**, 127-140.

Hecht, E. and Zajac, A. (1974) *Optics*. Addison-Wesley.

Hunt, C. W. and Worthington, M. H. (2000) Borehole electrokinetic response in fracture dominated hydraulically conductive zones. *Geophysical Research Letters.* **27** (9), 1315-1318.

Ishido, T. (1981) Experimental and theoretical basis of electrokinetic phenomena in rock-water systems and its application to Geophysics. *Journal of Geophysical Research.* **86** (B3), 1763–1775.

Ivanov, A. (1939) Effect of electrization of earth layers by elastic waves passing through them. *Comptes Rendus (Doklady) de l'Academie des Sciences de L'URSS.* **24**, 42-45.

Johnson, D. L., Koplik, J. and Dashen R. (1987) Theory of dynamic permeability and tortuosity in fluid-saturated porous media. *Journal of Fluid Mechanics*. **176**, 379-402.

Kallweit, R. S. and Wood, L. C. (1982) The limits of resolution of zero-phase wavelets. *Geophysics.* **47** (7), 1035-1046.

Kepic, A. W., Maxwell, M. and Russell, R. D. (1995) Field trials of a seismoelectric method for detecting massive sulphides. *Geophysics.* **60** (2), 365-373.

Knapp, R. W. (1990) Vertical resolution of thick beds, thin beds, and thin-bed cyclothems. *Geophysics.* **55** (9), 1183-1190.

Koefoed, O. and de Voogd, N. (1980) The linear properties of thin layers, with an application to synthetic seismograms over coal seams. *Geophysics*. **45** (8), 1254-1268.

Koponen, A., Kataja, M. and Timonen, J. (1997) Permeability and effective porosity of porous media. *Physical Review E*. **56** (3), 3319-3325.

Lang, S. (1993) *A first course in calculus (5 ed)*. Springer-Verlang. New York.

Long, L. T. and Rivers, W. K. (1975) Field measurement of the electroseismic response. *Geophysics*. **40** (2), 233-245.

Makurat, A. (2001) Normal and shear stress dependent single phase fracture and fracture cross flow in different lithologies. In: Proceedings of the *Fractured Rock 2001*. Ontario, Canada.

Martner, S. T. and Sparks, N. R. (1959) The electroseismic effect. *Geophysics*. **24** (2), 297-308.

Maxwell, M., Russell, R. D., Kepic, A. W. and Butler, K. E. (1992) Electromagnetic responses from seismically excited targets B: Non-piezoelectric phenomena. *Exploration geophysics*. **23**, 201-208.

Mikhailov, O. V., Haartsen, M. W. and Toksöz, M. N. (1997) Electroseismic investigation of the shallow subsurface: Field measurements and numerical modelling. *Geophysics*. **62** (1), 97-105.

Mikhailov, O. V., Queen, J. and Toksöz, M. N. (2000) Using borehole electroseismic measurements to detect and characterize fractured (permeable) zones. *Geophysics*. **65** (4), 1098-1112.

Millar, J. W. A. and Clarke, R. H. (1997) *Electrokinetic techniques for hydrogeological site investigations*. Groundflow Ltd, Marlborough.

Neev, J. and Yeatts, F. R. (1989) Electrokinetic effects in fluid-saturated poro-elastic media. *Physical Review B*. **40**.

Nolen-Hoeksema, R. C. (2000) Modulus-porosity relations, Gassmann's equations, and the low-frequency response to fluids. *Geophysics*. **65** (5), 1355-1363.

Nourbehecht, B. (1963) *Irreversible thermodynamic effects in inhomogeneous media and their applications in certain geoelectric problems*. Unpublished Ph.D. Thesis. Massachusetts Institute of Technology, Boston.

Nur, A., Mavko, G., Dvorkin, J. and Galmudi, D. (1998) Critical porosity: A key to relating physical properties to porosity in rocks. *The Leading Edge*. **17**.

Olivier, J. H. (1976) *Some engineering-geological aspects of tunnel construction in Karoo strata with special reference to the Oranje-Fish tunnel.* Unpublished Ph.D. thesis. University of the Free State. Bloemfontein.

Patra, H. P. and Mallick, K. (1980) *Geosounding principles, 2. Time-varying Geoelectric Sounding*. Methods in Geochemistry and Geophysics. Vol. 14B. Elsevier, Amsterdam.

Pride, S. R. (1994) Governing equations for the coupled electromagnetics and acoustics of porous media. *Physical Review B.* **50**, 15678–15696.

Pride, S. R. and Haartsen, M. W. (1996) Electroseismic wave properties. *Journal of the Acoustical Society of America.* **100** (3), 1301–1315.

Pride, S. R. and Morgan, F. D. (1991) Electrokinetic dissipation induced by seismic waves. *Geophysics.* **56** (7), 914–925.

Pride, S. R., Tromeur, E. and Berryman, J.G. (2002) Biot slow-wave effects in stratified rocks. *Geophysics.* **67** (1), 271–281.

Ranada Shaw, A., Denneman, A. I. M. and Wapenaar, C. P. A. (2000) Porosity and permeability effects on seismo-electric reflection. In: Proceedings of the *EAGE conference.* Paris, France.

Reuss, A. (1929) Berechnung der Fliessgrense von Mischkristallen auf Grund der Plastizitätbedingung für Einkristalle. *Zeitschrift für Angewandte Mathematik aus Mechanik.* **9**, 49-58.

Riemann, K. and van Tonder, G. J. (2001) The fractional flow dimension of fractured aquifers, obtained from and used with single-well and multiple-well tracer tests. In: Proceedings of the *IAH Conference 2001 - New approaches characterizing groundwater flow.* K.-P. Seiler and S. Wohnlich (eds.) Munich, Germany.

Rowsell, D. M. and De Swardt, A. M. J. (1976) Diagenesis in Cape and Karroo Sediments, South Africa, and its Bearing on their Hydrocarbon Potential. *Transactions of the Geological Society of South Africa.* **79** (1), 81-145.

Russell, R. D., Butler, K. E., Kepic, A. W. and Maxwell, M. (1997) Seismoelectric exploration. *The Leading Edge.* **16**, 1611-1615.

Sengbush, R. L. (1983) *Seismic exploration methods.* International Human Resource Development Corporation, Boston, MA.

Shaw, D. J. (1969) *Electrophoresis*. Academic Press, London.

Sheriff, R. E. (1999) *Encyclopedic Dictionary of Exploration Geophysics.* (3 ed.) The Society of Exploration Geophysicists, Tulsa, Oklahoma.

Telford, W. M., Geldart, L. P. and Sheriff, R. E. (1990) *Applied Geophysics*. Cambridge University Press, Cambridge.

Thompson, A. H. and Gist, G. A. (1993) Geophysical application of electrokinetic conversion. *The Leading Edge.* **12**, 1169-1173.

Thompson, R. R. (1936) The seismic electric effect. *Geophysics.* **1**, 327-335.

Thompson, R. R. (1939) A note on the seismic electric effect. *Geophysics.* **4**, 102-105.

Tuman, V. S. (1963) Streaming potentials at very high differential pressures. *Journal of Applied Physics.* **34** (7), 2014–2019.

Van der Voort, I., and van Tonder, G. J. (2000) *Analysing the geometry of South African fractured rock aquifers.* In: Proceedings of the *XXXth IAH Congress on Groundwater: Past Achievements and Future Challenges*, O. Solilo (eds.). Cape Town, South Africa. 349-353.

Van der Voort, I. (2001) *Risk Based Decision Tool for Managing and Protecting Groundwater Resources.* Unpublished Ph.D. thesis. University of the Free State. Bloemfontein.

Van Wyk, B., De Lange, F., Xu, Y., van Tonder, G. J. and Chiang, W.-H. (2001) *Utilization of tracer experiments for the development of rural water supply strategies for secondary aquifers*. Report to the Water Research Commission, P.O. Box 824, Pretoria 0001. WRC 733/1/01.

Voigt, W. (1928) *Lehrbuch der Kristallphysik.* B. G Teubner.

Wood, A. B. (1930) *A textbook of sound.* Macmillan Publishing Cooperation.

Appendix A - Vector and tensor operations in right-handed Cartesian co-ordinates

When employing a right-handed Cartesian co-ordinate system, a number of vector and tensor operations may be defined. These operations include taking the gradient of an n^{th} order tensor field to yield a $(n + 1)^{\text{th}}$ order tensor field and taking the divergence of an n^{th} order tensor field to yield a $(n - 1)^{\text{th}}$ order tensor field. These operations and others are presented in this appendix.

A1. The ∇ (nabla, del) operator in Cartesian co-ordinates

The ∇ operator is a vector operator that is defined in general orthogonal curvilinear co-ordinates as

$$\nabla \equiv \frac{\mathbf{e}_1}{h_1}\frac{\partial}{\partial s_1} + \frac{\mathbf{e}_2}{h_2}\frac{\partial}{\partial s_2} + \frac{\mathbf{e}_3}{h_3}\frac{\partial}{\partial s_3} \qquad \text{(A1.1)}$$

(Arfken, 1970), where s_1, s_2 and s_3 are the curvilinear co-ordinates and $\mathbf{e}_1$, $\mathbf{e}_2$ and $\mathbf{e}_3$ are unit vectors indicating the directions of increasing s_1, s_2 and s_3, respectively, and h_1, h_2 and h_3 are called scale factors. In Cartesian co-ordinates the scale factors are all equal to unity so that

$$\textit{Cartesian}: \qquad \nabla = \mathbf{i}\frac{\partial}{\partial x_1} + \mathbf{j}\frac{\partial}{\partial x_2} + \mathbf{k}\frac{\partial}{\partial x_3} \qquad \text{(A1.2)}$$

where x_1, x_2 and x_3 are the Cartesian co-ordinates, and **i**, **j** and **k** are unit vectors indicating the directions of increasing x_1, x_2 and x_3. With the above definition of the ∇ operator, the *gradient* of a scalar field, the *divergence* of a vector field and the *curl* of a vector field can be written by making use of the fact that in Cartesian co-ordinates the ∇ operator possesses properties analogous to those of ordinary vectors. Multiplication by a scalar quantity, taking the inner (dot) product with a vector and taking the cross product with a vector respectively yield

$$\nabla\psi = \mathbf{i}\frac{\partial\psi}{\partial x_1} + \mathbf{j}\frac{\partial\psi}{\partial x_2} + \mathbf{k}\frac{\partial\psi}{\partial x_3} \qquad \text{(A1.3)}$$

$$\nabla \bullet \mathbf{u} = \frac{\partial u_1}{\partial x_1} + \frac{\partial u_2}{\partial x_2} + \frac{\partial u_3}{\partial x_3} \qquad \text{(A1.4)}$$

$$\nabla \times \mathbf{u} = \mathbf{i}\left(\frac{\partial u_3}{\partial x_2} - \frac{\partial u_2}{\partial x_3}\right) + \mathbf{j}\left(\frac{\partial u_1}{\partial x_3} - \frac{\partial u_3}{\partial x_1}\right) + \mathbf{k}\left(\frac{\partial u_2}{\partial x_1} - \frac{\partial u_1}{\partial x_2}\right) \tag{A1.5}$$

where ψ is a scalar field and $\mathbf{u}$ is a vector field given by

$$\mathbf{u} = \mathbf{i}u_1 + \mathbf{j}u_2 + \mathbf{k}u_3$$

It should be stressed that Equations (A1.3), (A1.4) and (A1.5) are generally valid in Cartesian co-ordinates only. For other coordinate systems the operations described above are still possible, but their expressions are much more complicated and beyond the scope of this appendix.

A2. The gradient of a vector field

In Cartesian co-ordinates the gradient of a vector field may be defined by taking the outer (direct) product of the ∇ operator with the vector field. In dyadic notation we get

$$\begin{aligned} \nabla \mathbf{u} &= \left(\mathbf{i}\frac{\partial}{\partial x_1} + \mathbf{j}\frac{\partial}{\partial x_2} + \mathbf{k}\frac{\partial}{\partial x_3}\right)(\mathbf{i}u_1 + \mathbf{j}u_2 + \mathbf{k}u_3) \\ &= \frac{\partial u_1}{\partial x_1}\mathbf{ii} + \frac{\partial u_2}{\partial x_1}\mathbf{ij} + \frac{\partial u_3}{\partial x_1}\mathbf{ik} \\ &\quad + \frac{\partial u_1}{\partial x_2}\mathbf{ji} + \frac{\partial u_2}{\partial x_2}\mathbf{jj} + \frac{\partial u_3}{\partial x_2}\mathbf{jk} \\ &\quad + \frac{\partial u_1}{\partial x_3}\mathbf{ki} + \frac{\partial u_2}{\partial x_3}\mathbf{kj} + \frac{\partial u_3}{\partial x_3}\mathbf{kk} \end{aligned} \tag{A2.1}$$

An array of the nine components in Equation (A2.1) describes the 2nd order tensor giving the gradient of the vector field $\mathbf{u}$

$$\nabla \mathbf{u} = \begin{bmatrix} \frac{\partial u_1}{\partial x_1} & \frac{\partial u_2}{\partial x_1} & \frac{\partial u_3}{\partial x_1} \\ \frac{\partial u_1}{\partial x_2} & \frac{\partial u_2}{\partial x_2} & \frac{\partial u_3}{\partial x_2} \\ \frac{\partial u_1}{\partial x_3} & \frac{\partial u_2}{\partial x_3} & \frac{\partial u_3}{\partial x_3} \end{bmatrix} \tag{A2.2}$$

The components in each column of the above tensor are seen to be equal to the gradient of each component of the vector field $\mathbf{u}$, so that Equation (A2.2) may be written as

$$\nabla \mathbf{u} = \begin{bmatrix} | & | & | \\ \nabla u_1 & \nabla u_2 & \nabla u_3 \\ | & | & | \end{bmatrix} \tag{A2.3}$$

In index notation the gradient of a vector **u** is given by

$$\nabla \mathbf{u} = \frac{\partial u_j}{\partial x_i} = u_{j,i} \tag{A2.4}$$

In general, the gradient of an n^{th} order tensor may be defined in Cartesian co-ordinates as the outer product of the ∇ operator with the tensor, yielding a tensor of order $n+1$.

A3. The divergence of a tensor field

In Cartesian co-ordinates the divergence of a tensor field may be defined by using the dyadic notation. If τ is a tensor field the divergence of τ may be found by again using the fact that in Cartesian co-ordinates the ∇ operator possesses properties analogous to those of ordinary vectors. Taking the inner (dot) product of ∇ with τ yields

$$\begin{aligned}
\nabla \bullet \tau &= \left(\mathbf{i}\frac{\partial}{\partial x_1} + \mathbf{j}\frac{\partial}{\partial x_2} + \mathbf{k}\frac{\partial}{\partial x_3} \right) \bullet \begin{Bmatrix} \tau_{11}\mathbf{ii} + \tau_{12}\mathbf{ij} + \tau_{13}\mathbf{ik} + \\ \tau_{21}\mathbf{ji} + \tau_{22}\mathbf{jj} + \tau_{23}\mathbf{jk} + \\ \tau_{31}\mathbf{ki} + \tau_{32}\mathbf{kj} + \tau_{33}\mathbf{kk} \end{Bmatrix} \\
&= \mathbf{i}\left(\frac{\partial \tau_{11}}{\partial x_1} + \frac{\partial \tau_{21}}{\partial x_2} + \frac{\partial \tau_{31}}{\partial x_3} \right) + \\
&\quad \mathbf{j}\left(\frac{\partial \tau_{12}}{\partial x_1} + \frac{\partial \tau_{22}}{\partial x_2} + \frac{\partial \tau_{32}}{\partial x_3} \right) + \\
&\quad \mathbf{k}\left(\frac{\partial \tau_{13}}{\partial x_1} + \frac{\partial \tau_{23}}{\partial x_2} + \frac{\partial \tau_{33}}{\partial x_3} \right)
\end{aligned} \tag{A3.1}$$

The divergence of the 2^{nd} order tensor yields a 1^{st} order tensor. Using index notation and Einstein's summation convention, the divergence is given by

$$\nabla \bullet \tau = \frac{\partial \tau_{ji}}{\partial x_j} = \tau_{ji,j} \tag{A3.2}$$

In general, the divergence of an n^{th} order tensor may be defined in Cartesian co-ordinates as the inner product of the ∇ operator with the tensor, yielding a tensor of order $n-1$.

A4. The vector "Laplacian"

The Laplacian of a scalar field is defined as the divergence of the gradient of the field. This is often written as

$$\nabla^2\psi = \nabla \bullet (\nabla\psi) \tag{A4.1}$$

where ∇^2 is known as the Laplace operator. In Cartesian co-ordinates the Laplace operator may be written in vector form as

$$\nabla^2 = \frac{\partial^2}{\partial x_1^2} + \frac{\partial^2}{\partial x_2^2} + \frac{\partial^2}{\partial x_3^2} \tag{A4.2}$$

In Cartesian co-ordinates a vector "Laplacian" may be formally defined as

$$\nabla^2\mathbf{u} = \nabla \bullet (\nabla\mathbf{u}) \tag{A4.3}$$

where use is made of the definitions of the gradient of a vector field and the divergence of a tensor field, as described in previous sections. A useful identity that is often used as the definition of the vector "Laplacian" is

$$\nabla^2\mathbf{u} = \nabla(\nabla \bullet \mathbf{u}) - \nabla \times \nabla \times \mathbf{u}$$

In Cartesian co-ordinates the vector "Laplacian" results in a 1st order tensor (a vector) of which the components are simply given by the application of the Laplace operator to each component of the vector field, that is

$$\nabla^2\mathbf{u} = \mathbf{i}\,\nabla^2 u_1 + \mathbf{j}\,\nabla^2 u_2 + \mathbf{k}\,\nabla^2 u_3 \tag{A4.4}$$

In index notation the "Laplacian" of a vector $\mathbf{u}$ is given by

$$\nabla^2\mathbf{u} = \frac{\partial^2 u_i}{\partial x_j \partial x_j} = u_{i,jj} \tag{A4.5}$$

A5. Vector and tensor identities in Cartesian co-ordinates

With the definitions of the gradient of a vector field and the divergence of a tensor field given in the preceding sections, a number of useful identities may be derived. The identities listed below are of interest in this work.

$$\nabla \bullet \nabla \mathbf{u} = \nabla^2 \mathbf{u} = \nabla(\nabla \bullet \mathbf{u}) - \nabla \times \nabla \times \mathbf{u} \tag{A5.1}$$

$$\nabla \bullet (\nabla \mathbf{u})^T = \nabla \bullet \left[(\nabla \bullet \mathbf{u})\mathbf{I}\right] = \nabla(\nabla \bullet \mathbf{u}) \tag{A5.2}$$

A6. Taylor-series expansion of vector quantities

The i^{th} component of the vector quantity **u**(**x**+**dx**) may be expanded in a Taylor series as follows (Lang, 1993)

$$\begin{aligned} u_i(x_1 + dx_1, x_2 + dx_2, x_3 + dx_3) = \; & u_i(x_1, x_2, x_3) \\ & + \frac{\partial u_i}{\partial x_1} dx_1 + \frac{\partial u_i}{\partial x_2} dx_2 + \frac{\partial u_i}{\partial x_3} dx_3 \\ & + \left(\textit{Higher orders terms of } dx_1, dx_2 \textit{ and } dx_3\right) \\ \approx \; & u_i(x_1, x_2, x_3) + \nabla u_i \bullet \mathbf{dx} \end{aligned}$$

u(**x**+**dx**) may therefore be written as

$$\begin{aligned} \mathbf{u}(\mathbf{x} + \mathbf{dx}) &\approx \mathbf{u}(\mathbf{x}) + (\nabla u_1 \bullet \mathbf{dx})\mathbf{i} + (\nabla u_2 \bullet \mathbf{dx})\mathbf{j} + (\nabla u_3 \bullet \mathbf{dx})\mathbf{k} \\ &= \mathbf{u}(\mathbf{x}) + \begin{bmatrix} \frac{\partial u_1}{\partial x_1} & \frac{\partial u_1}{\partial x_2} & \frac{\partial u_1}{\partial x_3} \\ \frac{\partial u_2}{\partial x_1} & \frac{\partial u_2}{\partial x_2} & \frac{\partial u_2}{\partial x_3} \\ \frac{\partial u_3}{\partial x_1} & \frac{\partial u_3}{\partial x_2} & \frac{\partial u_3}{\partial x_3} \end{bmatrix} \bullet \mathbf{dx} \\ &= \mathbf{u}(\mathbf{x}) + (\nabla \mathbf{u})^T \bullet \mathbf{dx} \\ &= \mathbf{u}(\mathbf{x}) + \mathbf{dx} \bullet \nabla \mathbf{u} \end{aligned} \tag{A6.1}$$

Appendix B - Macroscopic transport coefficients

The transport coefficients listed in this appendix were derived by Pride (1994). The frequency-dependent complex dynamic permeability, electrokinetic coupling coefficient and electrical conductivity are respectively given by

$$k(\omega) = k_0 \left[\left[1 - i \frac{\omega}{\omega_t} \frac{4}{m} \right]^{1/2} - i \frac{\omega}{\omega_t} \right]^{-1} \tag{B1.1}$$

$$L(\omega) = L_0 \left[1 - i \frac{\omega}{\omega_t} \frac{m}{4} \left(1 - 2 \frac{\tilde{d}}{\Lambda} \right)^2 \left(1 - i^{3/2} \frac{\tilde{d}}{\delta_v} \right)^2 \right]^{-1/2} \tag{B1.2}$$

$$\sigma(\omega) = \sigma_0 \left[1 + \frac{2}{\sigma_f \Lambda} \left(C_{em} + C_{os}(\omega) \right) \right] \tag{B1.3}$$

where k_0, L_0 and σ_0 are the low-frequency (static) permeability, electrokinetic coupling coefficient and conductivity of the porous medium, respectively. ω_t is a transition frequency that separates the low frequency viscous flow from the high frequency inertial flow. It is given by

$$\omega_t = \frac{\phi}{\alpha_\infty k_0} \frac{\eta}{\rho_f} \tag{B1.4}$$

where ϕ and α_∞ are the porosity and tortuosity of the porous medium, respectively. η and ρ_f are the viscosity and mass density of the fluid. m is a dimensionless number consisting of geometric terms only and is defined as

$$m = \frac{\phi \Lambda^2}{\alpha_\infty k_0} \tag{B1.5}$$

The parameter Λ is porous material geometry term being a weighted volume-to-surface ratio as defined by Johnson *et al*. (1987). δ_v is the viscous skin depth defined as

$$\delta_v = \left[\frac{\eta}{\omega \rho_f} \right]^{1/2} \tag{B1.6}$$

The static coupling coefficient is given by

$$L_0 = -\frac{\phi}{\alpha_\infty}\frac{\epsilon_f \zeta}{\eta}\left[1 - 2\alpha_\infty \frac{\tilde{d}}{\Lambda}\right] \tag{B1.7}$$

where ϵ_f is the dielectrical permittivity of the fluid and ζ is the zeta potential. The length $\tilde{d}$ is less than or equal to the Debye length d, given by

$$d = \left[\frac{\epsilon_f k_B T}{e^2 z^2 N}\right]^{1/2} \tag{B1.8}$$

where e is the electronic charge and z is the ionic valence, assuming a z:z electrolyte. N is the ionic concentration in ions per cubic meter and $k_B T$ is the thermal energy where k_B is Boltzmann's constant. Experimental studies on quartz (Pride and Morgan, 1991) showed that the zeta potential is reasonably well represented as

$$\zeta = 0.008 + 0.026 \log_{10} C \tag{B1.9}$$

where C is the molar concentration of the electrolyte ($C = N / 6.022 \times 10^{26}$). The low frequency conductivity σ_0 is defined as

$$\sigma_0 = \frac{\phi}{\alpha_\infty}\sigma_f \tag{B1.10}$$

where σ_f is the fluid conductivity given by

$$\sigma_f = e^2 z^2 N (b_+ + b_-) \tag{B1.11}$$

where b_+ and b_- are the ionic mobilities of the cations and anions, respectively.

C_{os} is the electro-osmotic conductance due to the electrically induced convection of the excess double layer ions and is given by

$$C_{os}(\omega) = \frac{(\epsilon_f \zeta)^2}{2d\eta} P_0 \left(1 - \frac{2i^{3/2}}{P_0}\frac{d}{\delta_v}\right)^{-1} \tag{B1.12}$$

where

$$P_0 = \frac{16kTd^2 N}{\epsilon_f \zeta^2}\left[\cosh\left(\frac{ez\zeta}{2k_B T}\right) - 1\right] \tag{B1.13}$$

C_{em} is the excess conductance associated with the electromigration of double layer ions and is defined as

$$C_{em} = 4de^2z^2Nb\left[\cosh\left(\frac{ez\zeta}{2k_BT}\right)-1\right] \tag{B1.14}$$

Appendix C - A matrix method for analysing plane waves

C1. General description of the method

Aki and Richards (1980) give a description of a matrix method to study seismic plane waves in homogeneous media. When considering plane wave solutions to the system of equations that govern wave motion in homogeneous media, it is possible to write the equations in such a way that only first order depth derivatives of stress an displacement are needed (Aki and Richards, 1980). If the z-axis of a Cartesian co-ordinate system is taken as vertically downwards, the plane wave can then be studied in terms of an equation of the form

$$\frac{\partial \mathbf{h}}{\partial z} = \mathbf{A}\mathbf{h} \tag{C1.1}$$

where $\mathbf{h}$ is a column vector containing the non-zero physical quantities that are continuous across a welded interface, and $\mathbf{A}$ is a constant matrix with entries depending on the elastic properties of the medium and on horizontal (phase) slowness p and angular frequency ω. The advantage of using phase slownesses instead of phase velocities to describe the speed and direction of propagation of a plane wave, is illustrated in Figure C1.1. From Figure C1.1 we see that, for plane waves, phase slownesses may be added vectorially whereas phase velocities may not.

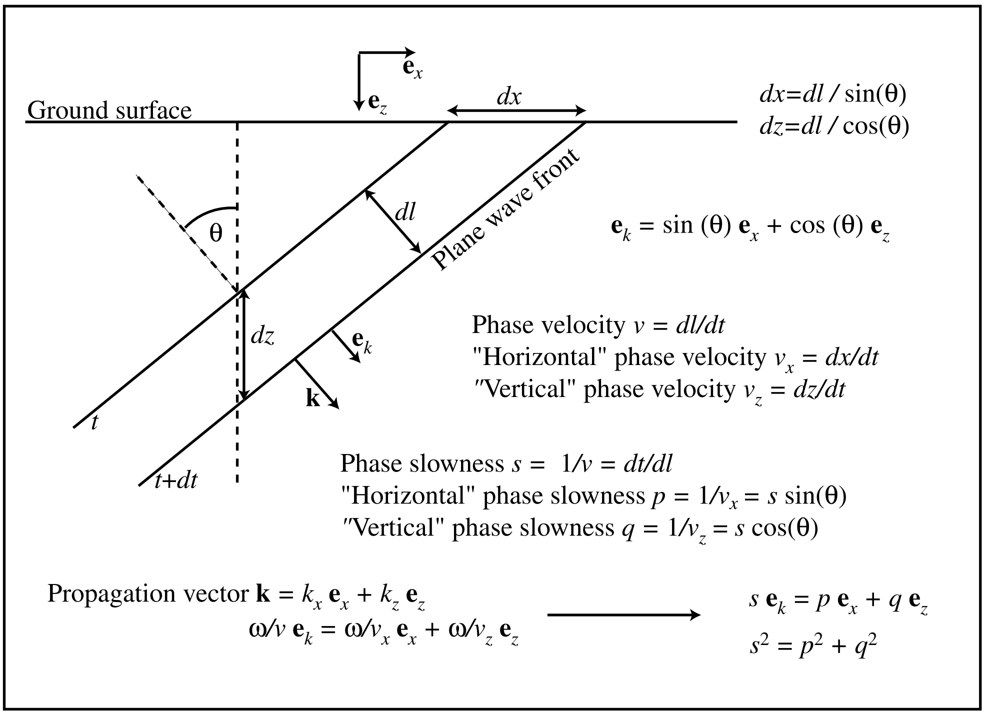

Figure C1.1. Plane wave propagation.

For plane waves propagating in the x-z plane the vector **h** may be expressed as $\mathbf{h} = \mathbf{f} \exp[i\omega(px\text{-}t)]$ where $\mathbf{f} = \mathbf{f}(z)$ is a column vector giving the depth-dependence of the physical quantities in vector **h**. Equation (C1.1) now becomes

$$\frac{\partial \mathbf{f}}{\partial z} = \mathbf{A}\mathbf{f} \tag{C1.2}$$

To illustrate the matrix method, consider plane shear waves with horizontal polarisation, (*SH*-waves) propagating in the x-z plane so that the particle displacement occurs in the y-direction. For this wave geometry Equations (2.13) and (2.19) become

$$\tau_{yx} = \mu u_{y,x} \tag{C1.3}$$

$$\tau_{yz} = \mu u_{y,z} \tag{C1.4}$$

$$\rho \ddot{u}_y = \tau_{yx,x} + \tau_{yz,z} \tag{C1.5}$$

The particle displacement may be described by an equation of the form

$$u_y(x,z,t) = f_{u_y}(z)\exp[i\omega(px - t)] \tag{C1.6}$$

where the $f_{u_y}(z)$ is a function giving the depth dependence of particle displacement. Equations (C1.3) and (C1.4) show that τ_{yx} and τ_{yz} are consequently also of the form

$$\tau_{yx}(x,z,t) = f_{\tau_{yx}}(z)\exp[i\omega(px - t)] \tag{C1.7}$$

$$\tau_{yz}(x,z,t) = f_{\tau_{yz}}(z)\exp[i\omega(px - t)] \tag{C1.8}$$

Substituting Equations (C1.6) to (C1.8) into Equation (C1.5) yields

$$\tau_{yz,z} = \omega^2\left(\mu p^2 - \rho\right)u_y \tag{C1.9}$$

Rewriting Equation (C1.4) in terms of $u_{y,z}$ gives

$$u_{y,z} = \mu^{-1}\tau_{yz} \tag{C1.10}$$

Equations (C1.9) and (C1.10) may be written in matrix form as

$$\frac{\partial}{\partial z}\begin{pmatrix} u_y \\ \tau_{yz} \end{pmatrix} = \begin{pmatrix} 0 & \mu^{-1} \\ \omega^2\left(\mu p^2 - \rho\right) & 0 \end{pmatrix}\begin{pmatrix} u_y \\ \tau_{yz} \end{pmatrix} \tag{C1.11}$$

which is in the form of Equation (C1.1). Note from the boundary conditions in Equations (2.26) and (2.27) that u_y and τ_{yz} are the (non-zero) physical quantities that are continuous across a welded interface. Inserting Equations (C1.6) and (C1.8) into Equation (C1.11) results in an equation of the form of Equation (C1.2) where **A** is the 2×2 matrix given in Equation (C1.11) and **f** is a column vector containing the depth-dependent terms of u_y and τ_{yz}

$$\mathbf{f}(z) = \begin{bmatrix} f_{u_y}(z) \\ f_{\tau_{yz}}(z) \end{bmatrix} \tag{C1.12}$$

If **b** is an eigenvector of **A** and λ is the associated eigenvalue, a particular solution to (C.1.2) is given by

$$\mathbf{f}(z) = \mathbf{b}\exp[\lambda(z - z_0)] \tag{C1.13}$$

where z_0 is a reference level for the phase. Consider the matrix **F** whose columns consist of the different solutions of the form given in (C1.13). If **A** is an $n \times n$ matrix we can find n eigenvalues and n linearly independent eigenvectors. The most general solution to (C1.2) is therefore a linear combination of the columns of **F**. If **w** is a vector of weighting constants, then the general solution of (C1.2) is given by

$$\mathbf{f} = \mathbf{F}\mathbf{w} \tag{C1.14}$$

An analysis of plane waves in terms of eigenvectors and eigenvalues is powerful due to the physical interpretation of Equation (C1.13). The characteristic equation of **A** is found to be

$$\begin{aligned} \lambda^2 &= -\omega^2(\rho/\mu - p^2) \\ &= -\omega^2(s^2 - p^2) \\ &= -\omega^2 q^2 \end{aligned} \tag{C1.15}$$

where s is the phase slowness and q is the vertical phase slowness. We therefore have the following eigenvalues for **A**

$$\lambda_1 = +i\omega q \qquad \lambda_2 = -i\omega q \tag{C1.16}$$

The corresponding eigenvectors are

$$\mathbf{b}_1 = \begin{pmatrix} 1 \\ +i\omega\mu q \end{pmatrix} \qquad \mathbf{b}_2 = \begin{pmatrix} 1 \\ -i\omega\mu q \end{pmatrix} \tag{C1.17}$$

From Equation (C1.13) we therefore have the following basic solutions for *SH*-waves

$$\mathbf{f}_1 = \begin{pmatrix} 1 \\ +i\omega\mu q \end{pmatrix} \exp\left[+i\omega q(z - z_0)\right] \tag{C1.18}$$

$$\mathbf{f}_2 = \begin{pmatrix} 1 \\ -i\omega\mu q \end{pmatrix} \exp\left[-i\omega q(z - z_0)\right] \tag{C1.19}$$

It is clear that Equation (C1.18) gives particle displacement and shearing stress for down-going *SH*-waves, while Equation (C1.19) gives particle displacement and shearing stress for up-going *SH*-waves. This observation allows us to get a physical interpretation of **w**. The first component of **w** gives the amount of down-going wave and the second component gives the amount of up-going wave present in the total wave system $\mathbf{f} = \mathbf{F}\mathbf{w}$. The matrix **F** can be factorised into a matrix $\mathbf{E}_f$, made up of the eigenvectors of **A**, and a diagonal matrix Λ_f containing the vertical phase factors

$$\begin{aligned} \mathbf{F} &= \begin{pmatrix} 1 & 1 \\ i\omega\mu q & -i\omega\mu q \end{pmatrix} \begin{pmatrix} \exp\left[+i\omega q(z - z_0)\right] & 0 \\ 0 & \exp\left[-i\omega q(z - z_0)\right] \end{pmatrix} \\ &= \mathbf{E}_f \Lambda_f \end{aligned} \tag{C1.20}$$

C2. Using the matrix method to calculating transmission and reflection coefficients

The matrix method illustrated here is an adaptation of the method presented by Ranada Shaw *et al.* (2000). The transmission coefficient (T_{sh}) and reflection coefficient (R_{sh}) of *SH*-waves on a boundary between two media can now be obtained. Consider an interface, at a depth of z_1, between two media. In the upper medium ($z < z_1$) the wave system is given by

$$\mathbf{f} = \mathbf{F}(\mathrm{z})\mathbf{w}_u = \mathbf{E}_f\, \Lambda_f(z)\, \mathbf{w}_u, \tag{C2.1}$$

where **F** is given by Equation (C1.20) with the values of ρ, μ and p appropriate for the upper medium. The components of $\mathbf{w}_u$ give the amounts of down-going and up-going waves in the upper medium. Similarly, in the lower medium we have $\mathbf{g} = \mathbf{G}(\mathrm{z})\mathbf{w}_l = \mathbf{E}_g\, \Lambda_g(z)\, \mathbf{w}_l$. Due to the continuity $\mathbf{f} = \mathbf{g}$ across $z = z_1$, so that

$$\mathbf{F}(z_1)\mathbf{w}_u = \mathbf{G}(z_1)\mathbf{w}_l \qquad \text{(C2.2)}$$

For convenience, choose the reference level of the phase so that $z_0 = z_1$. On the interface we therefore have $\Lambda_f = \mathbf{I}$, where $\mathbf{I}$ is the identity matrix, and $\mathbf{F} = \mathbf{E}_f$. Similarly we have $\Lambda_g = \mathbf{I}$ and $\mathbf{G} = \mathbf{E}_g$.

To solve for T_{sh} and R_{sh} we choose the weighting vectors as follows

$$\mathbf{w}_u = \begin{pmatrix} 1 \\ R_{sh} \end{pmatrix} \qquad \mathbf{w}_l = \begin{pmatrix} T_{sh} \\ 0 \end{pmatrix} \qquad \text{(C2.3)}$$

Substitution of the weighting vectors into Equation (C2.2) yields two scalar equations in the two unknowns T_{sh} and R_{sh} , given by

$$\begin{pmatrix} G_{11} & -F_{12} \\ G_{21} & -F_{22} \end{pmatrix} \begin{pmatrix} T_{sh} \\ R_{sh} \end{pmatrix} = \mathbf{D} \begin{pmatrix} T_{sh} \\ R_{sh} \end{pmatrix} = \begin{pmatrix} F_{11} \\ F_{21} \end{pmatrix} \qquad \text{(C2.4)}$$

where F_{ij} and G_{ij} indicate the entry occurring at the i^{th} row and j^{th} column of the matrices **F** and **G**. The reflection and transmission coefficients are consequently given by

$$\begin{pmatrix} T_{sh} \\ R_{sh} \end{pmatrix} = \mathbf{D}^{-1} \begin{pmatrix} F_{11} \\ F_{21} \end{pmatrix} \qquad \text{(C2.5)}$$

Although the matrix method is only illustrated for *SH*-waves in this appendix, the same reasoning can be applied to *SV* and pressure (*P*-) waves. Since plane *P*- and *SV*-waves both involve displacements in the *x*-*z* plane, these waves are coupled by boundary conditions on horizontal planes, and mode conversion between these wave types may occur at boundaries. The matrix method applied to the combined *P*-*SV* wave problem yields the following expressions for the matrices **E** and Λ (Aki and Richards, 1980)

$$
\mathbf{E}=\begin{pmatrix}
\dfrac{p}{s_P} & \dfrac{q_{SV}}{s_{SV}} & \dfrac{p}{s_P} & \dfrac{q_{SV}}{s_{SV}} \\
\dfrac{q_P}{s_P} & \dfrac{-p}{s_{SV}} & \dfrac{-q_P}{s_P} & \dfrac{p}{s_{SV}} \\
2i\omega\rho\dfrac{pq_P}{s_P s_{SV}^2} & \dfrac{i\omega\rho}{s_{SV}}\left(1-2\dfrac{p^2}{s_{SV}^2}\right) & -2i\omega\rho\dfrac{pq_P}{s_P s_{SV}^2} & \dfrac{-i\omega\rho}{s_{SV}}\left(1-2\dfrac{p^2}{s_{SV}^2}\right) \\
\dfrac{i\omega\rho}{s_P}\left(1-2\dfrac{p^2}{s_{SV}^2}\right) & -2i\omega\rho\dfrac{pq_{SV}}{s_{SV}^3} & \dfrac{i\omega\rho}{s_{SV}}\left(1-2\dfrac{p^2}{s_{SV}^2}\right) & -2i\omega\rho\dfrac{pq_{SV}}{s_{SV}^3}
\end{pmatrix}
$$

(C2.6)

$$
\Lambda=\begin{pmatrix}
e^{+i\omega q_P(z-z_0)} & 0 & 0 & 0 \\
0 & e^{+i\omega q_{SV}(z-z_0)} & 0 & 0 \\
0 & 0 & e^{-i\omega q_P(z-z_0)} & 0 \\
0 & 0 & 0 & e^{-i\omega q_{SV}(z-z_0)}
\end{pmatrix} \qquad \text{(C2.7)}
$$

where s_P and s_{SV} are the phase slownesses of the *P*- and *SV*-waves, and q_P and q_{SV} are the vertical phase slownesses of the *P*- and *SV*-waves, respectively. To obtain the transmission and reflection coefficients of a *P*-wave incident on an interface, for example, the weigthing vectors in the upper and lower media may be chosen as follows

$$
\mathbf{w}_u=\left(1,\quad 0,\quad R_{p-p},\quad R_{p-sv}\right)^T \qquad \mathbf{w}_l=\left(T_{p-p},\quad T_{p-sv},\quad 0,\quad 0\right)^T \qquad \text{(C2.8)}
$$

where $R_{p\text{-}p}$ and $T_{p\text{-}p}$ are the reflection and transmission coefficients of the *P*-wave components, whereas $R_{p\text{-}sv}$ and $T_{p\text{-}sv}$ are the reflection and transmission coefficients of the mode converted *SV*-waves. Substitution of the weighting vectors into Equation (C2.2) yields four scalar equations in the four unknowns. The transmission and reflection coefficients are given by

$$
\left(T_{p-p},\quad T_{p-sv},\quad R_{p-p},\quad R_{p-sv}\right)^T=\mathbf{D}^{-1}\left(F_{11},\quad F_{21},\quad F_{31},\quad F_{41}\right)^T \qquad \text{(C2.9)}
$$

where

$$
\mathbf{D}=\begin{pmatrix}
G_{11} & G_{12} & -F_{13} & -F_{14} \\
G_{21} & G_{22} & -F_{23} & -F_{24} \\
G_{31} & G_{32} & -F_{33} & -F_{34} \\
G_{41} & G_{42} & -F_{43} & -F_{44}
\end{pmatrix} \qquad \text{(C2.10)}
$$

C3. Using the matrix method to investigate the thin layer response

Consider a thin layer imbedded in another medium, with the top interface at depth $z = z_1$ and bottom interface at depth $z = z_2$, as in Figure C3.1.

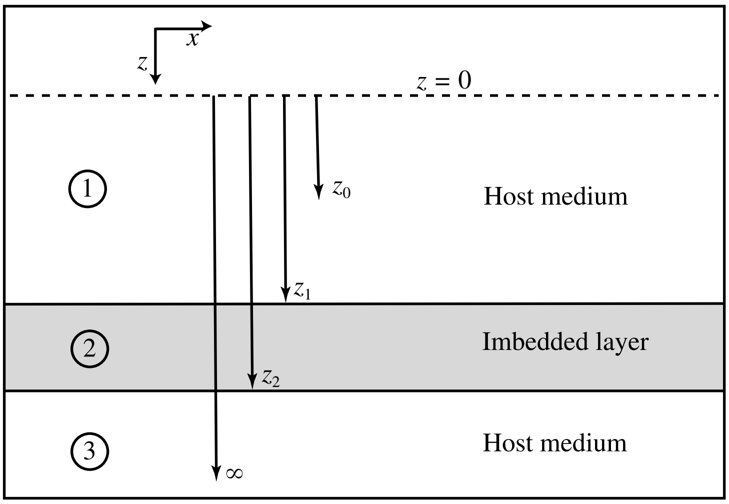

Figure C3.1. Model used for investigating the thin bed response.

According to Equation (C2.1) the vectors describing the wave-fields in the media 1, 2 and 3 are given by

$$\mathbf{f}_i = \mathbf{E}_i \Lambda_i \mathbf{w}_i \qquad i = 1, 2, 3 \tag{C3.1}$$

Since media 1 and 3 are the same, we have $\mathbf{E}_1 = \mathbf{E}_3$ and $\Lambda_1 = \Lambda_3$. The boundary conditions at each interface require that

$$\mathbf{f}_1 = \mathbf{f}_2 \quad \text{when } z = z_1 \tag{C3.2}$$

$$\mathbf{f}_2 = \mathbf{f}_3 \quad \text{when } z = z_2 \tag{C3.3}$$

The two boundary conditions give rise to two equations of the form

$$\mathbf{A}\,\mathbf{w}_1 = \mathbf{B}\,\mathbf{w}_2 \tag{C3.4}$$

$$\mathbf{C}\,\mathbf{w}_2 = \mathbf{D}\,\mathbf{w}_3 \tag{C3.5}$$

Eliminating vector $\mathbf{w}_2$ yields the following relation between $\mathbf{w}_1$ and $\mathbf{w}_3$

$$\mathbf{w}_1 = \mathbf{A}^{-1}\mathbf{B}\mathbf{C}^{-1}\mathbf{D}\,\mathbf{w}_3 = \mathbf{M}\,\mathbf{w}_3 \tag{C3.6}$$

With appropriate choices of the weighting vectors, Equation (C3.6) may be used to investigate the thin bed response. For example, to investigate the thin bed response to pressure wave excitation in the *P-SV* mode, the weighting vectors should be chosen as follows

$$\mathbf{w}_1 = \left(1, \quad 0, \quad w_{13}, \quad w_{14}\right)^T \qquad \mathbf{w}_3 = \left(w_{31}, \quad w_{32}, \quad 0, \quad 0\right)^T \tag{C3.7}$$

(This choice of weighting vectors corresponds to the situation where there is only a down-going pressure wave and reflected (up-going) pressure and shear waves in medium 1, while medium 2 carries only down-going pressure and shear waves.) The coefficients w_{13} and w_{14} should then be determined from Equation (C3.6) to evaluate the amplitudes of the *P* and SV-waves reflected from the thin layer.

Summary

The possibility of using surface electroseismic (ES) methods for groundwater exploration in fractured Karoo rocks is studied by investigating the criteria of vertical and lateral resolution of surface ES data and the ES thin bed response. The ES Fresnel zones for monochromatic excitation are found to be larger than their seismic equivalents and the lateral resolution of surface ES data is consequently poorer. Seismic velocity increases with depth result in larger ES Fresnel zones and poorer lateral resolution. As in seismics, only a single Fresnel zone can be identified for broadband excitation. Higher dominant frequencies and broader bandwidth result in higher lateral resolution.

Rayleigh's criterion for vertical resolution applied to ES data requires that the imbedded layer has a thickness of at least $\lambda/2$ to be deemed resolvable, where λ is the wavelength of the seismic wave under consideration. There are, however, two wavelengths to consider for ES phenomena – those of the Biot fast pressure and slow pressure waves. Since the wavelength of the slow pressure wave in saturated Karoo rocks may be a couple of orders of magnitude smaller than the wavelength of the fast pressure wave, the theoretical limit of resolution is determined by the slow pressure wave. This wave is, however, strongly dissipative and the practical limit of resolution seems to depend more strongly on the wavelength of the fast pressure wave.

A simplified approach to examine the ES thin bed response suggests that imbedded layers with thicknesses smaller than $\lambda/2$, where λ is the wavelength of the fast pressure wave, may be classified as electroseismically thin. Investigations by means of a full waveform approach that simultaneously takes the influence of the different wave types into consideration, supports the above observation.

The results of an ES field survey on a site where a localised fracture is known to occur, supports the idea, but does not conclusively proof, that the lateral and vertical resolution of surface ES data is insufficient to detect fractures with apertures in the millimetre to centimetre range.

The influence of porosity contrasts on ES reflection is studied by examining the change in the magnitude of the reflection coefficients when varying the porosity (and all porosity-dependent parameters, such as permeability) of a Karoo sandstone overlain by a Karoo mudstone. Increases in the sandstone porosity results in larger reflection coefficients, and consequently, stronger reflection. The possibility therefore exists to map porosity contrasts in a certain geological environment and thus identify zones more likely to be suitable as aquifers.

The possibility of using ES techniques as a non-invasive means of obtaining information on the elastic properties of the rock matrix is investigated by examining the electroseismic and magnetoseismic transfer functions at positions in boreholes. The transfer functions are dependent on various physical and chemical parameters, including the elastic parameters and none of these parameters can be determined unambiguously from the evaluation of the different transfer functions. The shear modulus of the porous frame may be estimated from measurements of the shear wave velocity in a fluid-saturated porous system. Since an approximate linear relation exists between the shear and bulk moduli of the porous frame, the bulk modulus may be estimated once the shear modulus is known.

Porosity changes due to aquifer deformation may lead to detectable changes in the transfer functions. The electroseismic transfer function of the fast pressure wave is insensitive to porosity changes in consolidated material. Although the electroseismic transfer function of the slow pressure wave is very sensitive to porosity changes, this wave is strongly dissipative and is notoriously difficult to measure. The magnetoseismic transfer function is sensitive to porosity changes and is likely to yield the most useful information on aquifer deformation.

Keywords: *electroseismic, resolution criteria, fracture detection, groundwater exploration, elastic parameters, aquifer deformation, ES reflection.*

Opsomming

Die moontlikheid om oppervlak elektroseismiese (ES) metodes te gebruik vir grondwatereksplorasie in gefraktureerde Karoo-gesteentes word bestudeer deur die kriteria van vertikale en laterale resolusie van oppervlak ES data en die dunlaagresponsie te ondersoek. Die ES Fresnel-zones vir monochromatiese opwekking is groter as hul seismiese ekwivalente en die laterale resolusie van oppervlak ES data is gevolglik swakker. Seismiese snelheidstoenames met diepte lei tot groter Fresnel-zones en swakker laterale resolusie. Soos in seismies kan slegs 'n enkele Fresnel-zone vir breëband-opwekking geïdentifiseer word. Bronne met hoër dominante frekwensies en breër bandwydte het hoër laterale resolusie tot gevolg.

Rayleigh se kriterion vir vertikale resolusie toegepas op ES data vereis dat die ingebedde laag a dikte van ten minste $\lambda/2$ moet hê, waar λ die golflengte van die seismiese golf in ondersoek is, om as oplosbaar beskou te word. Daar is egter twee golflengtes om in ag te neem - die van die Biot vinnige en stadige drukgolwe. Aangesien die golflengte van die stadige drukgolf in versadigde Karoo-gesteentes 'n paar ordegroottes kleiner as die golflengte van die vinnige drukgolf mag wees, word die teoretiese perke van resolusie bepaal deur die stadige drukgolf. Hierdie golf is egter sterk kwistend en die praktiese perke van resolusie blyk sterker afhanklik te wees van die golflengte van die vinnige drukgolf.

'n Vereenvoudigde benadering om die ES dunlaagresponsie te ondersoek dui aan dat ingebedde lae met diktes van kleiner as $\lambda/2$, waar λ die golflengte van die vinnige drukgolf is, as elektroseismies dun geklassifiseer mag word. Ondersoeke deur middel van 'n volle golfvorm-benadering wat gelyktydig die invloede van die verskillende golftipes in ag neem, ondersteun bostaande observasie.

Die resultate van 'n ES veldopname op 'n terrein waar 'n bekende gelokaliseerde fraktuur voorkom, ondersteun die idee, maar bewys nie onweerlegbaar nie, dat die vertikale en lateral resolusie van oppervlak ES data onvoldoende is om frakture met openinge in die millimeter- tot sentimeterbestek waar te neem.

Die invloed van porositeitskontraste op ES refleksie word ondersoek deur die verandering in die grootte van die refleksiekoeffisiënte te bestudeer wanneer die porositeit (en alle porositeitsafhanklike parameters, soos permeabiliteit) van 'n Karoo-sandsteen, oorlê deur 'n Karoo-moddersteen, verander word. Toenames in die sandsteenporositeit lei tot groter refleksiekoeffisiënte, en gevolglik sterker refleksie. Die moontlikheid bestaan dus dat porositeitskontraste in 'n spesifieke geologiese omgewing gekarteer kan word en dat zones wat meer waarskynlik geskik is as akwifere geïdentifiseer kan word.

Die moontlikheid om ES-tegnieke te gebruik as 'n nie-indringende metode om informasie oor die elastisiteitseienskappe van die gesteente-matriks te bekom word ondersoek deur die elektroseismiese en magnetoseismiese oordragsfunksies by posisies in boorgate te bestudeer. Die oordragsfunksies is afhanklik van verskeie fisiese en chemiese parameters, insluitend die elastisiteitsparameters, en geeneen van hierdie parameters kan eenduidig uit die evaluasie van die oordragsfunksies bepaal word nie. Die skeurmodulus van die poreuse raamwerk kan uit metings van die skeurgolfsnelheid in 'n vloeistofversadigde poreuse sisteem beraam word. Aangesien daar 'n bykans linieêre verband tussen die skeur- en die bulkmoduli van die poreuse raamwerk bestaan, kan die bulkmodulus geskat word sodra die skeurmodulus bekend is.

Porositeitsveranderinge as gevolg van akwifeerdeformasie mag lei tot waarneembare veranderinge in die oordragsfunksies. Die elektroseismiese oordragsfunksie van die vinnige drukgolf is onsensitief vir porositeitsveranderinge in gekonsolideerde materiaal. Alhoewel die elektroseismiese oordragsfunksie van die stadige drukgolf baie sensitief is vir porositeitsveranderinge, is hierdie golf baie kwistend en berug om moeilikheid te wees om te meet. Die magnetoseismiese oordragsfunksie is sensitief vir porositeitsveranderinge en sal waarskynlik die mees bruikbare inligting oor akwifeerdeformasie lewer.

Sleutelwoorde: *elektroseismies, resolusie kiteria, fraktuurwaarneming, grondwatereksplorasie, elastiese parameters, akwifeerdeformasie, ES refleksie.*